Fire Performance of Shear Studs in Transverse Deck Slabs

Ohk Kun Lim
(BSc MSc)

Faculty of Computing, Engineering and the Built Environment

Ulster University

Thesis Submitted for the Degree of

Doctor of Philosophy

April 2020

I confirm that the word count of this thesis is less than 100,000 words.

Contents

List of Figures

List of Tables

Nomenclature

Latin letters	
A	General area
D	Damage parameter
E	Elastic modulus, Energy
G	Shear modulus
L	Length of element or material
P	Shear resistance of the shear connection
Q	Energy transferred per time
U	Strain energy
W	Crack opening distance
F_ε	Fracture strain
G_f	Fracture energy
K_C	Deviatoric stress ratio between the tensile and compressive meridian
R_p	Reduction factor regarding the stud location in a rib
V_c	Configuration factor (view factor)
b	Width of the rib
c	Cohesion stress
d	Diameter, Distance
f	Stress
h	Convection coefficient
k	Empirical constant
p	Hydrostatic stress
q	Deviatoric stress, Heat flux
str	Stress triaxiality
t	Time
c_p	Specific heat of material
e_{mid-ht}	Distance between the edge of the stud shank and mid-height of the deck in the load-bearing direction
k_t	Transverse deck reduction factor
n_r	Number of studs in a rib

Subscripts	
bi	Biaxial stress state
c	Concrete
cc	Triaxial compressive state
deck	Trapezoidal deck
e	Experimental data
k	Characteristic value
sc	Headed shear stud
tri	Triaxial stress state
u	Ultimate value

Greek letters	
α, β, γ	Plasticity parameter for concrete model
ε	Strain
θ	Temperature
λ	Thermal conductivity
μ	Friction coefficient
ρ	Density of the material
σ	Stress
ϕ	Internal friction angle
ψ	Dilation angle
Φ_{sc}	Resistance factor in shear strength calculation
γ_M	Material safety factor
ε_G	Eccentricity of the plastic potential function
ε_R	Fracture strain in a uniaxial state
ε_{mi}	Emissivity parameter of materials
θ_L	Load angle
σ_{SB}	Stefan-Boltzmann constant [= 5.67×10^8 W/m^{2}K^4]

Abbreviations	
ANSI	American National Standard Institute
AISC	American Institute of Steel Construction

CDP	Concrete Damaged Plasticity
FEM	Finite Element Method
FLS	Fire Limit State
SRF	Strength Reduction Factor
ULS	Ultimate Limit State

Acknowledgement

I would like to express my sincere gratitude and appreciation to my supervisor Dr. Sengkwan Choi and Dr. Jianping Zhang for their endless support, encouragement and guidance throughout the course of my study.

I would also like to express my gratitude to the staff members of the research office and school of the built environment of Ulster University for their kind response and support.

I am truly indebted to Dr. J. Y. Choi, Dr. Sungwook Kang and Mr. Minjae Kwon for their technical support and encouragement. Additional gratitude is to Mr. Rumeel Ahmad Bhutta for his consistent help which makes me possible to finish my calculation.

Finally, I sincerely appreciate my family for their patience and support.

April 2020

Ohk Kun Lim

This work described herein was carried out by the candidate during a period from September 2014 to August 2019 under the supervision of Dr. Sengkwan Choi and Dr. Jianping Zhang.

Several publications and award related to this thesis are listed in the following:

1. Journal paper

- Lim, O. K., Choi, S., Kang, S., Kwon, M., Choi, J. Y., (2019) Experimental studies on the behaviour of headed shear studs for composite beams in fire, Steel and Composite Structures, *An International Journal*, 32(6), 743-752

- Lim, O. K., Choi, S., Kang, S., Kwon, M., Choi, J. Y., (2020) Fire performance of headed shear studs in profiled steel sheeting, *Journal of Constructional Steel Research*, 164, 105791

2. Conference paper

- Lim, O. K., Choi, S., Numerical studies on headed shear studs under elevated temperatures, Proceedings of the International Conference of Applications of Structural Fire Engineering (ASFE 2017), 247-255, September, 2017, Manchester, UK.

- Lim, O. K., Choi, S., Kang, S., Kwon, M., Choi, J. Y., Experimental studies on the behaviour of headed shear studs for composite beams in fire, The World Congress on Advances in Structural Engineering and Mechanics (ASEM 19), September, 2019, Jeju Island, Korea.

3. Award

- Lim, O. K., Research Graduate School Annual PhD Conference Award for Best Poster, Faculty of Art, Design & Built Environment, Academic year 2016/17, Ulster University.

Abstract

Steel and concrete composite structures are frequently utilised in multi-story buildings, as they maximise the material merits via composite action, which is achieved by a shear connection between the steel and concrete sections. The fire performance of the shear connection is a primary parameter in composite beam design, which has been investigated with a focus on adopting solid concrete slabs. Despite the popularity of embracing profiled steel sheeting in composite construction, the fire behaviour of shear studs embedded in a transverse deck slab remains to be confirmed.

This thesis presents experimental and numerical studies on the behaviour of the shear connection when headed shear studs are incorporated with a transverse deck slab both at ultimate and fire limit states. High-temperature push-out tests were experimentally conducted, and finite element models were developed using a commercial package, Abaqus. Concrete plasticity parameters for high-temperature applications were proposed to simulate a concrete-dominated fracture in the push-out test models. The accuracy of the developed numerical models was verified using experimental data, which demonstrate a strong correlation in the shear resistance and failure modes at different temperatures.

The failure mode transforms from a concrete pull-out into stud shearing as the temperature increases in the transverse deck specimen owing to a higher thermal degradation of stud material. The shearing location also approaches the bottom of the shear stud as fire exposure time increases. Parametric studies using the developed numerical models were conducted, including several variables such as the stud welding method, deck thickness, stud location, and number of studs in a trough. Although all the mentioned variables influence the shear resistance in the ultimate limit state, their effects decrease with increasing temperature. Since the current design code of EC4-1-2 (2014) shows a different response in comparison to experimental data, modified design rules for shear resistance calculation in the fire limit state have been proposed herein depending on failure modes.

Chapter 1
INTRODUCTION

1.1. Structures in fire

Fire safety has become a significant design criterion in modern construction, owing to the increasing scale of the size and risk of various combustible materials in buildings. A building should maintain stability for a designated period in the event of a fire to ensure the safety of occupants and firefighters. Active and passive fire protection methods are used to control fire spread and maintain structural stability according to the Approved Document B of the Building Regulations (DCLG, 2013) in the UK and the International Building Code (ICC, 2018) in the US.

Design guides provide different fire resistance ratings in accordance with the purpose group and type of building elements. To meet this design criterion with respect to structural fire engineering, the fire severity is first predicted for each element of a building, and the building components are designed to have a higher load-bearing capacity than the imposed load, including the effect of fire. Thus, a primary component, depending on the construction type, must be considered to maintain a load-bearing capacity for the duration of a fire.

Steel and concrete composite structures have been widely used in the UK, having accounted for 66.2 % of the multi-storey non-residential building market in 2017 (Steelconstruction.info, 2018). Since a composite construction has several benefits such as reduced construction time, improved construction safety, greater structural stability, and shallower floors. Composite construction can yield cost savings of approximately 7–12 % compared with other construction systems (Rackham *et al*., 2009). These advantages are

achieved by composite interactions and profiled steel decking. Concrete slabs with a trapezoidal deck are commonly utilised in modern construction, because the rib deck is used both as a working platform for stud welding and a formwork during concrete casting.

A concrete slab and steel beam are joined together in composite beams to act as a unit. A shear connector is employed between the concrete slab and steel beam to achieve a composite action. Consequently, the shear connector is a critical component in determining the stability of composite beams. For structural fire design, it must be evaluated whether the capacity of the shear connection is sufficient to maintain a stiffness under given temperature conditions.

Headed shear studs have been the most widely used for shear connectors because they provide rapid and reliable weldability after the development of the automatic stud welding machine. The headed shear stud is welded through the deck on to a flange of supporting beams when embracing a decking. Otherwise, it is welded directly on the steel flange in the case of adopting a solid concrete slab. A typical example of a composite floor with a trapezoidal deck is shown in Fig. 1-1. The headed shear studs are welded through the deck, and steel beams are positioned along the lines of the shear studs to achieve a composite interaction.

Figure 1-1. Typical composite beam construction (ArchiEXPO, 2018)

Much research has been done regarding the capacity of the shear connection embedded in a trapezoidal deck slab in the ultimate limit state (ULS) because the employment of trapezoidal deck slabs has been becoming more popular than solid slabs in composite construction. EC4-1-1 (2009) consider several parameters, such as the deck thickness, stud welding method, number of studs in a rib, reinforcement placement, and stud location in a trough to estimate the strength of the shear connection based on experimental investigations. Similar empirical formulas are also adopted in other design guidelines at ULS: BS5950-3.1 (2010), AISC 360-10 (2010), and CSA S16-01 (2001).

EC4-1-2 (2014) recommend using a strength reduction factor (SRF) to estimate the remaining strength proportionally at a given temperature. It is determined by multiplying the SRF and shear resistance at ULS. A different SRF is applied depending on the stud failure modes, and the lowest value is selected to design the composite beams. The SRF in EC4-1-2 (2014) was proposed by Zhao and Kruppa (1993) through high-temperature push-out tests. Most of the specimens used in the experiment incorporated a solid slab, and only two specimens made of a transverse deck slab. Although the shear resistance and failure mode are changed with respect to the slab types at ULS, the same SRF is used for design. It needs to be verified whether the shear resistance calculation method according to EC4-1-2 (2014) is valid in transverse deck applications.

Few researchers have addressed the load-bearing capacity of shear connections embedded in a transverse deck slab at the fire limit state (FLS). Mirza *et al*. (2011) carried out a high-temperature push-out test using transverse deck specimens. All the failure modes were a concrete-dominated failure. The shear resistance reduced by 41 % when the stud temperature approached 600 °C. Chen *et al*. (2015) conducted experimental and numerical studies using six specimens with a transverse deck slab. Two different failure modes, concrete rib shearing and stud shearing, were observed as the stud temperature increased. The shear resistance decreased by 31 % at the stud temperature of 600 °C. Discrepancies in the strength reduction and failure mode were found in comparison with the experiment of Mirza *et al*. (2011). This contrasting result may be caused by the different experimental conditions, such as the configuration of the specimen, dimensions of the decking, and heating profile of the furnace. Furthermore, the SRF in the case of the concrete-dominated failure in EC4-1-2 (2014) was proved to have an insufficient reduction compared to the

results of both experiments mentioned above. There remains a need for an evaluation of the behaviour of shear studs embedded in transverse deck slabs in a fire. This will contribute to filling a knowledge gap with respect to composite beam design for performance at elevated temperatures.

1.2. Context of this project

Aim and objectives

The aim of this research is to investigate the behaviour of the shear connection when headed shear studs are embedded in a transverse deck slab under elevated temperatures. In order to achieve this aim, experimental and numerical analyses are used. High-temperature push-out tests are performed with variations of the stud welding method and deck thickness. Comprehensive finite element models are developed and verified against the experimental results at different temperatures. Parametric studies are carried out to evaluate the behaviour of the shear connection in different construction conditions, such as the stud welding method, deck thickness, stud location, and number of studs in a trough. The objectives of this research are outlined as follows:

(1) To investigate the failure mode and failure mechanism of the shear connection embedded in transverse deck slabs in a fire.

(2) To analyse the SRF of EC4-1-2 (2014) which currently applied to composite beam design based on high-temperature push-out tests. Different calculation methods are recommended in EC4-1-2 (2014) depending on expected failure modes, and the smaller value is adopted to design.

(3) To evaluate the effect of the deck reduction factor defined in EC4-1-1 (2009) under elevated temperature. It has been proved to affect the load-bearing capacity of shear connections when embracing a transverse deck at ambient conditions. However, the effectiveness at high temperature has not been studied.

(4) To develop plasticity parameters of the concrete-damaged plasticity model for high-temperature applications.

(5) To conduct a parametric study based on verified finite element models to assess the influencing parameter in deciding the shear resistance and failure mode of shear connection at different levels of temperature.

(6) To propose design recommendations for the load-bearing capacity of shear connections in composite beams at high temperatures.

Summary of chapters

This thesis is organised into five major chapters describing experimental and numerical studies related to the behaviour of the shear connection in composite beams with a transverse deck slab in a fire.

A comprehensive review of previous work related to the shear connection in composite beams is described in Chapter 2. The failure mechanism of the shear connection and its influencing parameters are examined along with relevant design codes. The review is extended to experimental and numerical studies under elevated temperatures, demonstrating that little work has been done regarding shear studs embedded in a transverse deck at high temperature.

Chapter 3 presents the material constitutions of the push-out test components for a finite element model. The yield criteria of the steel and concrete materials are investigated, and concrete plasticity parameters are proposed for a high-temperature application.

A detailed experimental programme is explained in Chapter 4. Push-out test specimens are prepared including solid and transverse deck slabs with variations in the deck thickness, stud welding method, and concrete strength. A customised electric furnace is designed with respect to the configuration of the specimen. Push-out tests are conducted at ULS and FLS. The obtained shear resistances are compared with the design guidelines of EC4-1-2 (2014). The capacity of the shear connection and its failure modes are analysed based on the experimental results.

Chapter 5 presents the development and verification of three-dimensional thermomechanical finite element models. The thermal and mechanical models are developed separately and combined to analyse the performance of the shear connection in a fire using the Abaqus, a commercial software package. The developed models are verified at each step (thermal, mechanical, and thermomechanical evaluations) using the obtained experimental data provided in Chapter 4.

Parametric studies on the shear connection with a transverse deck slab are presented in Chapter 6. The shear resistance and failure modes are examined with respect to several parameters such as the temperature, stud welding method, deck thickness, stud location, and number of studs in a trough. Design guidelines for a transverse deck composite beam in a fire are proposed based on the numerical investigation.

Conclusions are drawn and recommendations for future works are offered in Chapter 7, which were extracted from the experimental and numerical studies presented in this research.

Chapter 2
LITERATURE REVIEW

2.1. Introduction

Extensive research has been conducted to evaluate the structural capacity of shear connections, as it determines a composite interaction in composite beams. Various types of shear connectors have been utilised in composite construction, such as bars, channels, and headed studs. Among these, the headed stud has been the most widely used since the mid-1950s, because the development of automatic stud welding machines has made the fastening process quick, reliable, and economical. Initially, shear studs were embedded in solid concrete slabs. Since the development of a trapezoidal configuration of steel decking, it has become more prevalent in composite constructions. The shear connection behaviour at high temperatures has been studied since the 1990s, and the majority of these works focus on the headed shear stud in a solid slab. In this chapter, the literature on the structural performance of shear studs and their evaluating methods is reviewed.

2.2. Structural design philosophy at ULS and FLS

Composite beams are composed of three major elements: a steel beam, concrete slab, and shear connector. The steel beam resists a tensile load, and the concrete slab withstands a compressive load. The shear connector transfers a shear force to obtain a composite action which makes the different components act together as a unit. The capacity of the shear connection is a primary parameter to maintain structural stability. Consequently, the shear connection must be stronger than an imposed structural load at both ULS and FLS.

The ULS design considers a failure of structural elements by adopting an expected characteristic load and characteristic strength of construction materials. The word 'characteristic' means that it contains statistical uncertainty. This reduces the probability of failure under extreme loading conditions. The calculated characteristic load has a 5 % probability of being exceeded by normally distributed values; the standard deviation with a factor of 1.64 is added to the mean value to obtain the characteristic load. Conversely, the characteristic material strength lies in a 5 % rejection limit, which indicates that the standard deviation is subtracted from the mean value. To obtain structural stability in ULS design, the characteristic material strength should be higher than the characteristic load. A partial safety factor is also added to improve the margin of safety. This factor is generally provided in design codes.

The limit state design concept can be extended to structural fire design considering an accidental load caused by fire. Structural stability can be identified by the load-bearing capacity (R), insulation (I), and integrity (E) at FLS. The integrity is the capacity of structures not to pass gases or flames in case of fire, which is determined by experimental investigations. When designing a composite beam according to EC4-1-2 (2014), the critical temperatures of the steel beam and concrete slab need to be checked. The calculated design temperature of elements should not exceed the critical temperature for the duration of a fire. Thermal insulation methods such as applying an intumescent coating and providing sufficient slab thickness are used to meet the insulation criterion. In the case of the load-bearing capacity, the resistance of a shear connection is compared with the calculated shear force acting on the steel and concrete sections at a given temperature. It is designed to resist the structural load considering the degraded material strength due to an elevated temperature. A partial safety factor is also utilised in FLS design.

2.3. Push-out test for shear connection

2.3.1. Standardised push-out test at ULS

Viest (1956) proposed a simplified experiment to investigate the capacity of a headed shear stud. Headed shear studs were welded on a steel beam flange, and two concrete slabs were cast beside the steel beam. The load–slip behaviour of the shear connection can be measured by imposing a structural load at the top of the steel beam; this is called a push-out test. Before casting the concrete slab, grease is applied to the beam flange to prevent bonding between the concrete slab and steel flange. Plaster is used at the bottom of the concrete slab to obtain a constant-friction condition during the push-out test.

The committee of composite construction in structural steel and concrete reported an urgently required code of practice for the building sectors in the UK, because the code guidance in 1964 was not appropriate for composite structure design (The Institution of Structural Engineers, 1964). The committee stated that, although the push-out test is widely used to assess the behaviour of shear connectors, the results from the literature showed dispersed data. The push-out test is profoundly influenced by the size and shape of the specimens, method of loading, and concrete slab conditions such as the dimensions, reinforcement, and concrete strength. Several critical variables need to be considered as follows:

1) *Form of the specimen*: when a load is applied to the steel beam, the concrete slab cannot separate freely because two slabs are firmly bedded at the base. Even if the concrete slab could be separated freely, the rotation of the slab before failure remains a problem.

2) *The number of shear connectors to be employed in the push-out test*: because a single shear connector cannot successfully distribute an applied load. It was suggested that the number of shear connectors and their lateral and longitudinal spacing need to be defined.

3) *The size and quality of the concrete slab*: the concrete slab size should be defined according to its applications, because it is related to failure modes of the shear connector in the push-out test.

4) *Reinforcement*: the reinforcement affects a failure mode of the push-out test, because longitudinal splitting can change the failure mode of the shear connection. The committee recommends defining the amount of reinforcement in a concrete slab.

5) *The dimensions of the steel member*: the committee argued that the flange dimensions influence the performance of the shear connector. Goble (1968) demonstrated that a shift in the failure mode from flange pull-out to stud connector shearing occurs when the ratio of the stud diameter to its weld flange thickness is less than approximately 2.7.

A standardised push-out test was first described in CP 117-1 (1965). It specifies the test conditions and specimen dimensions, as shown in Fig. 2-1. The interface between the concrete slab and the steel beam should be greased to prevent bonding, and the test should last more than 10 min for a static condition. The variables proposed by the committee of composite construction in structural steel and concrete were adopted: concrete slabs are bedded in a mortar or solid base, two studs are embedded in each slab, a reinforcement bar of 10-mm-diameter mild steel is used with a specific feature, and 254 × 146 × 43 UB is recommended for the steel sections. The same guidance was written in BS 5400-5 (1979) using SI units.

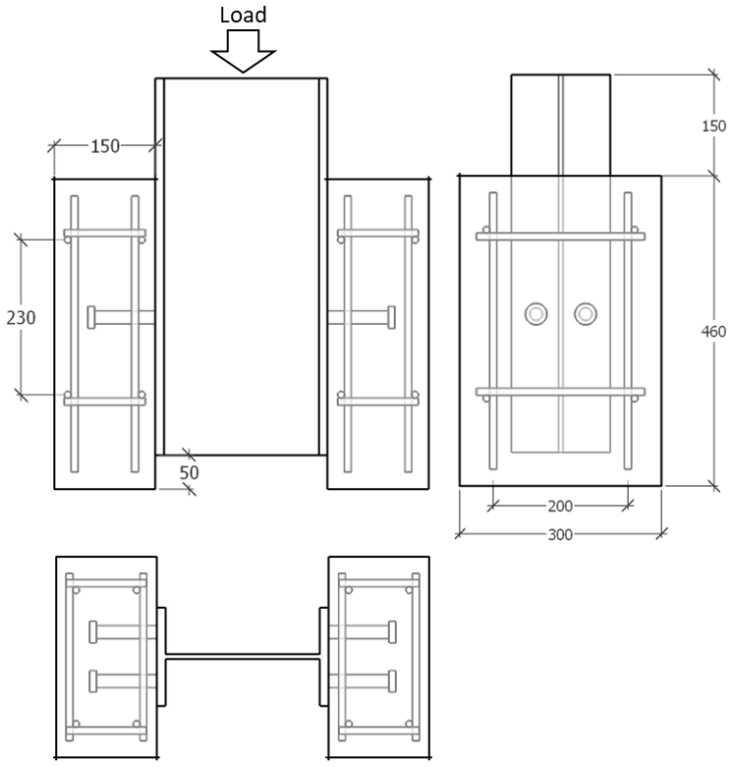

Figure 2-1. Push-out test specimen according to BS 5400-5 (1979)

The first draft of EC4 (EUR 9886 EN, 1985) contains a standard push-out test specimen, which is identical to that of BS 5400-5 (1979). Roik *et al*. (1989) found significant dispersion in existing data from push-out experiments when they investigated the shear resistance of headed stud connections. A modified specimen was subsequently proposed to reproduce more realistic composite beam conditions. The following test conditions were recommended:

- Concrete slab size increases to 1000 mm × 800 mm when the slab thickness is assumed as 150 mm: it varies with respect to the slab thickness and distance between the stud levels
- Studs are located on two levels
- A concrete slab is cast horizontally
- Curing condition of the concrete should be the same as for the concrete slab of the push-out test
- Measuring stud strength: test should be conducted at least five times
- Estimated time to failure exceeds 15 min
- Initial loading: 25 cycles with 40 % of the expected ultimate load

Several recommendations proposed by Roik *et al*. (1989) were adopted by the current EC4-1-1 (2009) in the standard push-out test section, in order to overcome drawbacks of the previous standard push-out test (BS 5400-5, 1979). The up-to-date EC4-1-1 (2009) changes the size of the specimen and specifies detailed conditions, as illustrated in Fig. 2-2. Johnson (2012) describes several reasons for the differences between the standard push-out tests of BS 5400-5 (1979) and EC4-1-1 (2009) as follows:

1) The size of the concrete slab was increased from 460 mm × 300 mm to 650 mm × 600 mm, whereas its thickness remained the same, at 150 mm. The enlarged slab improves the anchoring of the reinforcement. Consequently, it helps to avoid longitudinal splitting which would give unreasonably low strength in a push-out test.

2) The reinforcement bar was changed from a mild steel bar to a high-yield ribbed bar of the same diameter, 10 mm. The reinforcement area was also increased by raising the number of reinforcement bars. Higher shear stress was required to cause longitudinal splitting of the

concrete slab, owing to the high yield stress of the bar. The ribbed shape also gives a better bonding capacity between the concrete and reinforcement bars. The standard push-out test in BS 5400-5 (1979) was revised to use high-yield bars for reinforcement in 2005.

3) The shear connector placement was changed from one level to two levels to enhance the redistribution of applied loads. Consequently, eight shear studs are required in a specimen to evaluate the capacity of the shear connection.

4) The width of the steel flange was extended from 146 to 250 mm, such that a wider angle or block connector could be tested.

5) There are no casting conditions of the concrete slab in BS 5400-5 (1979); however, EC4-1-1 (2009) specifies that the concrete slab should be cast in a horizontal position, which was the identical condition to that used in beam construction. Casting the slab vertically increases the risk of poor compaction because of air pockets around the shear connection.

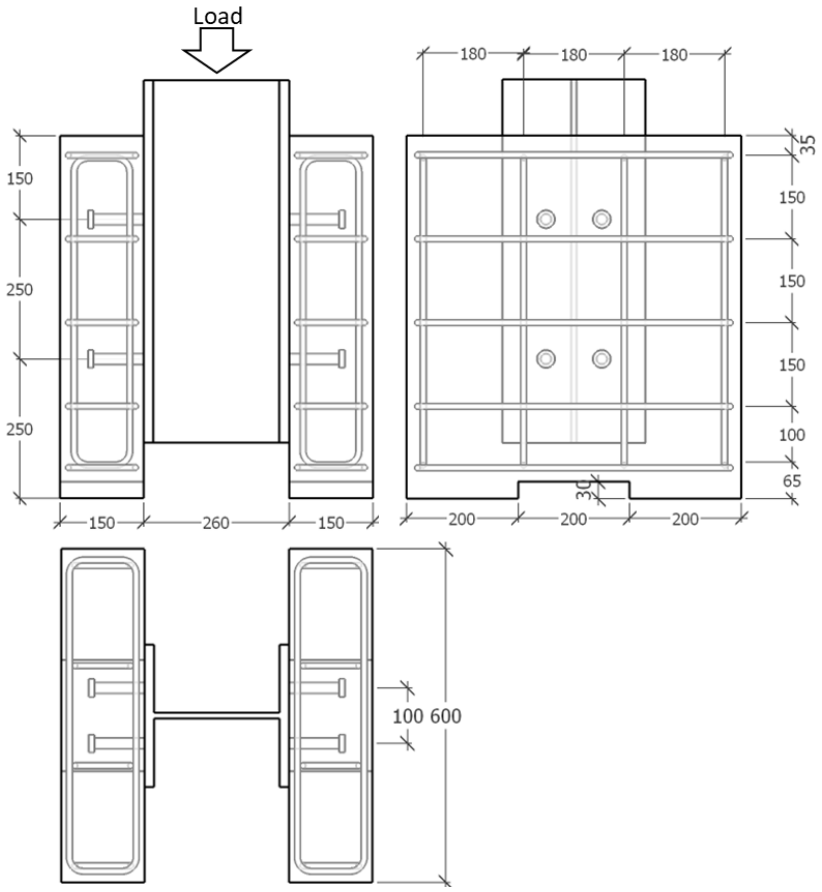

Figure 2-2. Push-out test specimen according to EC4-1-1 (2009)

The standardised push-out test in EC4-1-1 (2009) is specified with solid concrete slabs. There is no particular consideration of the test for transverse deck slabs. Hicks (2007) proposed a specimen, shown in Fig. 2-3, for a trapezoidal deck push-out test by enlarging the concrete slab width from 600 to 750 mm. Employing a deck slab results in concrete-dominated failures, such as concrete pull-out and rib shearing. Although the enlarged concrete slab cannot solve the brittleness problem, it helps to avoid cracking in the side section of the concrete slab in the case of concrete pull-out failure. Qureshi (2010) carried out push-out tests using a one-sided specimen with a transverse deck. Five headed shear studs were through-deck welded on a steel flange in a row, and an open trapezoidal deck was laid in a transverse direction to the steel beam; a single stud was embedded in a trough on the favourable side, and there were five troughs in the concrete slab. In that experiment, transverse cracking was observed at the last studded rib, which is the closest trough from a loading plate. A displacement load was applied to the top side of the steel beam, and the steel flange was placed underneath the concrete slab. The transverse cracking widened, and as a result, the last studded rib fractured with a rotation of the rib. This premature failure could cause an underestimation of the structural capacity of the shear connection.

The proposed specimen (Hicks, 2007) has two levels for the stud placement, which avoids an artificial failure mode caused by transverse cracking due to two un-studded decks at the top and bottom sides. Although all the recommendation of the committee of composite construction in structural steel and concrete from 1964 were adopted in the current EC4-1-1 (2009), there is still no guidance for the push-out test with transverse deck slabs. The shear resistance is strongly influenced by a size of the concrete cracking surface which formed as a cone-shape from the stud head in the case of the concrete pull-out failure. Enlarged concrete slab helps to avoid unmatured cracking surface. As presented in Table 2-1, the modified specimen proposed by Hicks (2007) was used for the push-out test in this study.

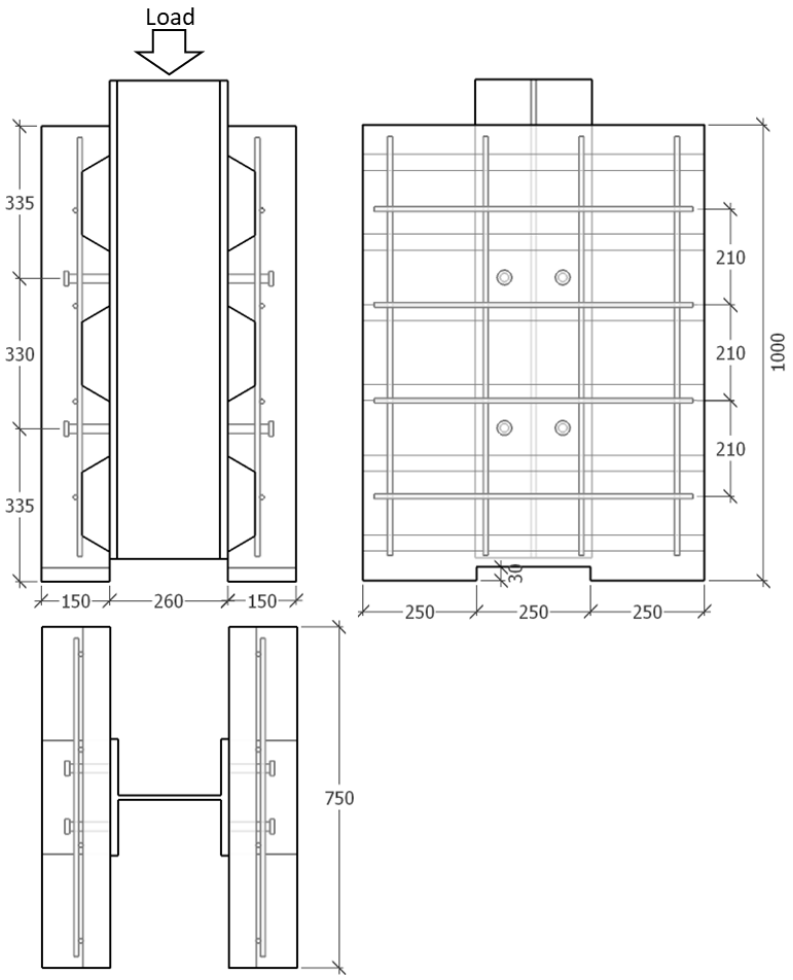

Figure 2-3. Push-out test specimen according to Hicks (2007)

Table 2-1. Comparisons of the push-out test specimen

	BS 5400-5 (1979)	EC4-1-1 (2009)	Hicks (2007)
Concrete slab	Solid slab	Solid slab	Transverse deck slab
Expected failure mode	Stud shearing	Stud shearing	Concrete-dominated
Concrete slab size	300 mm × 460 mm	600 mm × 650 mm	750 mm × 1000 mm
Number of studs in a slab	4	8	8
Level of installed stud	2	2	2

2.3.2. Modified push-out test at FLS

Few researchers have addressed the capacity of the shear connection in a fire, because heating and insulation equipment are required to conduct high-temperature push-out tests. A modified specimen based on the push-out test in EC4-1-1 (2009) was typically used, depending on the heating apparatus. The specimen configuration and heating profile were different for each experiment. Some of them followed the ISO 834 standard fire, whereas others used their own heating conditions. Therefore, a standardised test method for high-temperature applications is needed to obtain consistent experimental conditions. In this section, various experimental approaches to evaluate the behaviour of the shear connection at high temperatures are described.

Initially, Zhao and Kruppa (1993) amended a push-out test setup to investigate the high-temperature behaviour of shear studs. The specimen was prepared according to the recommendations of EC4-1-1 (1994) with the exception of the number of studs and size of the concrete slab. As an opening was cut in the cover, the steel section and inner part of the slabs were exposed to hot gases generated by the furnace gas chamber as depicted in Fig. 2-4(a). A designated load was applied to the steel section, after which the specimen exhibited the ISO 834 standard fire condition. This method was suitable to estimate the resistance of the shear connection with respect to the steel flange temperature, which could be directly measured during the heating process. In the case of a transverse deck specimen, a single level stud with slab dimensions of 600 width × 620 height × 150 thickness mm^3 was used, as illustrated in Fig. 2-4(b).

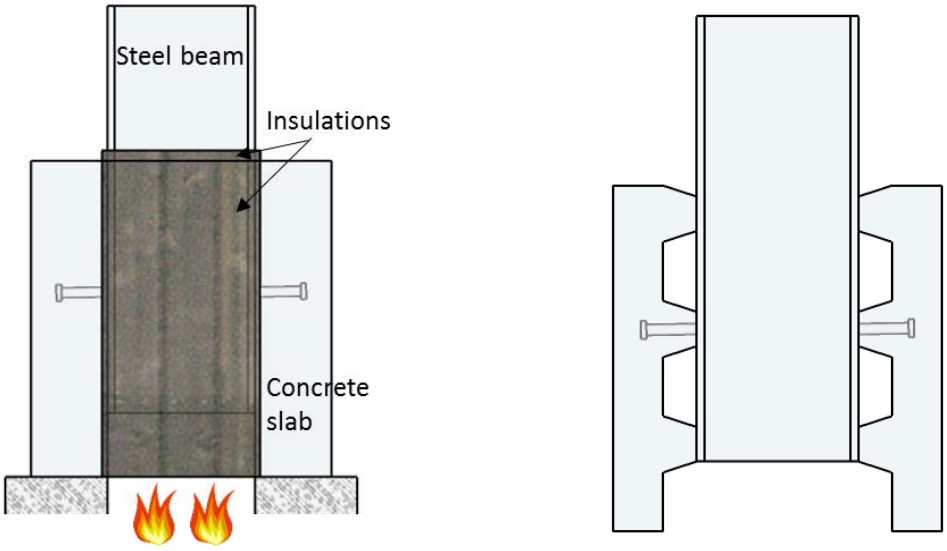

(a) High temperature test set-up (b) Trapezoidal deck specimen

Figure 2-4. High-temperature push-out test according to Zhao and Kruppa (1993)

Several specimens, structurally modified to include a one-sided concrete slab, were adopted for high-temperature push-out tests (Yasuda *et al*., 2008; Choi *et al*., 2009; Dara, 2015). A concrete slab was replaced by a furnace, and the applied heat energy was directly transferred to the steel beam and the inner side of the concrete slab. This modification results in similar test environments to the actual environment experienced by a composite beam in a fire. However, the results were technically difficult to compare to existing push-out test data at ULS, as they were obtained using specimens of different structural configurations.

Choi *et al*. (2009) positioned a portion of a specimen within an electric furnace and insulate the corners of the concrete slab to prevent heat loss, as shown in Fig. 2-5(a). This experimental setup made it possible to create a three-side exposure which closely resembled a realistic situation of a composite beam in a fire. The bottom of the concrete slab was restrained to prevent the specimen from moving outward, as a sudden fracture could inflict damage on the subsidiary equipment. Two-headed shear studs were placed in a side-by-side arrangement in a solid slab. The gas temperature at the enclosure of the test setup followed the ISO 834 standard fire. The heat was induced in a designated time; after that, a displacement load was applied by fixing the gas temperature. This test method was efficient to obtain the load-slip behaviour of the shear connection, although a possible error

should be considered because the stud temperature consistently increased by heat transfer from the steel beam during the loading process.

Dara (2015) used a similarly modified specimen for high-temperature experiments. The specimen was encased in an electric furnace. The specimen and half of the electric furnace are shown in Fig. 2-5 (b). The size of the concrete slab was 330 mm × 300 mm × 127 mm, and the headed shear stud was embedded in the centre of the slab. A 19-mm-thick steel plate was employed as a steel beam section. Its size was the smallest among the high-temperature push-out tests available in literature, because an electric furnace was wrapped around the specimen in this experiment. Two heating scenarios were used in this experiment. One was to induce a load after fixing the temperature of the test setup (scenario 1), and the other was to induce a load after reaching a designated temperature, without stopping the heating process (scenario 2). The heating process took more than 3 hours to approach a stud temperature of 760 ℃ in scenario 1, because the gas temperature in the furnace was different from the ISO 834 standard fire. An additional 90 min of heating was required in scenario 2. All the failure modes observed were stud shearing. However, the failure location was slightly different, as depicted in Fig. 2-6. The shearing occurs slightly apart from the weld collar at ULS, whereas the shearing location moved towards the stud root at high temperature. This indicates that the shear stud was more vulnerable to fire than the surrounding concrete. Comparing the stud temperature between scenarios 1 and 2, the stud temperature in scenario 2 showed a higher value. Additionally, a higher strength reduction was shown in scenario 2. Dara (2015) argued that the shear resistance reduction has a strong correlation with the temperature of the stud root area.

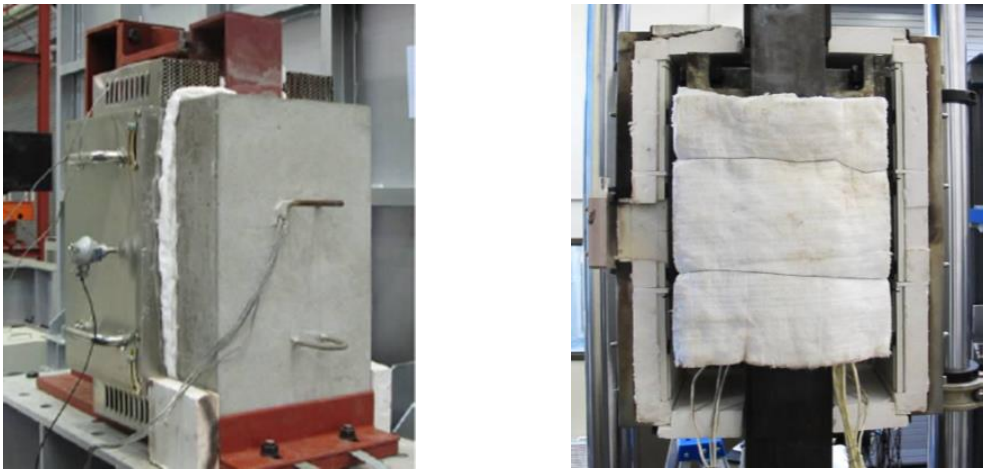

(a) Choi *et al*. (2009) (b) Dara (2015)

Figure 2-5. High-temperature push-out test using a modified specimen

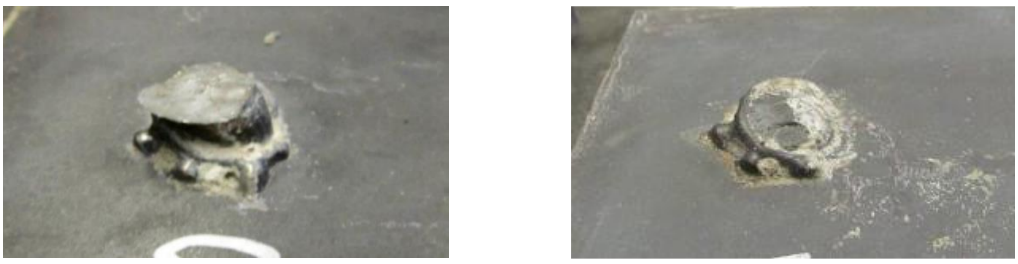

(a) at ULS (b) 700 ℃ in scenario 1

Figure 2-6. Stud shearing after the push-out test (Dara, 2015)

Mirza *et al*. (2011) investigated the effect of temperature on a headed shear stud. A total of 16 specimens were made using solid and transverse deck slabs. Their size was smaller than the recommendation of EC4-1-1 (2009), owing to the limitation of the furnace. The failure mode observed in the solid slab specimens was stud shearing near the weld collar, whereas a concrete-dominated failure caused by concrete crushing or cracking was found in the deck specimens. In this experiment, heat was applied until a designated temperature was reached, after which a load was induced to acquire the load–slip relationship at elevated temperature. When comparing the shear resistance at ULS and 600 ℃, it reduces to 66 % in the solid slab and 59 % in the transverse deck slab. They argued that the difference in the strength reduction comes from the different failure modes with respect to the slab type.

The current EC4-1-2 (2014) provides the strength reduction factor regarding the temperature of the stud and surrounding concrete according to stud shearing and concrete-dominated failure. Unlike the experimental investigation, a greater reduction has been found in the stud shearing failure than in concrete-dominated failure at FLS.

Twenty-four push-out tests were conducted by Chen *et al*. (2012) incorporating a headed shear stud in solid, parallel, and transverse deck slabs at both ULS and FLS. Three different temperatures (400 ℃, 500 ℃, and 600 ℃) measured at 10 mm from the stud base were used for high-temperature conditions. They argued that the location could represent the stud temperature as well as the most severely degraded position in the high-temperature push-out test. The specimen was modified in comparison to the EC4-1-1 (2009) recommendation, owing to the limitation of the furnace. The concrete slab size was reduced to 450 mm × 680 mm with 150 mm thickness around the shear stud. It also had a 250-mm-thick base around the bottom of the concrete slab. A single stud was embedded in each concrete slab in their experiment. Heat was applied through two electric heating plates which were attached at the side sections of the specimen, as shown in Fig. 2-7. Consequently, the web of the steel beam and the inner side of the concrete slab were directly heated from the electric heating plates. To obtain the load–slip behaviour of the shear connection at high temperature, a load was applied when the 10 mm stud temperature reached a designated value. It took more than 6 hours to reach a stud temperature of 600 ℃, because the gas temperature in the furnace could not follow the ISO 834 standard fire, as shown in Fig. 2-8. All the failure modes observed in the solid and parallel deck slabs were stud shearing, whereas the failure mode changed from concrete rib shearing to stud shearing as the temperature increased in the transverse deck slab; the failure mode changed at a stud temperature of approximately 500 ℃. This proves that the stud strength degradation was faster than that of the surrounding concrete as temperature increased. They reported that a higher strength reduction was observed in the solid slab specimen compared to the transverse deck specimen. When the stud temperature was 600 ℃, the shear resistance reduced to 37 % and 61 % in the solid and transverse deck slabs, respectively. This shows a different trend compared to the experiment of Mirza *et al*. (2011), which gave a higher strength reduction in the transverse deck specimen. This opposite result

may come from the different experimental conditions, such as the heating profile and specimen configuration.

Figure 2-7. High-temperature push-out test according to Chen *et al*. (2015)

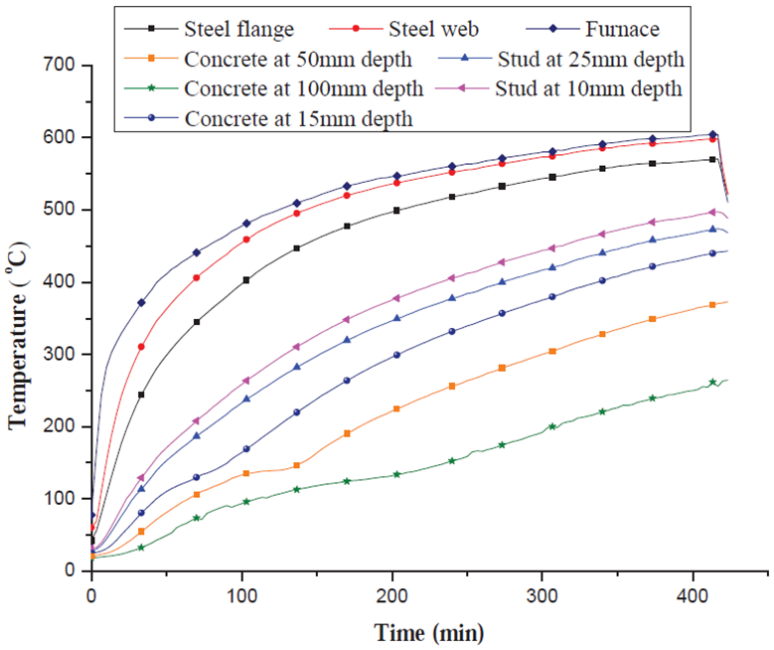

Figure 2-8. Temperature distribution of the specimen (Chen *et al*., 2012)

Imagawa *et al*. (2012) reported a shear resistance variation with respect to temperature. A modified specimen was adopted, which has one concrete slab and two headed shear studs placed in a side-by-side arrangement. The size of the concrete slab was 400 mm × 700 mm × 250 mm, which was smaller than the recommendation in EC4-1-1 (2009). The steel section was laid on a furnace, and a load was induced in the horizontal direction when the gas temperature reached a designated value. The target temperatures were 300 ℃, 500 ℃, and 700 ℃. Three different temperatures and ambient conditions were adopted in the experiment, and 12 push-out tests were conducted in total. In their modified push-out tests, the specimen was heated for 90 min before loading, because the temperature curve was different from the ISO 834 standard fire. When the specimen temperature reached 700 ℃, the shear resistance was reduced by approximately 30 % in comparison to the ULS value; in this condition, the upper flange temperature was 525 ℃, which resulted in a stud temperature of 420 ℃ according to EC4-1-2 (2014). The strength reduction was less than 15 % at enclosure temperatures of 300 ℃ and 500 ℃. In comparison with the solid slab experimental result of Chen *et al*. (2012), a similar reduction ratio was observed. This shows a reduction of approximately 25 % at a stud temperature of 400 ℃. However, the strength reduction at lower temperatures of 300 ℃ and 500 ℃ cannot be compared, because Chen *et al*. (2012) carried out their experiment at stud temperatures above 400 ℃. The same failure mode of stud shearing was found with all the solid slab specimens.

2.4. Headed shear studs embedded in solid slabs

2.4.1. Failure mechanics

Two failure modes of a headed shear stud in a solid concrete slab are stud shearing and stud over-turning (concrete crushing). When a force *P* acts on a steel beam which is connected to a stud base by welding, the weld collar first withstands a force *F1*, which leads to a strong concrete crushing effect in the direction of the loading, as shown in Fig. 2-9.

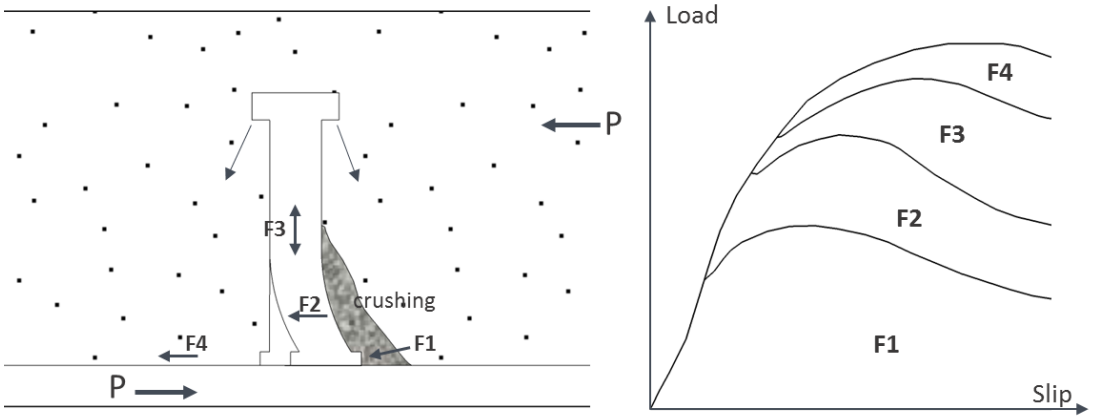

Figure 2-9. Headed stud in a solid concrete slab (Roik *et al*., 1989)

Johnson and Oehlers (1981) conducted a numerical study to investigate the influence of compacting concrete near a weld collar. It was shown that the shear resistance reduces by 29 % when the area next to the weld collar is void. A higher concrete bearing stress induces stud shearing at the interface of the stud shank and weld collar. Conversely, greater damage to concrete in the bearing zone causes a concrete crushing failure due to an eccentricity change, which causes a higher moment at the stud root. The location of the applied force (*F2*) is affected by the concrete crushed area. The larger the crushed area, the higher the location of the force (*F2*) alongside the stud shank. Oehlers and Bradford (1995) explain the eccentricity variation using the relative stiffness of steel and concrete. When concrete and a stud are touched as illustrated in Fig. 2-10, the applied force is uniformly distributed to the stud if the steel elastic modulus increases infinitely. Hence, the eccentricity moves to half of the stud height. This causes the flexural force to increase, and the shear resistance to

decrease: a concrete crushing failure occurs. If the steel elastic modulus approaches zero, the eccentricity moves to the bottom of the shear stud, which results in the flexural force becoming zero. In case of fire, the shear stud temperature increases more rapidly than the surrounding concrete owing to the configuration of composite beams and thermal conductivity of materials. A relative stiffness of concrete slab increases in comparison to the shear stud. As a result, a stud shearing failure can be expected at the stud root area which is the most severely damaged part by a temperature change.

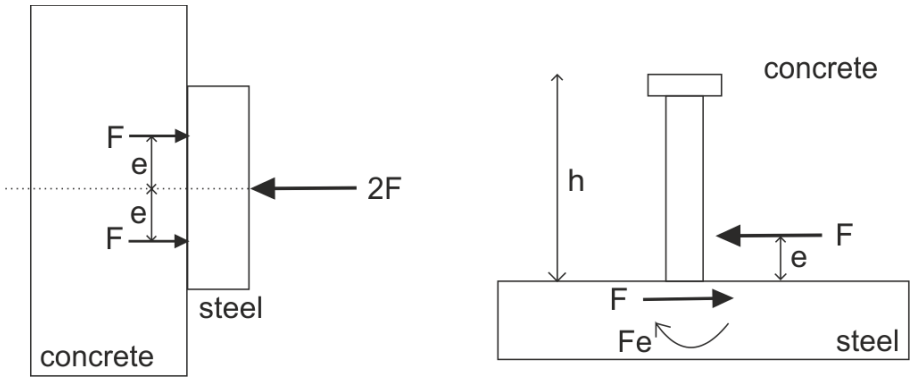

Figure 2-10. Eccentricity variation with respect to the relative stiffness of steel and concrete (Oehlers and Bradford, 1995)

The tensile stress (*F3*) occurred when the shear stud was embedded in a concrete slab, which results in a compressive stress in the concrete between the stud head and the steel flange. This is the cause of a concrete pull-out failure; however, it rarely occurs in a solid concrete slab. The friction force (*F4*) was induced by the compressive force at the flange. According to the standard push-out test in EC4-1-1 (2009), a greasing material should be applied to the flange to reduce this friction. The shear resistance in a solid concrete slab can be determined by a combination of these forces, *F1* to *F4*. Owing to these complicated mechanics, the shear resistance and ductility of the shear connection have been determined experimentally.

The behaviour of an individual stud is commonly examined by the push-out test described in EC4-1-1 (2009), because it is a simple method compared to the other full-scale composite beam experiments. When a load (*2P*) is applied vertically at the top of the steel beam, each

concrete slab withstands half of the applied force (*P*), as illustrated in Fig. 2-11. The shear stud transmits the load from the steel beam to the concrete slab. A shear force is applied at the bottom of the shear stud, and the location of the maximum force in the shear stud increases in correlation to the stud height, because the eccentricity was designed approximately 0.18 to 0.33 times the stud height (Xue *et al*., 2008). This eccentricity (*e*) incurs a moment at the stud root.

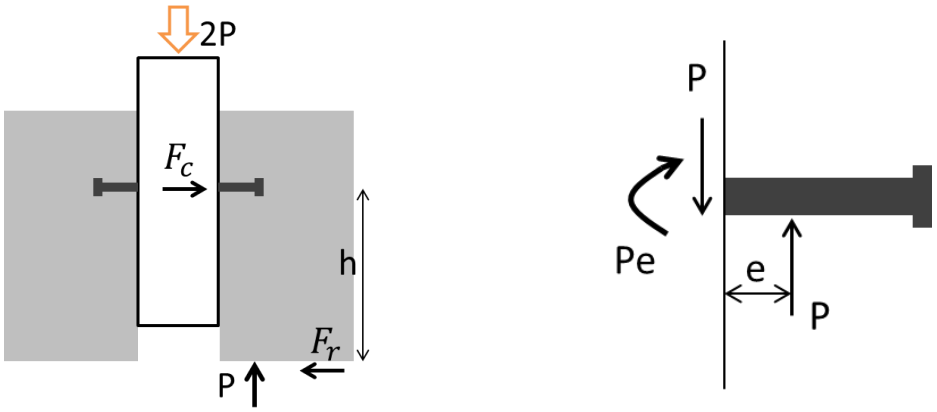

(a) Force distribution of the push-out test (b) Near the stud

Figure 2-11. Force distribution of the push-out test (Oehlers and Bradford, 1995)

If there is no action taken to avoid friction, the frictional force (*Fr*) is induced at the bottom of the concrete slab. In the case of a firmly restrained specimen, the friction force creates a compressive axial force (*Fc = Fr*) and moment (*Fc·h*). A shear resistance can be varied owing to the restrained condition of the specimen. If there is no friction force at the bottom of the concrete slab, the concrete slab is free to move in an outward direction. This action produces an additional tensile force at the stud shank, which tends to reduce the shear resistance. The code of practice (EC4-1-1, 2009) recommends using mortar or gypsum at the bottom of the specimen to control the additional friction effects and distribute the applied force uniformly.

Oehlers and Johnson (1987) reported the effect of the axial force on the shear resistance using a modified test setup. In their study, tensile loads were applied to achieve similar conditions of the push-out test to those of the beam test. They concluded that the shear resistance obtained from the push-out test was higher than that from the composite beam

test due to the friction force at the bottom of the concrete slab. Therefore, care should be taken to design the push-out test because boundary conditions affect the behaviour of the shear connection.

2.4.2. Influencing parameters

A shear connection is significantly affected by the material strength of the shear stud. This can be expressed by the ultimate tensile stress of the stud times the cross-sectional area of the stud shank that withstands a shear load and flexural force. The concrete compressive strength also profoundly affects the shear resistance by controlling the size of the crushed area. These significant factors were investigated and verified by many researchers and were incorporated to design codes such as EC4-1-1 (2009), BS 5950-3.1 (2010), and AISC 360-10 (2010). Aside from these factors, other parameters such as the stud height ratio, spacing between the shear studs, and size of the stud weld collar also affect the capacity of the shear connection.

Slutter and Driscoll (1962) proposed two empirical formulas with reference to the stud height to shank diameter ratio. When this ratio is less than 4.2, the shear resistance reduces as the ratio decreases. They argued that a shorter stud gives a smaller shear resistance than a longer stud. EC4-1-1 (2009) includes the stud height ratio to estimate the shear resistance; when the height ratio is larger than 4, its parameter becomes 1.

The surrounding concrete near the shear stud withstands both shear and compressive forces. As illustrated in Fig. 2-9, the shear force (*F1, F2*) is transmitted to the stud shank, and the compressive force (*F3*) is applied to the stud shank. This affects concrete crushing in the shear direction and cracking with a conical shape. Xue *et al*. (2012) conducted a push-out test to investigate the effect of the distance between the studs installed in a solid slab. The shear resistance reduces by 10 % when using several studs in a slab. In a high-strength concrete (HSC) slab, the stud ductility reduces because concrete crushing is difficult to initiate. Döinghaus *et al*. (2003) argued that stud slip increases in HSC when two studs are placed very close to each other. This makes the area of the concrete failure larger by overlapping among two studs. Based on these investigations, all the design guidelines recommend a minimum spacing between shear studs.

The weld collar of a shear stud withstands a shear force, which alleviates the force concentrated on a stud shank and distributes the shear force acting on the stud. Johnson and Oehlers (1981) argued that the shear resistance increases by 22 % compared to a shear connection without a weld collar. Xu and Liu (2016) carried out a parametric study regarding the stiffness variation of a shear connection depending on the existence of a weld collar. It showed a 10 % deviation in the shear stiffness depending on the weld collar. The effect of the weld collar becomes more significant when using HSC. Both slip and shear resistance reduces when the size of the weld collar decreases. Döinghaus *et al*. (2003) added a dimensional parameter of the weld collar using the empirical constant of 1.5 to calculate the shear resistance, because the size of the weld collar contributes to increasing the shear resistance, especially in HSC.

2.4.3. Design guidance

Numerous experiments have established that the resistance of the shear connection is related to various parameters such as the steel yield stress, concrete compressive strength, stud cross-sectional area, and concrete elastic modulus. Ollgaard *et al*. (1971) created an empirical formula based on 48 solid slab push-out tests. The considered variables were the concrete compressive strength, concrete tensile strength, concrete elastic modulus, concrete density, stud diameter, aggregate type, and number of shear studs per slab. Two failure modes were observed: one was stud shearing, and the other was concrete failure around the shear connection region. The shear stud was deformed and showed more curvature when the concrete strength was higher. The propagated concrete crack formed at 45 ° from the stud head.

The experiments showed that the shear resistance has a strong relationship with the concrete compressive strength and modulus of elasticity, whereas the concrete density does not affect the shear resistance. The cross-sectional area of the shear stud was proportional to the shear resistance when the compressive stress of the surrounding concrete was constant. They conducted a regression analysis using 48 experimental data with a logarithmic transformation to find major factors in deciding the shear resistance. The reported relationship is:

$$P_u = 1.83 A_{sc} f_c^{0.3} E_{cm}^{0.44} \quad (2\text{-}1)$$

where P_u: ultimate shear resistance
A_{sc} : cross-sectional area of the shear stud [mm^2]
f_c : compressive strength of concrete [*MPa*]
E_{cm}: elastic modulus of concrete [*MPa*]

For convenience, a simplified equation was proposed by rounding off the exponents to 0.5. Comparing the results, the correlation coefficient between the two formulas was less than 1.7 %; the difference between Eq. 2-1 and 2-2 is less than 1.7 %. This simplified equation was adapted to the AISC (American Institute of Steel Construction) code of practice (AISC 360-10, 2010) by limiting the tensile stress of the stud material as follows:

$$P_u = 0.5 A_{sc} \sqrt{f_c E_{cm}} = 0.39 d^2 \sqrt{f_c E_{cm}} \leq 0.75 A_{sc} f_u \quad (2\text{-}2)$$

where d : stud shank diameter [*mm*]
f_u : tensile stress of the stud material [*MPa*]

Lam and El-Lobody (2005) developed a simple numerical model to verify the effect of the shear stud diameter and concrete strength. The stress-strain curve of the steel and concrete were assumed to be bilinear. Two general failure modes in a solid slab were also observed in their four experiments; stud shearing and concrete crushing. A parametric study reveals that the structural capacity of the shear connection has a linear relationship with the stud shank diameter. The shear resistance increases with the stud diameter. This behaviour was consistently observed, regardless of the concrete strength. The shear stud capacity also varies with respect to the concrete strength. The shear connection failure was governed by concrete crushing when the concrete compressive strength decreased, which provided a relatively weaker shear connection. The effects of the stud diameter and concrete strength were also confirmed by experimental and numerical studies conducted by several researchers (Xu and Sugiura, 2013; Xue *et al*., 2008; Nguyen and Kim, 2009).

Oehlers and Johnson (1987) used 110 push-out tests to investigate the strength of shear connections in composite beams. They compared existing experimental data with axially

loaded push-out test data, because the shear resistance discrepancy between push-out and beam tests is due to the axial load. The considered parameters were similar to the study of Ollgaard *et al*. (1971), but they included the strength of the shear stud and the steel elastic modulus, because the ratio between the concrete and steel elastic modulus affects the dowel action of the shear connection (Oehlers and Bradford, 1995).

It was found that the shear resistance ratio between the push-out test and the axially loaded experiment was 0.81 through a statistical analysis (Oehlers and Johnson, 1987). This means that the push-out test results were 20 % higher than the shear resistance obtained from composite beam tests. The static failure load of the shear connections in composite beams can be expressed as follows:

$$P_u = KA_{sc}(E_{cm}/E_s)^{0.4} f_{cu}^{0.35} f_u^{0.65}$$
$$K = 4.1 - n^{-1/2} \quad (2\text{-}3)$$

where E_s: stud steel elastic modulus [*MPa*]
f_{cu}: cube strength of concrete [*MPa*]
n: number of studs subjected to similar displacement
K: an empirical constant

The parameter K allows a 90 % confidence level for the characteristic value of the shear resistance. The proposed formula assumes that the stud height is greater or equal to four times the stud diameter; the mean weld collar height is 0.31*d*; its material property ranges are $430 \text{ MPa} \leq f_u \leq 640 \text{ MPa}$, $0.05 \leq E_{cm}/E_s \leq 0.16$, and $0.05 \leq f_{cu}/f_u \leq 0.11$.

A shear connection exhibits substantial inelastic deformation before fracture. This ductility is measured by the slip of the shear stud. The maximum slip is defined as 6 mm in EC4-1-1 (2009) for a partial interaction design. The ductility of the shear stud depends on the concrete compressive strength because a higher concrete strength makes the stud more rigid. As a consequence, EC4-1-1 (2009) permits both the use of rigid and ductile failure to design composite beams by selecting the smaller value. The first draft of EC4 (1985) regarding composite steel and concrete structures proposed the following design rule for the shear resistance calculation:

$$P_k = 0.7\frac{\pi}{4}d^2 f_u \quad (2\text{-}4)$$

$$P_k = 0.36 L_{sc} d^2 \sqrt{f_{ck} E_{cm}} \quad (2\text{-}5)$$

where P_k : characteristic value of shear resistance [*kN*] $= P_d \times \gamma_M$
γ_M : material safety factor
d : stud diameter [*mm*] $16 \leq d \leq 25$
L_{sc} : ratio of the stud height to diameter
$L_{sc} = 0.2(h_{sc}/d + 1)$ for $3 \leq h_{sc}/d \leq 4$
$L_{sc} = 1$ for $h_{sc}/d > 4$
h_{sc} : stud height [*mm*]
f_u : tensile strength of the stud material $\leq$ 450 *MPa*
f_{ck} : characteristic value of the cylinder compressive strength of concrete

The above equations describe the shear resistance with respect to the stud shearing and concrete failure, respectively. It is assumed that the tensile strength of the stud material determines the shear connection integrity when the concrete slab is sufficiently rigid. On the contrary, the failure is determined by the concrete cracking or crushing when the concrete strength is relatively low. Eq. 2-5 was based on the experimental data of Ollgaard *et al*. (1971). To consider the ductile behaviour of the shear stud, the rigid shear force was calibrated to the lowest strength of the concrete. When $\sqrt{f_{ck} E_{cm}} = 687$ MPa and $f_u = 450$ MPa, the coefficient of 0.7 in Eq. 2-4 can be achieved (Mottram and Johnson, 1990).

Numerous experiments have been conducted to investigate the resistance of the shear connection; however, the results showed large variations. This was because each test had different experimental conditions and variables, such as a number of studs per specimen, material properties, concrete slab size, and loading condition. Statistical analyses were used to define an optimised formula which would be used for a wide range of composite structures. Roik *et al*. (1989) reported that the coefficients of Eq. 2-4 and 2-5 should be modified to 0.8 and 0.26 investigating a mean shear resistance value of existing push-out test data. A ratio between the mean and characteristic strength was used to calculate a partial safety factor. As a result, the coefficients in Eq. 2-6 and 2-7 were presented using the same material safety factor of 1.2.

In the draft of the EC4-1-1 (1994), the coefficient in Eq. 2-5 was modified from 0.26 to 0.29 because of the small number of studs in the test specimen and the less stiff behaviour of

studs in push-out tests (Johnson, 2011). Moreover, the ultimate stress limit of the stud material was increased from 450 to 500 MPa. The shear resistance of the headed shear stud is expressed in the current EC4-1-1 (2009):

$$P_k = 0.8\frac{\pi}{4}d^2 f_u \quad (2\text{-}6)$$

$$P_k = 0.29 L_{sc} d^2 \sqrt{f_{ck} E_{cm}} \quad (2\text{-}7)$$

where f_u : tensile strength of the stud material $\leq$ 500 *MPa*

The design guidelines for a shear stud in a solid slab are described in Table 2-2. Most of them have similar criteria to avoid premature failure and ensure a safe design. The shear resistance in BS 5950-3.1 (2010) is not provided by an equation, but as table values with respect to the concrete compressive strength based on the study of Oehlers and Johnson (1987). The experimental data will be evaluated with respect to EC4-1-1 (2009) because other design codes do not provide a shear resistance value at high temperatures.

Table 2-2. Shear connection design guidance for solid slab applications

	EC4-1-1 (2009)	BS5950-3.1 (2010)	AISC 360-10 (2010)	CSA S16-01 (2001)
Stud diameter (d)	16 – 25 mm	13 – 25 mm	< 2.5 times flange thickness	< 2.5 times flange thickness
Stud height	> 4d	65- 100 mm	> 4d	> 4d
Min. longitudinal spacing	5d	5d	6d	6d
Min. transverse spacing	2.5d	4d	4d	4d
Stud tensile strength	< 500 MPa	495 MPa[1]	-	415 MPa
Stud resistance calculation	Eq. 2-6 Eq. 2-7	Table value	Eq. 2-2[2]	Eq. 2-2

[1] According to BS 5400-5 (2005)
[2] Based on empirical formula; additional reduction factors are also added.

2.5. Headed shear studs embedded in transverse deck slabs

2.5.1. Failure mechanics

Profiled steel decks are widely used in modern construction. They act as a platform during stud welding and reinforcement bar placing. They also act as formwork during concrete casting. After curing a concrete slab, a profiled steel deck helps to withstand tensile loading caused by the deflection of slabs. The structural capacity of the shear connection varies with respect to the orientation of the steel decking. When the deck is laid parallel to the steel beam (primary beam application), the shear stud behaves in a ductile manner, which is similar to composite beams with a solid slab. On the contrary, relatively low-capacity and brittle behaviour is shown in a transverse deck orientation (secondary beam application).

Several failure modes have been observed in transverse deck push-out tests: concrete pull-out, rib shearing, rib punching, and stud shearing (Hawkins and Mitchell, 1984; Johnson and Yuan, 1998b; Lawson, 1997). Amongst these, the frequently observed failure modes at ULS have been concrete-dominated failures such as concrete pull-out and rib shearing, whereas stud shearing rarely occurs. Rib punching can be found when a shear stud has been welded in an unfavourable position. When a concrete slab is lightly reinforced, transverse cracking on the backside of the concrete slab can be observed, particularly where a pair of studs was embedded in a trough. In the following, detailed descriptions of failure modes and their theoretical resistance calculation methods are presented.

Concrete pull-out

Concrete pull-out failure is a concrete fracture with a pyramid or wedge shape around the shear stud. The surrounding concrete near the stud breaks away from the concrete slab. Hawkins and Mitchell (1984) reported that a concrete pull-out failure occurs with a pyramid-shaped surface, and a concrete crack initiates from the stud head to the bottom of the concrete slab with an angle of 45° (Fig. 2-12(a)). The failure suddenly appears because the tensile force acting on the stud shank was tolerated by the tensile stress of concrete. The friction and shear force at the crack surface influence on the capacity of the shear

connection. They argued that the shear resistance was determined by the cracking surface area and compressive strength of the concrete.

$$P_u = C_1 A_c \sqrt{f_c} \tag{2-8}$$

where C_1 : empirical constant
A_c : conical failure surface of concrete [mm^2]
f_c : concrete compressive stress [*MPa*]

The empirical constant of 0.45 was proposed based on push-out test results. Eq. 2-8 was adopted to calculate the shear resistance in the Canadian standard (CSA S16-01, 2001) with respect to the deck height and concrete density. Jayas and Hosain (1988) reported the empirical constant as 0.35 and 0.61 for deck heights of 75 and 38 mm, which are widely used deck shapes in Canada.

Lloyd and Wright (1990) carried out 42 push-out tests using transverse deck specimens with a through-deck welded shear stud. Concrete pull-out failure with a wedge-shaped fracture surface was observed in their experiment. When a force was applied from the left side, the concrete failure surface of the right side showed a larger damaged area, as illustrated in Fig. 2-12(b). The best-fitted equation was proposed using the wedge-shaped concrete area and regression analysis as follows:

$$P_u = \left(A_c \sqrt{f_{cu}}\right)^{0.34} \tag{2-9}$$

where f_{cu} : cube strength of concrete [*MPa*]

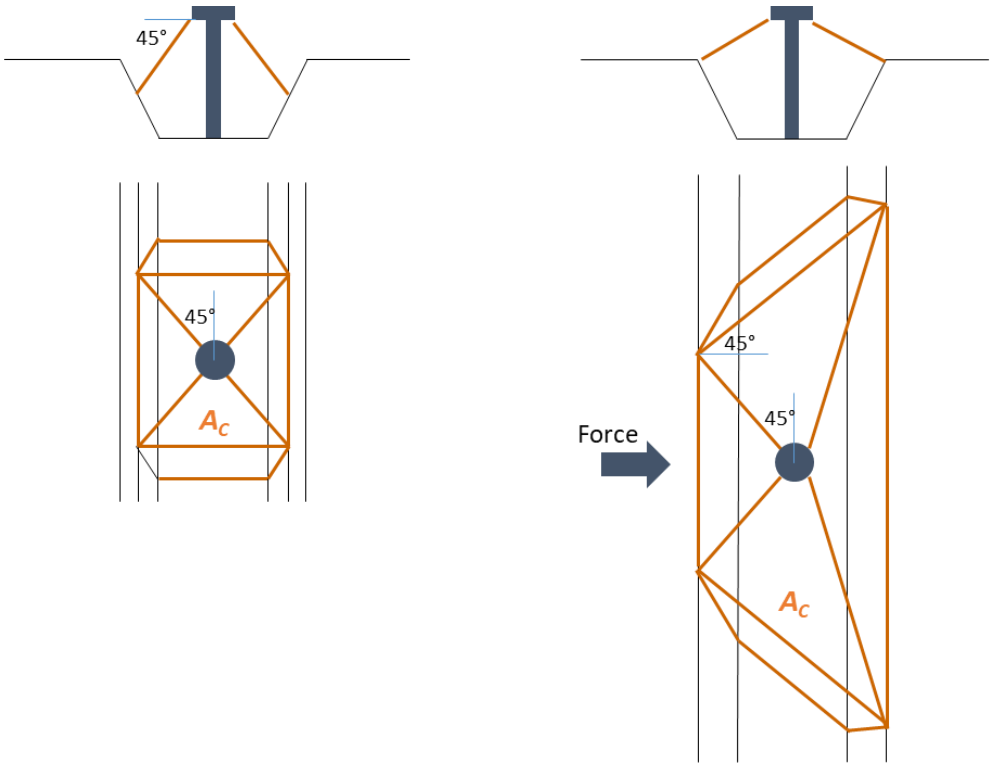

(a) Cone-type failure
(Hawkins and Mitchell, 1984)

(b) Wedge-type failure
(Lloyd and Wright, 1990)

Figure 2-12. Concrete failure surfaces with respect to the shape of the failure

Johnson and Yuan (1998b) explained that the concrete pull-out failure is caused by the rotation of a concrete block in a trapezoidal deck. A shear resistance formula was proposed, assuming that the concrete prism behaves plastically. When loads are applied, a slip occurs by an amount of δ_1, as illustrated in Fig. 2-13. This makes the concrete prism rotate by a small angle of θ_p, which affects the vertical separation of δ_2. The tension at the stud root also affects the uplift of δ_3. The relationships implied by the concrete rotation can be obtained from the geometry around the shear stud.

$$\theta_p = \frac{\delta_1}{h_p} \qquad \delta_2 = \left(\frac{b_0}{h_p}\right)\delta_1 \qquad \delta_3 = \left(\frac{e_r}{h_p}\right)\delta_1 \qquad (2\text{-}10)$$

It was assumed that the crack initiates from the point A, and the initial failure of the concrete block was neglected. The work due to the concrete pull-out failure was equal to the sum of the internal torsional work and the compressive work as follows:

$$P_u\delta_1 = W_{it} + T\delta_3 \tag{2-11}$$

where W_{it} : internal torsional work
T : axial force at the stud root

The internal torsional work can be expressed using the virtual height of the concrete block (*H*), assuming that the concrete block was subjected to tensile torque.

$$W_{it} = 2T\theta_p = v_{tu}H^2(b_0 - H/3)\theta_p \tag{2-12}$$

where v_{tu} : ultimate torsional stress ($= 0.8\sqrt{f_{cu}} \leq 5$)

It was found that the calculated concrete pull-out strength gave a reasonable value compared to test data when the virtual height (*H*) was equal to $0.75h_{sc}$. The shear resistance can be expressed in Eq. 2-13, which indicates that the shear connection was related to the axial force acting on the stud root.

$$P_u = \frac{1}{h_p}\left(0.56v_{tu}h_{sc}^2\left(b_0 - \frac{h_{sc}}{4}\right) + Te_r\right) \tag{2-13}$$

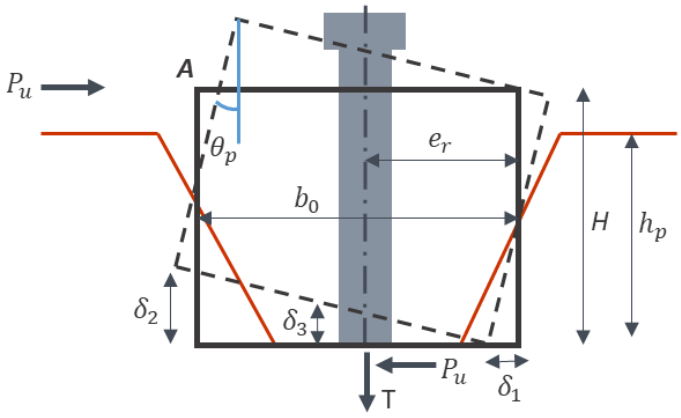

Figure 2-13. Concrete block rotation due to pull-out (Johnson and Yuan, 1998b)

Rib shearing

Rib shearing occurs at the connecting points of the deck rib through the least-resistance area. After failure, the metal deck is filled with concrete which is separated from the concrete slab. Only concrete near the shear stud is pried out at the concrete pull-out failure, whereas the concrete in the deck splits apart at the rib shearing failure. Hawkins and Mitchell (1984) observed that the rib shearing was prone to occur when the deck height and breadth were deeper and narrower, respectively. Jayas and Hosain (1988) also reported that the rib shearing rarely occurred on a broader rib deck specimen. Lloyd and Wright (1990) argued that the failure mode changed from concrete pull-out to rib shearing when the width of the specimen reduced below a critical value. In their experiments, all the specimens with deck widths smaller than the critical value of 473 mm showed the rib shearing failure. Thus, this failure mode was highly related to the geometry of the deck.

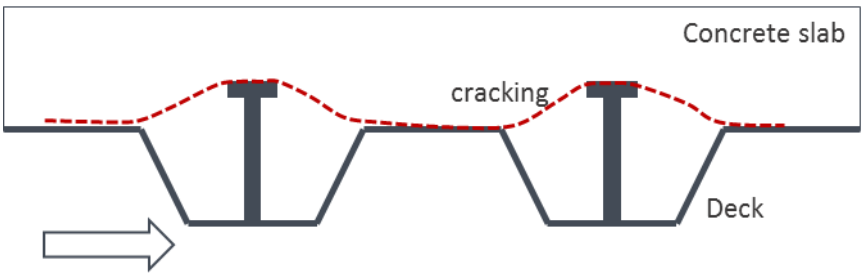

Figure 2-14. Rib shearing failure

Rib punching

Rib punching failure was easily observed when the shear stud was located in an unfavourable position. An applied load causes plastic deformation at the stud root, which occurs concrete crushing and deck bulging in the loading direction. This failure accompanies deck tearing. Roik *et al*. (1989) reported a resistance formula based on a yield hinge mechanism. It assumed that the maximum plastic moment was achieved when the stud capacity reaches its peak value. A coupled moment was developed at both the stud root and stud shank around the mid-height of the deck, as illustrated in Fig. 2-15.

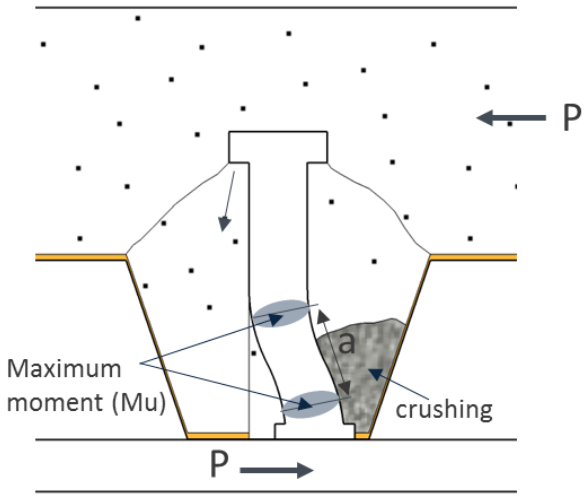

Figure 2-15. Rib punching failure (Roik *et al*., 1989)

The mean shear resistance can be determined as:

$$P_u = \frac{2M_u}{a} \tag{2-14}$$

where M_u : plastic moment at the shear stud
a : distance between the yield hinges

The distance (a) depends on the deck height (h_p) to the width (b), and thus it decreases when the deck height increases. Those relationships are given by:

$$M_u = \frac{f_u d^3}{6}$$
$$a = \mathrm{d}\left(0.8\left(\frac{h_p}{b}\right)^2 + 0.6\right) \tag{2-15}$$

Rib punching failure causes deck tearing, which means the deck strength affects the stud capacity in this failure mode. Johnson and Yuan (1998b) developed a shear resistance formula using the deck yield strength and concrete compressive strength around the stud root. Assuming that the deck yield strength (f_{yp}) is applied through the area, b_pt (deck breadth × deck thickness), and the concrete compressive stress is induced over some length (b_c), the shear resistance is given by:

$$P_u = b_p t f_{yp} + b_c x f_c \tag{2-16}$$

The tensile force induced at the stud root can be expressed assuming a force equilibrium at the concrete prism in Fig 2-16.

$$T_c = b_c y f_c \tag{2-17}$$

From the concrete prism geometry,

$$\frac{x}{y} = \frac{(e_f - y)}{h_p} \tag{2-18}$$

When $y = e_f/2$, the x in Eq. 2-18 shows its maximum length of $e_f^2/4h_p$. By using these relationships, the maximum shear resistance can be calculated as:

$$P_u = b_p t f_{yp} + \frac{e_f}{2h_p} T_c \tag{2-19}$$

The effective width of the deck is empirically derived as

$$b_p = 1.8(e_f + h_{sc} - h_p) \tag{2-20}$$

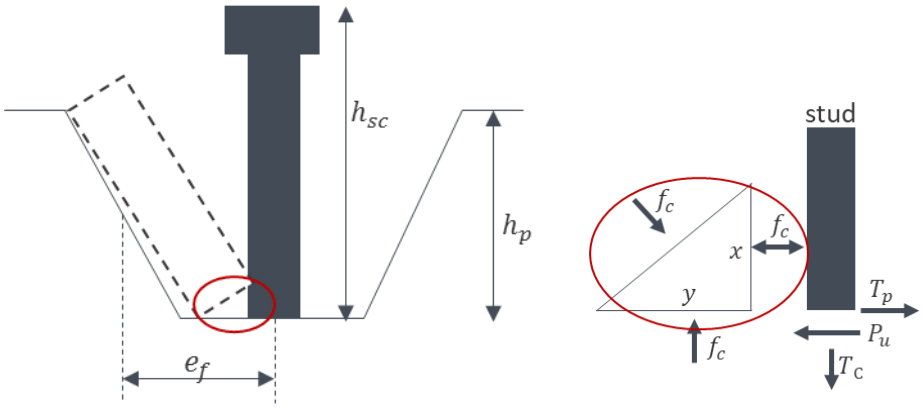

Figure 2-16. Rib punching failure (Johnson and Yuan, 1998b)

Stud shearing

Stud shearing is the dominant failure mode in a solid slab and parallel trapezoidal deck slab. In the case of a transverse deck application, it can only occur when the shear stud is located in a favourable and central position (Johnson and Yuan, 1998a). Its failure mechanism is the same as in the solid slab specimen.

2.5.2. Influencing parameters

It is generally accepted that the shear resistance in a transverse deck slab is smaller than that of a shear stud embedded in a solid slab. The failure mode of the shear stud is also different because the trapezoidal deck configuration, with variations in thickness, deck width, and depth, affects the capacity of the shear connection. Fisher (1970) and Grant *et al*. (1977) reported that the shear resistance shows a linear relationship with the ratio of the deck width to depth. In a deep deck, the shear resistance is stronger than that of a wide deck. Several design codes, such as EC4-1-1 (2009) and BS 5950-3.1 (2010), adopt this relationship as a reduction parameter.

The stud location in a trough also affects the shear resistance. In a favourable position, as depicted in Fig. 2-17, the shear connection withstands a heavier load in comparison to an unfavourably positioned shear stud, because of the size of the concrete bearing zone and different failure mode. Johnson and Yuan (1998a) carried out push-out tests with favourably and unfavourably positioned shear studs. The shear resistance in a favourable position was 25 % higher compared with an unfavourably positioned stud. Hicks (2007) also showed a 28 % difference in the shear resistance, depending on the stud location and based on composite beam tests. Qureshi *et al*. (2011b) conducted a numerical study to investigate the effects of the stud position and deck thickness. When the shear stud was installed at an unfavourable position, the deck thickness influenced the shear resistance. A linear relationship between the shear resistance and deck thickness was reported. This phenomenon is in line with its failure mode, which accompanies deck tearing; rib punching failure is frequently observed with an unfavourably positioned stud. The effect of the deck thickness decreases when the stud position moves to a favourable position. This means that the shear resistance is more dependent on concrete crushing than deck bulging. A modern

trapezoidal deck has a central stiffener which makes it difficult to weld the shear stud at the central position. EC4-1-1 (2009) recommends welding the shear stud at the centre of the deck trough. If this is impossible due to the deck stiffener, it suggests welding the shear studs in a staggered arrangement: one at an unfavourable position and the other at a favourable position.

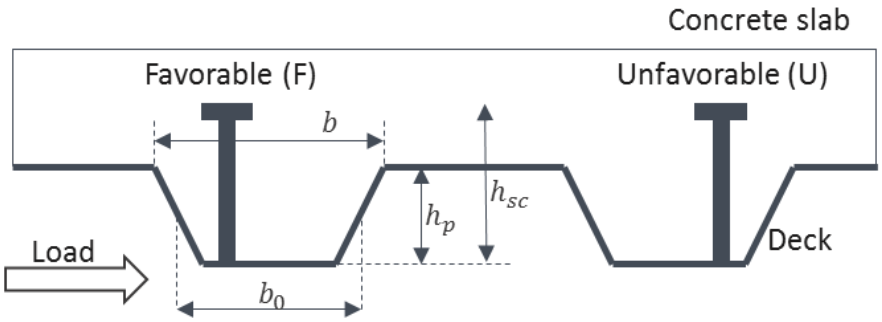

Figure 2-17. Shear stud in a transverse trapezoidal deck

The shear resistance is directly proportional to the number of studs in a solid slab application. However, it is not proportional to the number of studs in a transverse deck slab, owing to the different causes of failure. In the case of concrete pull-out failure, the concrete cracking area does not double in size when the number of studs in a trough is doubled. The distance between the shear studs is only added to the cracking area because the concrete cracking surfaces are connected, as shown in Fig. 2-18.

Figure 2-18. Concrete pull-out failure with a pair of studs (Smith and Couchman, 2010)

EC4-1-1 (2009) consider the effect of multiple studs, adopting the square root of the stud numbers: $1/\sqrt{n_r}$. The shear resistance reduces to 70 % when using a pair of studs. The limitation of the stud number in a trough was imprecise in EC4-1-1 (2009): 'not to exceed two in computation'. If someone adopts more than two studs, the resistance of each stud can be regarded as the two-stud calculation value because of its ambiguous definition. Furthermore, the experimental study conducted by Simms and Smith (2009) showed that the shear resistance of each shear connection was also reduced by 30 % when using three studs in a trough in comparison to using two studs in a trough. Thus, a clear explanation regarding the number of studs in use is required in EC4-1-1 (2009).

Three or more studs in a trough were permitted in BS 5950-3.1 (1990) by limiting the reduction factor to less than 0.6. The resistance ratio of the shear connection between a single stud and pair of studs was 0.7, which is the same value as EC4-1-1 (2009): $1/\sqrt{2} = 0.7$. Hicks (2007) carried out composite beam and push-out tests incorporating one and two studs per rib. The strength ratios of the pair to single stud were 0.6 for the push-out tests and 0.44 for the composite beam tests. The smaller resistance ratio in the beam test may have been caused by the uplift of the un-studded rib adjacent to the trough which has a pair of studs. Smith and Couchman (2010) also showed that the shear resistance reduces to 58 % of the single-stud capacity when using two studs in a rib based on their push-out tests. Moreover, it reduces to 35 % in the case of using three studs in a rib. According to these experimental studies, BS 5950-3.1 (1990) was revised in 2010. A maximum of two studs could be used in a trough, and its reduction ratio and limit value were also reduced.

The space between the studs in a trough affects the shear connection by controlling the concrete cracking area, because the concrete failure surface near the shear studs is shared when using two studs in a trough. Gnanasambandam (1995) carried out push-out tests with a wide ribbed metal deck using a variation of the transverse stud spacing from 38 to 76 mm and a 19-mm-diameter headed shear stud. The shear resistance increased by 15 % when increasing the stud spacing from 38 to 76 mm. In general, the larger the transverse spacing, the higher the shear resistance. However, it cannot increase consistently if there is a sufficient distance for an individual concrete cracking area around the shear stud. Qureshi *et al*. (2011a) reported that the shear resistance did not increase when the transverse spacing exceeded 200 mm with a pair of studs placed side by side in favourable positions.

For this reason, most of the design guidelines, such as EC4-1-1 (2009) and BS 5950-3.1 (2010), provide a minimum transverse spacing to avoid an unexpectedly small shear resistance.

Hicks (2009) also recommended that arranging shear studs side by side with a maximum transverse spacing in a trough is more beneficial to obtain a reliable shear connection than arranged in a line in the loading direction, because a larger concrete failure surface can be achieved in the side-by-side arrangement. Qureshi *et al*. (2011a) conducted a parametric study to compare the effects of the stud location between the side-by-side and staggered positions when a pair of studs were placed in a rib. It showed that the shear resistance reduced by 6 % compared to the strength of a single stud when a pair of studs were placed in the favourable positions, side by side, with a 200 mm transverse spacing. On the contrary, the shear resistance reduced by 14 % in the case of two studs being placed in a staggered position; one was in the favourable position, and the other was diagonally in the unfavourable position. These strength difference increased as the concrete strength increased.

The shear resistance is affected by the deck thickness and welding method. BS5950-3.1 (2010) recommends using a deck of 0.9 mm nominal thickness, whereas EC4-1-1 (2009) permits using a deck of over 1 mm in thickness. Hanswille (1993) reported the upper limit value of the reduction factor with respect to the deck thickness and welding method. Statistical analysis was carried out with variables such as the welding method (through-deck welding, direct welding with a pre-punched hole), deck thickness (1.2 mm, less than 1 mm) and number of studs (single, pair). In the case of a through-deck welded shear connection with a 1.2-mm-thick deck, the draft of EC4-1-1 (1994) gives a conservative value with a single stud and an overestimated value with a pair of studs. Therefore, the upper limit of the deck reduction factor (k_t) was proposed to have a conservative estimation, regardless of the number of studs. The dotted line in Fig. 2-19(b) was recommended as the upper limit value of 0.75. The ultimate stress of the shear stud and the stud diameter were assumed as 450 *MPa* and 19 *mm*, respectively.

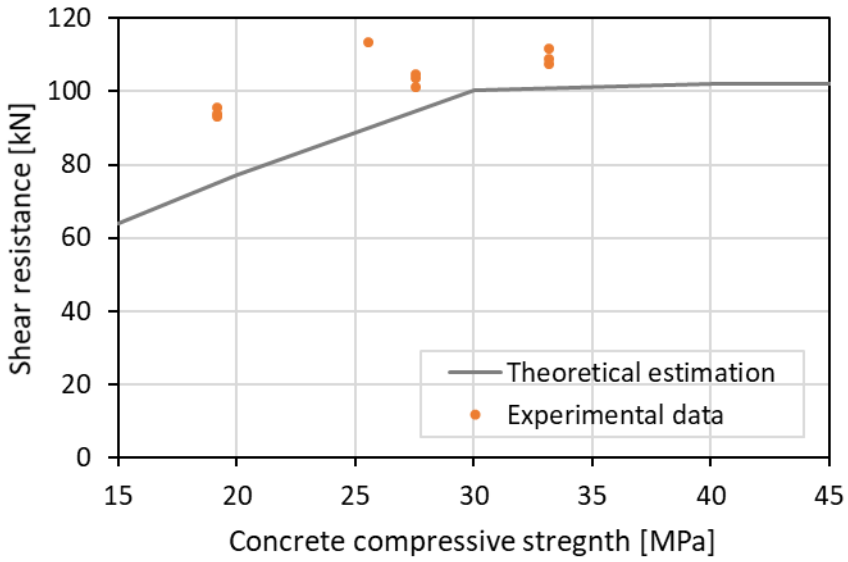

(a) 1.2 mm thickness, n_r=1

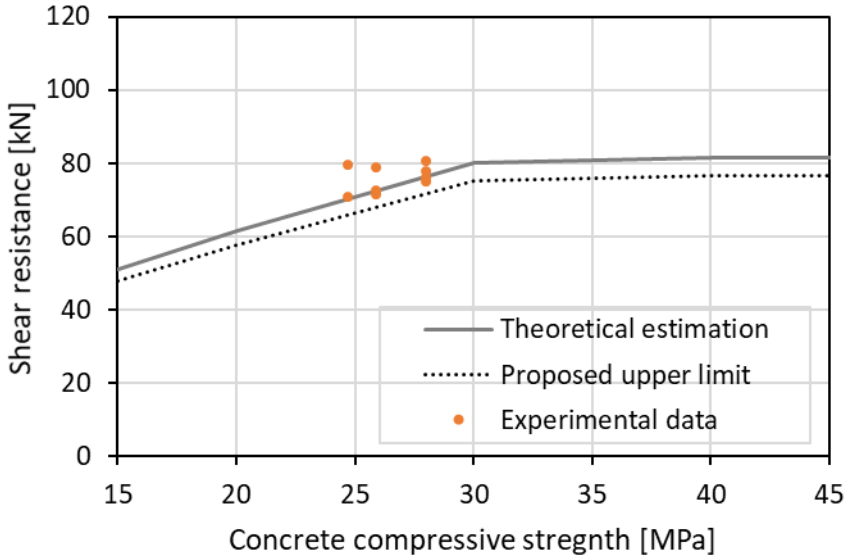

(b) 1.2 mm thickness, n_r=2

Figure 2-19. Experimental and theoretical data with 1.2t through-deck welding (Hanswille, 1993)

When using a steel sheeting thinner than 1 mm, the shear resistance of the experimental data was smaller in comparison to the draft of EC4-1-1 (1994). Fig. 2-20 illustrates the experimental and theoretical values. The reduction coefficient of 0.85 was recommended to obtain a conservative estimation according to the statistical study with a 95 % confidence level. When a pair of studs were embedded in a rib, the reduction coefficient of 0.7 was proposed by applying the same resistance reduction ratio as for the thicker-deck experimental data.

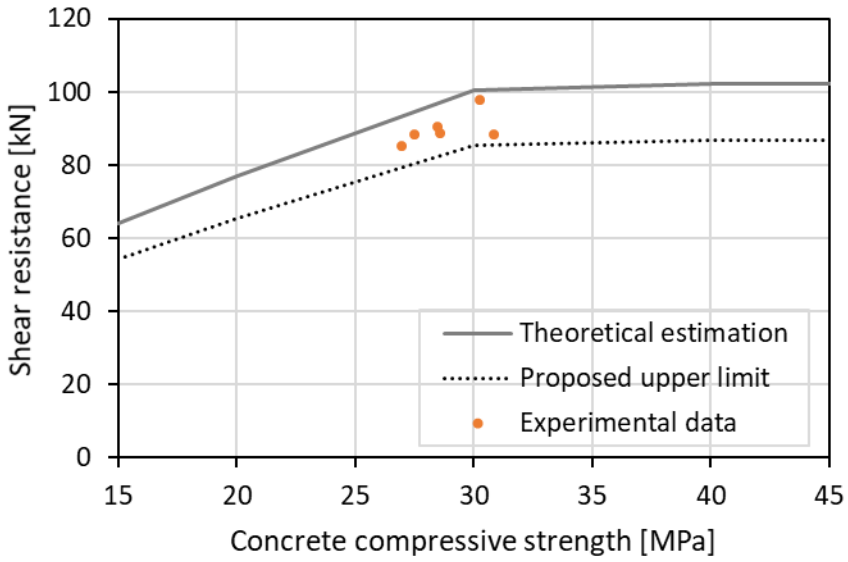

Figure 2-20. Experimental and theoretical data with 0.9t through-deck welding (≤1 mm thickness, n_r=1) (Hanswille, 1993)

The stud diameters of 19 and 22 mm were used to evaluate the shear resistance with a direct welding method. A higher reduction factor was observed compared to the result of the through-deck-welded specimen. Stark and Hove (1991) reported that the shear resistance of the directly welded stud on steel flanges was comparatively smaller than that of the through-deck-welded shear connection. The obtained upper limit values to consider the stud welding method were 0.75 for a single stud and 0.6 for a pair of studs. Based on the above statistical studies (Hanswille, 1993), EC4-1-1 (2009) adopted the upper limit value of the reduction factor to consider the deck thickness with respect to the number of studs and welding method, as presented in Table 2-3.

Table 2-3. Upper limits of $k_{t,max}$ for the reduction factor k_t (EC4-1-1 (2009), Table 6.2)

Number of studs per rib	Thickness of sheet [mm]	Stud diameter ≤ 20 mm Through-deck welding	Stud diameter = 19 mm or 22 mm Direct welding with holes
$n_r = 1$	≤ 1.0	0.85	0.75
	> 1.0	1.0	0.75
$n_r = 2$	≤ 1.0	0.70	0.6
	> 1.0	0.8	0.6

The effect of the reinforcement mesh location was investigated by Smith and Couchman (2010). They reported that the possibility of a concrete cracking surface changes with respect to the reinforcement mesh position, because the reinforcement bar prevents concrete cracking. Based on this experiment, the Steel Construction Institute (PN001a-GB, 2010) proposed an additional parameter (called a modification factor) to calculate the shear resistance according to the reinforcement mesh location. When using a single stud, its effect was negligible, which implied a modification factor of 1. In the case of a pair of studs, the modification factors of 0.7 and 0.9 were recommended according to the mesh position: 0.7 for the mesh laid above the stud head and 0.9 for the mesh applied at least 10 mm below the stud head. The effect of the mesh location was also investigated by Qureshi (2010) using a modified push-out test with a single stud per rib; a mesh fabric A193 was placed directly on the deck shoulder and 30 mm below the surface of the concrete slab. A meaningful difference in the shear resistance was found with respect to the mesh location. Lawson (1997) pointed out that transverse cracking at the concrete slab occurred when inadequate reinforcement was used for a push-out test specimen with two studs per rib. It can be deduced that the effect of the reinforcement location becomes significant when a higher shear resistance is required per trough.

The influencing parameters in shear resistance increase when adopting transverse deck slabs as summarised in Table 2-4. All of them are proved experimentally at ULS. However, it has not been investigated whether those effects are still valid at FLS.

Table 2-4. Influencing parameters in transverse deck applications at ULS

Parameter	Effect on shear connection
Deck width to depth	- Failure mode changes from rib shearing to concrete pull-out as the deck width to depth increases - Design codes adopt the deck reduction factor (k_t) considering the deck shape
Stud location in a trough	- Favourable sided studs give a higher shear resistance than unfavourably positioned studs.
Number of studs in a trough	- Increasing the stud numbers in a trough provides a weaker load-bearing capacity per each stud.
Deck thickness	- Shear resistance and deck thickness shows a linear relationship
Welding method	- Through-deck welded stud shows higher shear resistance than through-hole welded stud
Space between the studs	- Shear resistance decreases as the transverse spacing between the shear stud decreases
Reinforcement mesh location	- Shear resistance decreases as the reinforcement mesh closer to the top side of the concrete slab

2.5.3. Design guidance

Several design codes, such as EC4-1-1 (2009), AISC 360-10 (2010), and AS 2327.1 (2003), have adopted a reduction factor to calculate the shear resistance in profiled steel sheeting by multiplying the shear resistance in a solid slab, whereas the Canadian Standard (CSA S16-01, 2001) adopts a direct empirical formula. The shear resistance in a transverse deck is expressed using the deck reduction factor:

$$P_{deck} = k_t P_{solid} \tag{2-21}$$

where P_{deck} : shear resistance in a transverse deck slab
k_t : deck reduction factor of the transverse deck
P_{solid} : shear resistance in a solid slab

Fisher (1970) found that the shear resistance in a transverse deck shows a linear correlation with the ratio of the deck width to depth. In the regression analysis, the top measurement for the rib width was used, and the stud diameter was limited to less than 19 mm. Its relationship is given by:

$$k_t = C_2 \left(\frac{b}{h_p}\right) \leq 1.0 \tag{2-22}$$

where C_2 : experimental constant (= 0.5)
b : width at the top of the rib
h_p : deck depth [*mm*]

Grant *et al*. (1977) carried out 17 full-scale beam tests and analysed the stud behaviour by incorporating 58 additional beam tests conducted by other researchers. They introduced a stud height parameter, because concrete cracking starts from the head of the shear stud, which means the embedment length above the deck shoulder affects the concrete cracking area. The proposed deck reduction factor was:

$$k_t = \frac{C_3}{\sqrt{n_r}} \left(\frac{b_0}{h_p}\right) \left(\frac{h_{sc}}{h_p} - 1\right) \leq 1.0 \tag{2-23}$$

where C_3 : experimental constant (= 0.85)

n_r : number of studs in a rib
b_0 : average rib width [mm]
h_{sc} : stud height [mm]

The deck reduction factor was only valid within the experimental conditions, because it was derived empirically. The range of rib height was 38 to 76 mm, and the rib width was 57 to 152 mm. The deck width to height ratio was 1.5 to 2, and the stud height was 76 to 114 mm. The added parameter (the stud height) came from concrete-dominated failures, such as concrete pull-out or rib shearing, because these are the dominant failure modes in transverse deck specimens.

Several studies regarding the experimental constant (C_3) were conducted to verify the shear resistance embedded in transverse deck slabs (Roik *et al*., 1989; Stark and Hove, 1991). Stark and Hove (1991) reported that the empirical constant needs to be changed from 0.85 to 0.7 to have a conservative estimation based on their statistical analysis. A rigid failure (concrete-dominated failure) formula was used to calculate the shear resistance in profiled steel sheeting, because only 3 of 63 available test results show the ductile failure (stud shearing failure). The current standard EC4-1-1 (2009) uses Eq. 2-23 with the empirical constant of 0.7 for the shear resistance calculation in transverse deck applications. The limit value of the reduction factor was also adopted according to the deck thickness and number of studs in a trough, as described in Table 2-3.

A further modification in the deck reduction factor has been adopted in BS 5950-3.1 (2010); Eq. 2-23 is used for the deck reduction parameter with the empirical constant of 0.63 for a single stud in a trough. When two studs are placed in a trough, the empirical constant of 0.34 is used with the limit reduction factor of 0.45 based on composite beam and push-out tests (Hicks, 2007).

In the U.S., the same design formula is used for the shear resistance calculation in solid, parallel, and transverse deck slabs with different reduction parameters. It was derived from 202 push-out tests conducted by Rambo-Roddenberry (2002). The design guidance, AISC 360-10 (2010), recommends using the following equation:

$$P_u = 0.5A_{sc}\sqrt{f_c E_{cm}} \leq R_g R_p A_{sc} f_u \quad (2\text{-}24)$$

where R_g: reduction factor with respect to the number of studs in a rib.
= 1 for single stud, 0.85 for a pair of studs,
0.7 for three or more studs
R_p: reduction factor regarding the stud location in a rib
= 0.75 for favourable position ($e_{mid-ht} \geq 50$ *mm*)
= 0.6 for unfavourable position ($e_{mid-ht} < 50$ *mm*)
e_{mid-ht}: distance between the edge of the stud shank and mid-height of the deck in the load-bearing direction

Although the failure modes of the shear connection in a solid slab and profiled steel deck are different, the shear resistance in a solid slab is used as a base value to calculate the shear resistance in a transverse deck slab by incorporating a deck reduction factor. In Canada, a direct empirical formula is used for the shear resistance calculation based on composite beam and push-out tests carried out by Jayas and Hosain (1988, 1989). A concrete cracking surface is defined as a pyramidal shape for a single stud and a connected pyramidal shape for a pair of studs. Those definitions of the concrete failure surface were adopted as follows:

$$P_k = 0.35\Phi_{sc}\rho A_C\sqrt{f_{ck}} \leq P_{k,solid} \quad \text{for } h_p = 75 \text{ mm}$$
$$P_k = 0.61\Phi_{sc}\rho A_C\sqrt{f_{ck}} \leq P_{k,solid} \quad \text{for } h_p = 38 \text{ mm} \quad (2\text{-}25)$$

where Φ_{sc}: resistance factor (= 0.8)
ρ: concrete density
(= 1 for normal concrete, =0.85 for low-density concrete)
A_C: concrete cracking surface [mm^2]

Significant parameters such as the deck shape, stud height, number of studs, and stud spacing should be controlled to have an expected resistance of the shear connection in transverse deck applications. Table 2-5 shows these recommended parameters in several design codes.

Table 2-5. Shear stud design guidance for transverse deck applications

[mm]	EC4-1-1 (2009)	BS5950-3.1 (2010)	AISC 360-10 (2010)	CSA S16-01 (2001)
Deck depth (h_p)	>= 40	35-80	$(b_0/h_p \cong 1.5)$	38, 75
Mean width of rib (b_0)	> 50	> 100	-	-
Stud height above deck	> 2d	35	25	-
Deck thickness	Around 1 mm	0.9	-	-
Max. number of stud in a trough	2	2	3	-
Shear resistance calculation	Reduction formula	Reduction formula	Table value	Empirical formula
Min. transverse spacing	4d[1]	4d	4d	-
Max. longitudinal spacing	< 800 or 4ds[2]	< 600 or 4ds	< 900 or 8ds	-

[1]d: stud diameter [*mm*]
[2]ds: total slab thickness [*mm*]

A composite beam should withstand exposure to fire without collapse for a designated duration, such as 30, 60, or 90 min, depending on the purpose of the building. When designing the fire resistance of a composite beam, the following criteria should be considered in EC4-1-2 (2014):

- Whether the temperature of the steel member exceeds a critical temperature under the designated fire resistance time.
- Whether the temperature of the concrete compressive force acting region exceeds 250 ℃, because thermal degradation starts above that temperature.
- Whether the tensile force generated in a composite beam at high temperature exceeds the resistance of the shear connection, because a collapse may occur without composite action between the steel and concrete sections.

The shear resistance at high temperature is an important parameter to avoid a collapse or the sudden fracture of composite beams in a fire situation. The draft of EC4-1-2 (1994) used

the maximum stress level of the stud material ($f_{v,\theta}$) to calculate the shear resistance at high temperature in the case of a rigid failure:

$$P_{k,\theta} = f_{v,\theta} P_k \tag{2-26}$$

where $P_{k,\theta}$: characteristic value of shear resistance at high temperature [*kN*]
$f_{v,\theta}$: maximum stress level of the stud material at high temperature
P_k: characteristic value of shear resistance at ULS [*kN*]

The maximum stress level of the stud material ($f_{v,\theta}$) means the yield stress reduction with respect to temperature. Thermal degradation starts from 400 ℃, which indicates that there is no strength reduction below 400 ℃. Zhao and Kruppa (1993) argued that Eq. 2-26 is not sufficiently conservative in comparison with their high-temperature experimental data. Thus, the ultimate strength reduction factor of the stud material was incorporated into the calculation at high temperatures in the current EC4-1-2 (2014), as presented in Eq. 2-27. An empirical constant of 0.8 was adopted not only to compensate for the strain-hardening effect less than 400 ℃, but also to further reduce the strength above that temperatures. They also confirmed that the stud temperature (5 mm from the bottom of the shear stud) did not exceed 80 % of the upper flange temperature when the specimen was exposed to the ISO 834 standard fire.

$$\begin{aligned} SRF &= 0.8 k_{u,\theta} && \text{for stud shearing failure} \\ SRF &= k_{c,\theta} && \text{for concrete-dominated failure} \end{aligned} \tag{2-27}$$

where SRF: strength reduction factor with respect to temperature
$k_{u,\theta}$: reduction factor for the yield strength of structural steel giving the strain hardening stress level at elevated temperature
$k_{c,\theta}$: reduction factor for the compressive strength of concrete giving the strength at elevated temperature
θ: temperature of the shear stud or surrounding concrete [℃]

The temperature-dependent shear resistance can be calculated by multiplying the *SRF* and shear resistance at ULS. This relationship was adopted by the current EC4-1-2 (2014).

$$P_{k,\theta} = SRF \cdot P_k \tag{2-28}$$

where $P_{k,\theta}$: characteristic value of shear resistance at high temperature [*kN*]

When a transverse deck is adopted, the temperature-dependent shear resistance can be calculated using two reduction factors (deck shape and thermal degradation) from the shear resistance in a solid slab. The procedure is illustrated in Fig. 2-21. Stud shearing is a common failure mode of the shear connection in a solid slab, whereas it is a concrete-dominated failure mode such as concrete pull-out or rib shearing in a transverse deck slab. Nevertheless $P_{k,solid1}$ is used as a base value to calculate the shear resistance in a transverse deck slab; the deck reduction factor is also added regardless of the failure mode of a shear connection according to the current EC4-1-2 (2014).

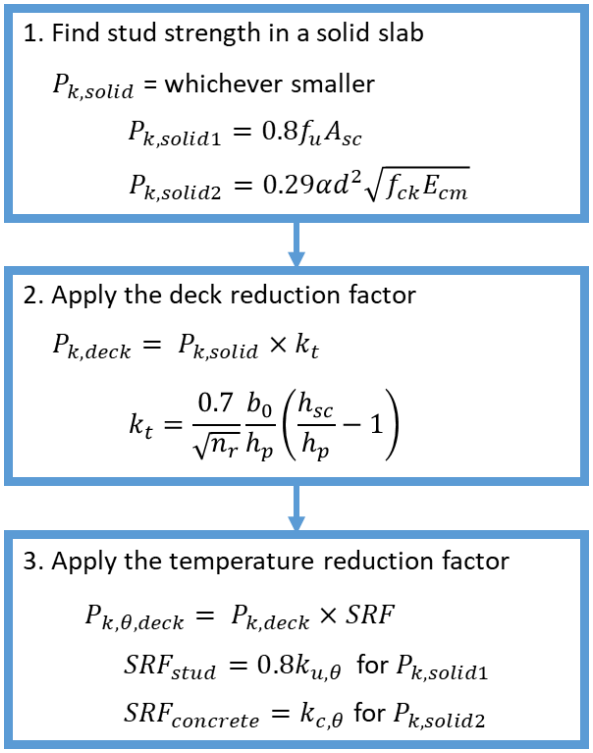

Figure 2-21. Calculation procedure of shear resistance at high temperatures according to EC4-1-2 (2014)

Limited experimental data are available regarding the high-temperature behaviour of shear connections. Most of such studies used a solid slab instead of a transverse deck slab, which is more widely used currently. The current EC4-1-2 (2014) provides the strength reduction factor with respect to the flange temperature based on the experimental study of Zhao and Kruppa (1993). Their empirical formula was obtained based on solid slab specimens. However, this reduction formula has been used regardless of the slab type. A load ratio of the existing experimental data with reference to its ambient value and the SRF for stud failure in EC4-1-2 (2014) are plotted in the same graph in Fig. 2-22. Since the ultimate strength of steel decreases from 300 ℃, the SRF starts to reduce above that temperature. It shows a similar trend as a temperature rises broadly, a deviation at medium to low temperatures still can be found.

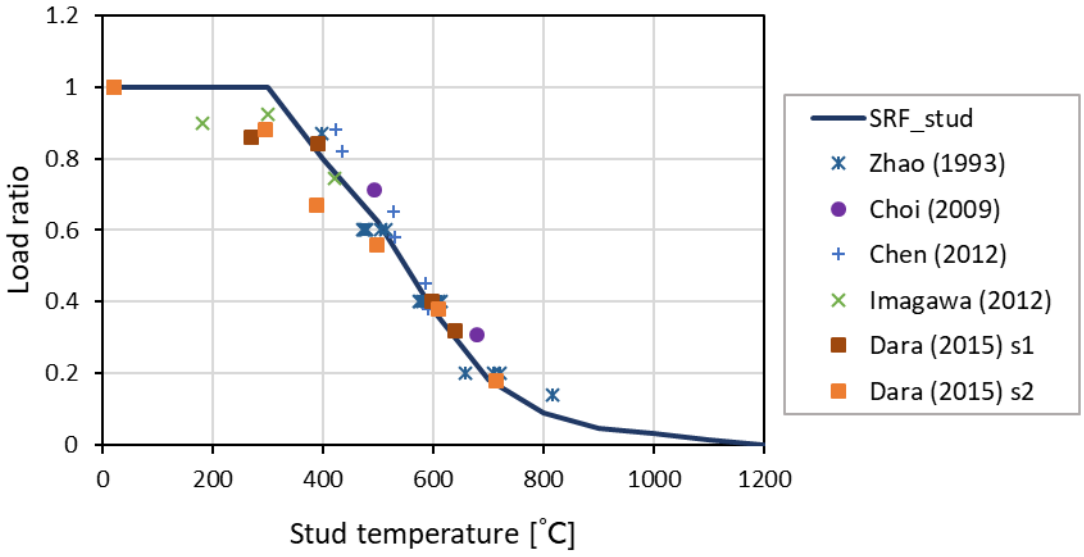

Figure 2-22. Strength reduction ratio of the headed shear stud in a solid slab

Unlike using solid slab specimens, a different strength reduction was observed in experiments incorporating transverse deck slab. A higher strength reduction factor was observed in the experiment of Mirza *et al*. (2011), whereas it was smaller in the push-out test of Chen *et al*. (2012) in comparison to their experiment of solid slab specimens. It is difficult to compare these experimental results directly, because the specimen sizes and heating process were totally different.

2.6. Numerical work

Few studies have been conducted regarding the shear connection behaviour under elevated temperature using numerical approaches. Most of them adopted solid concrete slabs and proposed a strength reduction factor with respect to temperature. All the proposed design criteria do not consider the failure mode which changes as temperature rises. In this section, existing numerical works are investigated.

The temperature distribution of the shear stud in a high-temperature push-out test was analysed by Quevedo and Silva (2013). They developed a two-dimensional model adopting the cross-section of a specimen as the modelling domain. Rectangular elements with a size of less than 10 mm were used, and smaller elements were applied around the shear stud. The temperature variation with respect to the stud diameter and height was investigated. The temperature of the surrounding concrete greatly decreased as the stud height increased, because it was measured at the mid-height of the shear stud. They pointed out that the measuring location of the surrounding concrete should be changed from half to one-quarter of the stud height, because it was the most severely damaged area during the push-out test. The recommended concrete temperature was 60 % of the flange temperature to calculate the shear resistance when it breaks down caused by concrete-dominated failure.

Mirza and Uy (2009) developed a numerical model to investigate the shear stud behaviour incorporating solid and transverse deck slabs at high temperatures. A structural model was verified using push-out test data at ULS, and existing temperature distribution data were adopted instead of conducting a thermal analysis. The temperature of the numerical model was normalised into 11 sections, as shown in Fig. 2-23: three sections for the steel beam and eight sections for the concrete slab, including the shear stud. A two-dimensional temperature profile was incorporated into the three-dimensional structural model. High-temperature properties such as the thermal conductivity, specific heat, thermal expansion, concrete compressive stress-strain curve, and steel tensile stress-strain curve were referenced from EC2-1-2 (2014) and EC3-1-2 (2009). A three-dimensional brick element was adopted in this numerical model, and the arc-length method provided in Abaqus was used for the numerical solution.

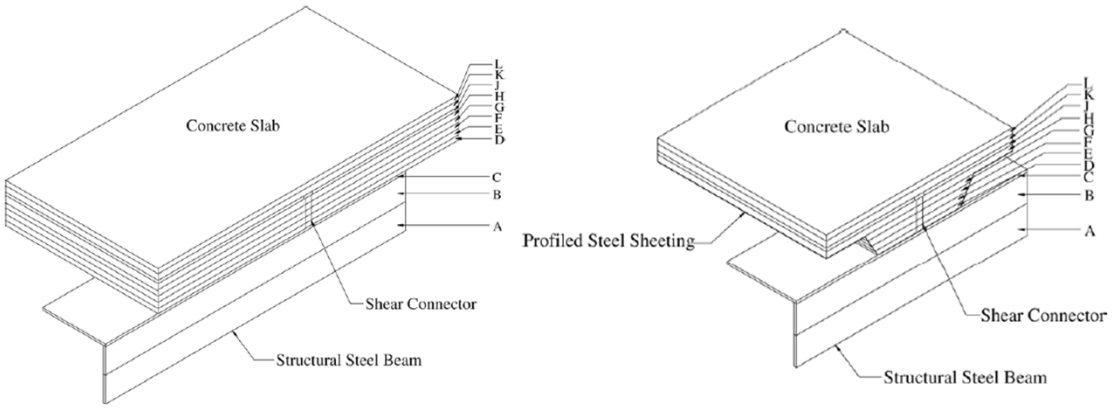

Figure 2-23. Temperature sections of the numerical model (Mirza and Uy, 2009)

According to their parametric study, the shear resistance reduced by 35 % in a solid slab specimen when exposed to the ISO 834 standard fire for 10 min. After 180 min of heating, the shear resistance reduced by 57 %. Significant degradation was shown during the first 20 min, after which the shear resistance decreased slowly. In the case of a transverse deck specimen, the shear resistance reduced by 25 % and 31 % when exposed to fire for 10 and 180 min, respectively. They proposed the strength reduction ratio with respect to the fire exposed time (t) as follows:

For a shear stud embedded in a solid slab

$$\begin{aligned} SRF_\theta &= -3.45 \times 10^{-2} t + 1 && \text{for } 0 \text{ min} \le t \le 10 \text{ min} \\ SRF_\theta &= -9.4 \times 10^{-3} t + 0.7483 && \text{for } 10 \text{ min} \le t \le 20 \text{ min} \\ SRF_\theta &= -1.1 \times 10^{-3} t + 0.5837 && \text{for } 20 \text{ min} \le t \le 120 \text{ min} \\ SRF_\theta &= -6 \times 10^{-5} t + 0.4527 && \text{for } 120 \text{ min} \le t \le 180 \text{ min} \end{aligned} \quad (2\text{-}29)$$

For a shear stud embedded in a transverse deck slab

$$\begin{aligned} SRF_\theta &= -2.51 \times 10^{-2} t + 1 && \text{for } 0 \text{ min} \le t \le 10 \text{ min} \\ SRF_\theta &= -6 \times 10^{-4} t + 0.7549 && \text{for } 10 \text{ min} \le t \le 60 \text{ min} \\ SRF_\theta &= -2 \times 10^{-4} t + 0.7279 && \text{for } 60 \text{ min} \le t \le 180 \text{ min} \end{aligned} \quad (2\text{-}30)$$

Mirza and Uy (2009) argued that a shear stud embedded in a transverse deck slab is more robust at high temperature, because the air gap formed by the deck acts as a protective layer. Comparing the proposed strength reduction factor with EC4-1-2 (2014), it shows a relatively small degradation for both solid and transverse deck slabs, as plotted in Fig. 2-24. Moreover, it also provides a different response in comparison to the experimental investigation of Mirza *et al*. (2011). In their numerical model, the same temperature value was used for the flange and bottom layer of the concrete, which means that the stud root temperature was the same as the flange temperature. The adoption of the two-dimensional temperature data in the structural model could be a reason for the different strength reduction. Therefore, more detailed temperature data should be incorporated into a thermomechanical model.

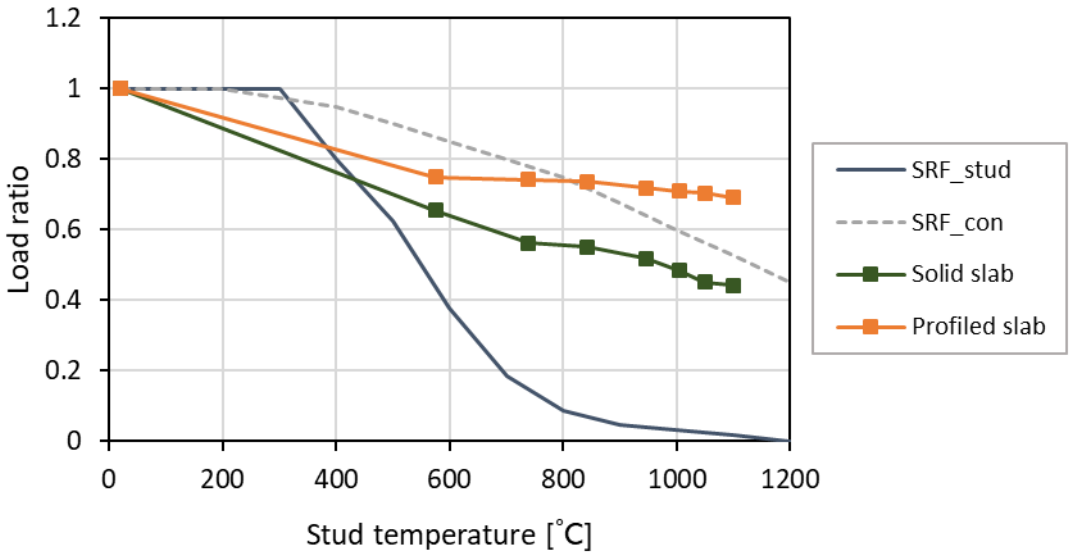

Figure 2-24. Strength reduction according to Mirza and Uy (2009)

Wang (2011) developed a three-dimensional thermomechanical finite element model to investigate the shear stud behaviour under elevated temperatures. First, a thermal analysis was conducted using a three-dimensional quadratic solid element. A thermal conductance of 0.3 W/m^{2}K was assumed for all the contact layers; one was between the stud and the surrounding concrete and the other was between the steel flange and the concrete slab. A

resultant emissivity of 0.8 and shadow factor were adopted to simulate radiative heat transfer in the thermal model. Each nodal temperature was incorporated into a mechanical model to consider the structural deformation and thermal degradation simultaneously. For the mechanical analysis, the von Mises criteria and Drucker–Prager model were adopted for the steel and concrete materials using an arc-length procedure. A linear contact stiffness was used between the shear stud and surrounding concrete. A contact stiffness of 20 kN/mm was selected after a trial-and-error procedure. The thermal expansion of steel and concrete were assumed as 14×10^{-4} and 18×10^{-4}, respectively, to incorporate the thermal stress caused by temperature variations.

The developed model was calibrated using the experimental results of Zhao and Kruppa (1993). The thermal analysis shows that the stud temperature was approximately 100 ℃ to 150 ℃ higher than the surrounding concrete, and the temperature differences between the top and bottom of the stud were 500 ℃ and 350 ℃ when exposed to fire for 60 and 120 min, respectively. The failure modes observed were stud shearing and concrete-dominated failure in the solid and trapezoidal deck slabs. The stress distribution of the shear stud at fracture under high temperature is shown in Fig. 2-25. The maximum stress was observed at around 35–45 mm in the solid slab, whereas it occurred approximately 55 mm from the stud root in the trapezoidal deck slab. Xue *et al*. (2008) reported that the maximum stress at the shear stud was observed around 18–33 mm at ULS based on their experimental study using solid slab specimens. Thus, it can be assumed that thermal degradation of the stud material makes the position of the maximum stress higher, because the stud root area is degraded by the elevated temperature.

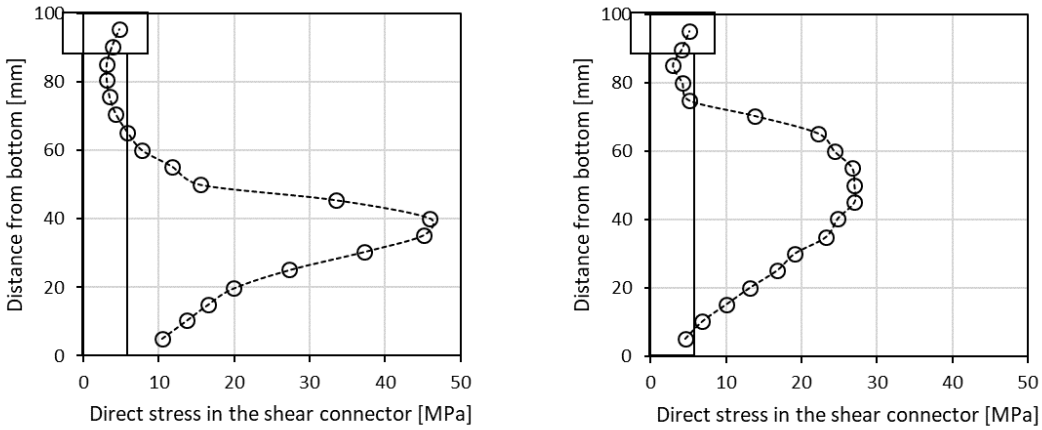

(a) Stud in a solid slab (b) Stud in a transverse deck slab

Figure 2-25. Stress distribution of the shear stud at failure under high temperature (Wang, 2011)

High-temperature shear stud behaviour in a transverse deck was investigated using a three-dimensional thermomechanical finite element model by Chen *et al*. (2015). In the thermal analysis, the convection coefficient of 35 W/m^{2}K and emissivity of 0.7 were adopted according to the Eurocode guidance. The natural fire condition was used, because the gas temperature in the furnace could not follow the ISO 834 standard fire. The identical contact property was used for the boundary between the shear stud and the surrounding concrete, as well as the interface between the steel flange and the concrete slab. The Coulomb friction model with a friction coefficient of 0.1 was adopted for the tangential behaviour, and the hard contact model was used in the normal direction. The coefficient of thermal expansion was defined as a constant value both for the steel and concrete. Half of the push-out test specimen was adopted in the model using a three-dimensional eight-node linear brick element. The nonlinear behaviour was calculated using a dynamic explicit analysis provided in Abaqus/Explicit. The von Mises criteria and concrete damaged plasticity (CDP) model were used for the steel and concrete models. They argued that the developed thermomechanical model is also suitable for the ISO 834 standard fire condition. Although the thermal gradient between the ISO 834 standard fire and a slow heating profile was different, the load–slip relationship gives similar behaviour with respect to the stud root temperature. The strength reduction factor was proposed based on parametric studies, assuming that the headed shear stud was embedded in a transverse deck, as follows:

$$
\begin{aligned}
SRF &= 1 && \text{for } 20\,℃ \le \theta \le 200\,℃ \\
SRF &= -4.508\theta^3 10^{-9} + 3.413\theta^2 10^{-6} - 0.00113\theta + 1.125 \\
& && \text{for } 200\,℃ < \theta < 800\,℃ \\
SRF &= 0.5 - \theta/2000 && \text{for } 800\,℃ \le \theta \le 1000\,℃
\end{aligned}
\tag{2-31}
$$

The stud temperature was acquired at 5 mm from the stud root using the thermal analysis, because Zhao and Kruppa (1993) measured at the same position to define the stud temperature. As shown in Fig. 2-26, the strength reduction ratio curve was located between the stud and concrete failure curves of EC4-1-2 (2014). The failure mode changed at approximately 500 ℃ from concrete-dominated failure to stud shearing in their experiment. However, the same SRF was proposed regardless of the failure mode change. Over most of the temperature range, it shows relatively low degradation compared with the stud shearing criterion in EC4-1-2 (2014).

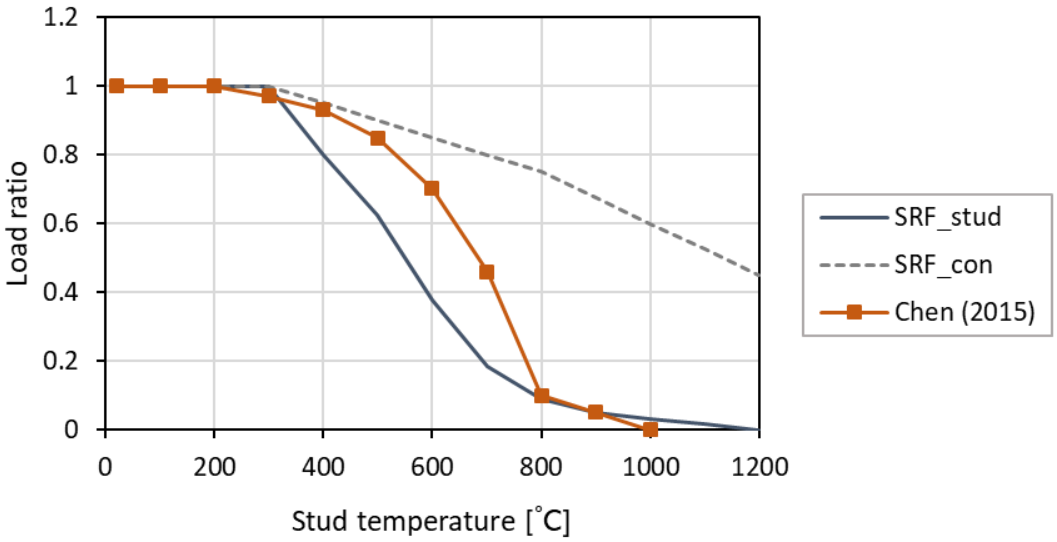

Figure 2-26. Strength reduction ratio with a transverse deck slab (Chen *et al*., 2015)

Dara (2015) performed thermomechanical modelling using the same procedures as Chen *et al*. (2015). Heat was applied for a specific period until the stud temperature reached a designated value, following which a load was applied. The strength reduction factor with

respect to the stud temperature was reported using the simulation results. Although EC4-1-2 (2014) defines the stud temperature as 80 % of the flange temperature, the stud root temperature showed approximately 90–95 % of the flange temperature. This different temperature ratio was caused by different experimental conditions, such as the heating rate, configuration of the specimen, and experimental setup; the gas temperature was also different from the ISO 834 standard fire. They reported the strength reduction factor with reference to the stud temperature as follows:

$$\begin{aligned} SRF &= 1 && \text{for } 20\,℃ \le \theta \le 100\,℃ \\ SRF &= 1.0757 - 0.0008\theta - 10^{-9}\theta^3 && \text{for } 100\,℃ < \theta \le 700\,℃ \end{aligned} \tag{2-32}$$

At a medium-to-low temperature, the strength degradation was higher than the EC4-1-2 (2014) recommendation, as plotted in Fig. 2-27. The stud material degradation became more localised as the temperature increased, which observed regardless of the slab type in the case of stud shearing failure at high temperature. The modelling results indicate that the strength reduction occurs when the stud temperature is higher than 100 ℃. The current EC4-1-2 (2014) gives an unconservative estimation at medium-to-low temperatures, compared with the proposed strength reduction factor in Eq. 2-32.

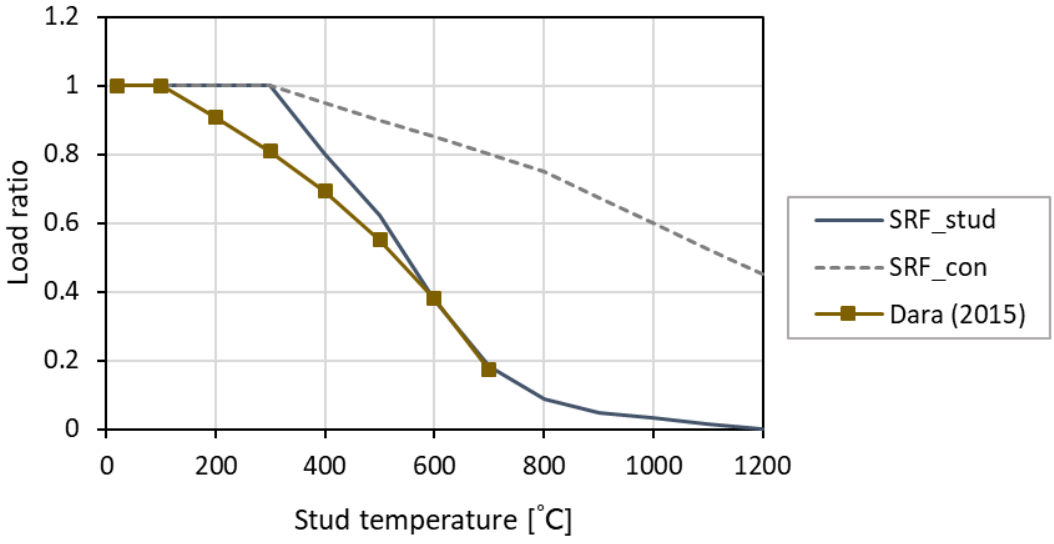

Figure 2-27. Strength reduction ratio with a solid slab (Dara, 2015)

2.7. Summary and conclusions

A comprehensive review of the shear connection test methods and shear resistance estimation at both ULS and FLS incorporating solid and transverse deck slabs was conducted. Several strength reduction factors with respect to temperature reported in the literature were also compared with the current design code, EC4-1-2 (2014). The temperature of the stud root was a primary parameter in the case of the stud shearing failure. However, the shear resistance in a transverse deck at different temperatures shows ambiguous data, not only because its experimental data were limited, but also the experimental results give different thermal degradations. Although the shear resistance of transverse deck composite beams is influenced by several parameters, such as the deck thickness, stud welding method, stud spacing, and number of studs in a trough, only the temperature effect was investigated regardless of slab type in previous high-temperature push-out tests.

The review of previous studies shows that there is a knowledge gap with respect to the shear connection behaviour at high temperature, especially when incorporating a transverse deck slab. The previous studies and the knowledge gap can be summarised as follows:

- The standard test method for the shear connection has been discussed since 1964, and several design codes adopt the push-out test with a specific configuration, test conditions, and procedure. Limited experimental data are available at FLS, and all of them used different test conditions such as a temperature profile, specimen configuration, and experimental setup. As a result, diverged behaviour has been reported.
- A considerable difference in the shear resistance reduction was found in the available high-temperature experimental data when the shear stud was embedded in a transverse deck slab. A higher thermal degradation was observed in comparison to a companion solid slab specimen in the experiment of Mirza *et al*. (2011), whereas a smaller shear resistance reduction was shown in the investigation of Chen *et al*. (2012). The current EC4-1-2 (2014) provides the identical thermal degradation formula, regardless of the slab type, to calculate the shear resistance at high temperature. It is established based on high-temperature push-out tests with solid

slab specimens. Thus, the effect of temperature on the shear resistance incorporating a transverse deck slab must be evaluated.

- Much research has been conducted on the headed shear stud behaviour with both solid and transverse deck slabs using experimental and numerical analysis at ULS. When embracing a transverse deck slab, the deck reduction factor recommended by EC4-1-1 (2009) is used to estimate the shear resistance at FLS. However, no study has been carried out to investigate the effect of the transverse deck parameters such as the deck thickness, stud welding method, and stud location in a trough under elevated temperatures.
- Limited numerical analyses are available to examine the stud behaviour in a fire. The existing numerical models only consider the temperature parameter without relation to deck configurations. Furthermore, the number of studs in a trough is still controversial at ULS, which reports in the adoption of different empirical constants to calculate the shear resistance in EC4-1-1 92009) and BS 5950-3.1 (2010). To the best of the author's knowledge, no study has been conducted to investigate the structural capacity of the shear connection in a transverse deck slab at high temperature considering deck parameters such as the deck thickness, stud welding method, stud location, and number of studs in a trough.

In order to broaden the knowledge of the shear stud behaviour embedded in a transverse deck slab, experimental and numerical studies are carried out, as discussed in the subsequent chapters.

Chapter 3
MATERIAL CONSTITUTIONS

3.1. Introduction

A composite beam is composed of a steel beam, concrete slab, and shear connectors. The shear connector is usually welded onto the steel beam, and it is also embedded into the concrete slab. The behaviour of the shear connection is highly influenced by the characteristics of the concrete material, such as its stiffness degradation, crushing, and cracking. These concrete fractures are determined by the implemented material properties and yield criteria when conducting numerical modelling. Steel is a pressure-independent material, which means the failure criterion does not change according to hydrostatic stress. Conversely, concrete is a pressure-dependent material, as well as having a different strength under tension and compression. To illustrate these material responses, the von Mises criterion and concrete damaged plasticity (CDP) model were used for steel and concrete, respectively. In this section, the material constitutive models and their yield criteria at both ULS and FLS are described.

3.2. Material constitutive models

3.2.1. Steel property

Steel shows similar ductile behaviour under tension and compression. When a tensile load is applied, it first elongates and eventually fractures. On the contrary, it squashes when a

compressive load is induced. It is generally accepted that the tensile and compressive stress-strain curves are regarded as the same, because the stress-strain relationship of steel shows a similar form prior to the occurrence of a fracture or squashing. A typical engineering stress-strain curve from a steel tensile test is plotted in Fig. 3-1. It uses the initial cross-sectional area and specimen length to calculate the stress and strain. When a tensile load is applied at the end of a tensile test coupon, the stress in the material is evenly distributed. An irreversible plastic deformation starts to develop after reaching the yield stress (σ_y). Beyond the ultimate stress (σ_u), which is defined as the maximum endurable strength of the material, the stress is concentrated in a weak area whereas the stress is relieved in the other areas. Similarly, the strain at the weak area increases, and the strain at the other areas reduces. The stress concentration in the weak area is accelerated when the bearing area becomes small. Finally, the tensile test coupon fractures when the load is continuously applied beyond the ultimate stress.

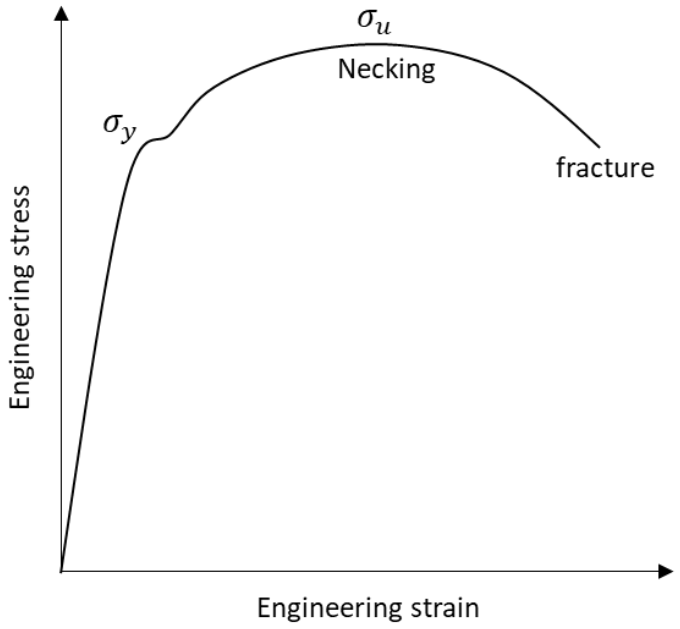

Figure 3-1. Engineering stress-strain curve of steel

The cross-sectional area at a necking zone is reduced when a load is continuously induced beyond the ultimate stress. A material failure occurs with a higher stress in the necking zone, because the area reduction increases the stress, although the applied force is constant. The

concept of true stress is used to consider this necking area reduction. The true stress is higher than the engineering stress after a material yield occurs. The true stress-strain relationship shows an increasing trend, which can be calculated as follows:

$$\sigma_{true} = \sigma_{eng}(1 + \varepsilon_{eng})$$
$$\varepsilon_{true} = \ln(1 + \varepsilon_{eng}) \quad (3\text{-}1)$$

where, σ_{true}, ε_{true} : true stress and strain
σ_{eng}, ε_{eng} : engineering stress and strain

When conducting a tensile coupon test, a tensile load was applied in the longitudinal direction and compressive loads were applied in the other two transverse directions at weak zones after necking. The tensile load is a dominant component in deciding the material strength at a stable zone, while compressive loads are continuously increased at the weak zone until fracture. This force combination is expressed as a stress triaxiality, which is defined as the ratio of a hydrostatic stress to a deviatoric stress. This ratio can be expressed as follows:

$$str = \sigma_m / q \quad (3\text{-}2)$$

where, str : the stress triaxiality
σ_m : the mean stress
q : the deviatoric stress

The effect of the hydrostatic stress becomes significant in the necking zone. In a lower stress triaxiality state, a void in the medium grows mainly in the longitudinal direction in accordance with the magnitude of the deviatoric stress. On the other hand, the hydrostatic stress is primarily influenced on a fracture after necking occurs. The developed hydrostatic stress in the necking zone increases the stress triaxiality, which means the compressive force component related to the necking zone reduction is more crucial to the fracture than an applied tensile load. Lemaitre (1985) reported the stress triaxiality in the damaged materials using a strain energy concept. This relationship was adopted for the ductile damage calculation in numerical models.

$$F_\varepsilon = \varepsilon_R \left[\frac{2}{3}(1+\nu) + 3(1-2\nu)str^2\right]^{-s0} \quad (3\text{-}3)$$

where, F_ε : fracture strain
ε_R : fracture strain in a uniaxial state
ν : Poisson's ratio
$s0$: a material property constant (s0=1 for steel)

3.2.2. Steel model

EC4-1-2 (2014) provides the stress-strain relationships of structural steel depending on temperature, based on experimental investigations. It is divided into four parts: the elastic, transit, plastic, and descending parts. The elastic modulus and tensile stress are reduced as the temperature increases. Strain-hardening occurs below 300 ℃ in the plastic region. It is assumed that the stress reduces from the strain of 15–20 %, regardless of temperature, in the descending part. If the yield and ultimate stresses are 350 and 427 MPa, the stress-strain relationship is as plotted in Fig. 3-2.

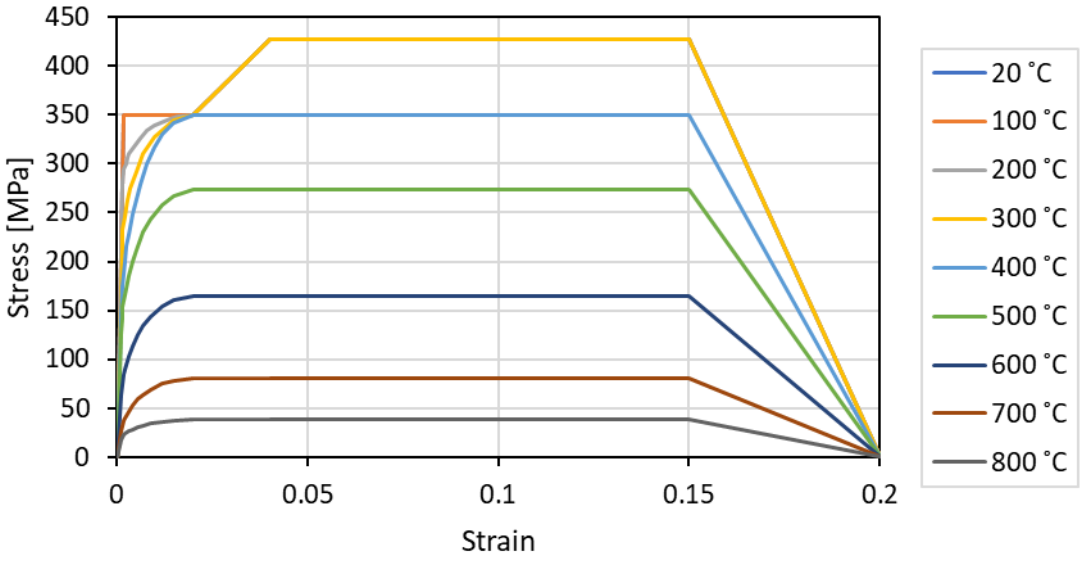

Figure 3-2 Temperature-dependent stress-strain curve of steel in EC4-1-2 (2014)

A shear connection is expected to have a ductile behaviour to avoid a sudden collapse of composite beams. EC4-1-1 (2009) also recommends having a stud slip larger than 6 mm before fracture. Progressive damage occurs at the stud root area before the stud shearing failure. A ductile damage function available in Abaqus was adopted to illustrate the descending part of the stress-strain curve. Hillerborg and Petersson (1976) reported the fracture energy of the material, which is defined as the energy per unit area to create a crack. This concept is incorporated into a finite element model to express the evolution of damage. The fracture energy can be expressed using an equivalent plastic strain and deviatoric stress as follows (Simulia, 2015):

$$G_f = \int_{\bar{\varepsilon}_0^{pl}}^{\bar{\varepsilon}_f^{pl}} qL_e d\bar{\varepsilon}^{pl} = \int_0^{\bar{u}_f^{pl}} q d\bar{u}^{pl} \tag{3-4}$$

where G_f : fracture energy [*N/mm*]
$\bar{\varepsilon}_f^{pl}$: equivalent plastic strain at fracture
$\bar{\varepsilon}_0^{pl}$: equivalent plastic strain at the onset of damage
q : deviatoric stress [*MPa*]
L_e : characteristic length of an element [*mm*]
$\bar{u}_f^{pl}$: equivalent crack displacement at fracture [*mm*]

The stress-strain curves in Fig. 3-2 are expressed as the engineering stress-strain relationship. This can be converted to the true stress, true strain, and plastic strain as shown in Table 3-1, by assuming that the fracture strain in a uniaxial state is 0.22, and the diameter of the tensile specimen reduces by 30 % at failure.

Table 3-1. Stress-strain values of the tensile test model

σ_{eng} [*MPa*]	ε_{eng}	σ_{true} [*MPa*]	ε_{true}	ε^{pl}	
350	0.00175	350	0.00175	0	
350	0.02	357	0.0198	0.018	
427	0.04	444	0.0392	0.0369	
427	0.15	491	0.1397	0.1372	
427	0.22	521	0.1988	0.1962	
-	-	584	0.713	0.71	Diameter reduction 30% $\sigma_{true} = 625\varepsilon_{true}^{0.2}$

The true stress–plastic strain relationship and stress triaxiality are shown in Fig. 3-3 and Fig. 3-4. The true stress increases consistently, because the reduced cross-sectional area is taken into account in the stress calculation. The fracture strain decreases as the stress triaxiality increases, which means the effect of the compressive directional force increases at the necking area. In this calculation, the elastic modulus and Poisson's ratio were assumed as 200 *GPa* and 0.26, respectively.

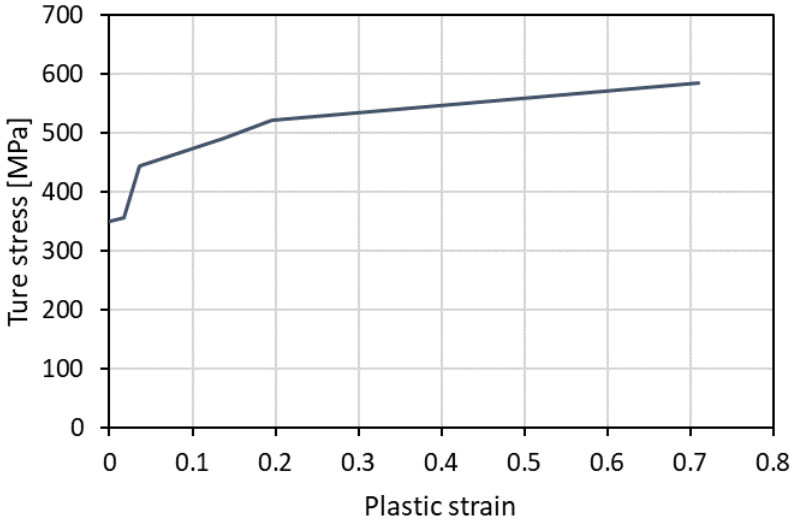

Figure 3-3 True stress-plastic strain curve of steel

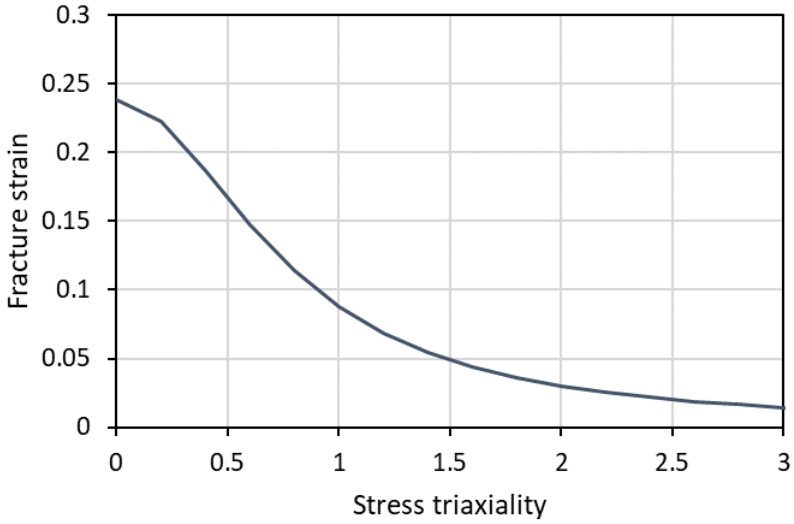

Figure 3-4 Fracture strain-stress triaxiality relationship (Lemaitre, 1985)

A simple tensile model was used to verify the ductile damage function at the descending part. A quadrant of half-length of the full-scale stud shank (19 mm diameter and 100 mm length) was modelled. It has a length of 50 mm and a radius of 9.5 mm. Symmetric boundary conditions were incorporated by restricting the motion in opposite directions of each surface, as presented in Fig. 3-5 (a). The smallest mesh size was 2.8 mm × 2.3 mm × 5 mm, which is the same size of the shear stud mesh in the push-out test model. To implement the fracture displacement concept, a characteristic length must be defined. The characteristic length varies with respect to the type and size of elements. In the case of a first-order element, it is defined as a typical crossed line of the element (Simulia, 2015). The equivalent crack displacement at fracture can be obtained using the characteristic length of the element and plastic strain as follows:

$$\bar{u}_f^{pl} = L_e\left(\bar{\varepsilon}_f^{pl} - \bar{\varepsilon}_0^{pl}\right) = 2.3(0.71 - 0.1962) \tag{3-5}$$

The descending part of the stress-strain curve after the onset of damage is highly affected by the fracture displacement, which was calculated as 1.18 mm in the simple tensile model of the shear stud. The longer the fracture displacement, the larger the softening slope appears. For a simple verification, a linear reduction in the descending part was assumed according to EC4-1-2 (2014). A strong correlation was observed between the design and modelling data, as depicted in Fig. 3-5(b). This ductile damage function was applied to the numerical model for the steel sections.

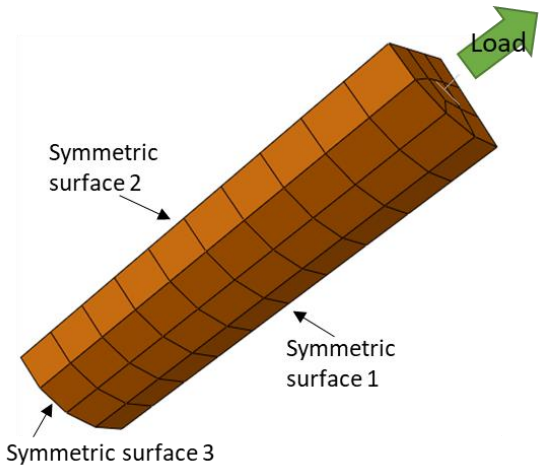

(a) 1/8 tensile test model

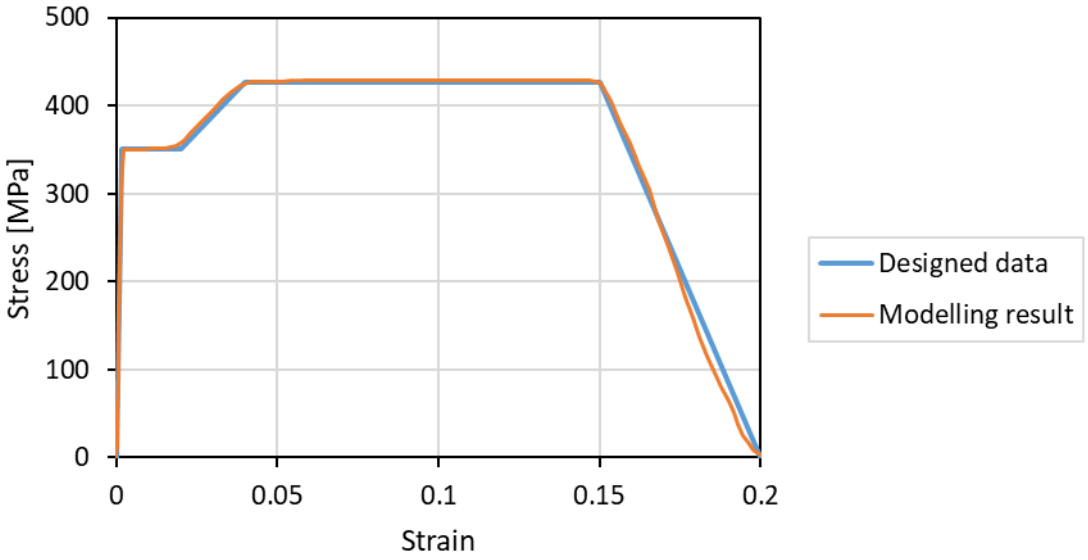

(b) Tensile test modelling data

Figure 3-5 Simple tensile test model of the shear stud

3.2.3. Concrete property

Concrete is a heterogeneous material composed of aggregates, water, cement, and various additives. Concrete strength is dependent on the bonding property of a cement paste, because it makes the aggregates bond together. This nature of concrete affects its behaviour in a highly nonlinear manner when loads are imposed. Concrete is strong under compression compared to its strength under tension, which is approximately 8–15 % of its compressive strength (Shi, 2009). Microvoids exist in a concrete medium, and these microvoids are compressed at the beginning of the compression. After the elastic region (typically 30–40 % of its peak stress), microcracks are generated around the aggregates because of sliding, opening, and propagation of the voids. Before the peak stress, the volume of a concrete material is reduced by the compression of the microvoids. Conversely, the volume is expanded after the peak stress, owing to the relocation of the aggregates and progressive cracking in the medium. Progressive cracking plays a significant role in concrete softening behaviour. The coalescence of microcracks makes progressive cracks throughout the material in the softening region, as illustrated in Fig. 3-6. A specimen is divided into several columns due to vertical cracks, which leads to compressive softening behaviour after the peak stress.

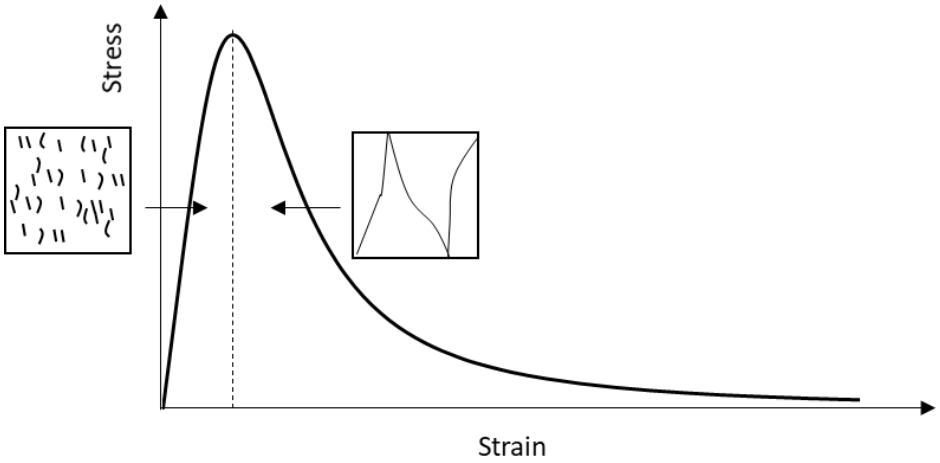

Figure 3-6 Typical uniaxial compressive stress-strain curve of concrete (Vonk, 1992)

Unlike a uniaxial stress state, a yield stress in a multiaxial stress state is dependent on a confining pressure and stress state in the medium (Green and Swanson, 1973); it shows a higher strength than in the uniaxial case, because the confinement stress applies more energy to the specimen. Kupfer and Hilsdorf (1969) conducted biaxial compressive experiments, which showed that the biaxial compressive stress is 16–25 % higher than the corresponding uniaxial strength. The biaxial strength ratio varies according to the stress state, as shown in Fig. 3-7. Newman and Choo (2003) reported that the equi-biaxial compressive stress is 1.1–1.3 times higher than its uniaxial stress, depending on the concrete strength. Papanikolaou and Kappos (2007) carried out a statistical study regarding the ratio of the equi-biaxial to the uniaxial compressive strength. The stress ratio decreases as the uniaxial compressive strength rises; for example, the ratio is 1.08 and 1.2 when the uniaxial compressive stress is 90 and 20 MPa, respectively.

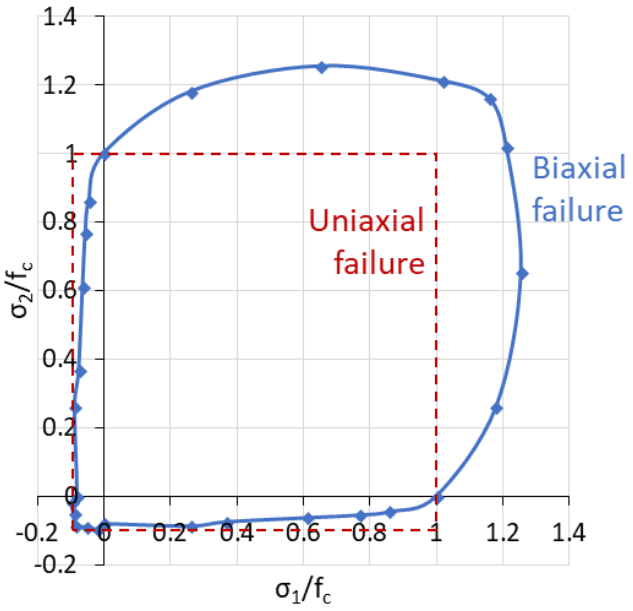

Figure 3-7 Biaxial stress relationship (Kupfer and Hilsdorf, 1969)

In a triaxial stress state, the compressive strength increases more than the stress in the biaxial state. It has been experimentally proved that the stress-strain characteristic becomes ductile, and the peak stress increases when the confinement pressure rises, as plotted in Fig. 3-8. This is because hydrostatic stress affects the movement of aggregates in concrete. Crack coalescence and propagation are also limited by the confinement pressure. Consequently, the concrete behaviour becomes ductile with respect to the confining pressure. Poinard *et al*. (2010) conducted an experimental investigation of concrete damage depending on confinement stress levels. When the confining pressure was 200 MPa, the unloading and reloading slopes showed a similar value. Its slope did not change according to the strain increase, which means that the material damage was relatively small compared to the stress in the uniaxial stress state. Thus, it can be concluded that the concrete strength and material degradation vary with respect to the compressive confinement stress in a multiaxial stress state.

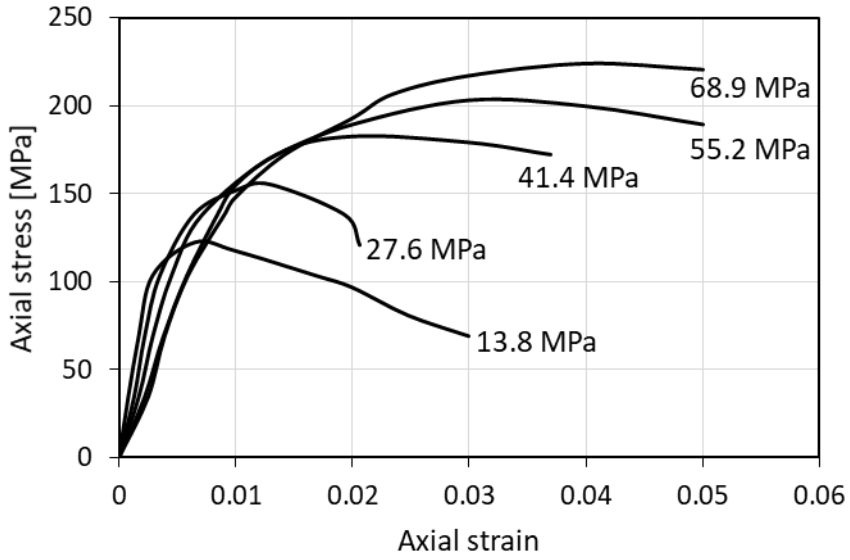

Figure 3-8 Axial stress-strain relationship in given confinement stress levels under triaxial compressive state (Li and Ansari, 1999)

Concrete is mainly used in construction to withstand compressive stresses, and its tensile strength is ignored in design. The elastic limit is approximately 60–80 % of the peak stress under tension (Taqieddin, 2001). Progressive cracking starts above this stress, and sudden cracking occurs beyond the peak stress. Considering this failure characteristic, it is assumed that the tensile stress and strain are linear until the peak stress is reached. The tensile stress reduces rapidly in the descending part, because the directions of the generated cracks, which are nominal to the applied loads. This reduces the force-applied area. The tensile behaviour in a multiaxial state is similar to its uniaxial stress, because the tensile strength is only dependent on a paste strength that bonds the aggregates together.

3.2.4. Concrete compressive model

Much research has been conducted to estimate concrete compressive behaviours, in order to design structures and to anticipate fractures of concrete. Popovics (1973) reported an empirical formula for a uniaxial compression when the strain value at the maximum stress was 0.003 to 0.004. The calibrated data were only available in the strain range obtained from the experiments. The relationship is:

$$\sigma_c = f_{cm}\frac{\varepsilon_c}{\varepsilon_{c1}}\frac{n}{n-1+\left(\frac{\varepsilon_c}{\varepsilon_{c1}}\right)^n} \tag{3-6}$$

where, σ_c : compressive stress [*MPa*]
ε_c : compressive strain
f_{cm} : mean value of concrete cylinder compressive strength [*MPa*]
ε_{c1} : compressive strain at f_{cm}
$n = 0.058 f_{cm}$ for a normal weight concrete

Darwin and Pecknold (1977) presented a uniaxial compressive stress-strain curve using an enveloped curve of cyclic loading experimental data. It was divided into two parts. A parabolic ascending part was adopted from the study of Saenz (1964), and a linear descending part was proposed using an enveloped curve. The stress of this second part was linearly reduced from the maximum stress to 20 % of the maximum stress. The stress-strain curve was available up until four times the peak strain. Its relationship is:

$$\sigma_c = \frac{\varepsilon_c E_{cm}}{1+\left[\frac{E_{cm}}{E_L}-2\right]\frac{\varepsilon_c}{\varepsilon_{c1}}+\left(\frac{\varepsilon_c}{\varepsilon_{c1}}\right)^2} \quad \text{for } \varepsilon_c \le \varepsilon_{c1} \tag{3-7}$$

$$\sigma_c = f_{cm}\left(0.2+0.8\frac{\varepsilon_{cu1}-\varepsilon_c}{\varepsilon_{cu1}-\varepsilon_{c1}}\right) \quad \text{for } \varepsilon_{c1} < \varepsilon_c \le \varepsilon_{cu1} \tag{3-8}$$

where, E_{cm} : secant elastic modulus of concrete
$E_L = f_{cm}/\varepsilon_{c1}$
$\varepsilon_{cu1} = 4 \times \varepsilon_{c1}$

Carreira and Chu (1985) provided a compressive stress-strain relationship for plain concrete by conducting a regression analysis of 43 existing experimental data. Most of the specimens were cylindrical with an aspect ratio of 2. The proposed formula was controlled by the B_c value, which was calibrated by the peak compressive stress. It can express the ascending and descending part simultaneously, as follows:

$$\sigma_c = f_{cm}\frac{B_c(\varepsilon_c/\varepsilon_{c1})}{B_c - 1 + (\varepsilon_c/\varepsilon_{c1})^{B_c}} \quad (3\text{-}9)$$

where, $B_c = (f_{cm}/4.7)^3 + 1.5$

The compressive stress-strain behaviour of concrete was also provided in EC2-1-1 (2014). It assumed a linear relationship less than 40 % of the peak stress, and a parabolic curve was used to illustrate the stress change. The same formula was adopted in both the ascending and descending parts. The stress-strain relationship in the descending part ended abruptly, because the compressive stress was only available until the designated strain value. The stress-strain curve is given by:

$$\sigma_c = f_{cm}\frac{R\eta - \eta^2}{1 + (R-2)\eta} \quad (3\text{-}10)$$

where, $\eta = \varepsilon_c/\varepsilon_{c1}$
$R = 1.05E_{cm}\varepsilon_{c1}/f_{cm}$

The uniaxial compressive stress-strain curves of C30 concrete are plotted in Fig. 3-9 using Eq. 3-6 to 3-10. The ascending part has a similar behaviour compared to the others, whereas the descending part shows a different response. The ascending part can be regarded as an intrinsic characteristic of concrete, because the same stress-strain curves were repeatedly observed in the experimental results as well as the empirical formulas. Thus, the stress-strain curve of EC2-1-1 (2014) was adopted for the ascending part in the numerical modelling.

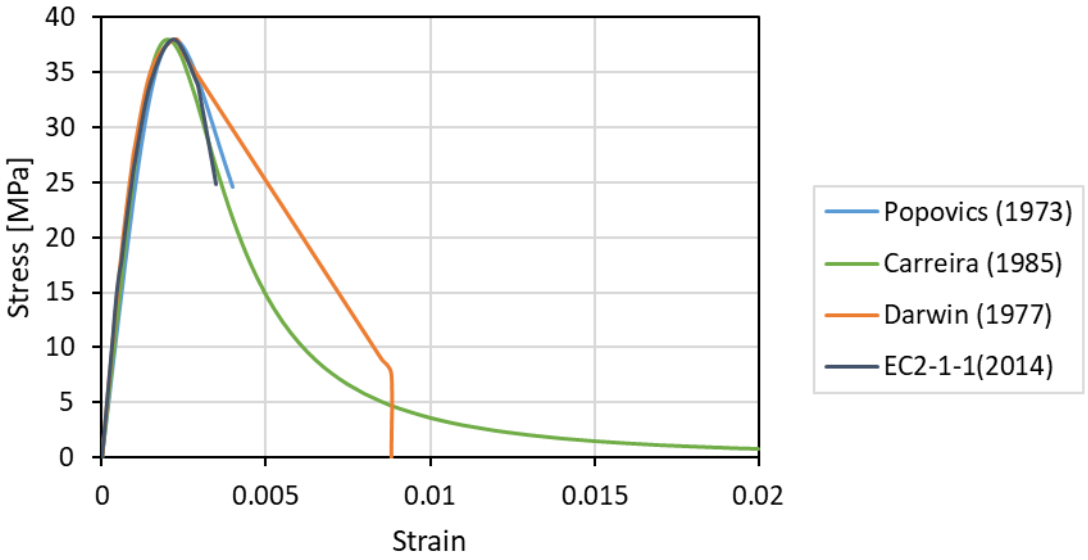

Figure 3-9. Comparison of uniaxial compressive stress-strain curve

The descending curve of the compressive stress is related to a yield stress calculation in the CDP model. If the nominal compressive stress is zero, the effective stress also becomes zero, although the damage parameter is not fully developed. Therefore, the softening curve should be defined until a higher strain value to obtain a stable calculation in the CDP model. Although linear and parabolic curves are recommended in EC4-1-2 (2014) for numerical applications, as the descending part of a concrete compressive model, the parabolic curve was adopted in this study to obtain the compressive stress-strain relationship with a higher strain value. This can illustrate the yield stress in a severely damaged state of concrete in the CDP model.

The temperature-dependent compressive stress-strain curve was also taken from EC4-1-2 (2014), which is based on the study of Popovics (1973): Eq. 3-6 with n = 3 for normal-weight concrete. This stress-strain curve is regarded to contain a transient strain value and widely used for high-temperature modelling (Purkiss and Li, 2013; Law, 2010). EC4-1-2 (2014) also provides stress reduction factors as well as ultimate and peak strain values with respect to temperature. The linear response was assumed until 40 % of the peak stress and the parabolic response was adopted beyond the elastic region. The stress-strain curve of C30 concrete at different temperatures is illustrated in Fig. 3-10. These relationships can be rewritten by incorporating a temperature parameter as follows:

$$\sigma_{c,\theta} = 3f_{c,\theta}\left(\frac{\varepsilon_c}{\varepsilon_{c1,\theta}}\right) / \left[2 + \left(\frac{\varepsilon_c}{\varepsilon_{c1}}\right)^3\right] \quad (3\text{-}11)$$

where, $\sigma_{c,\theta}$: compressive stress in the concrete at a temperature [*MPa*]
$f_{c,\theta} = k_{c,\theta} \times f_{cm}$
$k_{c,\theta}$: reduction factor for the compressive strength of concrete under elevated temperatures
ε_c : compressive strain in the concrete
$\varepsilon_{c1,\theta}$: compressive strain at $f_{c,\theta}$

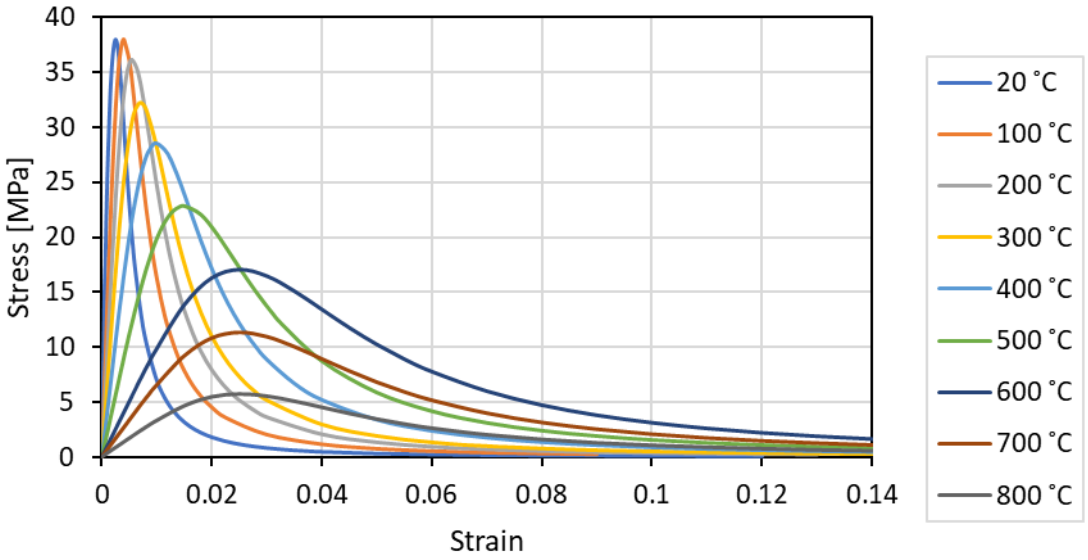

Figure 3-10. Uniaxial compressive stress-strain curve at different temperatures

3.2.5. Concrete tensile model

A linear stress-strain relationship is assumed below the peak stress in a concrete tensile model, because sudden cracking is observed in the softening region. Cornelissen *et al*. (1986) carried out a statistical study regarding the tensile stress reduction of concrete. Numerous experimental data showed that the tensile stress reduces exponentially in the softening region. The following function was adopted for the tensile stress-strain curve in the descending part, according to Hordijk (1990):

$$\frac{\sigma_t}{f_t} = \left[1 + \left(c_1 \frac{W}{W_c}\right)^3\right] exp\left(-c_2 \frac{W}{W_c}\right) - \frac{W}{W_c}(1 + c_1^3) exp(-c_2) \quad (3\text{-}12)$$

where, $c_1 = 3$ and $c_2 = 6.93$: empirical constants
W : crack opening distance [*mm*]
$\mathrm{W_c} = 5.14\, G_F / f_t$
f_t : peak uniaxial tensile stress [*MPa*]
G_F : concrete fracture energy [*N/mm*]

The maximum tensile stress and fracture energy are needed to illustrate the tension softening curves at a given temperature. The tensile stress was assumed to reduce linearly from 100 ℃ to 600 ℃ according to EC2-1-2 (2014). The fracture energy at ULS was taken from CEB-FIB 90 (1993), and its temperature-dependent value was referenced from experimental data. Zhang and Bicanic (2002) experimentally investigated the concrete fracture energy at high temperatures. The fracture energy increased by 57 % at 300 ℃, after which it reduced by 18 % at 600 ℃ in comparison to its ambient value, as depicted in Fig. 3-11. The magnitude of the fracture energy at a high temperature is slightly different depending on heat treatment conditions, such as the heat holding time and heating rate; the fracture energy ratio was the same with respect to its ambient condition; it reached its peak value at approximately 300 ℃, and then decreased with increasing temperature (Nielsen and Bicanic, 2003). Thus, a tensile softening curve of Eq. 3-12 was also used for high-temperature modelling by incorporating the temperature-dependent tensile stress of EC4-1-2 (2014) and the fracture energy ratio extracted from the experimental investigations of Zhang and Bicanic (2002).

The tensile softening curve of C30 concrete at different temperatures is illustrated in Fig. 3-12. The maximum crack opening distance at high temperature was assumed to be 0.2 *mm*, because concrete cannot withstand a tensile load when a critical crack width is exceeded.

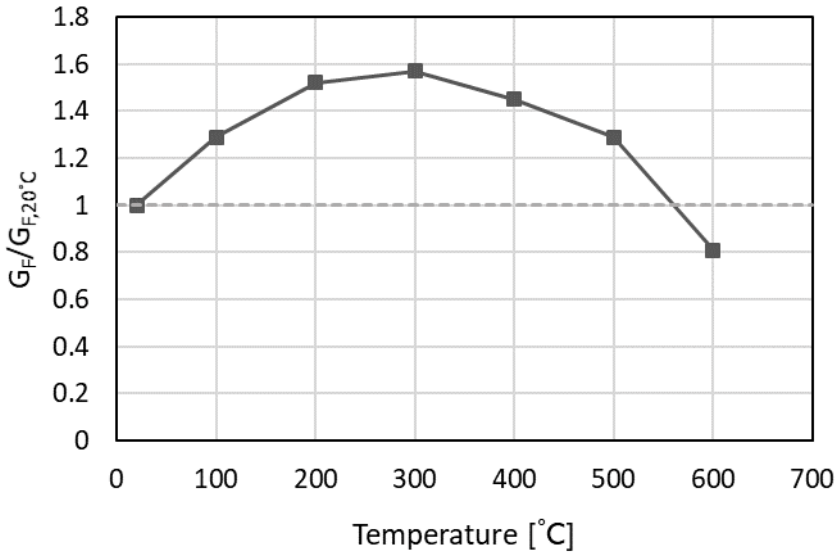

Figure 3-11. Temperature-dependent concrete fracture energy (Zhang and Bicanic, 2002)

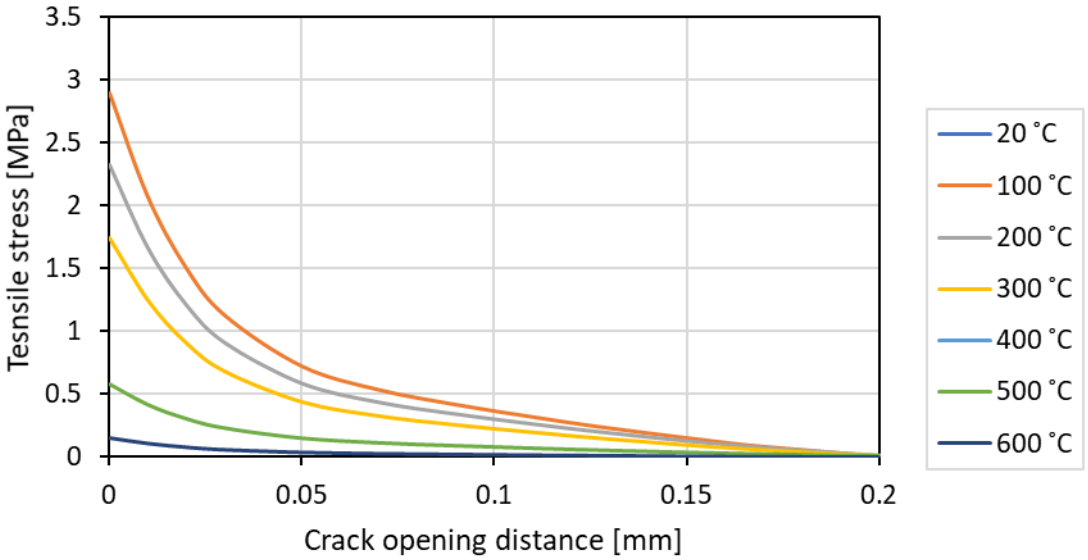

Figure 3-12. Tensile softening curve at different temperatures

3.3. Yield criterion

3.3.1. von Mises criterion

A material volume and shape change can be expressed by volumetric and deviatoric strain energies. That is, the total strain energy can be divided into a volumetric (hydrostatic) and distortion (shear) strain energy. This relationship is given by:

$$U_T = U_V + U_S \tag{3-13}$$

where, U_T : total strain energy
U_V : volumetric strain energy
U_S : deviatoric strain energy

Failure occurs when the deviatoric stress exceeds its yield criterion. The yield criterion using the deviatoric strain energy is called the von Mises criterion, which can be derived using the total and volumetric strain energies as follows:

$$\begin{aligned} U_T &= \frac{1}{2}\sigma_1\varepsilon_1 + \frac{1}{2}\sigma_2\varepsilon_2 + \frac{1}{2}\sigma_3\varepsilon_3 \\ &= \frac{1}{2E}(\sigma_1^2 + \sigma_2^2 + \sigma_3^2) - \frac{\nu}{2E}(2\sigma_1\sigma_2 + 2\sigma_2\sigma_3 + 2\sigma_3\sigma_1) \end{aligned} \tag{3-14}$$

$$U_V = \frac{1}{2}\sigma_m\varepsilon = \frac{1-2\nu}{6E}(\sigma_1 + \sigma_2 + \sigma_3)^2 \tag{3-15}$$

$$U_S = U_T - U_V = \frac{1}{12G}[(\sigma_1 - \sigma_2)^2 + (\sigma_2 - \sigma_3)^2 + (\sigma_3 - \sigma_1)^2] \tag{3-16}$$

where, σ_i : principal stress ($i = 1, 2, 3$)
ε_i : principal strain ($i = 1, 2, 3$)
σ_m : mean stress (=$(\sigma_1 + \sigma_2 + \sigma_3)/3$)
ν : Poisson's ratio
E, G : elastic and shear modulus

Assuming a uniaxial tensile stress state; that is, $\sigma_2 = \sigma_3 = 0$ and $\sigma_y = \sigma_1$.

$$U_S = \frac{1}{6G}\sigma_y^2 \tag{3-17}$$

$$\sigma_y = \sqrt{\frac{1}{2}[(\sigma_1 - \sigma_2)^2 + (\sigma_2 - \sigma_3)^2 + (\sigma_3 - \sigma_1)^2]} \tag{3-18}$$

The second invariant of the deviatoric stress can be expressed as:

$$J_2 = \frac{1}{6}[(\sigma_1 - \sigma_2)^2 + (\sigma_2 - \sigma_3)^2 + (\sigma_3 - \sigma_1)^2] \tag{3-19}$$

The yield stress is proportional to the second invariant of the deviatoric stress:

$$\sigma_y = \sqrt{3J_2} \tag{3-20}$$

The von Mises criterion is expressed using the second invariant of the deviatoric stress (J_2), which indicates that the yielding begins when the deviatoric stress reaches a critical value as follows:

$$f(J_2) = \sqrt{J_2} - c \tag{3-21}$$

where, c : critical value

The yield locus of the von Mises stress shows an elliptical shape which is inclined at 45° to the principal stress axis, as shown in Fig. 3-13. In a triaxial state, the yield surface is extended along the hydrostatic axis infinitely with a cylindrical shape, which means that the hydrostatic stress does not affect the shape of the yield surface.

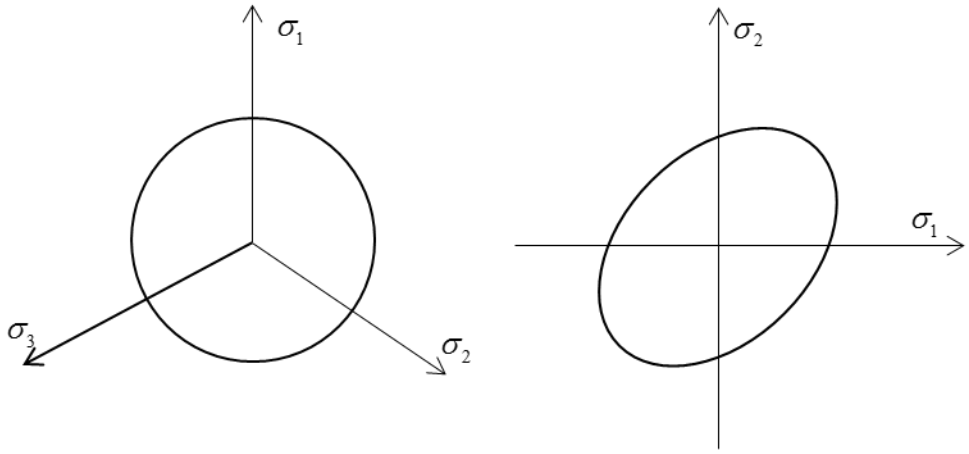

Figure 3-13. von Mises yield locus with principal stress axis

3.3.2. Concrete Damaged Plasticity (CDP) model

Four- and five-parameter models show curved meridians, which provide an accurate estimation compared to experimental results (Han and Chen, 1985; Bangash, 2001). Lubliner *et al.* (1989) reported the CDP model by adopting additional two dimensionless constants from the DP criterion. Lee and Fenves (1998) modified this criterion by incorporating an effective stress concept, because it gives a more realistic value in a damaged material; the effective stress is defined as an applied force divided by an undamaged area. This can illustrate a curved failure surface as well as a different yield stress between the compressive and tensile meridians. Several numerical studies have been conducted using this CDP model to investigate the behaviour of a shear stud in a composite beam (Qureshi *et al.*, 2011b; Mirza and Uy, 2009; Nguyen and Kim, 2009; Xu and Sugiura, 2013). The yield criterion takes the following form:

$$F(\bar{\sigma}, \varepsilon_c^{pl}) = \sqrt{3\bar{J}_2} + \alpha\bar{I}_1 + \beta\langle\hat{\bar{\sigma}}_{max}\rangle - \gamma\langle-\hat{\bar{\sigma}}_{max}\rangle - (1-\alpha)\bar{c}_c(\varepsilon_c^{pl}) \qquad (3\text{-}22)$$

where, $\hat{\bar{\sigma}}_{max}$: effective maximum principal stress
$\overline{c_c}(\varepsilon_c^{pl})$: effective compressive cohesion stress
α, β, γ: plasticity parameters

The four parameters are α, β, γ, and effective compressive cohesion stress which is defined from a uniaxial compressive stress-strain relationship. These parameters are calculated according to the following formulas:

$$\alpha = \frac{(f_{b0}/f_c) - 1}{2(f_{b0}/f_c) - 1}, \quad \beta = \frac{\bar{c}_c(\varepsilon_c^{pl})}{\bar{c}_t(\varepsilon_t^{pl})}(1-\alpha) - (1+\alpha), \quad \gamma = \frac{3(1-K_C)}{2K_C - 1} \qquad (3\text{-}23)$$

α and β can be obtained from uniaxial and biaxial experimental data. When β and γ go to zero, this criterion becomes the DP yield function. α can be derived assuming that the initial cohesion is the uniaxial compressive stress, and the yielding occurs at the equi-biaxial stress state: $\bar{c}_c = f_c$, $(f_{b0}, f_{b0}, 0)$. Assuming the obtained failure surface lies on the uniaxial tensile yield state, β can be derived using the α value: $(f_t, 0, 0)$. In the CDP model, the uniaxial compressive and tensile stress changes with respect to the damage parameter. Thus, β can be varied according to the stiffness degradation of concrete material, as presented in Eq. 3-23.

The parameter γ is only available in a triaxial compressive stress state ($\hat{\bar{\sigma}}_{max} < 0$), owing to the Macaulay brackets $< >$. The $\hat{\bar{\sigma}}_{max}$ can be defined as the following forms (Lubliner *et al*., 1989) according to the stress state: the tensile meridian ($\sigma_1 > \sigma_2 = \sigma_3$) and compressive meridian ($\sigma_1 = \sigma_2 > \sigma_3$).

$$\hat{\bar{\sigma}}_{max,TM} = \frac{1}{3}\left(\bar{I}_1 + 2\sqrt{3\bar{J}_2}\right) \qquad \text{for TM (Tensile Meridian)} \qquad (3\text{-}24)$$

$$\hat{\bar{\sigma}}_{max,CM} = \frac{1}{3}\left(\bar{I}_1 + \sqrt{3\bar{J}_2}\right) \qquad \text{for CM (Compressive Meridian)} \qquad (3\text{-}25)$$

Substituting Eq. 3-24 and 3-25 into Eq. 3-22, the deviatoric stress is expressed as:

$$\left(1 + \frac{2}{3}\gamma\right)\sqrt{3\bar{J}_2} + \left(\alpha + \frac{\gamma}{3}\right)\bar{I}_1 = \bar{c}_c(1-\alpha) \qquad \text{for TM} \qquad (3\text{-}26)$$

$$\left(1 + \frac{1}{3}\gamma\right)\sqrt{3\bar{J}_2} + \left(\alpha + \frac{\gamma}{3}\right)\bar{I}_1 = \bar{c}_c(1-\alpha) \qquad \text{for CM} \qquad (3\text{-}27)$$

The magnitudes of the tensile and compressive deviatoric stress are different. Let us define the ratio of the tensile to the compressive stress as K_C,

$$K_C = \frac{\left(\sqrt{3\bar{J}_2}\right)_{TM}}{\left(\sqrt{3\bar{J}_2}\right)_{CM}} \quad \text{at a given } I_1 \tag{3-28}$$

This can be derived as follows:

$$K_C = \frac{3+\gamma}{3+2\gamma} \qquad 0.5 < K_C \leq 1 \tag{3-29}$$

Thus, γ can be expressed as:

$$\gamma = \frac{3(1-K_C)}{2K_C - 1} \tag{3-30}$$

By adopting the load angle θ_L, Eq. 3-26 and 3-27 can also be expressed as a single form.

$$\left(1 + \frac{2\gamma}{3} cos\theta_L\right)\sqrt{3\bar{J}_2} + \left(\alpha + \frac{\gamma}{3}\right)\bar{I}_1 = \bar{c}_c(1-\alpha) \tag{3-31}$$

where, $0 \leq \theta_L \leq 60°$
$\theta_L = 0$ for TM
$\theta_L = 60°$ for CM

Eq. 3-31 illustrates the three-dimensional stress relationships according to the deviatoric stress, hydrostatic stress, and load angle. The deviatoric stress changes with respect to the load angle at a given hydrostatic stress.

3.4. Plasticity parameters of the CDP model

3.4.1. Shape of the failure surface

The failure surface of the CDP model is illustrated in accordance with the K_C parameter in Fig. 3-14. When the K_C value is 0.5, the failure surface shows a triangular shape, which means that the compressive deviatoric stress is twice the tensile deviatoric stress. On the contrary, the yield surface changes to a circular shape when the K_C value approaches 1, which is the same as the DP criterion. The deviatoric stress increases when the K_C value decreases at a given hydrostatic stress, owing to the different shape of the failure surface. This effect becomes more significant in higher hydrostatic states. As a consequence, the K_C value affects both the shape of the failure surface and magnitude of the deviatoric stress. This can be used to control the maximum deviatoric stress in a triaxial compressive state. Lubliner *et al.* (1989) recommend using a K_C value of 0.667 based on their numerical modelling data at ULS. They also reported that the typical range of the K_C value is between 0.64 and 0.8. However, various K_C values have been used to model concrete behaviour, owing to the complex properties of concrete, such as 0.59 (Pavlovic *et al.*, 2013) and 0.7 (Lopez-almansa *et al*., 2014).

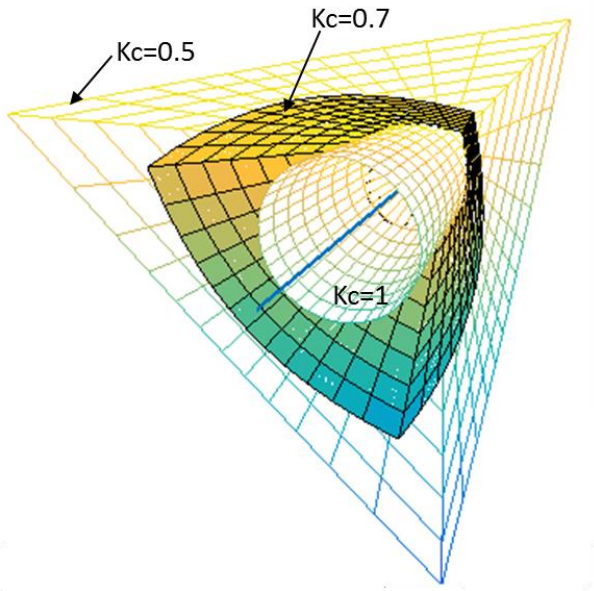

Figure 3-14. Failure surface with respect to K_C value

The effective compressive cohesion stress is taken from the uniaxial stress–plastic strain relationship; a uniaxial compressive stress-strain curve and damage parameter are used to define the effective cohesion stress. This parameter affects the yield surface in a uniaxial and biaxial compressive state, because the magnitude of the deviatoric stress is similar to the maximum uniaxial compressive stress. Its effect decreases in a triaxial compressive state, because the triaxial compressive stress is much higher than the uniaxial compressive stress. Rodriguez *et al.* (2013) adopted an additional cohesion stress term depending on the confinement stress level to overcome obtaining a small stress in a triaxial compressive state when using identical plasticity parameters of a uniaxial stress state. The difference in the failure surface with respect to the cohesion stress is depicted in Fig. 3-15. It can be observed that its effect is comparatively small as the hydrostatic stress increases.

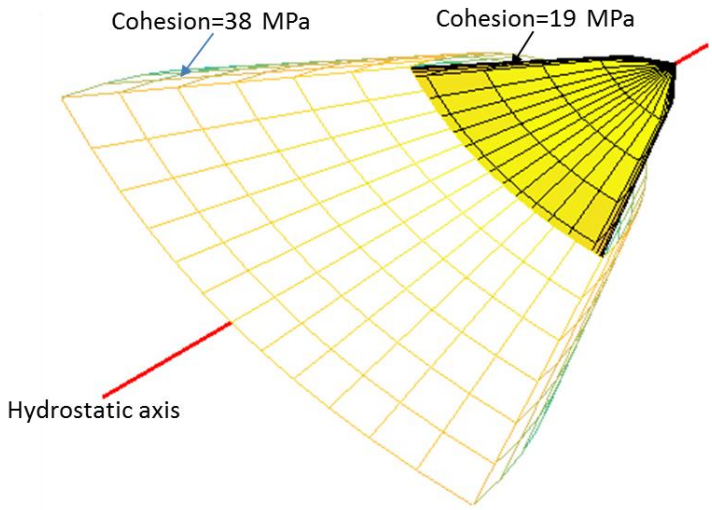

Figure 3-15. Failure surface with different cohesion stress

3.4.2. Flow rule

Concrete volume expands when an excessive compressive force is applied. This expansion leads to an increase in both volumetric and deviatoric plastic strains. A flow rule defines the volumetric expansion and deviatoric stress change with respect to material hardening and softening by using a plastic strain rate vector. In the CDP model, this behaviour can be explained by a non-associated flow rule with a dilation angle parameter. A DP hyperbolic

function is used for the flow rule, which has a tension cut-off such as the Rankin criterion in a low-confinement region and a linear DP criterion in a highly confining stress state (Simulia, 2015). The plastic potential function (G) is:

$$G(\sigma) = \sqrt{(\varepsilon_G \sigma_{t0} tan\psi)^2 + \bar{q}^2} + \bar{p} tan\psi \tag{3-32}$$

where, ε_G : eccentricity of the plastic potential function
ψ : dilation angle
$\bar{q} = \sqrt{3\overline{J_2}}$: effective deviatoric stress
$\bar{p} = -\overline{I_1}/3$: effective hydrostatic stress

An eccentricity defines the distance between the plastic potential function and asymptote line in the $\bar{p}$-axis. Increasing the value of the eccentricity increases the curvature of the plastic potential function in a low-confinement level. The dilation angle shows a maximum value at region A in Fig. 3-16. After that, it reduces exponentially, and it is saturated at region B. When the eccentricity is zero, the flow potential equals to a linear DP function. This means that the dilation angle shows the same value throughout the whole region.

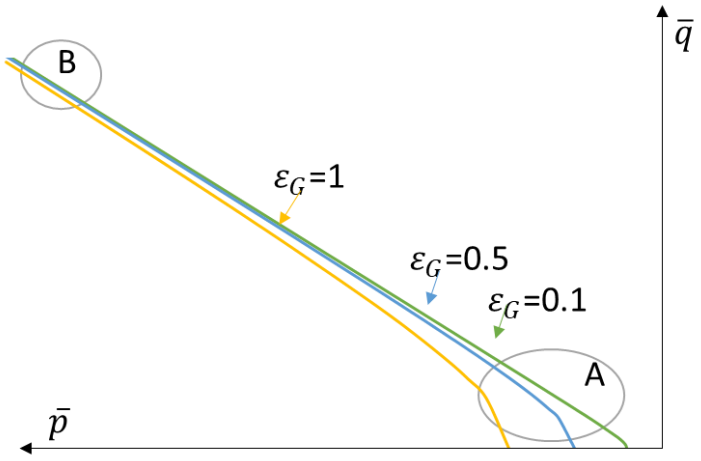

Figure 3-16. Drucker-Prager hyperbolic function with respect to the eccentricity value

The dilation angle defines the slope of the plastic potential function at a highly confining pressure state in the $\bar{p} - \bar{q}$ plane (Region B in Fig. 3-16). This term represents the volume expansion rates with respect to the hydrostatic stress. The relationship between the dilation angle and volumetric strain is shown in Fig. 3-17. The plastic strain rate vector is orthogonal to the plastic potential function by a normality rule. It is composed of a volumetric (ε_v^p, horizontal component) and deviatoric strain vector (ε_d^p, vertical component). Because the direction of the volumetric strain vector is parallel to the hydrostatic axis, the material volume expands with respect to the applied forces. Increasing the value of the dilation angle makes concrete more ductile, because the plastic strain generates a larger volumetric strain with a relatively small deviatoric strain. Conversely, a plastic potential function with a relatively small dilation angle shows a brittle behaviour; it shows a large deviatoric strain with a small volume expansion. According to the parametric study of a reinforced beam subjected to four-point bending (Malm, 2006), it showed a brittle response when using the dilation angle of 10°, whereas a ductile behaviour was observed with the dilation angle of 50.3°. Investigating the CDP model regarding the non-associated flow rule, various dilation angles were used in the range of 13° to 53°. Lee and Fenves (1998) used the dilation angle of 36° to verify a monotonic uniaxial loading model of concrete. In a biaxial model, the dilation angle of 28° was used by comparison with experimental data. Jankowiak and Lodygowsk (2005, 2010) used the CDP model to simulate a four-point bending of a notched concrete beam. Different dilation angles of 38° and 49° were used to simulate the same concrete beam with C50 concrete. Lopez-almonsa *et al.* (2014) used the dilation angle of 13° to model a reinforced concrete framed structure. These modelling data show that the dilation angle changes with respect to the loading condition (uniaxial or biaxial loading), concrete plasticity parameters, and structure type (plain or reinforced concrete).

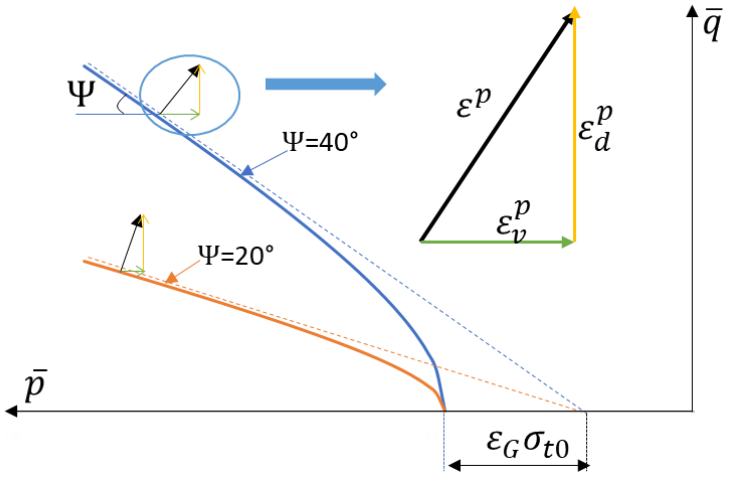

Figure 3-17. Effect of the dilation angle on the plastic potential function

3.4.3. Damage function

Material damage occurs by the formation of micro defects and cracks in a medium. It can be simply defined as the ratio between the damaged and intact area. The range of a damage parameter is 0 to 1, where 0 means no damage and 1 indicates a completely damaged state. Two scalar damage variables are required for the CDP model, because the tensile and compressive behaviours are totally different. When a force is imposed, the area to withstand the stress reduces because of the increment in the damaged area. This relationship can be expressed by using the effective stress concept as follows:

$$D = 1 - \frac{\bar{A}}{A} = \frac{A - \bar{A}}{A}$$

$$F = \sigma A = \bar{\sigma}\bar{A} \qquad (3\text{-}33)$$

$$\sigma = \frac{\bar{A}}{A}\bar{\sigma} = (1 - D)\bar{\sigma}$$

where $\bar{\sigma}$: effective stress
σ: nominal stress
D: damage parameter
A: intact area
$\bar{A}$: effective area (intact area – damaged area)

A damage parameter is used to convert a nominal stress to an effective stress and vice versa. This process is called a damage correction step in an elastoplastic stress calculation procedure; a detailed calculation procedure is provided in Appendix B. There are several methods to define the damage function: internal energy variation with exponential function (Lubliner *et al*., 1989), constant ratio between inelastic and plastic strain (Kratzig and Polling, 2004), and stress reduction ratio (Pavlovic *et al*., 2013). These are calculated based on a uniaxial stress-strain curve, because the cohesion stress in the CDP model is defined using a uniaxial compressive stress–plastic strain relationship. The damage function affects the plastic strain calculation. This damage function successfully illustrates a softening behaviour in uniaxial and biaxial compressive states. However, it does not show a good correlation in a triaxial compressive stress state, because the damage function is defined based on its uniaxial stress state. This is an intrinsic limitation of the CDP model for triaxial compressive applications.

An exponential form of the compressive damage function is used to express a stiffness degradation and plastic strain development. In the case of a uniaxial compressive state, a typical damage value at the peak stress is approximately 0.3 to 0.4, and it increases exponentially in the softening region (Lee and Fenves, 1998; Gernay *et al*., 2013). However, the stiffness degradation is not observed in a highly confined triaxial compressive state (Poinard *et al*., 2009), which means that the compressive damage function changes with respect to confinement stresses. The concrete surrounding the shear stud exhibits approximately nine times the uniaxial compressive stress in the push-out test (Oehlers and Bradford, 1995). A relatively smaller compressive damage at the peak stress in comparison to the uniaxial stress state was assumed in this study, because a triaxial compressive stress was applied to the surrounding concrete of the shear stud in the push-out test. The stress reduction ratio was used to describe tensile damage development. It successfully illustrates a degraded state in the tensile softening region because a linear response was assumed until the peak stress is reached. The damage function in both the compressive and tensile state is given by:

$$D_c = 1 - exp(-C\varepsilon_c^{in})$$
$$D_t = 1 - \sigma_t / f_t \quad (3\text{-}34)$$

where, D_c and D_t : compressive and tensile damage
C : constant value for the compressive damage
ε_c^{in} : compressive inelastic strain

The compressive and tensile damage functions of C30 concrete are plotted in Fig. 3-18 and 3-19 for different temperatures. The tensile damage function shows the same relationship with respect to temperature, because the maximum crack opening distance was assumed as 0.2 mm, regardless of temperature.

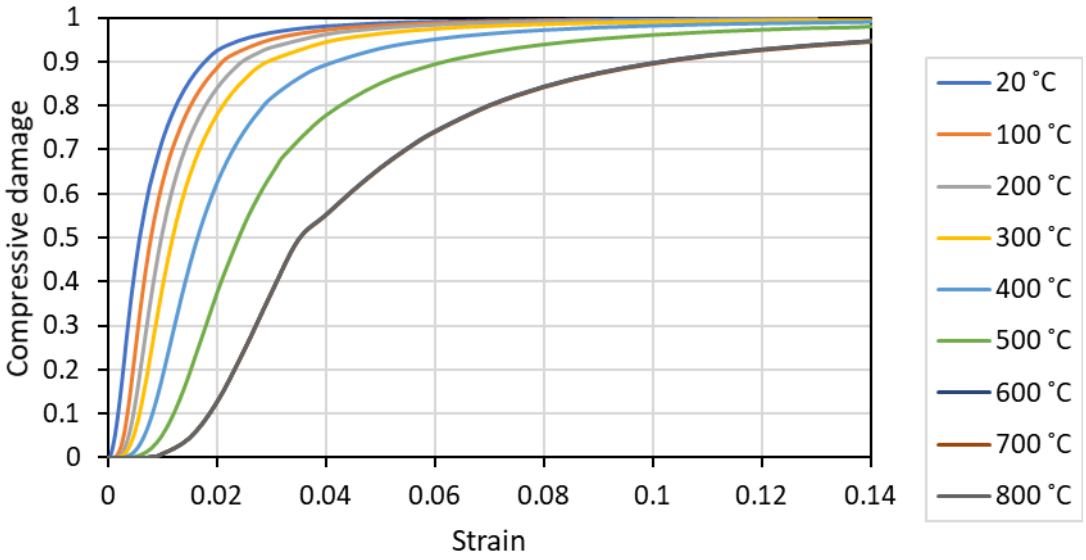

Figure 3-18. Compressive damage relationship depending on temperatures

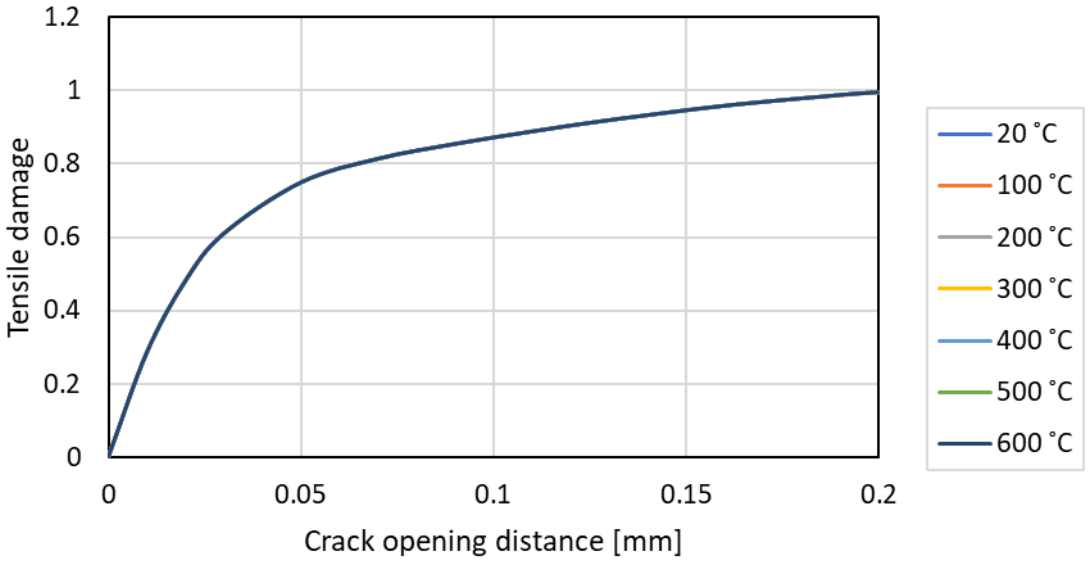

Figure 3-19. Tensile damage relationship depending on temperatures

3.5. Plasticity parameters of the CDP model at high temperatures

3.5.1. Poisson's ratio

Poisson's ratio of concrete decreases with increasing temperature, which has been observed in various experiments (Schneider, 1988; Bahr *et al*., 2013; Hammoud *et al*., 2014). Dehydration of the bonding pastes makes concrete weaker at high temperature. This micro defect interferes with the concrete expansion in the unloading direction. Hammoud *et al*. (2013) reported the Poisson's ratio with a temperature range of 20 ℃ to 700 ℃ using a three-order polynomial function. It decreases from approximately 0.2 at 20 ℃ to 0.14 at 700 ℃. This relationship was adopted for high-temperature numerical modelling.

$$\nu(\theta) = a\theta^3 + b\theta^2 + c\theta + d \tag{3-35}$$

where, ν: Poisson's ratio
θ: concrete temperature [℃]
a = −1.3567E−10, b = 2.66E−07, c = −2.1133E−04, d = 0.2041: empirical constants

3.5.2. Biaxial stress ratio

A stress ratio of the equi-biaxial to the uniaxial compressive state is required to calculate the α parameter. As this ratio increases, and the biaxial stress curve becomes steeper with increasing temperature. Papanikolaus and Kappos (2007) reported that the stress ratio increases when the uniaxial compressive strength decreases, based on a statistical analysis of experimental data at ULS. They also proposed an exponential formula according to the uniaxial compressive strength for the stress ratio calculation. Although that statistical study was based on ULS data, the same trend can be observed at high temperatures.

Several experiments were conducted to investigate concrete biaxial behaviour at high temperatures (Kordina *et al.*, 1986; He and Song, 2008). Although it shows scattered values depending on the experiments, both results provide the same trend of the stress reduction with respect to temperature, as plotted in Fig. 3-20. The observed stress degradation ratio of the uniaxial stress was different from the recommendation of EC2-1-2 (2008). This is caused by different experimental conditions, such as the heating rate, temperature holding time, temperature measurement method, and specimen production process.

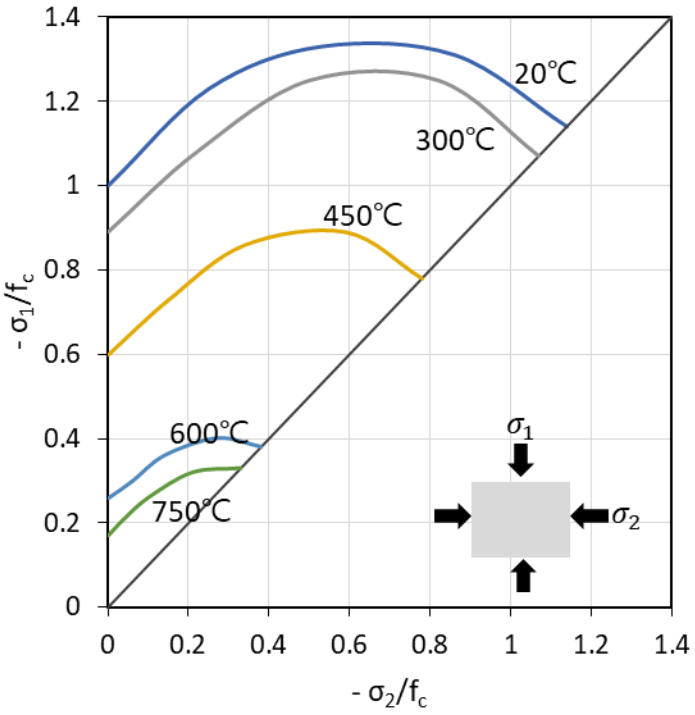

(a) Kordina *et al*. (1986)

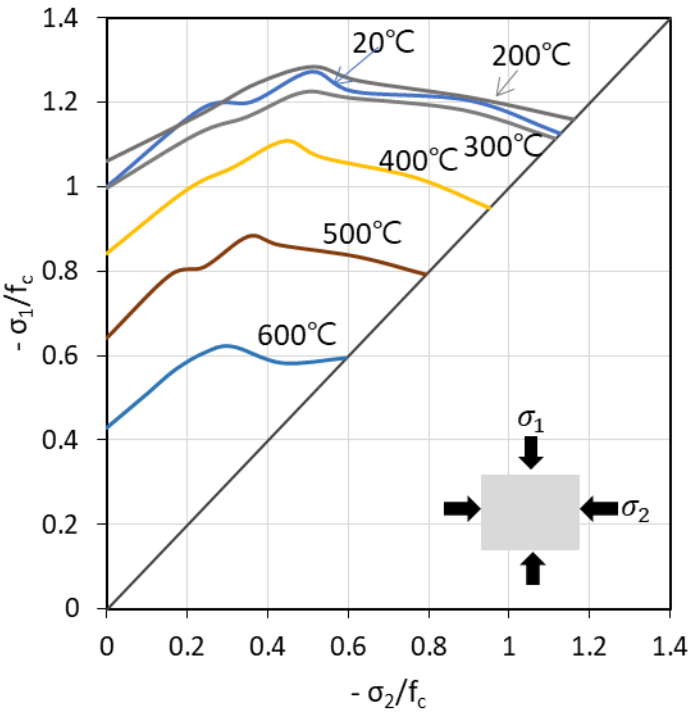

(b) He and Song (2008)

Figure 3-20. Biaxial compressive stress relationship at high temperatures

The uniaxial stress reduction ratio between the experimental data of Kordina *et al*. (1986) and EC2-1-2 (2008) shows significant differences around 600 ℃, whereas the other experimental data (He and Song, 2008) show dissimilar values in the range 300–400 ℃, as presented in Table 3-2.

Table 3-2. Experimental data under biaxial compressive state

Temperature [℃]	Stress reduction factor (EC2-1-2)	Experimental data 1 (Kordina *et al.*, 1986)		Experimental data 2 (He and Song, 2008)	
		$\sigma_{c\theta}/f_c$	f_{b0}/f_c	$\sigma_{c\theta}/f_c$	f_{b0}/f_c
20	1	1	1.14	1	1.13
200	0.95	-	-	1.04	1.1
300	0.85	0.89	1.2	1.0	1.12
400	0.75	-	-	0.84	1.13
450	0.675	0.60	1.3	-	-
500	0.60	-	-	0.64	1.23
600	0.45	0.26	1.46	0.43	1.39
750	0.225	0.17	1.94	-	-

The biaxial stress relationship of Kordina *et al*. (1986) and biaxial failure surface of the CDP model incorporating the uniaxial stress reduction factor of EC2-1-2 (2008) and the experimental temperature of Kordina *et al.* (1986) are plotted in Fig. 3-21(a). They show a similar shape of the yield stress curves; however, the uniaxial stress reductions at a given temperature were different. When the biaxial failure surface of the CDP model was plotted by referencing the uniaxial stress degradation and temperature of EC2-1-2 (2008), it demonstrated a strong correlation, as shown in Fig. 3-21(b). Assuming that the uniaxial stress reduction obtained from experiments is equal to the values of EC2-1-2 (2008), the corresponding temperature according to EC2-1-2 (2008) is adopted for calculation because the thermal degradation of concrete highly depends on the experimental conditions. For example, the experimental data at 300 ℃ can be regarded as the stress at 260 ℃ according to the stress reduction factor of EC2-1-2 (2008). In the same manner, the measured value at 600 ℃ corresponded to the stress at 727 ℃.

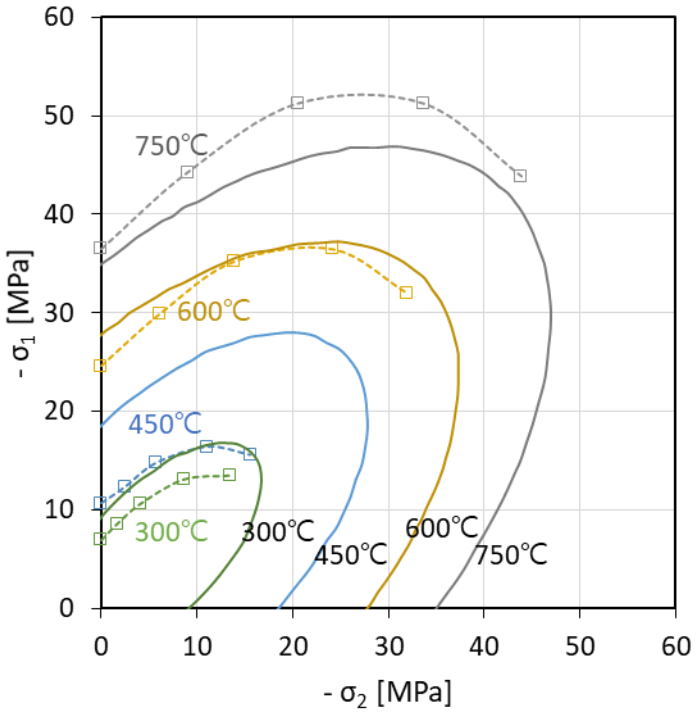

(a) Biaxial stress relationship

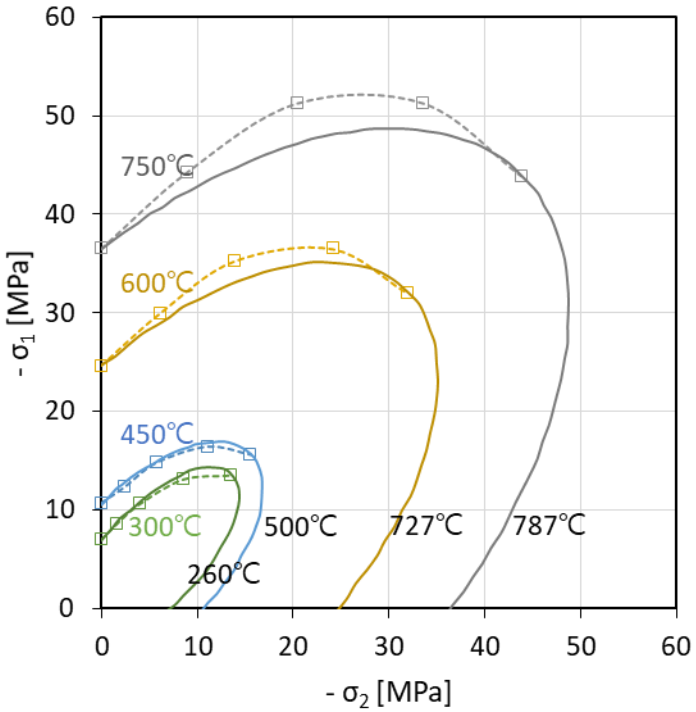

(b) Biaxial stress relationship with uniaxial strength reduction factor of EC2-1-2

Figure 3-21. Comparison between experimental data (Kordina *et al*., 1986) and CDP model

The biaxial stress ratio for different temperatures is provided in Table 3-3 by comparing the stress reduction factor of EC2-1-2 (2008) and experimental data (Kordina *et al*., 1986; He and Song, 2008). The obtained biaxial stress ratio of the equi-biaxial to the uniaxial stress shows an increasing trend with increasing temperature, as plotted in Fig. 3-22. Linear interpolated data were assumed for the intermediate temperature region, for which experimental data does not exist. The biaxial stress ratio is expressed as a combination of four linear functions depending on the concrete temperature, considering the data in Table 3-3. These relationships are given by:

$$
\begin{aligned}
f_{b0}/f_c &= 1.16 && \text{for } \theta < 100℃ \\
f_{b0}/f_c &= 1.16\left(1 + 0.05\left(\frac{\theta - 100}{300}\right)\right) && \text{for } 100℃ \le \theta < 400℃ \\
f_{b0}/f_c &= 1.22\left(1 + 0.18\left(\frac{\theta - 400}{300}\right)\right) && \text{for } 400℃ \le \theta < 700℃ \\
f_{b0}/f_c &= 1.44\left(1 + 0.35\left(\frac{\theta - 700}{100}\right)\right) && \text{for } 700℃ \le \theta \le 800℃
\end{aligned}
\tag{3-36}
$$

Table 3-3. Biaxial stress ratio calibrated by the stress reduction factor of EC2-1-2 (2008)

Temperature [℃]	Stress reduction factor (EC2-1-2)	Experimental data 1 (Kordina *et al.*)		Experimental data 2 (He and Song)		f_{b0}/f_c	Reference
		$\sigma_{c\theta}/f_c$	f_{b0}/f_c	$\sigma_{c\theta}/f_c$	f_{b0}/f_c		
20	1	1	1.14	1	1.13	1.16	Kupfer (1969)
100	1	-	-	-	-	1.16	No reduction
200	0.95	-	-	-	-	1.19	-
260	0.89	0.89	1.2	-	-	1.2	Experiment 1
300	0.85	-	-	-	-	1.21	-
400	0.75	-	-	-	-	1.22	-
473	0.64	-	-	0.64	1.23	1.23	Experiment 2
500	0.60	0.60	1.3	-	-	1.3	Experiment 1
600	0.45	-	-	-	-	1.38	-
613	0.43	-	-	0.43	1.39	1.39	Experiment 2
700	0.30	-	-	-	-	1.44	-
727	0.26	0.26	1.46	-	-	1.46	Experiment 1
787	0.17	0.17	1.94	-	-	1.94	Experiment 1

Gernay *et al*. (2013) reported a formula for the equi-biaxial stress ratio at different temperatures for concrete modelling. They used three linear functions from ambient to 750 ℃, with a maximum value of 1.86, which shows an analogous value to Eq. 3-36.

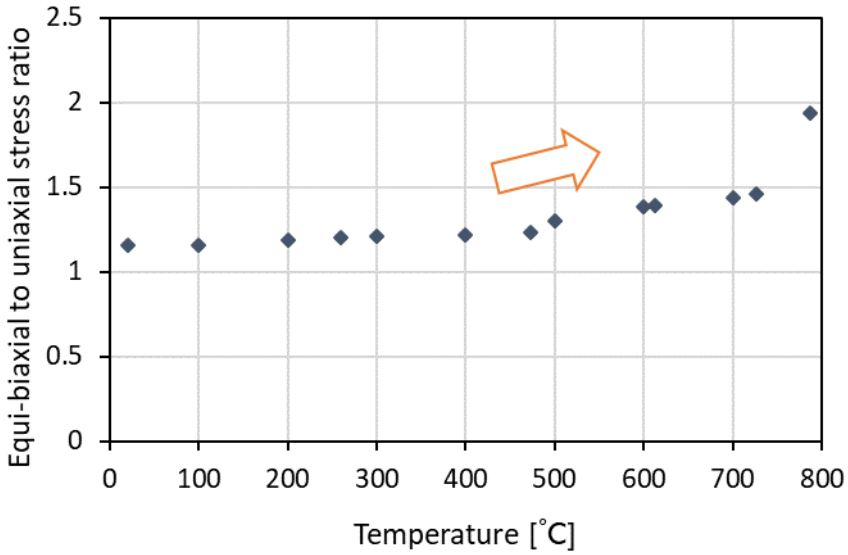

Figure 3-22. Temperature-dependent relationship between the biaxial and uniaxial stress

3.5.3. K_C value

In a triaxial compressive state, concrete strength changes with respect to the confinement pressure. The stress-strain characteristic becomes ductile, and the peak stress increases when the confinement pressure rises, as already observed in Fig. 3-8. Richart *et al*. (1928) reported the relationship between axial and confinement stresses as a linear function. Although a parabolic function was also reported to illustrate triaxial compressive stress relationships, the linear function is still widely used owing to its simplicity (Candappa *et al*., 2001). The confined axial stress can be expressed as:

$$f_{cc} = f_c + k\sigma_3 \tag{3-37}$$

where, f_{cc} : axial stress at triaxial compressive state
k: material constant
σ_3 : confining stress (=σ_2)

The material constant (*k*) in Eq. 3-37 indicates the slope of failure points in a triaxial compressive state. Richart *et al*. (1928) initially presented its value as 4.1 based on their experiments. The empirical expression with the material constant of 4.1 successfully illustrates an axial stress at a triaxial stress state in a low-confinement condition. Ansari and Li (1998) reported the *k* value as 2.7 for a highly confined state. Its confinement level exceeds 1, which means the confinement stress is higher than the uniaxial compressive stress.

Several experiments (Hammoud *et al*., 2014; He and Song, 2010) have been conducted to evaluate the triaxial compressive strength with respect to changes in temperature. The axial stress in a triaxial state increases with respect to the growth of a confinement level, and it is also reduced as the temperature rises. Thermal damage makes concrete weaker and changes the relationship between the axial and confining stresses. A temperature-dependent *k* value is required to illustrate the axial stress in a triaxial compressive state at high temperatures. This can be obtained from a high-temperature experiment which measured the residual stress of a concrete specimen after it exhibits a designated temperature, because concrete damage caused by a temperature does not recover when it cools to ambient temperature, as described in EC4-1-2 (2014). The slope of the curve which connects the failure points was increased in accordance with an increase in temperature. This makes the *k* value increase as with the temperature. The *k* value at ULS was assumed to be 2.7 based on the study of Ansari and Li (1998) because the concrete surrounding the shear stud in the loading direction was in a highly confined state in the push-out test. The temperature-dependent *k* value can be achieved from the experimental data of Hammoud *et al*. (2014). The *k* values obtained from experiments are presented in Fig. 3-23.

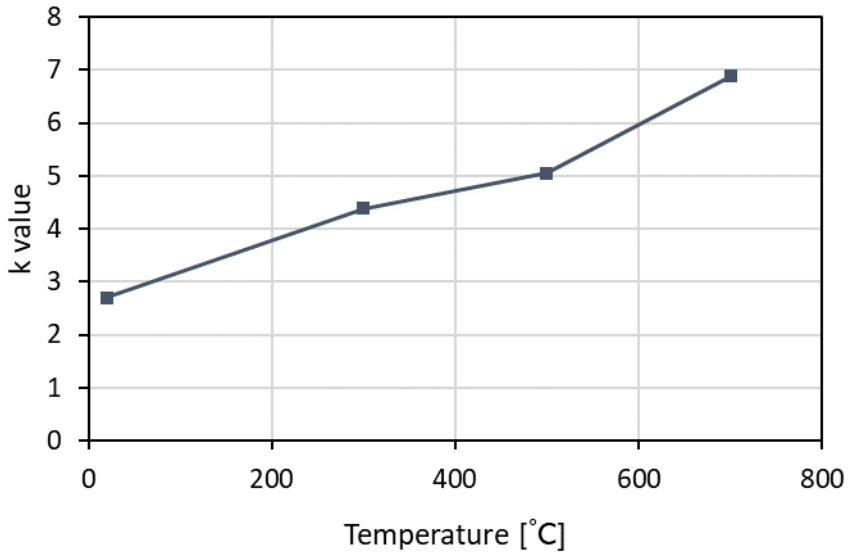

Figure 3-23. k value variation depending on temperatures

The stress ratio between the triaxial compressive and tensile meridians at the same hydrostatic stress level is defined as the K_C value, which determines the failure surface shape of the CDP model. This can be derived using the first stress invariant (I_1) at the biaxial and triaxial compressive states and the temperature-dependent *k* value. In a π-plane, the first stress invariant (I_1) shows an identical value over the plane. Consequently, it can be assumed that biaxial and triaxial deviatoric stresses lie on the same yield surface (Yu *et al*., 2010). The first stress invariant (I_1) at the biaxial and triaxial compressive states in the π-plane can be expressed using Richart's formula.

$$I_{1,bi} = f_{b0} + f_{b0} = 2(f_{b0}/f_c)f_c$$
$$I_{1,tri} = f_{cc} + \sigma_3 + \sigma_3 = f_c + (k+2)\sigma_3 \quad (3\text{-}38)$$

where, $I_{1,bi}$: first stress invariant at biaxial compressive state
$I_{1,tri}$: first stress invariant at triaxial compressive state

When the equi-biaxial stress ratio and the *k* value are defined as 1.16 and 2.7 at ULS, the relationship between the confinement and compressive stresses can be obtained as follows:

$$\sigma_3 = \left[\frac{2(f_{b0}/f_c) - 1}{k + 2}\right] f_c = 0.28 f_c \tag{3-39}$$

where, $I_{1,bi} = 2.32 f_c$

$I_{1,tri} = f_c + 4.7\sigma_3$

By using the deviatoric stresses at the equi-biaxial and triaxial compressive states, the K_C value can be calculated using the deviatoric stresses at the triaxial compressive and tensile meridians. In the π-plane, the deviatoric stress at a compressive and tensile meridian can be regarded as the stress in an equi-biaxial and triaxial condition. Thus, the K_C value can be obtained using the second invariant of the deviatoric stress (J_2) as follows:

$$K_C = \frac{\sqrt{3J_2}_{TM}}{\sqrt{3J_2}_{CM}} = \frac{(f_{b0}/f_c) f_c}{f_c + (k-1)\sigma_3} = \frac{1.16 f_c}{f_c + 1.7\sigma_3} = 0.78 \tag{3-40}$$

The K_C values at high temperatures can be achieved in the same calculation procedure at ULS using the equi-biaxial stress ratio and the *k* value. Both the equi-biaxial stress ratio and the *k* value increase as the temperature rises, whereas the K_C value decreases with increasing temperature. This indicates that the stress difference between the triaxial compressive and tensile states increases with increasing temperature. The calculated K_C values are provided in Table 3-4.

Table 3-4. Temperature-dependent K_C values

Temperature [°C]	k value	K_C value	$K_C/K_{C,ULS}$
20	2.7	0.78	1
300	4.39	0.69	0.88
500	5.05	0.68	0.86
700	6.88	0.64	0.82

As discussed in Section 3.4.1, various K_C values are used for concrete modelling at ULS. A reduction ratio of the temperature-dependent K_C value was investigated to apply to a wide range of concrete models which adopt different K_C values at ULS. Considering the obtained reduction ratios provided in Table 3-4, a linear function can be used for the temperature-dependent K_C value, as plotted in Fig. 3-24. The following formula was adopted in this study to simulate concrete behaviour at high temperature based on the K_C value at ULS.

$$K_{C,\theta} = K_{C,20℃}\left(1 - 0.23\left(\frac{\theta - 20}{780}\right)\right) \qquad 20℃ \le \theta \le 800℃ \qquad (3\text{-}41)$$

where, $K_{C,\theta}$: temperature-dependent K_C value

$K_{C,20°C}$: K_C value at 20 ℃

The CDP model permits using a K_C value with a range of 0.5 to 1, because the γ parameter cannot be calculated when the K_C value goes to 0.5, as given by Eq. 3-23. Thus, the minimum K_C value was limited to 0.51 for the high-temperature modelling. A calculated triaxial stress with respect to the K_C value is presented in Appendix B.5.

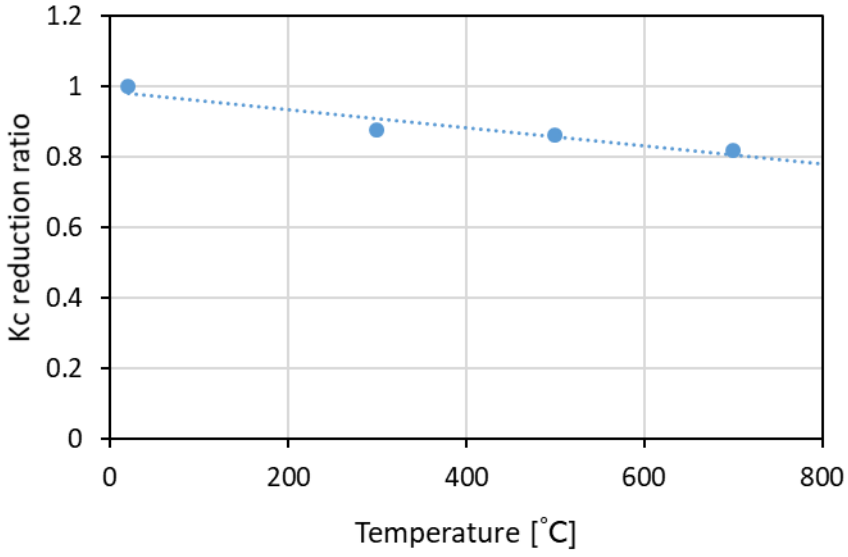

Figure 3-24. Normalised K_C value with respect to temperature

3.5.4. Dilation angle

The angle of dilation stands for the ratio of the volumetric to deviatoric strain rates. It represents the volume expansion rate with respect to a plastic strain change. The relationship between the friction and dilation can be simply explained using a sawtooth model. As shown in Fig. 3-25(a), a friction coefficient (μ) represents the friction between a concrete block and a flattened surface. This assumes that there is no volume expansion during the sliding of this concrete block; pure friction is considered. The friction coefficient can be expressed as a function of the friction angle as follows:

$$\mu = \frac{\tau}{\sigma_n} = tan\phi_{cv} \tag{3-42}$$

where, μ : friction coefficient
τ : shear stress [*MPa*]
σ_n : normal stress [*MPa*]
ϕ_{cv} : internal friction angle with constant volume [degree]

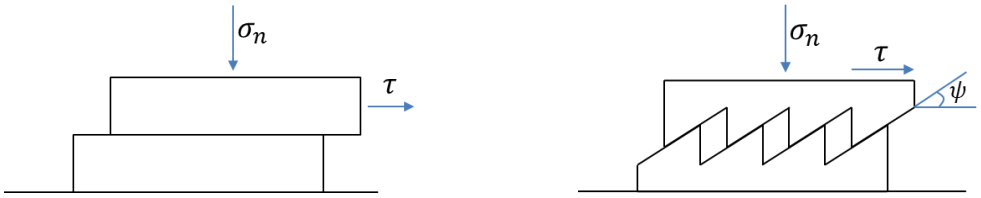

(a) Friction with constant volume (b) Friction with dilation

Figure 3-25. Sawtooth model for concrete dilation (Houlsby, 1991)

Unlike friction with a constant volume, an inner friction accompanied by volume expansion is also observed in concrete. The friction coefficient in Fig. 3-25(b) can be expressed as $\mu' = \tan\phi = \tan(\phi_{cv} + \psi)$, which means that the internal friction angle is composed of a constant-volume friction angle (ϕ_{cv}) and a dilation angle (ψ). The concrete friction angle is greater than or equal to its dilation angle, depending on the volume expansion of the concrete. Among the concrete yield functions, the Mohr-Coulomb criterion uses an internal friction angle to illustrate the failure surface of concrete. It has a hexahedral yield surface, whereas the CDP model shows a smooth yield surface with respect to the K_C value.

Assuming that the deviatoric stress at the compressive meridian is the same between these two yield functions, the internal friction angle can be expressed as a function of the plasticity parameters of the CDP model. From this relationship, the ratio of the dilation angle can be obtained with respect to the temperature in the condition that the portion of the dilation angle (ψ) is constant at the internal friction angle (ϕ).

The Mohr-Coulomb criterion is:

$$|\tau| = c - \sigma_n tan\phi \tag{3-43}$$

where, c : cohesion stress
ϕ : internal friction angle

The shear (τ) and nominal stress (σ_n) terms can be replaced by the principal stress components from the stress relationships of Mohr's circle. This is given by:

$$(\sigma_1 - \sigma_3) = 2ccos\phi - (\sigma_1 + \sigma_3)sin\phi \tag{3-44}$$

where, $\sigma_1 > \sigma_2 > \sigma_3$: principal stresses

The principal stresses in a triaxial state also can be expressed using the deviatoric stress, hydrostatic stress, and Lode angle. The derivation of this relationship is described in Appendix A.

$$\begin{bmatrix}\sigma_1\\ \sigma_2\\ \sigma_3\end{bmatrix} = \frac{2}{\sqrt{3}}\sqrt{J_2}\begin{bmatrix}\cos\theta_L\\ \cos(\theta_L - 2\pi/3)\\ \cos(\theta_L + 2\pi/3)\end{bmatrix} + \begin{bmatrix}I_1/3\\ I_1/3\\ I_1/3\end{bmatrix} \tag{3-45}$$

where θ_L : Lode angle

By substituting Eq. 3-45 into Eq. 3-44, the Mohr-Coulomb criterion can be expressed by the first invariant of the stress (I_1) and the second invariant of the deviatoric stress (J_2) terms as follows:

$$2[(sin\phi + 1)cos\theta_L + (sin\phi - 1)cos(\theta_L + 2\pi/3)]\sqrt{3J_2} + 2sin\phi I_1 - 6ccos\phi = 0 \quad (3\text{-}46)$$

Assuming that the deviatoric stress at the compressive meridian is the same for the Mohr-Coulomb and CDP models, the internal friction angle can be expressed as the material parameters of the CDP model.

In the case of the compressive meridian ($\theta_L = 60°$), the Mohr-Coulomb criterion is given by:

$$(3 - sin\phi)\sqrt{3J_2} + 2sin\phi I_1 - 6ccos\phi = 0 \quad (3\text{-}47)$$

The internal friction angle of the Mohr-Coulomb criterion at the compressive meridian can be calculated as the inclination angle:

$$tan\,\phi_{CM,Mohr-Coulomb} = \frac{2sin\phi}{3 - sin\phi} \quad (3\text{-}48)$$

From Eq. 3-31, the internal friction angle of the CDP model at the compressive meridian can be obtained by setting the Load angle as 60°:

$$tan\,\phi_{CM,CDP} = \frac{3\alpha + \gamma}{3 + \gamma} \quad (3\text{-}49)$$

By combining Eq. 3-48 and 3-49, the relationship between the internal friction angle and the plasticity parameters of the CDP model can be expressed as follows:

$$sin\phi = \frac{3\alpha + \gamma}{\alpha + \gamma + 2} \quad (3\text{-}50)$$

The internal friction angle at designated temperatures was calculated using the temperature-dependent plasticity parameters which were already obtained in Section 3.5.2

and 3.5.3. A normalised dilation angle was plotted by assuming that the dilation angle has a constant ratio at the internal friction angle. Furthermore, the normalised value is convenient to apply to high-temperature concrete modelling with reference to its ULS values. It increases exponentially depending on the temperature, as depicted in Fig. 3-26.

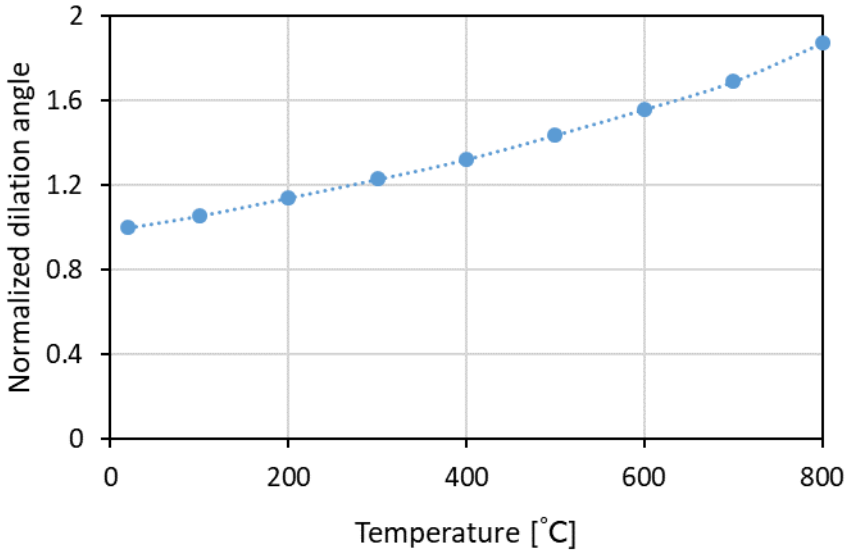

Figure 3-26. Normalised dilation angle value with respect to temperatures

The concrete dilation angle as a function of temperature is proposed for numerical modelling by incorporating the dilation angle at ULS as follows:

$$\Psi_\theta = \Psi_{20℃} \times 0.9681 exp(0.0008\theta) \quad (3\text{-}51)$$

where Ψ_θ: temperature-dependent dilation angle
$\Psi_{20℃}$: dilation angle at ULS
θ: temperature

3.6 Summary and conclusions

The material characteristics of steel and concrete have been briefly reviewed, and their stress-strain relationships at both ULS and FLS were defined for numerical modelling. For a steel material, the stress-strain curve of EC4-1-2 (2014) was used incorporating a different yield and ultimate stress obtained from experiments. The ductile damage function was also adopted to illustrate the strength degradation. The concrete stress-strain relationship was adopted from EC2-1-1 (2014) and EC4-1-2 (2014). A parabolic curve was used for the ascending and descending parts to avoid a sudden drop in the stress as well as to ensure a stable solution in the numerical calculation.

To illustrate the failure of steel and concrete materials, the von Mises criterion and CDP model were adopted, respectively. The CDP model requires four material parameters, which consisted of three material constants (α, β, γ) and a uniaxial compressive cohesion stress. Those material parameters can be obtained from existing literature for ULS applications. However, the temperature-dependent values are not available. Therefore, the concrete plasticity parameters depending on temperature were proposed based on high-temperature experimental data. Their characteristics are summarised as follows:

- The stress ratio of the equi-biaxial to the uniaxial state determines the α and β parameters in the CDP model. The equi-biaxial stress ratio is proposed with four linear functions, which shows an increasing trend as temperature rises. This variation makes the yield surface more ductile, and thus the biaxial compression and tension show a higher growth in comparison to the uniaxial stress value.
- Temperature-dependent K_C value is proposed using a linear function with reference to its ULS value for various applications. It decreases as temperature rises, which means the shape of the concrete failure surface becomes triangular.
- An exponential function is presented to illustrate the dilation angle change with temperature. It is derived using the temperature-dependent plasticity parameters (α, β, γ) of the CDP model. The dilation angle increases as temperature rises, which results in a more ductile behaviour at a higher temperature.

Chapter 4
EXPERIMENTAL INVESTIGATIONS

4.1. Introduction

Twelve push-out tests were carried out under ambient and fire conditions using specimens with solid and transverse deck slabs. A customised electric furnace was designed to simulate the ISO 834 standard fire (ISO 834-1, 1999) according to the configuration of the specimen. A failure mode transition and shear resistance reduction were observed as the surrounding temperature rose. The detailed experimental setup, procedure, and results are described herein.

4.2. Experiment design

4.2.1. Push-out test specimen

The standardised push-out test in EC4-1-1 (2009) specifies using a headed shear stud embedded in a solid slab; a piece of steel beam is connected with two concrete slabs by using shear connectors. There is, however, no guidance on either adopting a trapezoidal deck or high-temperature experiment. Hicks (2009) reported a push-out test specimen utilising a transverse deck with enlarged concrete slabs, in which were embedded two levels of a shear connection. The larger concrete slab helps to avoid cracking at the side section of the concrete ribs in the case of concrete pull-out failure. The stud arrangement inhibits an artificial failure mode caused by the rotation of the concrete rib. In this study, the standard push-out test specimen was modified to incorporate a transverse deck according to the

recommendations of Hicks (2009). A 30-mm recess space at the bottom of the concrete slab was not applied to avoid heat dissipation during the high-temperature experiment.

Twelve specimens were prepared with different slab types, deck thickness, and stud welding methods, as presented in Table 4-1. Two specimens of each slab type were tested at ULS: solid slab specimens (S-1, S-2), 1.2-mm through-deck-welded specimens (T1-1, T1-2), and 0.9-mm through-hole-welded specimens (T2-1, T2-2). Two specimens used for a high-temperature experiment were fabricated in the first concrete cast, which shows a compressive strength of 51 MPa: solid slab specimen (SH-1) and 1.2-mm through-deck-welded specimen (T1H-1). Four specimens were prepared for a high-temperature experiment using a second lot of the concrete, which has a compressive strength of 32 MPa: 0.9-mm through-hole-welded specimens (T2H-1, T2H-2, T2H-3, T2H-4).

Table 4-1 Detailed specifications of the push-out test specimens

Specimen	Slab type	Profiled steel sheeting thickness [*mm*]	Stud welding method	Concrete strength [f_{cm}, *MPa*]	Test condition
S-1	Solid	-	Direct welding	51	Ambient
S-2					
SH-1					Fire
T1-1	Trapezoidal	1.2	Through-deck welding	51	Ambient
T1-2					
T1H-1					Fire
T2-1	Trapezoidal	0.9	Direct welding through the deck hole	32	Ambient
T2-2					
T2H-1					Fire
T2H-2					
T2H-3					
T2H-4					

Dimensions

An H-beam dimension of 350 × 350 with 1100 mm length and a unit weight of 156 kg/m was used as the steel section. The size of the concrete slab was 750 mm breath × 1050 mm height with a depth of 150 mm. A 10-mm-diameter ribbed bar was placed on a steel decking shoulder for the reinforcement of the trapezoidal deck slabs, and two layers of the reinforcement bar were used in the solid slabs. The spacing of the reinforcement was determined to be 180 mm in the horizontal direction, considering the location of the shear stud, and 230 mm in the vertical direction, according to EC4-1-1 (2009). The push-out test specimens with respect to the slab type are shown in Fig. 4-1. The detailed dimensions are provided in Appendix C.

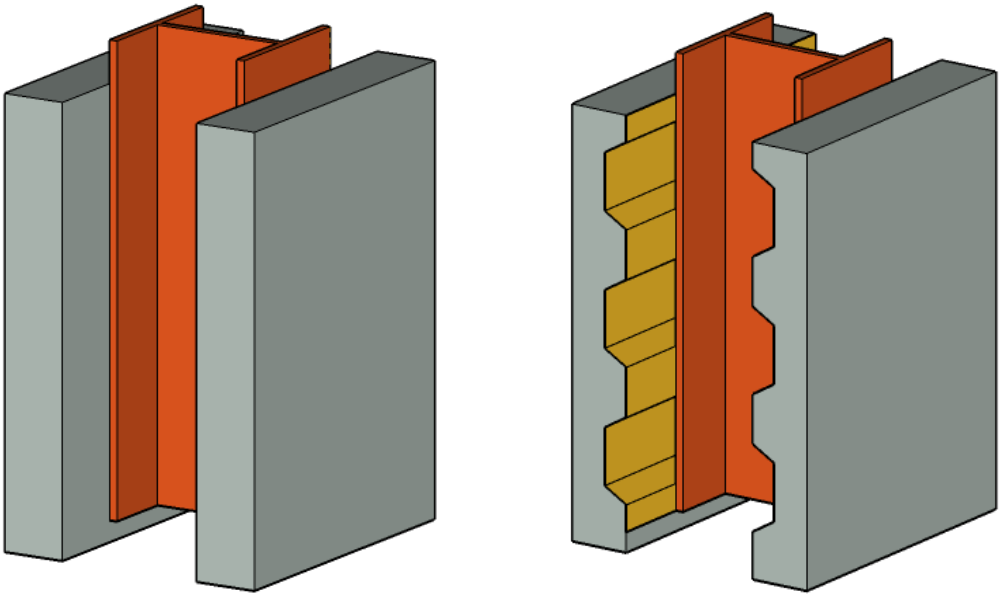

(a) Solid slab specimen (b) Trapezoidal deck specimen

Figure 4-1. Push-out test specimens

Specimen fabrication

The Kingspan Multideck 60-V2 was used for the trapezoidal deck which has been used in composite constructions. It has a 61 mm height and 155 mm average breadth as illustrated in Fig. 4-2. The ribbed metal decks were placed perpendicular to a steel beam.

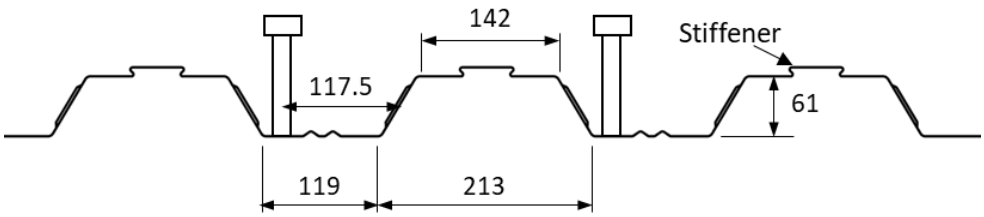

Figure 4-2. Dimensions of trapezoidal deck (Multideck 60-V2)

A headed shear stud of 19 mm diameter × 100 mm height was adopted as a shear connector. An automatic welding machine was used to achieve the reliability of the welding process. The shear stud was directly welded on the steel flange for the solid slab specimen. The shear stud was placed in a favourable side in the transverse deck specimen because of a corrugation in the middle of the web; the distance from the mid-height of the rib in the loading direction to the centre of the shear stud was 117.5 mm. Through-deck welding was used when utilising the 1.2-mm-thick steel decking, whereas the shear stud was directly welded on the steel flange via a 34-mm-diameter hole when adopting the 0.9-mm-thick steel decking.

After welding the shear studs, k-type thermocouples were attached to the stud shank. Concrete was poured three times by equally dividing the slab height and vibrating for 5 to 10 s at each step to avoid poor compaction or air pockets. The concrete was steam-cured for four days, which shows the temperature range of 45 ℃ to 90 ℃ according to the distance from the heaters. The specimen fabrication process is schematically depicted in Fig. 4-3.

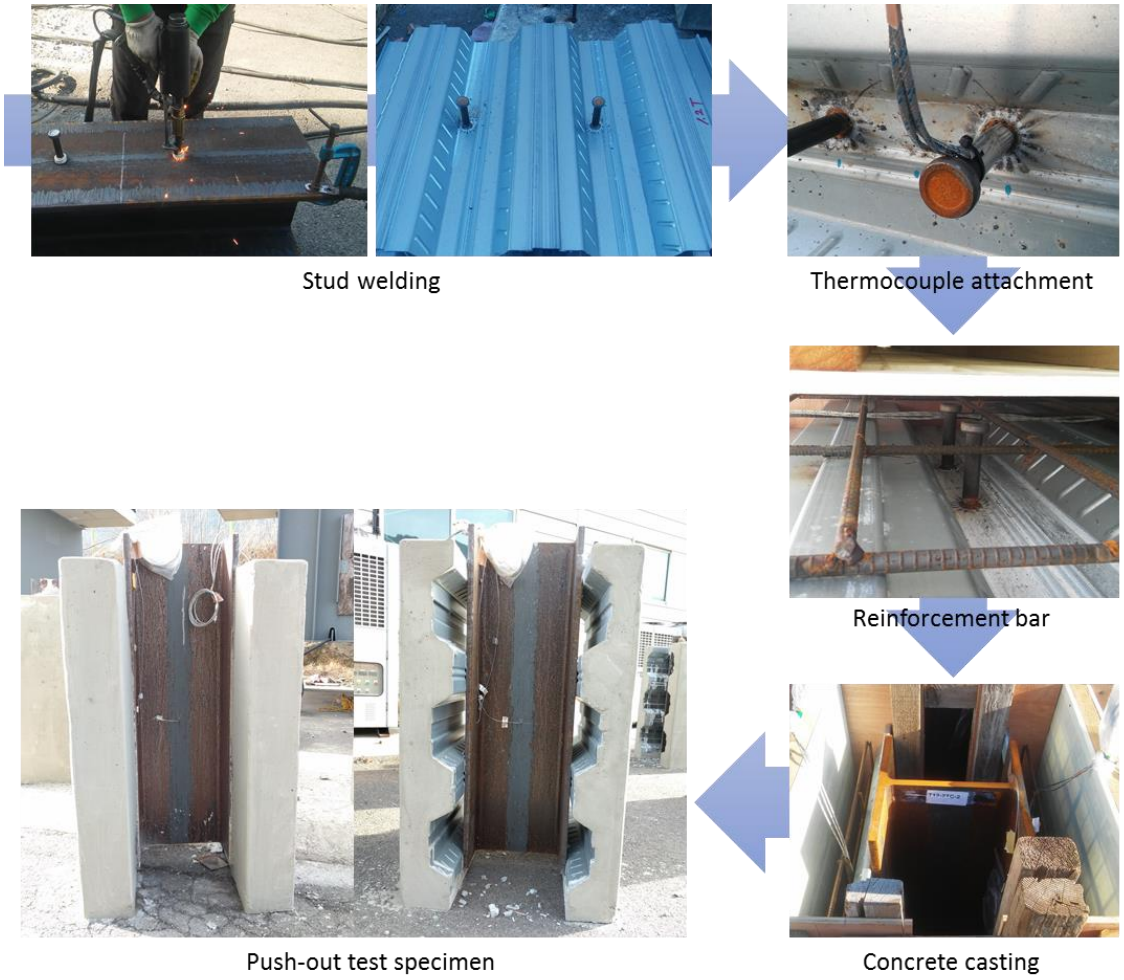

Figure 4-3. Production process of push-out test specimen

4.2.2. Heating equipment

A customised electric furnace was prepared to apply to the modified push-out test specimen. Two customised electric furnaces were designed to be attached along the side profile of the modified push-out test specimen. This configuration offers a designated fire load on the steel section. Heat energy was applied to the concave areas of the specimen, and the top and bottom openings were insulated to maintain the temperature distribution during the heating process. An assembly drawing of the specimen and electric furnaces is illustrated in Fig. 4-4.

Each furnace contains 12 heating tubes, as shown in Fig. 4-5(a), and the tube temperature was regulated by the magnitude of the input current through a programmable logic controller, as presented in Fig. 4-5(b). A gas temperature was measured at the enclosure between the furnace and the concave area of the specimen to check that the steel beam and underside of the concrete slab exhibit the ISO 834 standard fire condition. The gas temperature successfully follows the standard fire curve, and this condition was used to illustrate a fire condition.

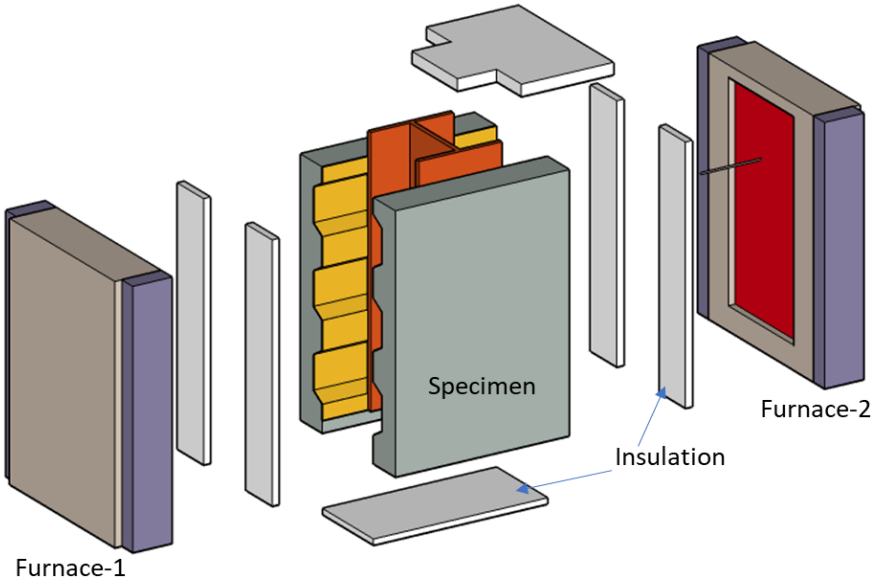

Figure 4-4. Assembly drawing of the heating equipment and specimen

(a) Inside of the furnace

(b) Control panel

Figure 4-5. Electric heater and control panel

4.2.3. Measuring instruments

K-type thermocouples were used to measure the temperature of the web, flange, and shear stud. The temperature of the surrounding concrete was not measured. They were installed in 2mm-diamter hole at the web and flange, whereas a thermal resistive tape was used to attach the thermocouple to the stud shank. The gas temperature (T0) at the enclosure between the electric furnace and concave area of the specimen was monitored to verify the designated fire condition. The specific locations of the thermocouple are illustrated in Fig. 4-6. The diameter and height of the weld collar is 26 mm and 5 mm, respectively. The temperature data were collected every 0.2 s by a data logger, which was connected to a computer.

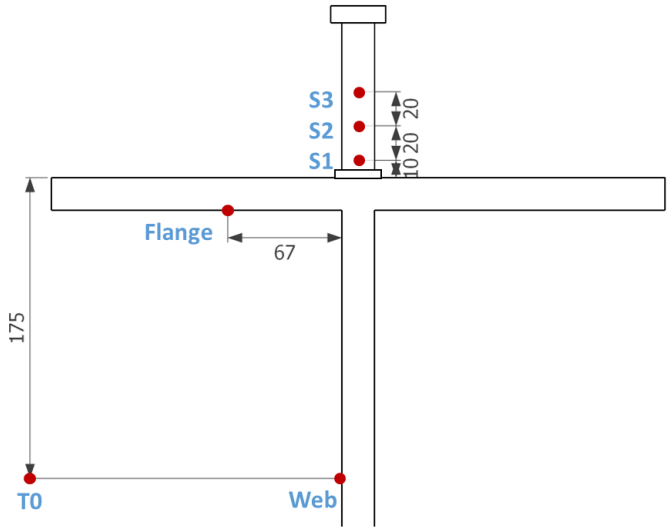

Figure 4-6. Locations of the thermocouple at the specimen

A structural load was imposed through a load cell, which was connected to a hydraulic actuator. A square plate swivel jig was placed between the top side of the steel beam and the actuator, which has a maximum capability of 2500 kN. Linear variable differential transformers (LVDTs) were used to collect displacement variations during the experiment. At each outer side of the slab, three LVDTs were installed as shown in Fig. 4-7. The relative slip between the loading plate and concrete slab was obtained using LVDT1 and LVDT2, and the lateral deviation was measured using LVDT3.

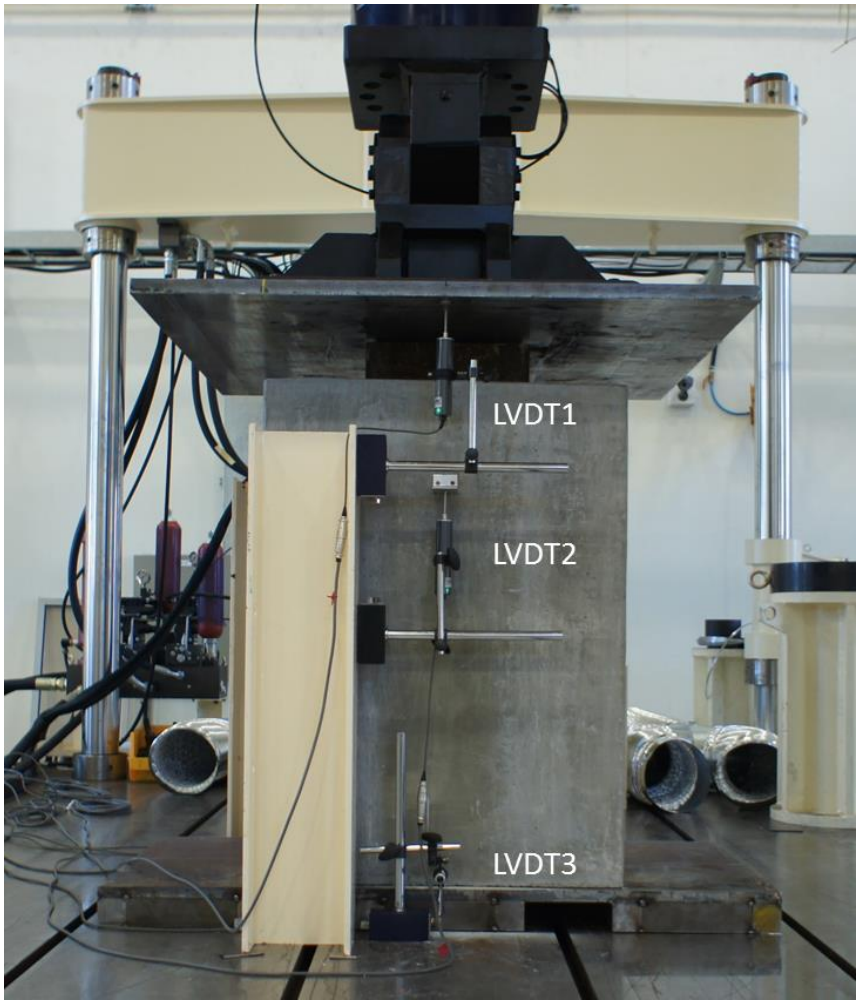

Figure 4-7. LVDT setup for the experiment

4.3. Material properties

The push-out test specimen was composed of a concrete slab, headed shear stud, rib deck, reinforcement bar, and steel beam. Among these, the compressive and tensile stress of the concrete slab and ultimate stress of the headed shear stud are the most influential parameters in determining the strength of the shear connection, as the failure modes are stud shearing, concrete crushing, and concrete pull-out. Thus, the material data of the concrete slab and shear stud were measured, and nominal values were adopted for the other materials.

4.3.1. Concrete

The specimens were made from casting two different batches of concrete. The solid slab specimen and through-deck-welded specimen with 1.2 mm deck thickness were fabricated together. The through-hole-welded specimen with 0.9 mm deck thickness was made in sequence. The concrete compressive strength at ambient condition was measured using a cylindrical specimen with a 100 mm diameter and 200 mm height, as presented in Fig. 4-8. Three concrete specimens were evaluated on the first day of each experiment. The measured average cylinder compressive strengths (f_{cm}) were 51 and 32 MPa. The tensile strength and secant modulus of elasticity were calculated according to EC2-1-1 (2014). The measured and calculated values are provided in Table 4-2.

Table 4-2. Concrete properties at ambient condition

Specimen	f_{cm} [*MPa*]	f_{ck} [*MPa*]	f_{ctm} [*MPa*]	E_{cm} [*MPa*]
Solid slab 1.2 mm deck	51	43	3.68	35866
0.9 mm deck	32	24	2.5	31186

Figure 4-8. Concrete compressive strength test using a cylindrical specimen

4.3.2. Steel

The shank part of the headed shear stud was machined to prepare a tensile test coupon in accordance with ISO 6892-1 (2016). Three coupons were tested using an Instron 5967 universal testing machine as shown in Fig. 4-9. The measured average yield and ultimate stresses at ULS were 415 and 473 MPa, respectively, with an elongation of 25 %. The steel property data of other parts such as the deck, beam, and reinforcement were taken from manufacture's data and relevant design code.

Table 4-3. Shear stud properties at ambient condition

	Yield stress [*MPa*]	Ultimate stress [*MPa*]	Elongation [*%*]
Coupon 1	412	475	25.1
Coupon 2	415	477	22.8
Coupon 3	416	468	25.2

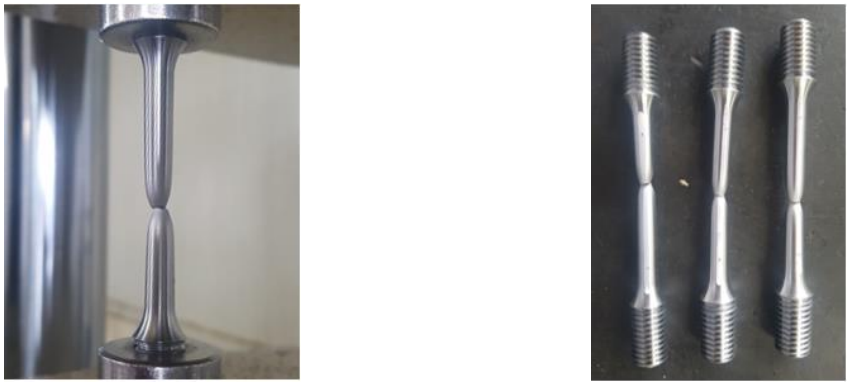

(a) During the test (b) After the test

Figure 4-9. Tensile test of the headed shear stud specimen

The trapezoidal deck of the Multideck 60-V2 has the minimum yield stress of 350 MPa. The SD400 and SM490A materials referenced from the Korean Building Code (KBC 2018) were used for the 10-mm-diameter ribbed bar and the steel beam, respectively. The yield stress of the SD400 is 400 MPa. The SM490A material has the minimum yield and ultimate stress of 345 and 490 MPa, respectively. The elastic modulus of 205 GPa was used for a numerical model, which is the recommended value in the design guidance of KBC 2018 (MILT, 2018).

4.4. Experimental procedures

Test procedure at ULS follows the generic guidance on the push-out test in EC4-1-1 (2009), which specifies an initial cyclic loading and measuring range of the applied load. All the specimens exhibit a cyclic loading phase with a range of 30 % to 5 % of an estimated failure load to break a bond between the steel beam and concrete slab and stabilise the specimen. The expected failure load was calculated from EC4-1-1 (2009). A displacement load was applied immediately after the cyclic loading process. The load–slip behaviour was acquired until the applied load reduced to 20 % of the maximum obtained strength. In the case of the high-temperature experiment, a specimen was subjected to the ISO 834 standard fire condition applying a constant load which was 20 % to 60 % of the expected failure load. Although the time-slip relationship can be collected from this procedure, it is suitable to replicate a fire situation. The fire elapsed time and shear resistance were achieved at the high-temperature experiments.

4.4.1. Structural loading

An induced load and time relationship is illustrated in Fig. 4-10, according to the experimental procedure as follows:

- A specimen is placed on a sand layer to reduce friction and balance the uneven base of the concrete slabs.
- A load is applied as 30 % of the expected failure load, following which a repeated load with a range of 5 % to 30 % of the estimated shear resistance is applied for 25 cycles. The load is controlled at 5 kN/s in this step.
- A displacement load is applied until the load is reduced to 20 % of the maximum experienced load at the rate of 0.01 mm/s.
- During the test, the applied load and displacement variations in the vertical and outward directions are measured.

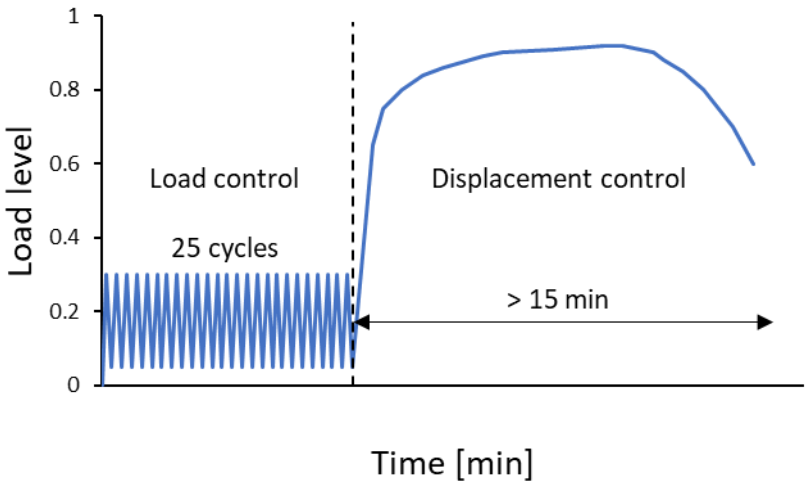

Figure 4-10. Loading procedure of the push-out test at ULS

4.4.2. Structural and fire loading

Imposed thermal and structural loads with respect to the fire elapsed time are plotted in Fig. 4-11. All the specimens exhibited a cyclic loading phase before the test, separately. The detailed procedure is as follows:

- A specimen is placed on a sand layer to reduce friction and balance the uneven base of the concrete slabs.
- The electric furnaces are attached at the side sections of the specimen.
- A constant load is applied at 5 kN/s to a designated value.
- A thermal load is induced to have the gas temperature (T0) at the enclosure area to follow the ISO 834 standard fire.
- Temperature, time, and displacement variations in the vertical and outward directions are measured during the test.

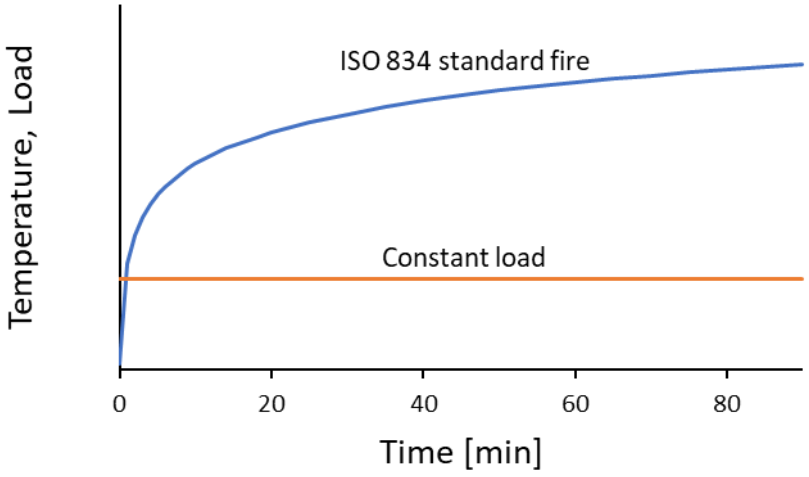

Figure 4-11. Loading procedure of the push-out test at FLS

4.5. Experimental results

All the push-out test specimens with solid and transverse deck slabs were tested at ambient and fire conditions. The repeatability and stability of the electric furnaces were verified before conducting the high-temperature experiment. The shear resistance and failure modes varied as the temperature increased. In this section, the experimental results are presented in detail.

4.5.1. Temperature profile

Verifying the ISO 834 standard fire condition

The push-out test specimens were exposed to the ISO 834 standard fire, which shows a rapid increase at the beginning and gradual increase after approximately 10 min of heating. A heating programme was designed to increase linearly to 540 ℃ for the first 4 min to produce the rapid temperature boost region. The gas temperature starts to increase linearly within a short period. The electric furnace draws up to 180 A at this stage. The gas temperature (T0) successfully complies with the ISO 834 standard fire, as plotted in Fig. 4-12 and 4-13.

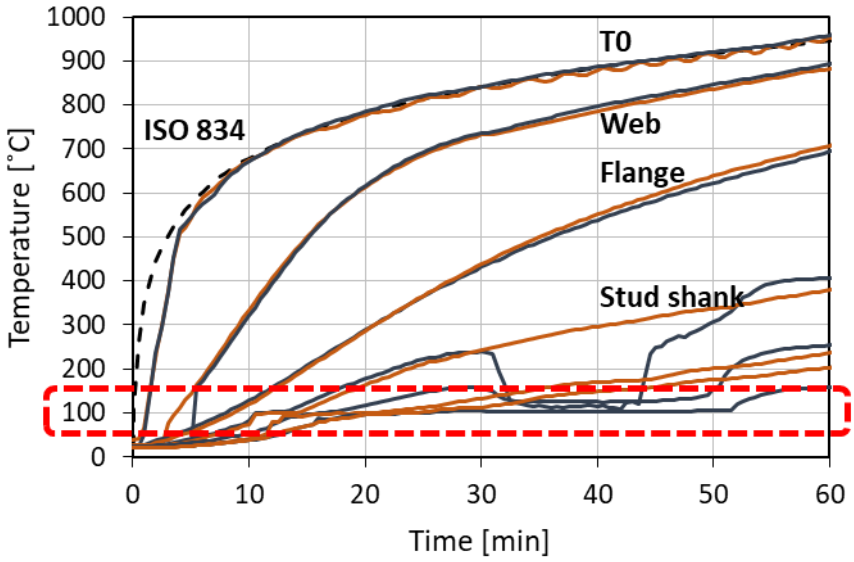

Figure 4-12. Temperature distributions of solid slab specimen

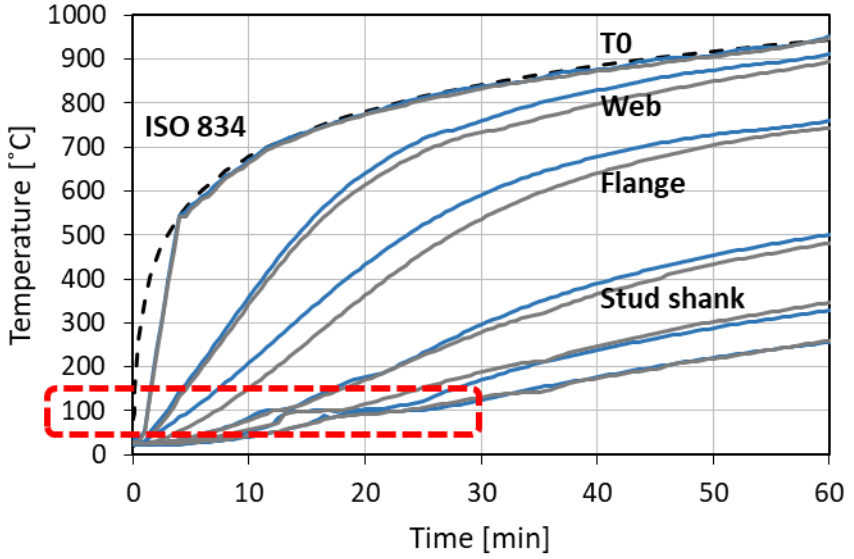

Figure 4-13. Temperature distributions of transverse deck specimen

Temperature distributions of push-out test specimens

The temperature of the web and flange showed strong repeatability and stable increasing during the heating process. However, the temperature measured at the stud shank showed approximately 100 ℃ for a certain period. This stagnation time increased when the measuring location receded from the steel flange. A deeper position in the concrete slab experiences less heat transfer, such that the evaporation of free water takes longer. The temperature obtained at 50 mm from the stud root shows a longer temperature stagnation time than that measured at 10 mm: S3 and S1 in Fig. 4-6. This temperature disturbance continued up to 50 min in the solid slab specimens, and it lasted approximately 25 min in the specimen with transverse deck slabs.

During the heating process, water smeared out from the backside of the concrete slab owing to a pressure difference in the concrete medium, as presented in Fig. 4-14(a). Consequently, the thermocouple at the stud shank was disturbed in measuring the temperature owing to free water and chemically bonded water in the concrete. It showed a stagnation around 100 ℃ as well as a lower temperature for all specimen types. More temperature congestion was shown in the solid slab specimen in comparison to the rib deck specimen. This phenomenon also demonstrates the influence of the travelling moisture in the concrete slab, because a large amount of concrete was present around the shear stud in the solid slab specimen.

Approximately 20 min after inducing a thermal load, spalling occurs at the concrete slab accompanied by a loud sound. When the heated specimen cools, moisture and concrete spalling traces were found at the concave area of the concrete slab. Evaporated water smeared out by high pressure in the concrete slab through the fire-exposed and unexposed surfaces. The concrete damage, near the steel flange depicted in Fig. 4-14(b), was caused by high pressure within pores in the evaporation of free water. A higher temperature of the steel beam leads to a rapid phase change of the moisture in the concrete slab.

(a) Water smeared out (b) Water traces

Figure 4-14. Outside and inside of the specimen during and after the heating process

When the failure mode is stud shearing, the temperature at the shearing position of a stud is the critical parameter in determining the structural capacity. The stud temperature in EC4-1-2 (2014) is defined as 80 % of the flange temperature. However, this temperature ratio can be changed by the experimental conditions, such as moisture content of the concrete, heating process, and configuration of the experimental setup. Dara (2015) reported a temperature ratio of 90–95 %.

In order to avoid the effect of concrete moisture in measuring the stud temperature, a thermocouple was installed by drilling the steel flange. The measured temperature around 3 mm above the steel flange shows approximately 90 % of the flange temperature (orange line in Fig. 4-15), whereas the temperature obtained at the outside of the stud shank around 10 mm departed from the steel flange shows 55 % of the flange temperature (green line in Fig. 4-15). Although there is a difference of 7 mm in the position, the temperature discrepancy is too high when considering the thermal conductivity of the steel material. Therefore, the temperature ratio between the stud root to steel flange can be regarded as 90 % in this experimental condition; although EC4-1-2 (2014) defines the temperature ratio of 80 %.

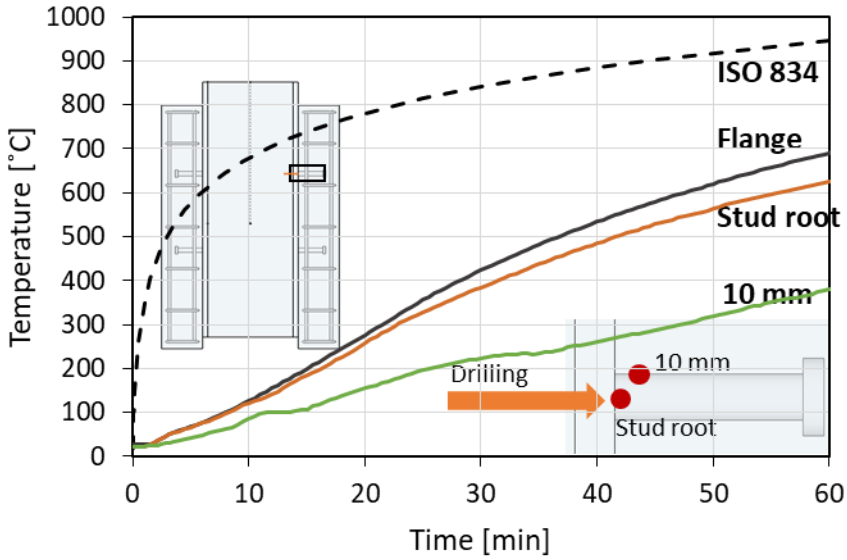

Figure 4-15. Thermocouple installation and measured temperature at the stud root

4.5.2. Structural capacity of shear connections at ULS

Six push-out tests were conducted with variations in the slab type, stud welding method, and deck thickness. Two specimens were used for each experimental condition to confirm the repeatability of the push-out tests. The shear resistance and failure mode of the shear connection at ULS are discussed in this section.

Solid slab specimen

As discussed in Section 4.3, the material properties of the solid slab specimens, such as the concrete strength, stud ultimate strength, and steel beam stress have the same values as those of the 1.2-mm transverse deck specimens. In terms of the structural aspects, the only difference is the absence of the profiled steel sheeting between the steel beam and the concrete slab. The average shear resistance of 141 kN at ULS was observed from the push-out tests. This did not exceed 5 % of each measured value, which means that the experiments were stable according to the standard test evaluation method of EC4-1-1 Annex B (2009). The load–slip relationships, plotted in Fig. 4-16, were acquired until the

applied load reduced to 20 % of the maximum experienced load. Beyond the maximum shear resistance, the applied load reduced stepwise accompanied by a loud sound in accordance with the tearing of the shear stud; the shear stud tore consecutively. The applied load dropped significantly when the stud shearing occurred, whereas it decreased gradually between the stud fractures. A highly ductile behaviour was observed, because the cause of the failure was shearing of the steel component. The characteristic slip was in the range of 13 to 18 mm.

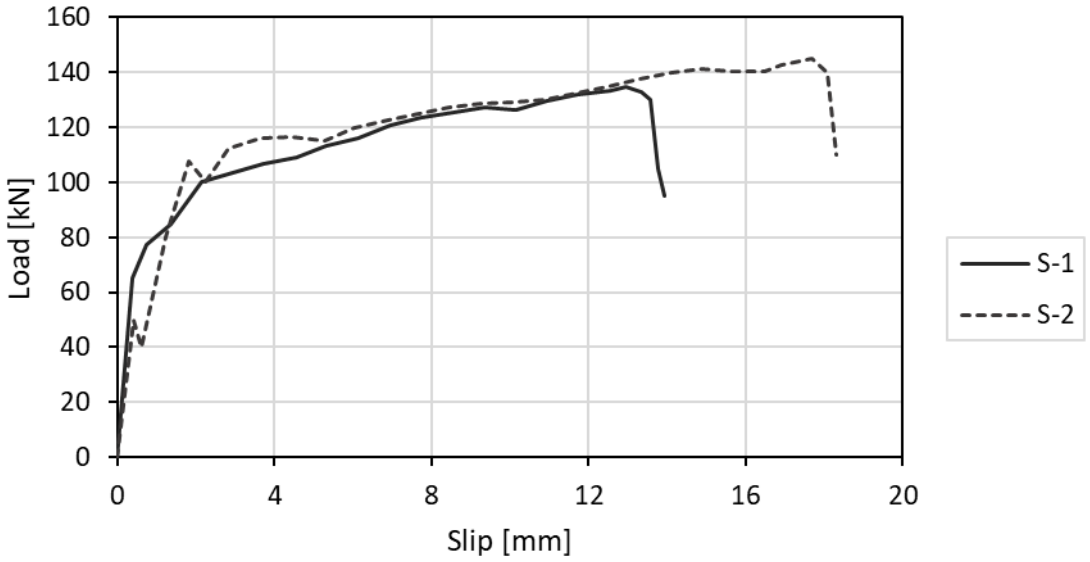

Figure 4-16. Load-slip curve of solid slab specimen at ULS

The failure mode of all the solid slab specimens was stud shearing located at just above the weld collar. The stud shank was significantly bent, and its curvature increased towards the bottom of the shear stud. The deformed shape of the shear stud and the crushed concrete in the adjacent area are shown in Fig. 4-17(a). The concrete debris remained adjacent to the weld collar along the loading direction, which indicates that a high pressure developed between the weld collar and the surrounding concrete block. After finishing the push-out test, a specimen was cut vertically along the centre line of the welded studs using a waterjet machine. It took approximately 60 min to complete the cutting process. By observing a cutting plane around the location of the shear stud, the cause of failure of the shear

connection can be visualised. Concrete compaction and crushing are observed in Fig. 4-17(b). The crushed concrete area was increased alongside the stud shank in the stud root direction, which is consistent with the deformed shape of the stud shank. The concrete crushing also occurs beneath the stud head, owing to the force acting in the stud shank direction and considering the attached concrete under the stud head. No crack was found at the cutting plane or outside of the concrete slab. Only the compressive crushing near the shear stud was observed. This phenomenon indicates that the shear resistance is highly dependent on the ultimate strength of the stud material in the case of the solid slab specimen. An identical explanation was also reported from other experiments (Xue *et al.*, 2008; Pavlovic *et al.*, 2013).

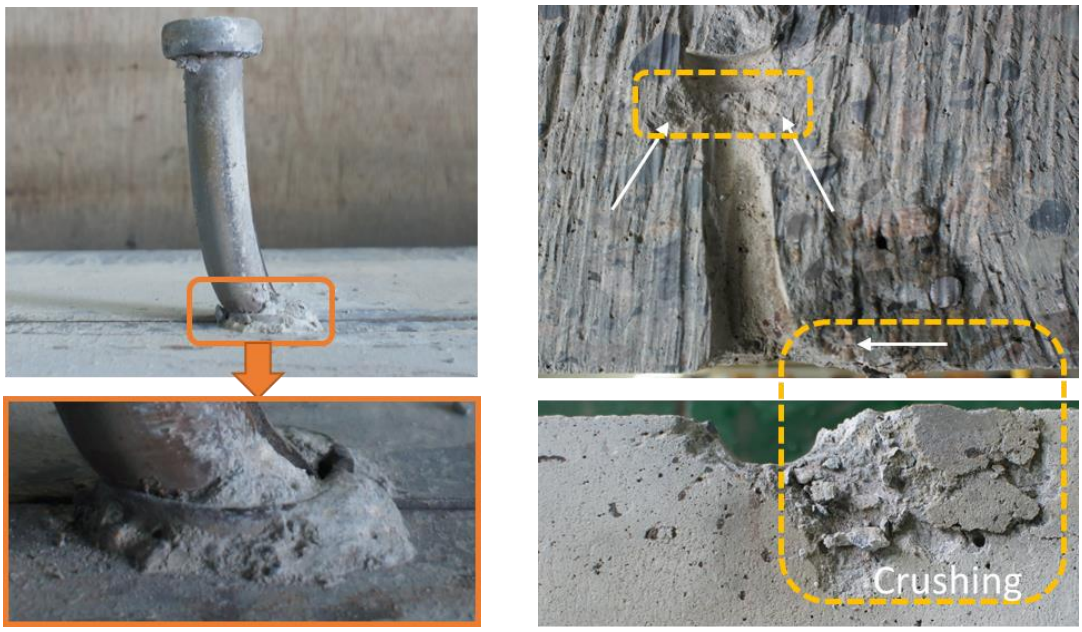

(a) Around the shear stud (b) Around the surrounding concrete

Figure 4-17. Stud and surrounding concrete deformation at ULS

Transverse deck specimen

Two specimens (T1-1 and T1-2) have through-deck-welded shear studs on a steel flange via a 1.2-mm-thick deck which was placed in the transverse direction to the steel flange. A shear resistance of 129 kN was measured, as plotted in Fig. 4-18. Although the magnitude of slip at the maximum load was different, both experiments showed an analogous capacity of the shear connection. As the concrete pull-out failure determined the structural capacity in both of the push-out tests, this difference in the slip pattern is understood to be induced by the heterogeneous characteristics of concrete. After completing the experiments, the propagation of a transverse crack was observed on the backside of a concrete slab in T1-1, whereas the other concrete slab in T1-1 and both concrete slabs in T1-2 did not show cracking.

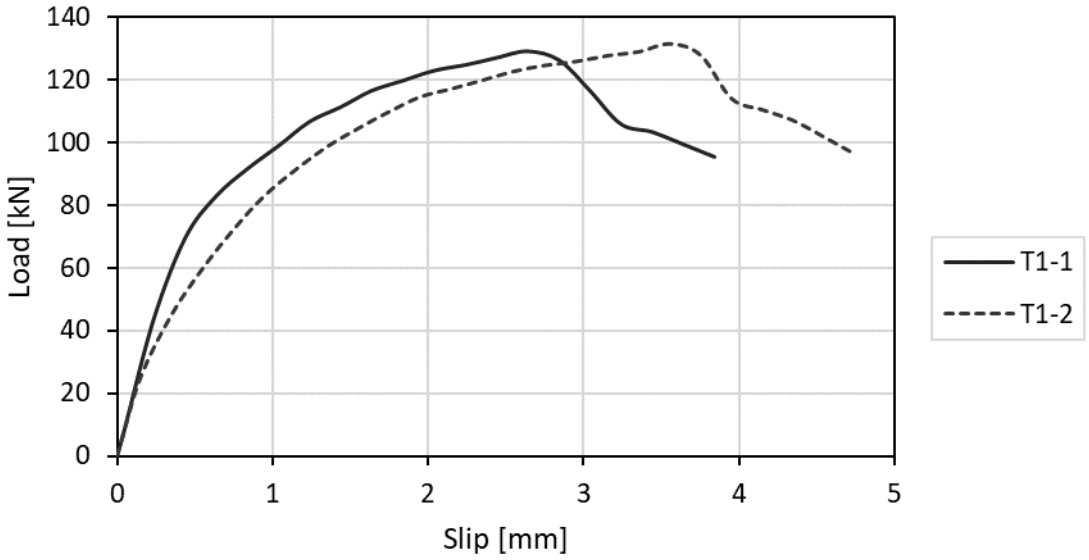

Figure 4-18. Load-slip curve of 1.2-mm through-deck-welded specimen at ULS

Two specimens (T2-1 and T2-2) were also fabricated by direct stud welding on the steel flange incorporating a 0.9-mm-thick deck with a 34-mm-diameter hole at the stud location. An average shear resistance of 86.5 kN was obtained with the concrete pull-out failure, as presented in Fig. 4-19. In comparison to T1-1 and T1-2, the capacity of the shear connection

in T2-1 and T2-2 reduces by 33 % owing to differences in the concrete strength, deck thickness, and stud welding method.

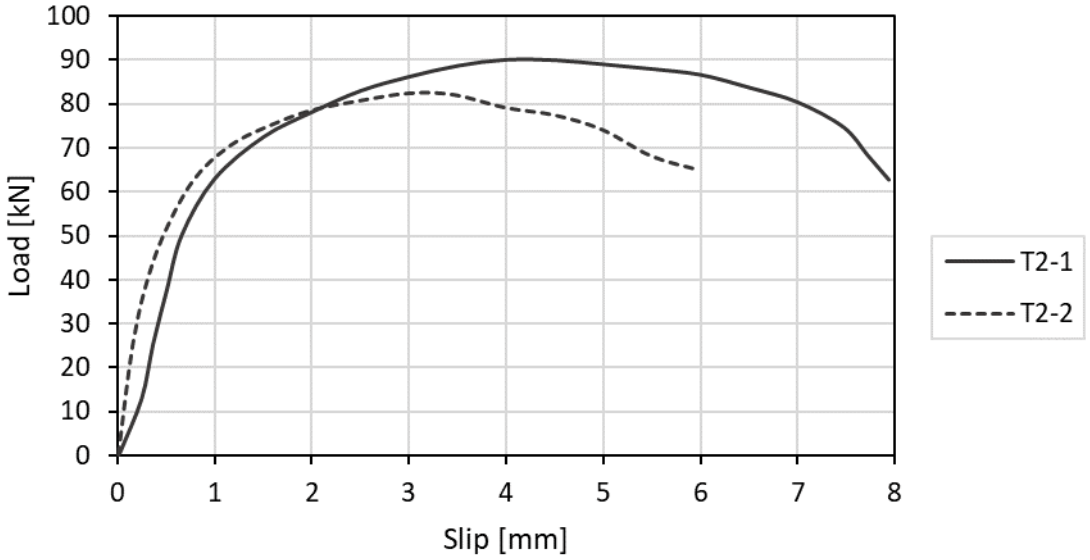

Figure 4-19. Load-slip curve of 0.9-mm through-hole-welded specimen at ULS

Concrete cracking in an area surrounding the shear stud was observed when examining the waterjet-cut surface, as shown in Fig. 4-20. Shear stud overturning caused by a moment at the stud root leads to the formation of a concrete crack in the rib. The crack starts from the deck stiffener to the deck shoulder via the head of the shear stud, which means that the size of the deck stiffener can be an influencing parameter in a composite beam employing a modern trapezoidal deck. This increases the concrete cracking surface compared to a deck without a deck stiffener. The deck stiffener and deck shoulder were deformed in the downward direction because of the concrete failure surface and moment at the stud root. A distinct crack was observed at the lower level rib (around stud 2 in Fig. 4-20), which implies that the shear stud withstands a higher load by virtue of the configuration of the push-out test setup; in the same manner, the lower-level stud fails earlier than the upper-level stud in the solid slab specimen. Unlike the push-out test of the solid slab specimen, a large deformation of the stud shank was not observed, because the failure is induced not by the stud but by the concrete crack in a rib.

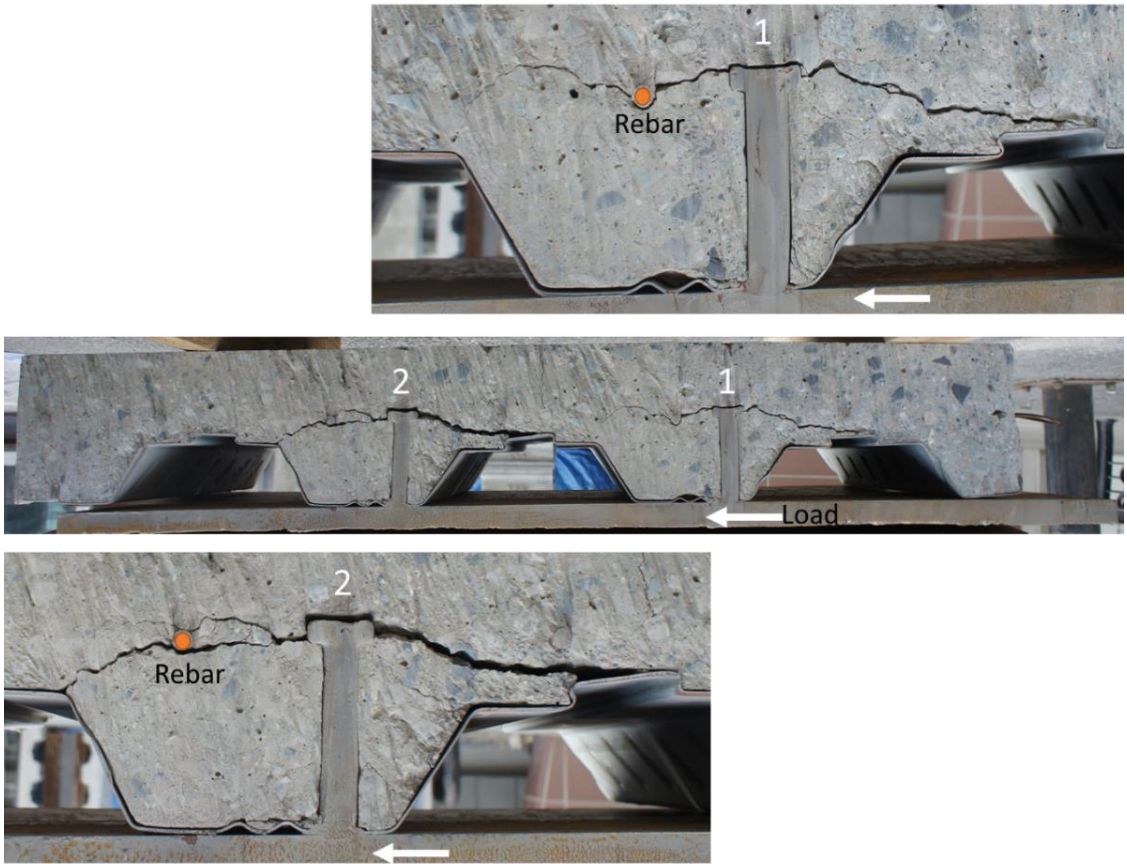

Figure 4-20. Cutting plane of the transverse deck specimen

4.5.3. Structural capacity of shear connections at FLS

Six high-temperature push-out tests were carried out with different slab types, stud welding methods, and deck thickness under the three-sided exposure to the ISO 834 standard fire. A loading scenario was designed to complete inducing a structural load, prior to applying a fire load. The load-bearing capacity with respect to the fire exposure time and its corresponding failure modes are discussed in this section.

Solid slab specimen

Applying the structural load of 162 kN (40.5 kN per shear stud), the stud shearing failure was observed when exposed to 80 min of the ISO 834 standard fire, as plotted in Fig. 4-21. A slip starts to increase in the adverse direction against the imposed loading up to 4 *mm*, because

the induced structural loading was smaller than the generated fire loading caused by the thermal expansion of the steel and concrete sections at a given temperature.

The thermal degradation of the steel and concrete material causes a slip direction change beyond 60 min of heating. Furthermore, the slip increased rapidly when a fracture occurred, because the shearing of a thermally degraded stud material was the cause of the failure. As shown in Fig. 4-22(a), the shearing occurred at the bottom of the weld collar, and stud shank deformation could only be found near the stud root area; whereas the shearing observed right above the weld collar at ULS. This indicates that the strength at the stud root was significantly reduced compared to the rest of the stud. When a fire load was applied to the push-out specimen, the steel beam exhibited the highest temperature, and the temperature reduced in the concrete slab direction. Considering this temperature gradient, the temperature at the stud root was higher than the rest of the stud. As a result, shearing occurred at the stud root area. The crushed concrete area was also reduced according to the deformed shape of the shear stud, as shown in Fig. 4-22(b). Relatively small concrete compaction and crushing were found around the shear stud in the loading direction in comparison to the experiment at ULS.

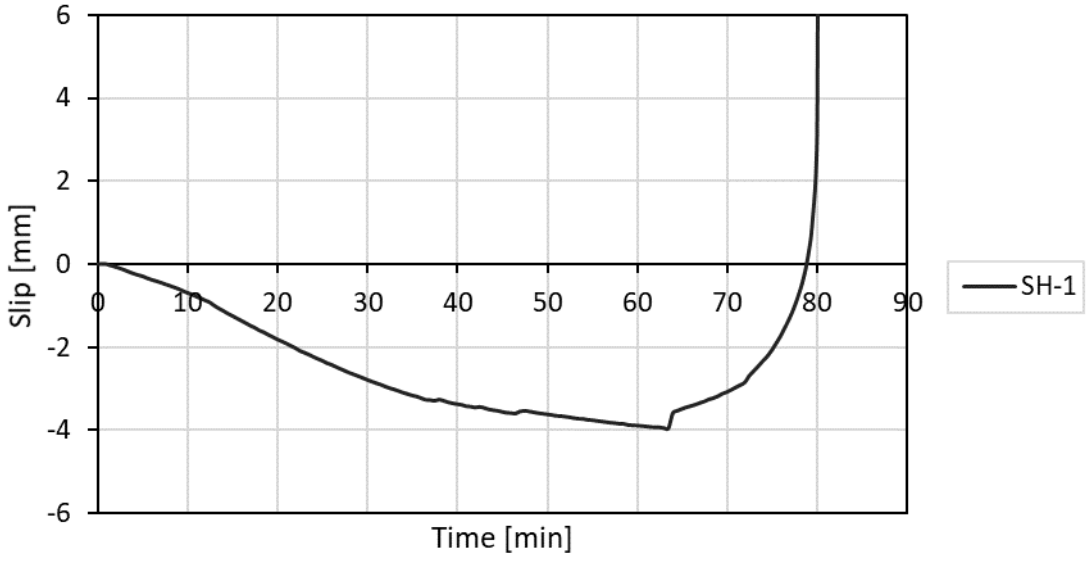

Figure 4-21. Load-slip curve of the solid slab specimen at FLS

Although stud shearing is the failure mode of the solid slab specimen, regardless of temperature, the stud curvature and shearing location were different. Considerable differences in the deformed shape of the shear stud and concrete crushed area were found by comparing the cutting planes in Fig. 4-17 and 4-22.

(a) Around the shear stud (b) Around the surrounding concrete

Figure 4-22. Stud and surrounding concrete deformation at FLS

Transverse deck specimen

The 1.2-mm through-deck-welded specimen, subjected to a constant structural load of 81 kN (20.3 kN per shear stud), was heated in accordance with the ISO 834 standard fire. A negative slip was also observed during the heating process. It consistently increases for 40 min, and gradually decreases from 40 to 80 min of heating, as plotted in Fig. 4-23. The slip value rapidly changes from negative to positive directions at 81 min of heating, accompanied by the stud shearing failure. As a result, the steel beam and concrete slab were totally detached, which caused a loud bang sound because the underside of the steel beam hits the floor. The observed shearing location was at the bottom of the stud weld collar at the upper-level stud (stud 1 in Fig. 4-24), whereas it was at the steel flange at the lower-level stud (stud 2 in Fig. 4-24).

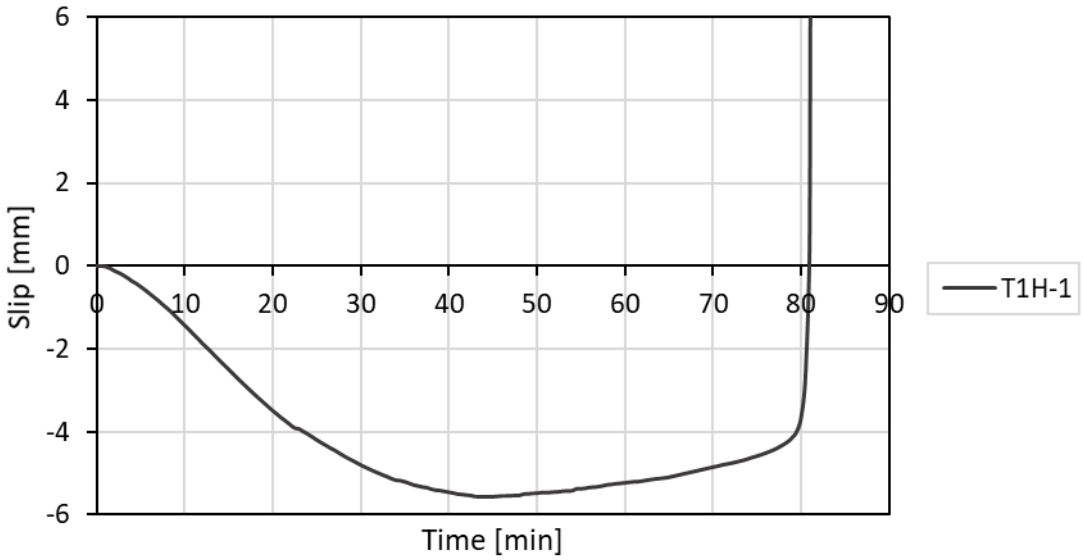

Figure 4-23. Time-slip curve of the transverse deck specimen at FLS (1.2 mm deck)

(a) After the experiment (b) Stud shearing failure

Figure 4-24. Failure of the 1.2-mm through-deck-welded specimen at FLS

When the shear stud was directly welded to a steel flange incorporating the 0.9-mm-thick deck with a 34-mm-diameter hole, the identical failure mode of the stud shearing was observed at the high-temperature push-out test. This indicates that the strength of the shear stud is a key parameter in determining the capacity of the shear connection at FLS. The fire resistance time was affected by the thermal degradation of the steel material and the imposed load. The amount of the negative slip was determined by the equilibrium of the imposed structural load and the thermal load caused by the temperature difference. Therefore, under the lower structural loading, a longer fire resistance period and higher negative slip were found, as plotted in Fig. 4-25.

The stud root sheared after approximately 77 min of the heating process under the imposed static loading of 121.6 kN (30.4 kN per shear stud); both experiments (T2H-1, T2H-2) show a comparable slip–time behaviour. The same failure mode of the stud shearing was observed when applying a higher loading of 182.4 N (45.6 kN per shear stud). The T2H-3 and T2H-4 specimens show a deviation of approximately 8 min in the fire resistance time owing to the extent of the concrete crushing. The T2H-3 specimen shows a relatively higher concrete damage after finishing the push-out test. Severe deformation at the stud root area and concrete crushing were shown simultaneously.

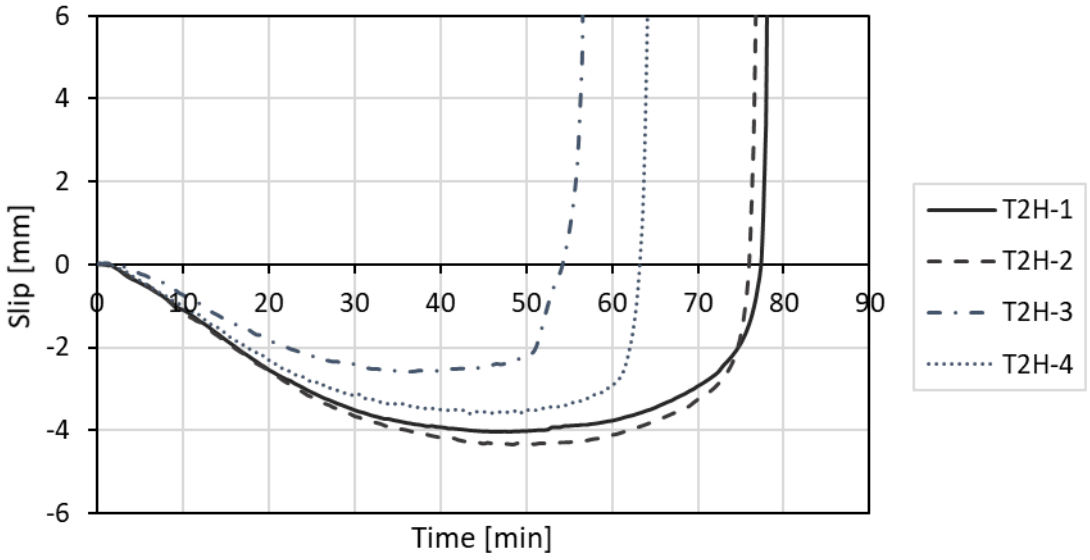

Figure 4-25. Time-slip curve of the transverse deck specimen at FLS (0.9 mm deck)

In terms of the failure mode, stud shearing was observed at FLS, whereas concrete pull-out failure was found at ULS. Because the stud root area exhibits a higher temperature compared to the surrounding concrete considering the heat path and the thermal conductivities of steel and concrete. A higher thermal degradation of the steel material section is the cause of the failure mode change. As shown in Fig. 4-26(b), half of the stud shank was sheared because the stud shearing was accompanied with a concrete crushing; the other shear stud in the same specimen was utterly detached. When a smaller load was applied (T2H-1, T2H-2), all the shear studs embedded in the specimen were completely sheared off, which is the same failure mechanism as for the solid slab specimen. The steel flange and bottom of the stud weld collar were sheared, as presented in Fig. 4-26(a). Therefore, it can be concluded that the primary cause of the failure is the thermal degradation of the steel materials (shear stud and steel flange) at high temperature, regardless of the slab type.

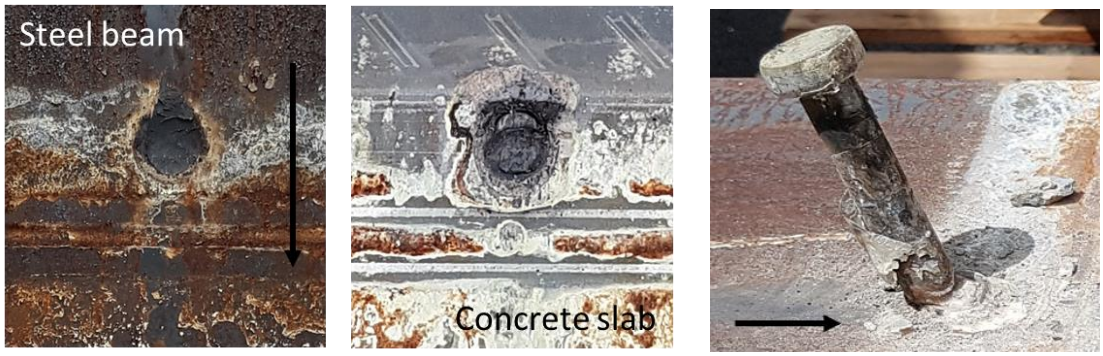

(a) Specimen T2H-1 (b) Specimen T2H-3

Figure 4-26. Failure of the 0.9-mm through-hole-welded specimen at FLS

4.5.4. Analytical works

The obtained shear resistance was compared with several design guidances as presented in Table 4-4. EC4-1-1 (2009) gives a conservative estimation regardless of the slab type, whereas AISC 360-10 (2010) predicts an overestimated value in the 0.9-mm deck specimen because it does not consider the deck thickness and stud welding method when calculating the shear resistance. In general, the analytical calculation of EC4-1-1 (2009) provides a conservative estimation, because scattering factors are included in the characteristic strength formula to include deviations among the available experimental data based on the statistical study of Roik *et al*. (1989). Therefore, the deck thickness and stud welding method should be examined when calculating the shear resistance in the transverse deck application at ULS.

Table 4-4 Comparisons of the shear resistance at ULS

Specimen	P_e [*kN*]	$P_{e,k}$ [*kN*]	P_{EC4} [*kN*]	P_{AISC} [*kN*]	$P_{e,k}$ $/P_{EC4}$	$P_{e,k}$ $/P_{AISC}$	Failure mode
S-1	135	121.5	107.5	100.8	1.13	1.2	Stud shearing
S-2	145						
T1-1	130	115.2	102	100.8	1.13	1.14	Concrete pull-out
T1-2	128						
T2-1	90	74.7	68	100.8	1.1	0.74	Concrete pull-out
T2-2	83						

EC4-1-2 (2014) provides the shear resistance in a fire for solid and trapezoidal deck composite beams by incorporating a strength reduction factor to the shear resistance at ULS. Table 4-5 presents the empirical reduction parameter obtained from the high-temperature push-out tests compared with the Eurocode guidance. A uniform prediction can be obtained at ULS, whereas irregular strength reductions are shown for the FLS. The more conservative estimation is achieved when the shear resistance at ULS is comparatively small, because the Eurocode uses the same deck reduction factor (k_t) regardless of the cause of the failure, and the thermal degradation is directly applied to the shear resistance obtained at ULS.

Therefore, the analytical calculation of the resistance reduction shows a difference of more than a factor of 2 in the 0.9-mm through-hole-welded specimen (T2H specimens).

Table 4-5. Comparisons of the shear resistance at FLS

Specimen	$P_{e\theta}$ [*kN*]	Failure time [*min*]	Stud temp.[1] [℃]	$P_{e\theta}/P_e$[2]	$P_{k\theta,EC4}/P_{k,EC4}$[3]
SH-1	40.5	80	687.2	0.29	0.21
T1H-1	20.3	81	761.3	0.16	0.13
T2H-1	30.4	78.1	743.4	0.35	0.14
T2H-2	30.4	76.8	736.9	0.35	0.15
T2H-3	45.6	56.6	677.1	0.53	0.23
T2H-4	45.6	64.1	691.8	0.53	0.20

[1]92% of the flange temperature is used based on the thermal analysis
[2]average value of the shear resistance at ULS
[3]according to the stud shearing failure of the EC4-1-2 (2014); Eq. 2-26 in Chapter 2

4.6. Discussion

4.6.1. Temperature distribution

The stud temperature at the shearing location is a critical parameter in determining the shear resistance, especially when the failure mode is stud shearing. Zhao and Kruppa (1993) experimentally demonstrated that the temperature ratio of the stud root to steel flange does not exceed 80 %. The ratio decreases to as low as 40 % at the beginning of the experiment, and gradually increases as the flange temperature rises. However, a higher temperature ratio of 90 % was observed through the experiments conducted for this thesis, as presented in Section 4.5.1; in particular, the measured temperatures are illustrated in Fig. 4-15. This difference was induced by differences in the experimental conditions, such as the type of furnace, heating method, and specimen configuration. Zhao and Kruppa (1993)

induced a hot gas through the underside of the push-out test specimen, whereas both concave areas at the side sections of the specimen were heated in the present experiment. Although the gas temperature followed the ISO 834 standard fire, the heat transfer from the electric furnace to the steel section was different, owing to the shadow effect, in comparison with the experimental conditions of Zhao and Kruppa (1993). Various temperature ratios were also reported in the existing literature. According to the experiment conducted by Choi *et al*. (2009), the ratio was monitored in the range of 80 % to 83 %, and the lowest value of 77 % was recorded during the initial stage of heating. Dara (2015) carried out a modified push-out test by placing the specimen into a customised electric furnace, as shown in Fig. 2-5(b). The temperature ratio was observed as approximately 90–95 %. With respect to these results, the temperature ratio is significantly influenced by the heating rate and the configuration of the test specimen according to the heat source. The temperature ratio becomes a critical parameter when the stud temperature reaches its maximum. This reduces the strength of the shear stud, and the stud shearing failure occurs.

The web part of the steel beam shows the same temperature profile, regardless of the specimen type, whereas a different temperature profile was observed at the flange part of the steel beam during the heating process. The flange temperature of the trapezoidal deck specimen showed a higher value than the solid slab specimen, as plotted in Fig. 4-27. The maximum difference of 160 ℃ was measured at 26 min into the heating process, and the temperature differences reduced to 50 ℃ at 60 min. Although the identical heating scenario was applied to the specimens, the temperature at the flange part was different owing to the shape of the contact layer between the steel beam and the concrete slab. In the case of the solid slab specimen, convective and radiative heat is applied to the underside of the flange, and heat conduction occurs from the top side of the flange to the bottom of the concrete slab. On the contrary, convective and radiative heat is applied through the underside and part of the top side of the flange in the trapezoidal deck specimen. The heat conduction area between the flange and the concrete slab is also relatively small. The contact area between the top fibre of the flange and the profiled concrete slab is only 46 % of that of the solid slab specimen. In other words, the radiative and convective heat transfers occur through the voids in the trapezoidal specimen.

These different heating conditions lead to dissimilar temperature profiles at the steel flange, depending on the slab type, as shown in Fig. 4-27. The stud temperature is profoundly influential on the shear resistance, especially when the failure mode is stud shearing. The temperature ratio of the stud to the steel flange was 90 % in the experiment with the solid slab specimen. An equal temperature ratio was observed in the transverse deck specimen by numerical modelling, as explained in Chapter 5. It is concluded that the shear stud embedded in the transverse deck slab exhibits a higher temperature than that in the solid slab when exposed to the same heating conditions.

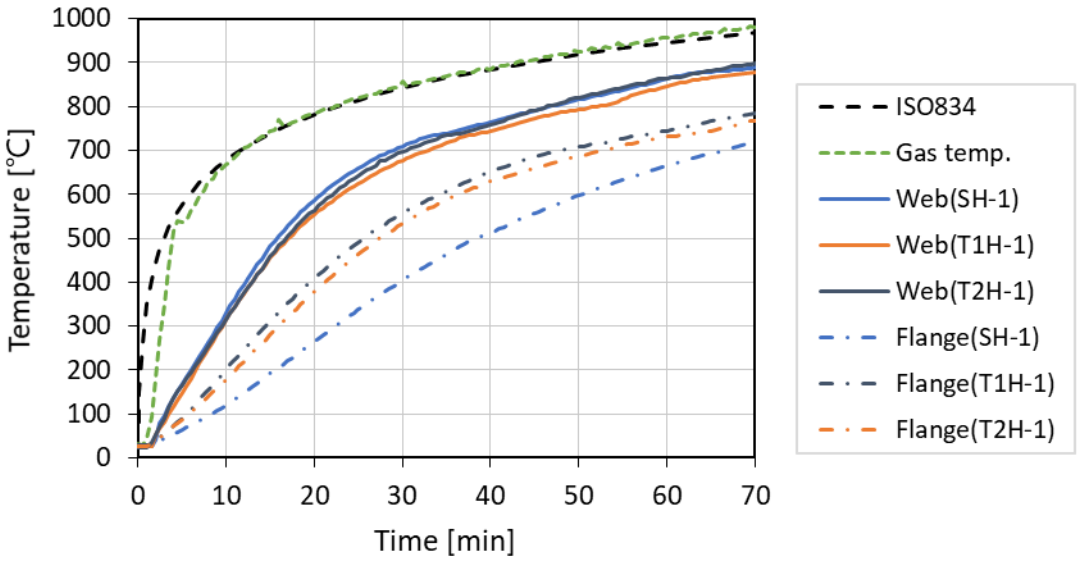

Figure 4-27. Comparison of the temperature with different types of slab

4.6.2. Structural capacity of shear connection

A failure mode change from concrete pull-out to stud shearing was found in the transverse deck specimens as the temperature rose. Comparing with existing experimental research (Chen *et al.*, 2015; Yasuda *et al.*, 2008), the identical phenomenon is also observed, as plotted in Fig. 4-28; the empty symbols indicate concrete-dominated failure and the filled symbols represent stud shearing failure. When the shear resistance at high temperature was compared with the analytical prediction of the stud shearing failure according to EC4-1-2

(2014) without adopting the transverse deck reduction factor (k_t), it gives a strong correlation as the failure mode is the stud shearing. The cause of the stud shearing failure is an excessive load at the stud root area, which is higher than the stud ultimate strength and smaller than the strength of the surrounding concrete at a given temperature. Although the shear resistances at ULS are considerably different with respect to the deck geometry and stud welding method, the shear resistance under high temperatures converges to the solid slab design guidance of EC4-1-2 (2014), regardless of the slab type. Considering this experimental investigation, the shear resistance calculation method of the solid slab specimen can be used for the transverse deck application when the stud shearing failure occurs at high temperature.

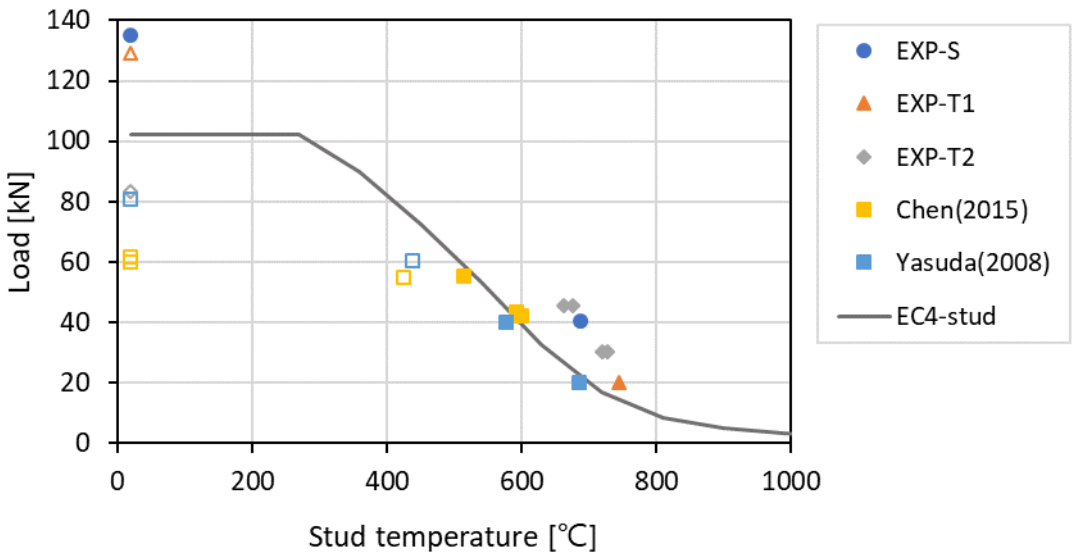

Figure 4-28. Comparison of the Eurocode guidance with experimental data

4.7. Conclusions

The performance of the headed shear stud embedded in a transverse deck and solid slab at both ULS and FLS has been investigated with regard to the slab type, deck thickness, and stud welding method. Twelve push-out tests were conducted using a customised electric furnace which successfully simulates the ISO 834 standard fire. A relatively higher flange temperature was observed in the transverse deck specimen compared to the solid slab specimen, whereas an analogous value was measured at the web part. The thermal degradation of the stud root area varied depending on the slab type under the same heating condition, which indicates that employing a transverse deck is more vulnerable to fire than adopting a solid slab, as the failure mode is stud shearing.

The stud shearing failure was observed in the solid slab specimen regardless of the temperature, whereas the failure mode changed from the concrete pull-out to the stud shearing in the transverse deck specimen as the temperature rose. When the stud shearing failure occurs in a fire, the temperature of the stud root area is the critical parameter in determining the shear resistance, regardless of the slab type. Since the SRF for stud shearing failure in EC4-1-2 (2014) is based on experiments with solid slab specimens, it provides an approximation of the degraded load-bearing capacity of the shear stud embedded in transverse deck slabs. Although the deck reduction factor (k_t) should be added in shear resistance calculation for transverse deck applications, it causes a highly conservative estimation at FLS when the expected failure mode is the stud shearing. Therefore, the shear resistance calculation method according to EC4-1-2 (2014) needs to be modified considering the failure mode change.

Chapter 5
DEVELOPMENT OF FINITE ELEMENT MODEL

5.1. Introduction

A three-dimensional thermomechanical finite element model has been developed using the commercial software Abaqus to investigate the shear stud behaviour in a fire. The temperature distribution and structural performance at ULS were analysed and verified separately. Then, the developed models were combined to evaluate the capacity of shear connections at FLS. This was also validated against the high-temperature experimental results. The developed model considered concrete slab types and decking parameters such as thickness, welding method, and stud location. A detailed procedure for developing the numerical model is described herein.

5.2. Thermal model

5.2.1. Thermal parameters

The thermal conductivity affects the temperature distribution in a medium, such as a steel beam and concrete slab in high-temperature push-out tests. The conductive heat flux is determined by the thermal conductivity and temperature gradient. The thermal conductivity of steel decreases as the temperature increases, because activated atoms and molecules interfere with transferring heat energy. The thermal conductivity of concrete is specified by a range using an upper and lower limit. The lower limit value was adopted in

the thermal model according to the recommendation of EC2-1-2 (2008), because it gives more realistic temperature distributions. The thermal conductivities of steel and concrete are plotted in Fig. 5-1 and 5-2 which were taken from EC4-1-2 (2014).

The specific heat of a material is the required energy per unit mass of the material to increase its temperature by one degree. EC4-1-2 (2014) provides the specific heats of steel and concrete, and their values were adopted in the thermal analysis. The specific heat of steel shows a rapid increase at approximately 735 ℃ owing to a metallurgical change, as presented in Fig. 5-3. The specific heat of concrete, shown in Fig. 5-4, was adopted without considering a rapid change at approximately 115 ℃ caused by evaporation of water in the concrete. The moisture content of concrete was expressed using the LATENT HEAT option in Abaqus. The moisture content of the concrete slab was taken as 5 % to consider water dispersion from the backside of the concrete slab during the heating process. As the latent heat of the water vapour is 2.26 MJ/kg, an overall evaporation energy of 11.3×10^4 J/kg was assumed to apply between 95 °C and 105 °C for a stable calculation.

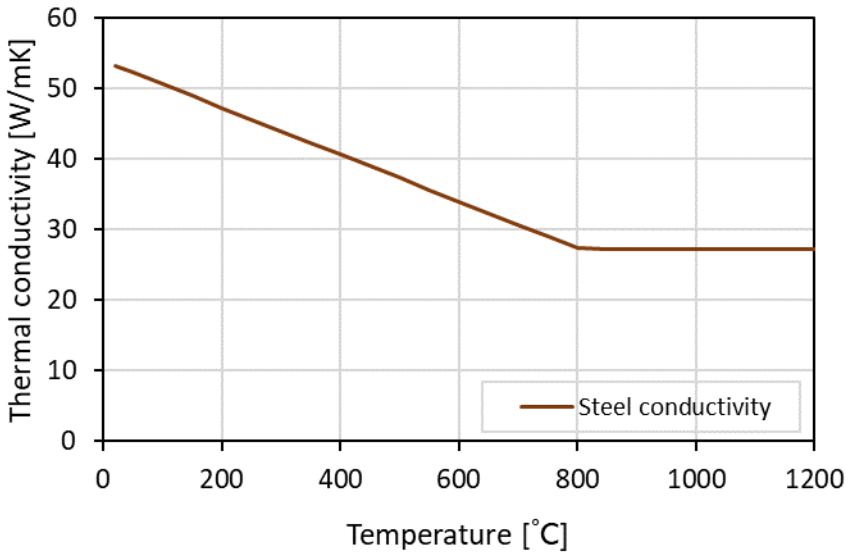

Figure 5-1. Thermal conductivity of steel

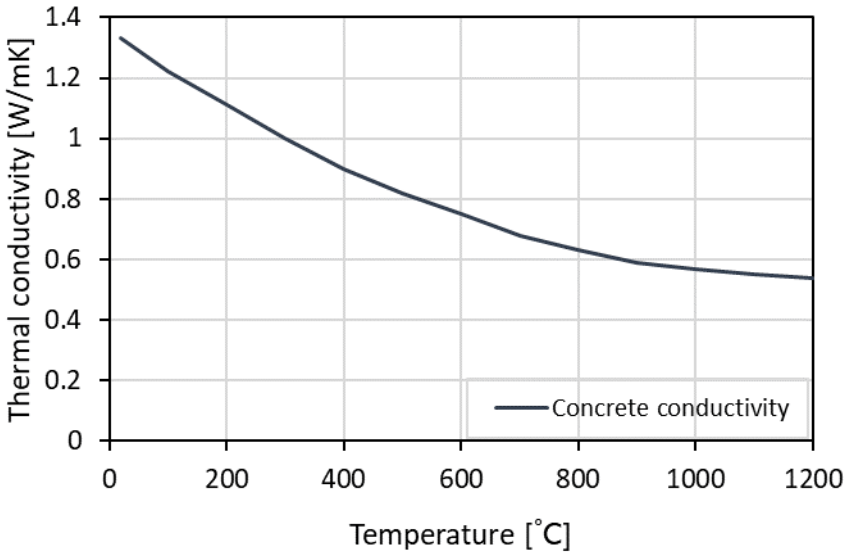

Figure 5-2. Thermal conductivity of concrete

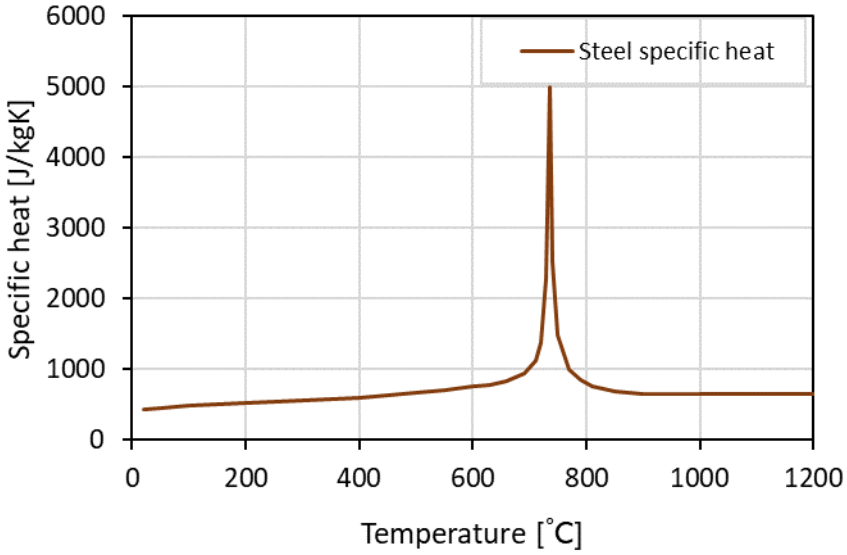

Figure 5-3. Specific heat of steel

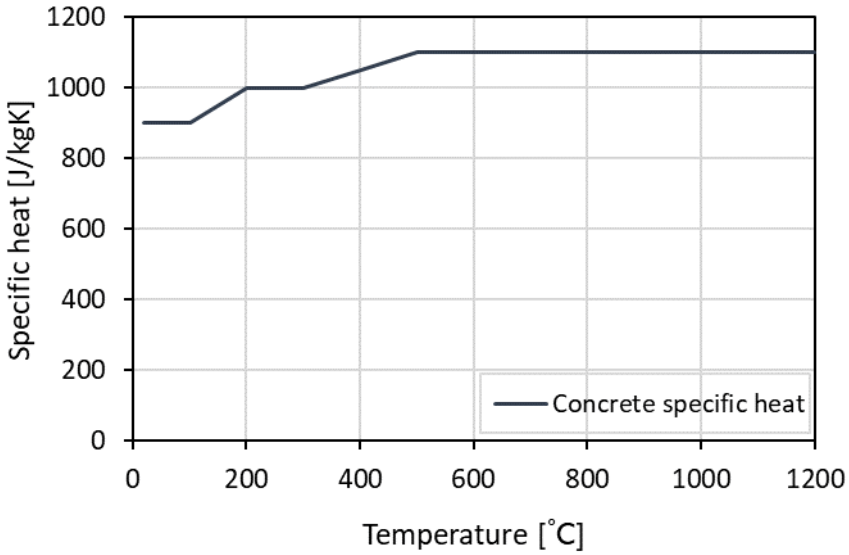

Figure 5-4. Specific heat of concrete

The material density is required to calculate the mass and internal energy during the thermal analysis. The steel density can be regarded as a constant value without regard to temperature, because it is composed of a single material. The uniform density of 7850 kg/m^3 was used for the steel sections of the push-out test specimen. Concrete density reduces with increasing temperature due to the evaporation of moisture and cement paste. The concrete density of 2400 kg/m^3 was used under ambient conditions, and a linearly decreasing function referenced from EC2-1-2 (2008) was adopted at high temperatures, as plotted in Fig. 5-5.

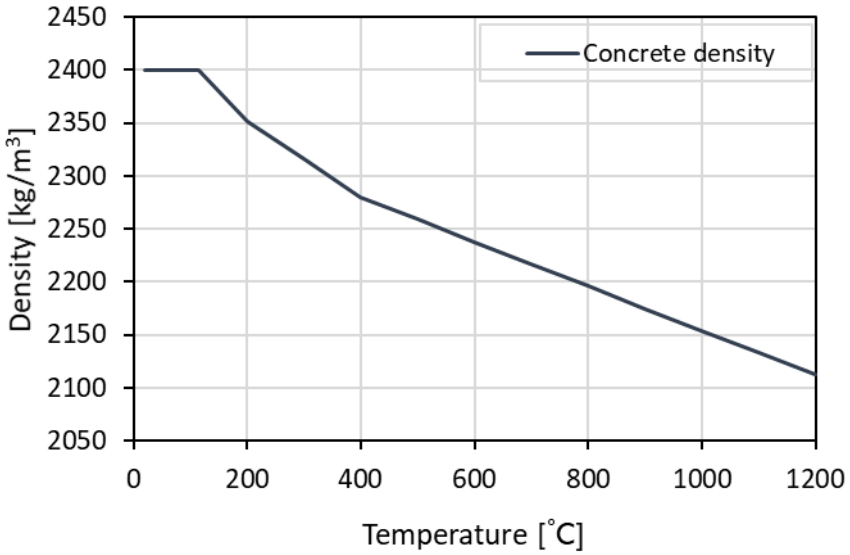

Figure 5-5. Normal-weight concrete density

A push-out test specimen has two primary thermal contact layers. One is the interface between the steel beam and concrete slab (or trapezoidal deck), and the other is the boundary between the shear stud and the surrounding concrete: layers 1 and 2 in Fig. 5-6. The heat from the electric furnace is directly applied to the web, underside of the steel beam flange, and adjacent surface of the concrete slab. This thermal energy is transferred by convection and radiation, and it is delivered through the materials and thermal contact surfaces by conduction.

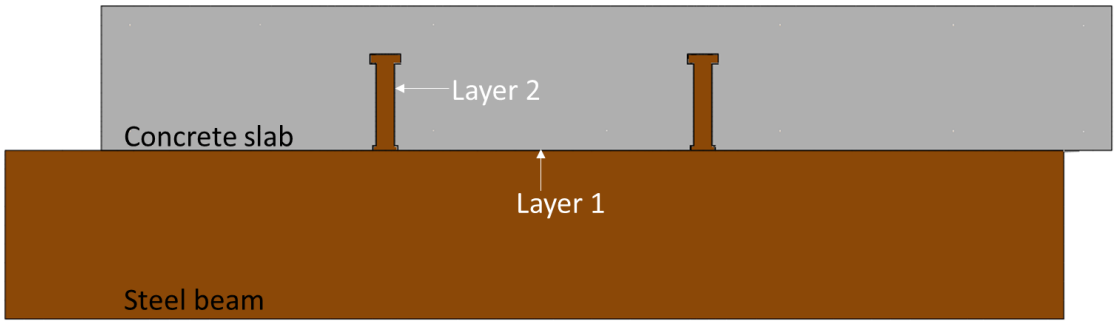

Figure 5-6. Thermal contact surfaces of the push-out test specimen

It is possible to generate air gaps at the interface between the steel and concrete sections in the case of a fire (Ghojel, 2004; Ding and Wang, 2008) because the steel and concrete have different coefficients of thermal expansion. Moisture evaporation and spalling of concrete also facilitate the generation of voids at the boundary. As a result, heat transfer is impeded at the contact layers. Ghojel (2004) carried out an experimental and numerical study to investigate the thermal conductance at a steel and concrete interface using a concrete-filled tubular (CFT) column. The thermal conductance of 160 $\mathrm{W/m^2K}$ was reported at 25 ℃ using a mean value of the experimental study, which shows a large range of tolerance: 40–225 $\mathrm{W/m^2K}$ at 25 ℃. It decreases as the temperature rises, and it was also highly affected by the geometry of the test specimen (circle or square), loading method, and concrete spalling. Ding and Wang (2008) modelled the temperature distribution of a CFT column using the thermal conductances of 100 and 200 $\mathrm{W/m^2K}$. The calculated temperature profile showed a strong correlation with the experimental data when using 100 $\mathrm{W/m^2K}$. They argued that the thermal conductance between a steel and concrete should be determined by comparison with experimental data because it is difficult to define an exact value owing to heterogeneous properties of concrete and irregular conditions at the contact layers. Maraveas *et al.* (2012) conducted temperature modelling of composite beams by assuming a perfect thermal contact at the steel and concrete boundary. Although a higher thermal conductance was used, it shows an analogous result compared to experimental data. Considering various existing studies, the thermal conductance at a contact layer is highly affected by the experimental conditions, and it is necessary to verify modelling data against experimental data. In this study, different thermal conductances within the abovementioned range were used depending on the specimen type, because their concrete strengths and curing conditions were different.

Radiative heat transfer is proportional to the configuration factor and the resultant emissivity. The surface emissivity of a material indicates its ability to emit thermal radiation. In the case of the unprotected steel beam (H-beam), the resultant emissivity has a range of 0.2 to 0.7 (Purkiss, 2013; EC4-1-2, 2014). The emissivity value of a fire and corresponding steel surface varies with respect to the geometry and induced heat flux (Pettersson *et al*., 1976). EC3-1-2 (2009) recommends the emissivity of a fire and steel section as 1 and 0.7, whereas EC1-1-2 (2013) gives the emissivity of steel as 0.8 for a conservative design. A

former EC3-1-2 (2001) suggests the emissivity of fire and steel section as 0.8, which gives a resultant emissivity of 0.64. Pettersson *et al*. (1976) reported the emissivity of a fire and a steel structure as 0.85 and 0.8 based on their experimental data when the steel section was fully engulfed in the fire. This gives a resultant emissivity of 0.7. The American Institute of Steel Construction (AISC 360-10, 2010) recommends the resultant emissivity of the steel beam that supports a concrete slab on the top flange as 0.5 and 0.7 according to the aspect ratio of the steel beam. When the flange width-to-beam depth ratio is smaller than 0.5, the recommended resultant emissivity is 0.7. Otherwise, it is 0.5 for beams of aspect ratio greater than or equal to 0.5, because the widened flange interferes with radiative heat from a fire. An experimental study regarding the beam aspect ratio and resultant emissivity shows the same trend as the AISC code of guidance (Pettersson *et al*., 1976), because a broader concave region interferes with thermal radiation. Considering the code of guidance and experimental data, the resultant emissivity of the steel beam shows a range of 0.5 to 0.7. Whichever value is used, a verification against experimental data is needed (Purkiss, 2013). In this model, the resultant emissivity of 0.7 was used according to Pettersson *et al*. (1976) and EC3-1-2 (2009), and a configuration factor of each surface was considered when calculating the radiative heat flux.

The configuration factor is used to compensate for the geometrical effect between the electric furnace and the receiving surface. It was calculated at each surface in accordance with the high-temperature push-out test setup, as shown in Fig. 5-7. Assuming that the steel beam is infinitely long compared to the diameter of the stud shank to simplify the calculation, the configuration factor was calculated using parallel and orthogonal arrangements. It can be estimated as follows (Siegel and Howell, 2002):

$$\Phi_{fire-surface1} = 0.5\left(1 + H - \sqrt{1 + H^2}\right)$$
$$\Phi_{fire-surface2} = \sqrt{1 + H^2} - H \qquad (5\text{-}1)$$

where $H = B/W$: ratio of the breadth (B) to the width (W)

The width (W) and breadth (B) in Fig. 5-7 is 350 mm and 365.5 mm, respectively. The thickness of the steel flange is 19 mm. The calculated configuration factor for Surface 1 and

2 are 0.299 and 0.368. The obtained configuration factor with the resultant emissivity of 0.7 was incorporated into the thermal model, and it was slightly modified comparing the temperature distributions of experimental data.

A convection coefficient determines the amount of the heat flux caused by the movement of hot gas. At the initial stage of a fire, convective heat flux profoundly affects the increasing temperature. Its effects are reduced with the growth of the fire, whereas the radiative effects increase. EC4-1-2 (2014) recommends a convection coefficient of 25 and 9 W/m^2K when exposed to the ISO 834 standard fire and ambient, respectively. The recommended value was adopted for the thermal analysis, as the gas temperature around the push-out test specimen was controlled in accordance with the ISO 834 standard fire.

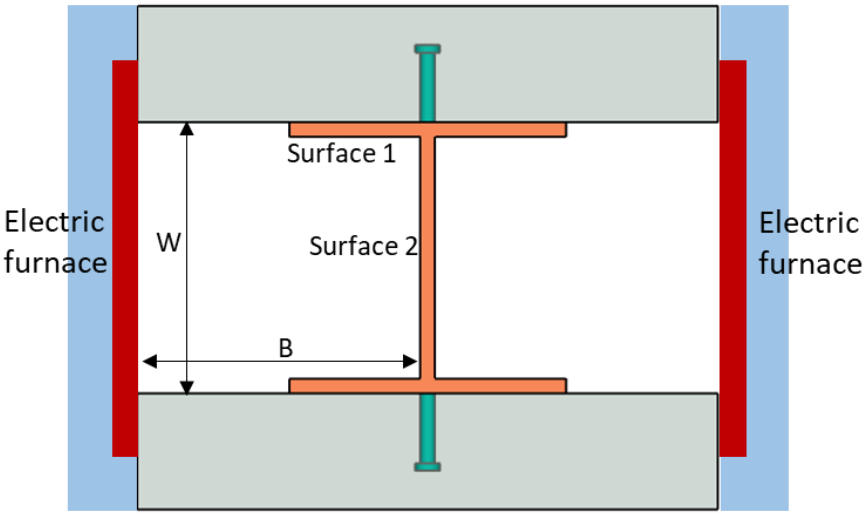

Figure 5-7. Cross-sectional view of the push-out test specimen with electric furnaces

5.2.2. Developing thermal models and verification

An eight-node linear brick element (DC3D8) was selected for the steel beam, concrete slab, and shear stud. A four-node quadrilateral shell element (DS4) and two-node link element (DC1D2) were used for the deck and reinforcement bar. A finer mesh was applied to the shear stud and its surrounding concrete because failure occurs in that area.

Temperature profiles of the solid and transverse deck slab models are presented in Fig. 5-8 when exposed to the ISO 834 standard fire for 60 min. The web part of the steel beam shows the highest temperature, and the temperature decreases along the shear stud in the concrete slab direction. Heat was transferred from the steel beam to the concrete slab via the shear stud. Comparatively higher temperatures can be found at the steel flange in the transverse deck model, because additional convective and radiative heat were applied through the top side of the flange and rib deck.

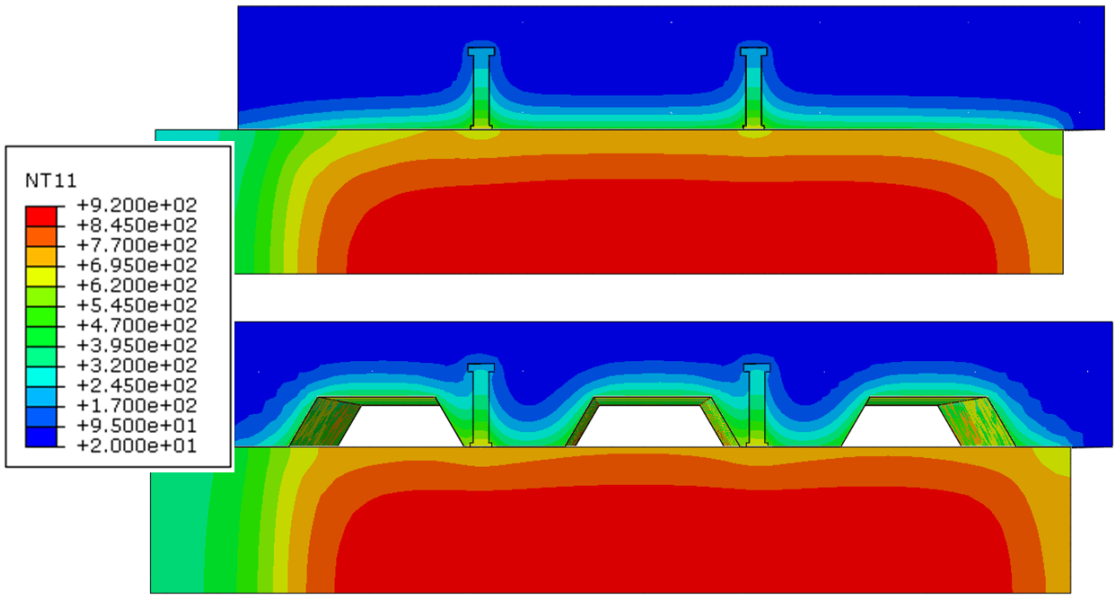

Figure 5-8. Temperature profile at 60 *min* of heating

Three thermal models were developed according to the slab type and stud welding method: a solid slab model (SH), 1.2-mm through-deck-welded model (T1H) and 0.9-mm through-hole-welded model (T2H). The developed numerical models were validated against the experimental data by comparing the web and flange temperature according to the fire elapsed time. Strong correlations are achieved as provided in Fig. 5-9 to 5-11.

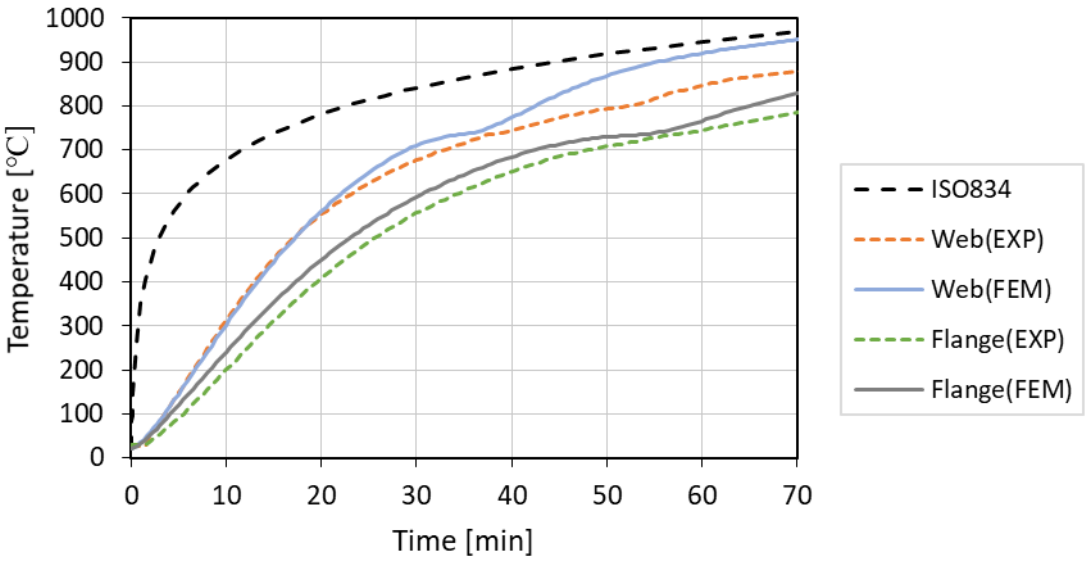

Figure 5-9. Temperature verification of the solid slab model (SH)

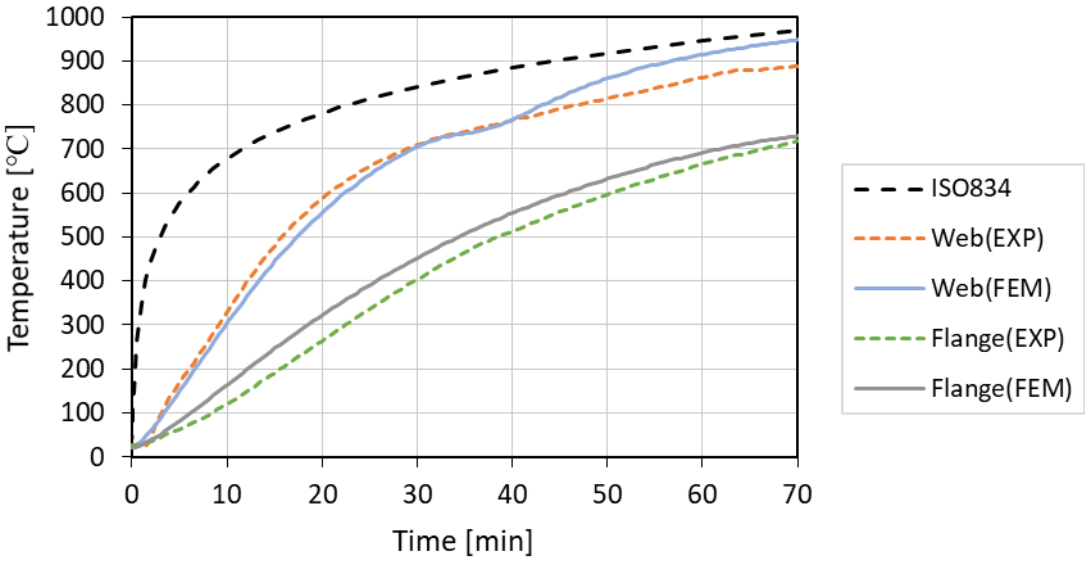

Figure 5-10. Temperature verification of the 1.2-mm through-deck-welded model (T1H)

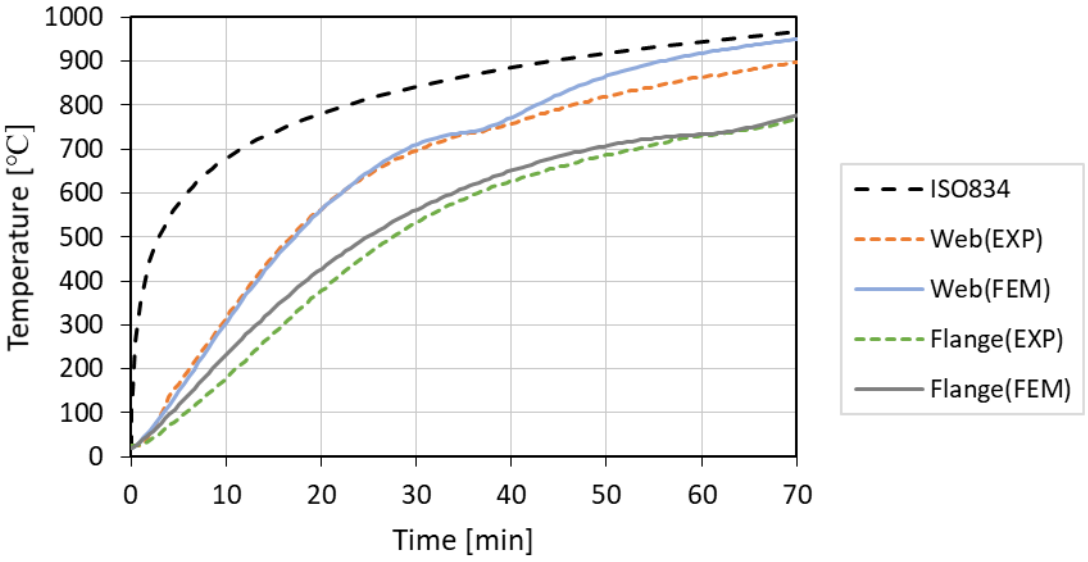

Figure 5-11. Temperature verification of the 0.9-mm through-hole-welded model (T2H)

The stud temperature was collected at 5 mm from the bottom of the shear stud, and the flange temperature was acquired at the bottom side of the beam flange. The temperature ratio between the stud and flange approaches 90 % as the heating time increases. This gave an analogous temperature ratio in comparison to the experimental result, as plotted in Fig. 5-12. The temperature ratio decreased at the beginning of the heating process, because the shear stud was indirectly heated, and the steel flange was directly exposed to the electric furnace. The temperature ratio of the transverse deck model showed a higher drop up to 70 % at the beginning of the heating process, and it continuously increased with the heating time. As presented in Fig. 5-8, the steel flange of the transverse deck model shows a higher temperature at a given heating time, which causes a different temperature ratio depending on the slab type.

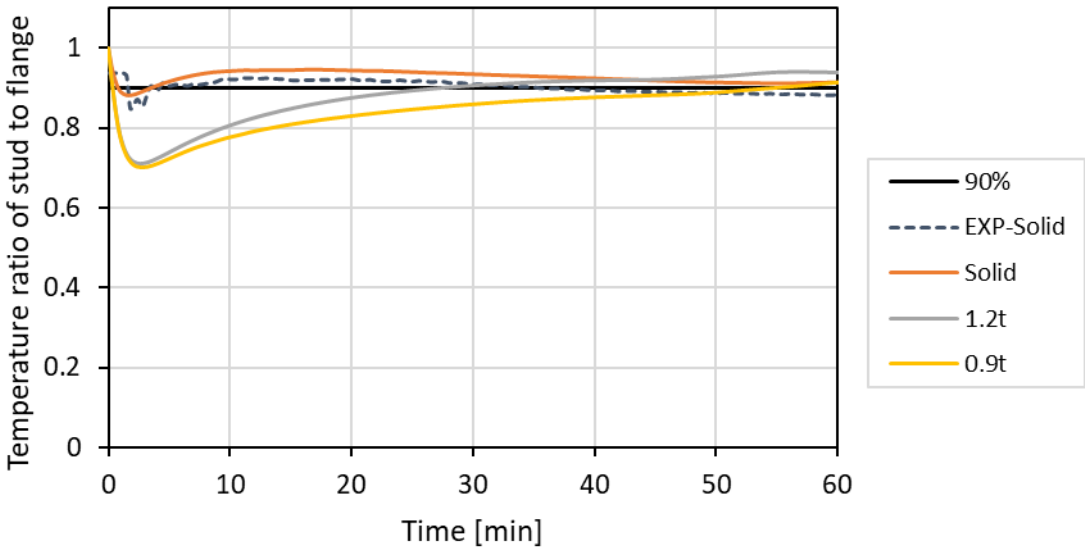

Figure 5-12. Temperature ratio of the stud to flange according to the fire exposure time

5.3. Mechanical model

5.3.1. Element selection

An element is a minimum calculation unit of objects. The principal of the finite element method is that the physical behaviour of a whole domain is interpreted by calculating each element individually. The number of element nodes plays an important role in calculating the entire domain behaviour, because the nodal degree of freedom determines its behaviour. The domain is divided into several finite components, and the calculation method changes with respect to the element type.

An appropriate number of integration points is also required to calculate the strain energy of elements. More computation time is needed when adopting higher-order elements, owing to the number of calculation points. It can be decreased by using a reduced integration which infers one order fewer integration points than a full integration element. Calculation errors such as hourglass, shear locking, and volumetric locking may occur depending on the number of integration points and order of elements. An element with

reduced integration produces a less stiff result, which helps to avoid an overestimation of the stiffness matrix. Therefore, selecting an appropriate element is essential to improve the calculation stability and obtain an accurate solution.

When conducting the push-out test, severe deformation is expected around the shear stud in the form of stud shearing and concrete crushing. The bottom area of the shear stud takes strong shear and tensile stresses. A nonlinear stress distribution is also anticipated at the contact surface between the shear stud and the surrounding concrete. An eight-node linear brick element with reduced integration (C3D8R) was used for the shear stud, steel beam, and concrete slab. A first-order element is less sensitive to distortion, and reduced integration is beneficial to avoid shear locking. A four-node doubly curved thin shell element with reduced integration (S4R) was adopted for the trapezoidal deck, and a two-node linear three-dimensional truss element (T3D2) was employed for the reinforcement bars. A finer mesh was applied around the stud shank and its surrounding concrete. Typical mesh size was 25 mm, and the smallest mesh size was 5 mm in the push-out test model.

5.3.2. Contact properties

When two objects touch, a force is transmitted through a boundary. This causes stress discontinuities at the contact surfaces owing to the deformation and relative sliding of the objects. The transmitted forces are divided into normal and tangential components at the contact surface. The induced force is transmitted as a friction force, which makes it difficult for the objects to move along the tangential direction at the boundary, because it is proportional to a friction coefficient and the normal directional force. The friction coefficient between steel and concrete can be obtained from experimental investigations, which are affected by the boundary conditions such as the roughness of the steel plate, moisture contents of concrete, temperature, and surface contamination. Rabbat and Russel (1985) carried out a friction test using a steel plate and concrete block. They concluded that the friction coefficient was 0.57 for a dry interface with a normal stress range of 0.14 to 0.69 MPa. Baltay and Gjelsvik (1990) reported a friction coefficient of 0.47 between a steel plate and concrete slab when the normal force range was 0 to 468 MPa. In this study, the friction coefficient of 0.47 was adopted at the steel and concrete interlayers: the boundary between

the shear stud and surrounding concrete as well as between the trapezoidal deck and concrete slab. A friction coefficient of 0.2 was assumed at the top of the steel flange in the trapezoidal deck model, whereas a smaller value of 0.02 was used to the solid slab model because the top surface of the steel flange was greased to avoid bonding.

A hard contact method assumes that a contact pressure is infinitely increased in the normal direction when contact occurs. This describes a physical behaviour realistically, but it is difficult to converge because of a significant discontinuity at the contact boundary. To avoid the rapid stress change at the contact surface, a penalty method can be used by assuming that the contact pressure is proportional to a penalty stiffness, i.e. a spring element is added at the contact surface. When an excessive shear force is applied to the shear stud, the bottom of the stud shank experiences a substantial deformation. In this case, the penalty method is recommended to analyse the normal contact behaviour (King and Rechards, 2013). A scale factor option in Abaqus was incorporated into the concrete slab interfaces to control the contact stiffness and overclosure in the normal direction. A hard contact method was also used at the concrete slab bedding and steel flange.

The overlap between contact surfaces is the cause of excessive deformation of elements because the penetrated nodes move to the contact boundary at the beginning of the analysis. This movement induces a higher acceleration, which causes a relatively large deformation speed. Abaqus controls the deformation speed by limiting the ratio of the deformation to the wave propagation speed. The material constitutive relationship is invalid under an excessive deformation speed. In this research, the general contact option was used because it resolves the initial overclosures using strain-free adjustments; the over closed nodes move to the contact boundary without strains at the beginning of the analysis.

5.3.3. Developing mechanical models and verification

The von Mises criterion was used for the nonlinear response of steel materials, such as the shear stud, steel beam, trapezoidal deck, and reinforcement bar. The yield and ultimate stresses were taken from the experimental data and design values, as explained in Chapter 4. A stress triaxiality, reported by Lemaitre (1985), was used accompanied by a ductile damage function available in Abaqus to illustrate a stress reduction after the onset of damage. The damage function of the shear stud was calibrated using experimental data from the tensile coupon tests.

The nonlinear concrete behaviour was illustrated by the CDP model, which has four parameters to illustrate a failure surface in a multiaxial stress state. Different values of the dilation angle and deviatoric stress ratio at the tensile and compressive meridians were adopted, depending on the concrete strength. The recommended plasticity parameters in Abaqus were adopted for the ULS modelling: the dilation angle of C43 and C24 concrete were 42° and 50°, the deviatoric stress ratio of C43 and C24 concrete were 0.67 and 0.75, the compressive stress ratio of the equi-biaxial to uniaxial stress state was 1.16, and the eccentricity of the plastic potential function was 0.1. The temperature-dependent plasticity parameters were incorporated using the proposed formula in Chapter 3 with reference to this ULS value: Eq. 3-36 for the equi-biaxial stress ratio, Eq. 3-41 for the K_c value, Eq. 3-51 for the dilation angle. An exponential function was used to model a compressive damage development referring to Lubliner *et al*. (1989). Although typical damage values at the peak stress were 0.3 to 0.4 for a uniaxial and biaxial compressive state, the compressive damage value at the peak stress was assumed as 0.16, because a triaxial compressive state was expected at the surrounding concrete near the shear stud. Tensile damage was defined as a function of the reduced stress based on the maximum tensile stress, and the maximum crack opening distance was assumed as 0.2 mm, regardless of the temperature.

Boundary conditions

The loading surface and boundary conditions of the developed numerical model are provided in Fig. 5-13. Owing to the quarter symmetry calculation, the web of the steel beam (Surface 1) was restricted to move in the *y*-direction. The shear stud, concrete slab, steel beam, and trapezoidal deck (Surface 2) were confined to move in the *x*-direction. The bottom of the concrete slab (Surface 3) was also restrained in the *z*-direction. Identical boundary conditions were applied to the solid slab and transverse deck models. A displacement load was slowly induced at the loading surface to ensure a quasi-static analysis. The loading rate of 0.2 mm/s was used based on the natural frequency calculation of the specimen and the sensitivity analysis.

To illustrate the through-deck-welded shear stud, a tie option available in Abaqus was used between the bottom of the stud weld collar and the steel flange. The side sections of the weld collar were also combined with the deck hole, which has the same diameter as the weld collar. In the case of the through-hole-welded and solid slab models, the bottom of the stud weld collar was only tied to the steel flange.

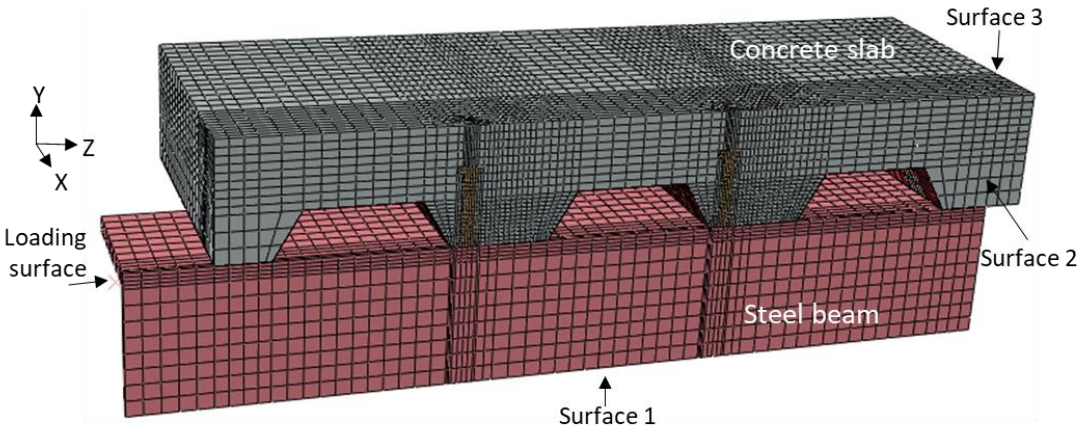

Figure 5-13. Boundary conditions of the 1.2-mm through-deck-welded model (T1)

Verification

A load–slip relationship was obtained from the developed finite element models. It was verified against the experimental results, which show a strong correlation regarding the shear resistance, slip capacity, and failure modes according to the specimen types. In the case of the solid slab model, the shear resistance consistently increased after loading started. It suddenly dropped, accompanied the stud shearing failure around 15 mm slip, as plotted in Fig. 5-14. Investigating the stress and damage contour near the shear stud at failure, the maximum stress was formed directly above the stud weld collar, and the stud shank was about to shear. The concrete elements around the stud root in the loading direction also showed higher damage, which indicates a crushed concrete area. Comparing the experimental investigation provided in Fig. 4-17 and the damage contour illustrated in Fig. 5-15, a similar response was found.

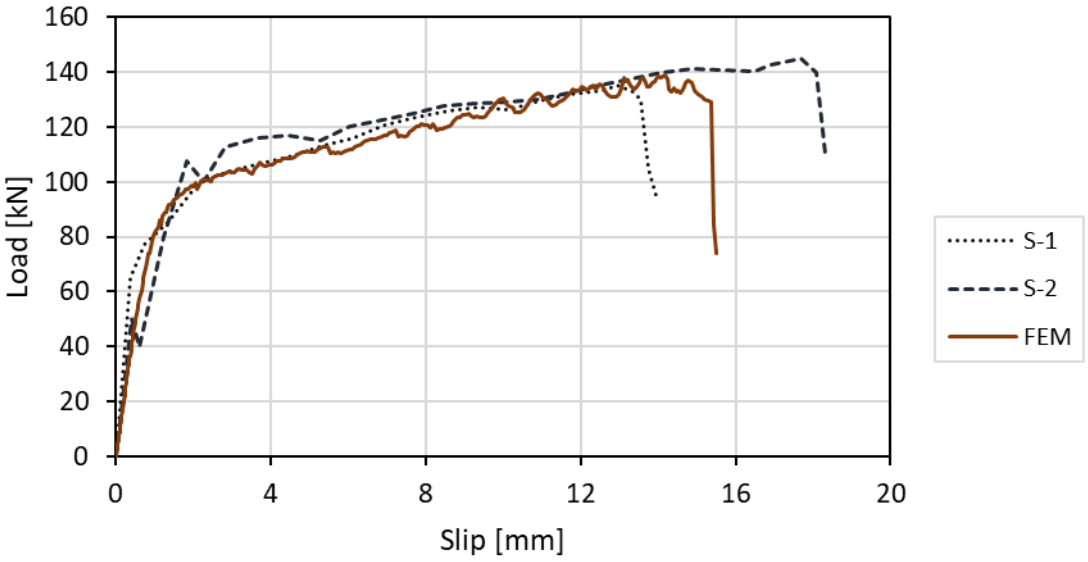

Figure 5-14. Verification of the solid slab model (S)

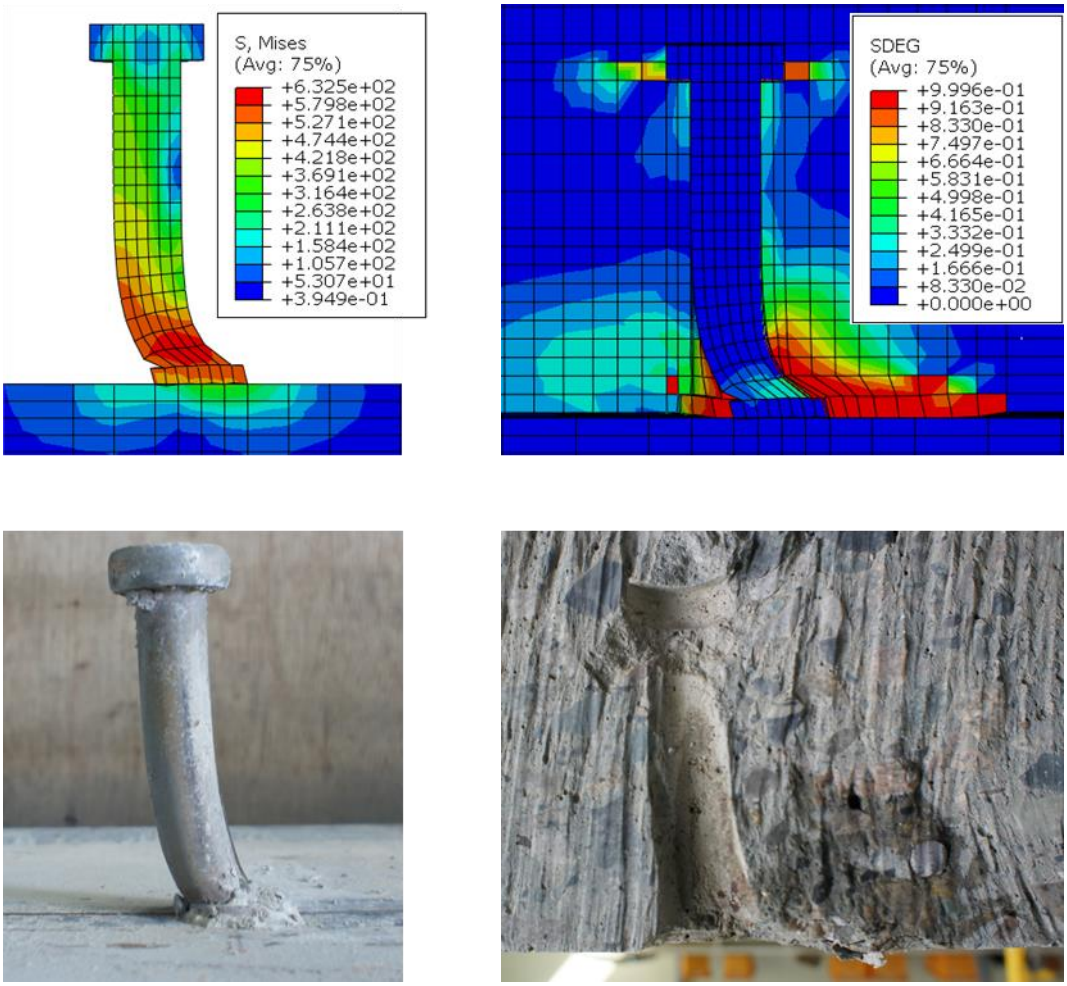

(a) stress contour (b) damage contour

Figure 5-15. Stress and damage contour of the solid slab model (S)

Unlike the load-slip relationship of the solid slab model, the shear resistance reduced gradually after reaching the maximum load in the transverse deck models, because the cause of failure is not by shear stud but the concrete in a trough. Concrete cracking occurs around the rib, which was wrapped by the steel deck. The load–slip curve of the developed model successfully illustrates the shear stud behaviour regardless of the stud welding method, as shown in Fig. 5-16 and 5-18. The failure mode observed in the 1.2-mm through-deck-welded specimen was concrete pull-out, which causes a concrete crack around the concrete rib. The damage contour at the maximum shear resistance of the numerical model showed a cone-shaped crack as depicted in Fig. 5-17. Higher tensile damage was observed around the lower-level stud (stud 2), whereas relatively small damage was found between the upper-level stud and the adjacent deck shoulder (stud 1). This concrete cracking

behaviour coincides with the experimental investigation, as shown in Fig. 4-20. The 0.9-mm through-hole-welded model showed a relatively larger crushed area in comparison with the 1.2-mm through-deck-welded model, owing to the stud welding method as shown in Fig. 5-19. The steel deck near the stud root withstands the shear force and acts as a unit in the through-deck-welded specimen, whereas the shear force causes concrete crushing at the gap between the shear stud and deck hole in the through-hole-welded specimen.

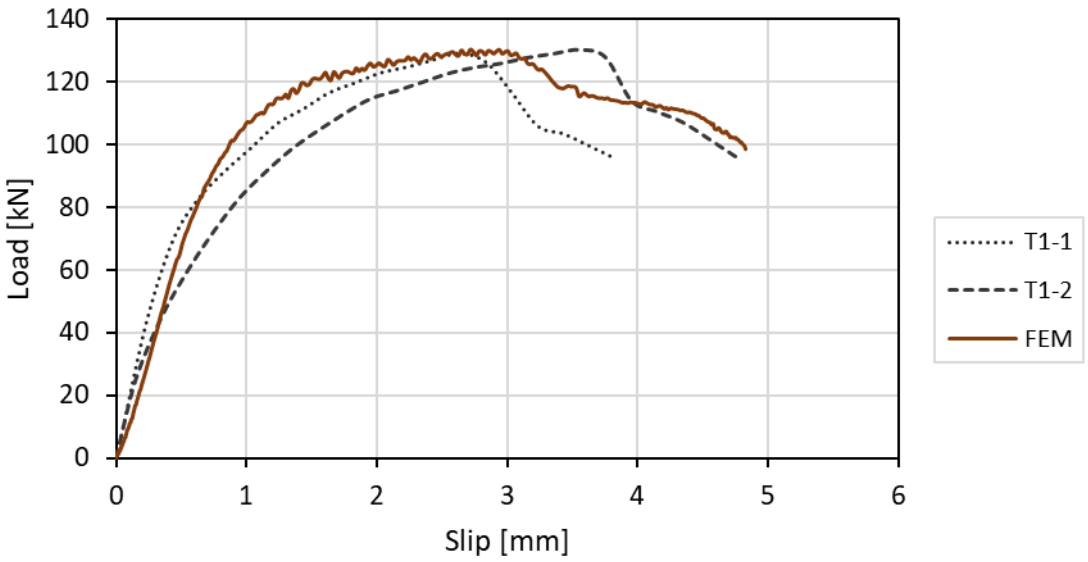

Figure 5-16. Verification of the 1.2-mm through-deck-welded model (T1)

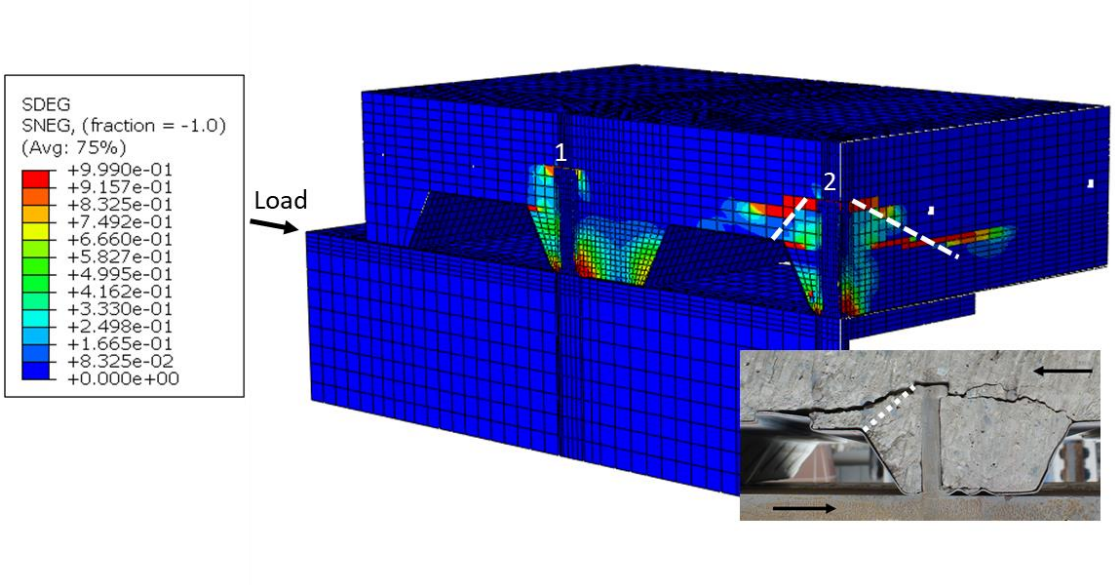

Figure 5-17. Damage contour of the 1.2-mm through-deck-welded model (T1) at the peak load

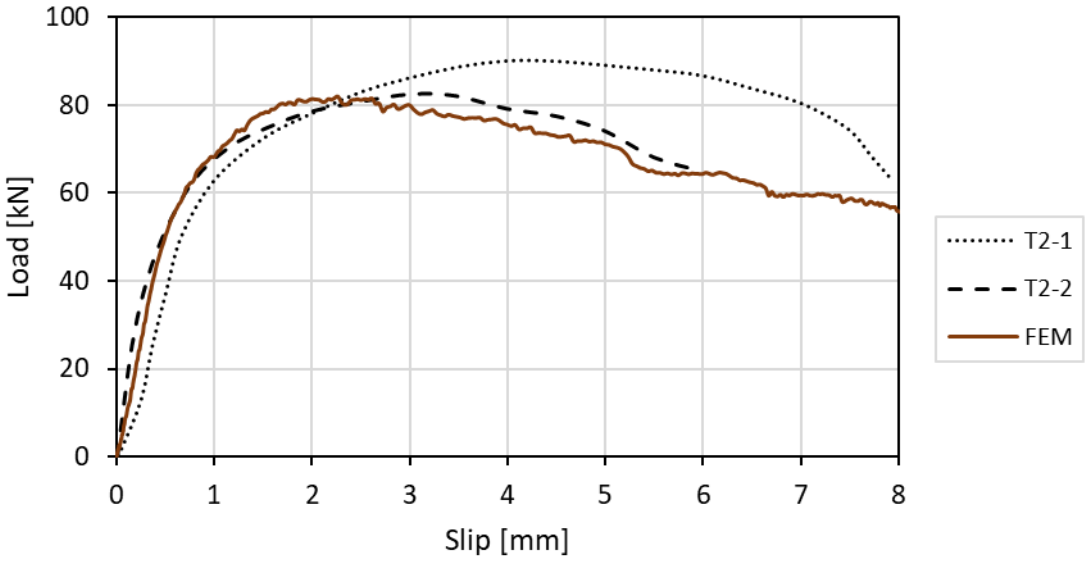

Figure 5-18. Verification of the 0.9-mm through-hole-welded model (T2)

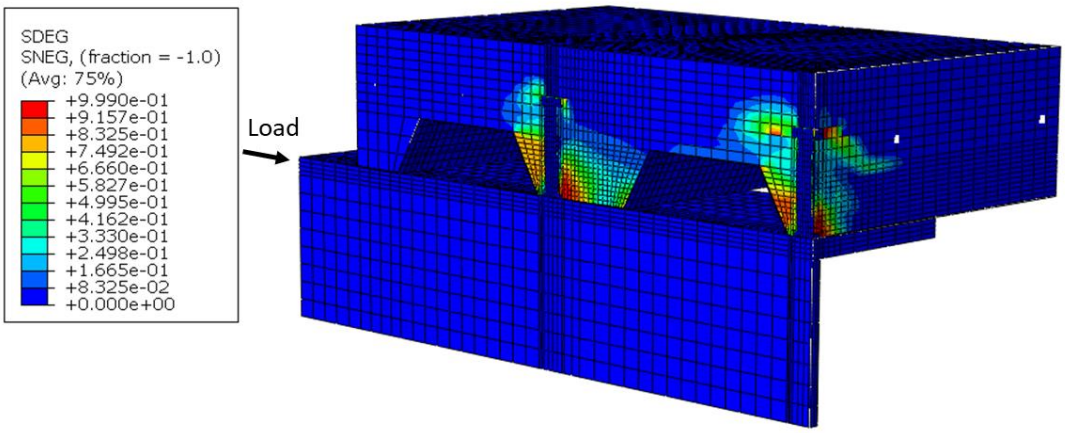

Figure 5-19. Damage contour of the 0.9-mm through-hole-welded model (T2) at the peak load

The modelling method and material properties for the numerical model are summarised in Table 5-1. Temperature-dependent material properties and thermal analysis data according to the fire elapsed time are incorporated for the thermomechanical model which is described in the following section.

Table 5-1. Summary of the numerical model parameters

Parameter	Descriptions
Modelling	- Quasi-static analysis using a dynamic explicit method - Sequentially thermomechanical coupled method for high-temperature model
Element	- Eight-node brick element (C3D8) for stud and concrete - Minimum mesh size: 5 mm
Mechanical contact	- General contact method with a penalty and hard contact method in tangential and normal behaviour, respectively.
Thermal contact	- 40 ~ 225 W/m^2K depending on contact layers
Stud model	- von Mises criterion - Ultimate and yield stresses are 473 MPa and 415 MPa
Concrete model	- Concrete damaged plasticity model with C43 and C24 concrete - A parabolic curve for compression and exponential curve for tensile behaviour

5.4. Thermomechanical model

5.4.1. Modelling procedure

The thermal and mechanical models were combined to evaluate the structural performance of the shear stud in a fire. A constant load was initially applied to the loading surface, and then a fire load was induced until failure occurs, according to the experimental procedure of the high-temperature push-out test. Nodal temperature data were assigned to the mechanical model with respect to the exposure time of the ISO 834 standard fire. The incorporated temperature values not only create a thermal stress but also define the thermal degradation of the materials. The same mesh arrangement as for the thermal model was applied to the mechanical model. The CTE of steel and concrete determine the thermal stress by generating a thermal displacement at given temperatures. The thermal elongation property of steel and concrete, taken from EC2-1-2 (2008), was converted to the CTE by dividing by the temperature of materials, which are provided in Fig. 5-20. Isotropic thermal elongation was assumed for the thermomechanical model.

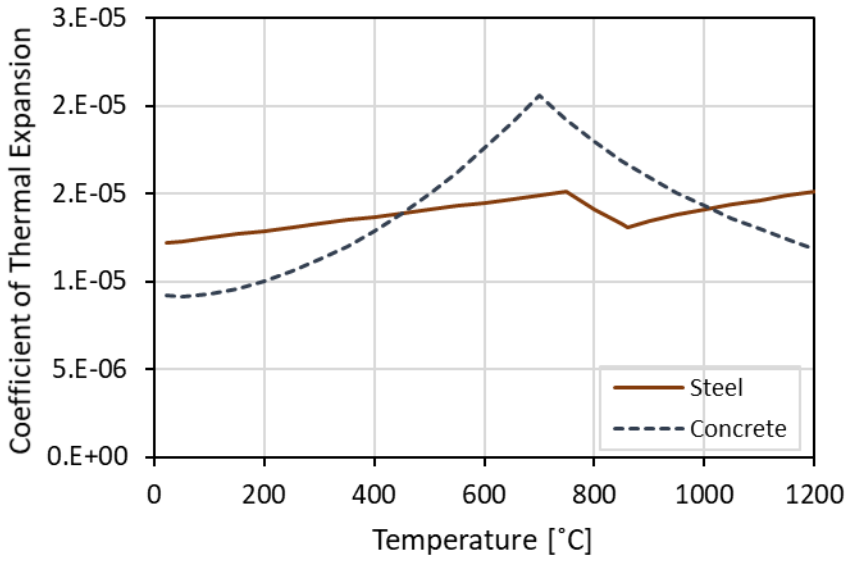

Figure 5-20. Coefficient of Thermal Expansion (CTE) of concrete and steel

5.4.2. Verification of the thermomechanical models

The slip variation with respect to the fire exposed time was investigated from the high-temperature push-out test models. The numerical results showed a strong correlation with the experimental data, as presented in Fig. 5-21, 5-24, and 5-27 according to the specimen types. It successfully illustrates a negative displacement and sudden slip change from the negative to positive direction as the temperature rises.

In the case of the solid slab model (SH model), the loading surface moves in the negative direction for approximately 4 mm, and the slip decreases rapidly at 80 min of heating accompanied the stud shearing failure. Unlike the solid slab model at ULS as shown in Fig. 5-15, the shearing occurs at the stud weld collar as presented in Fig. 5-22. The shearing location shifts from the stud shank to the steel flange as the temperature rises, which coincides with the experimental investigation; a large deformation was found at the weld collar, and the crushed concrete area was relatively small in comparison to the experiment at ULS.

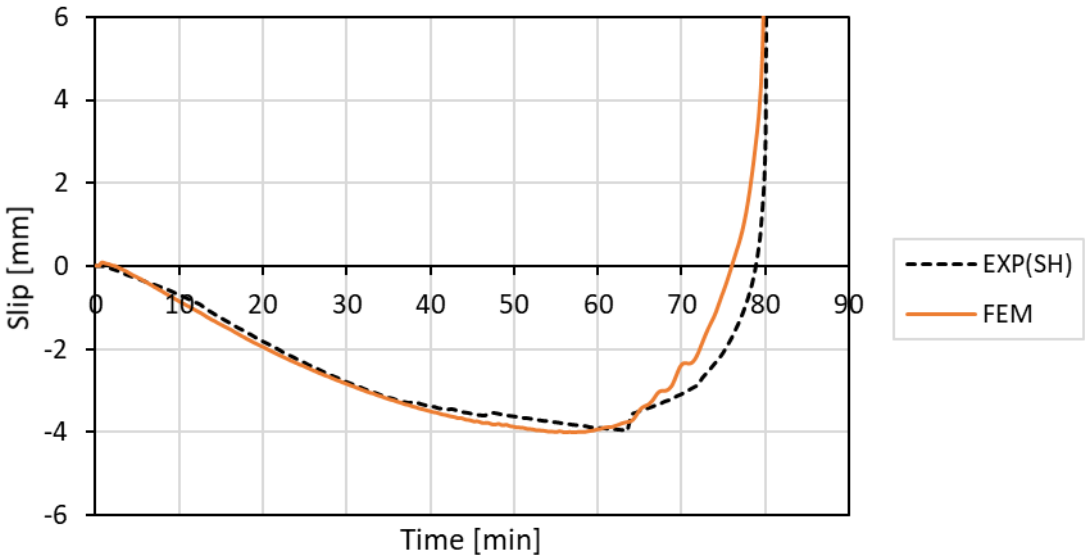

Figure 5-21. Verification of the solid slab model (SH)

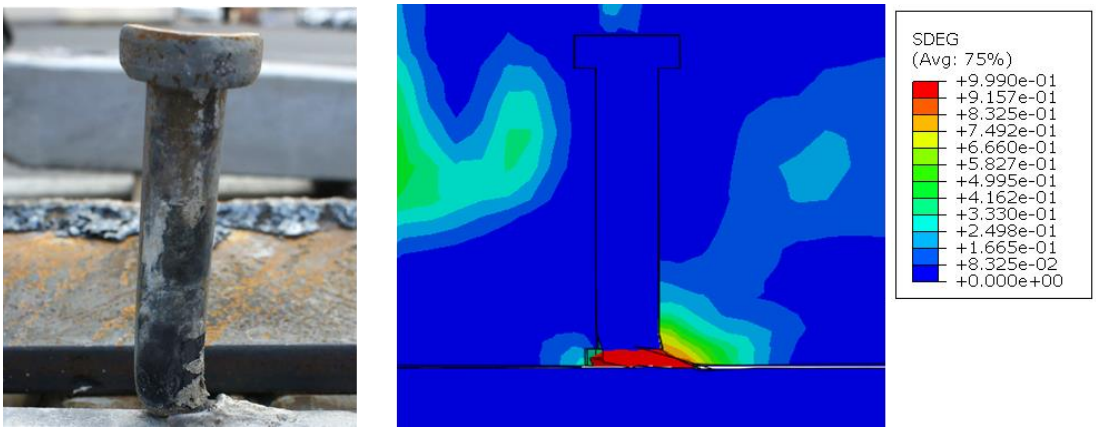

Figure 5-22. Damage contour of the solid slab model at failure (SH)

In order to ensure a quasi-static analysis, a kinetic energy (ALLKE) should have a relatively small value than the internal energy (ALLIE) during the modelling. The ratio of ALLKE to ALLIE showed less than 5 % as depicted in Fig. 5-23, which is recommended to control less than 5 ~ 10 % in the Abaqus manual (Simulia, 2015). The transverse deck model also shows the energy ratio of less than 5 % as depicted in Fig. 5-25.

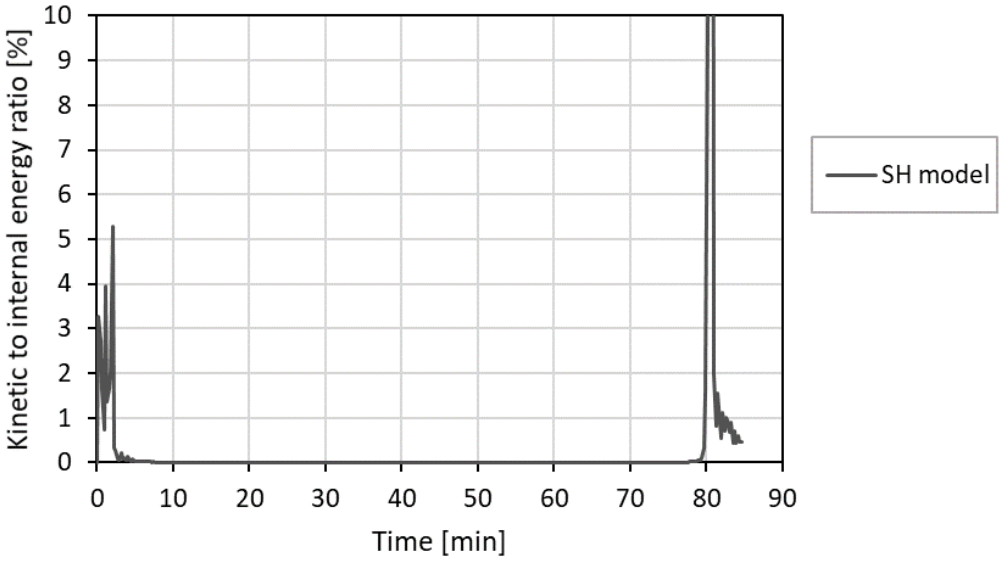

Figure 5-23. Kinetic to internal energy ratio of the solid slab model (SH)

The bottom of the stud shank was sheared off at 81 min of heating in the 1.2-mm through-deck-welded model (T1H model). This failure mode indicates that the applied thermal and mechanical loads exceed the thermally degraded strength of the shear stud. Owing to the rapid degradation of the shear connection, the slip change from the negative to positive direction took less than 1 min in both the experimental and numerical observations. Investigating the damage contour at failure (Fig. 5-26), the interface between the bottom of the shear stud and top side of the steel flange was severely deformed, and comparatively less damage was found around the concrete rib. This successfully illustrates the failure mode of the 1.2-mm through-deck-welded specimen, as already observed in Fig. 4-24.

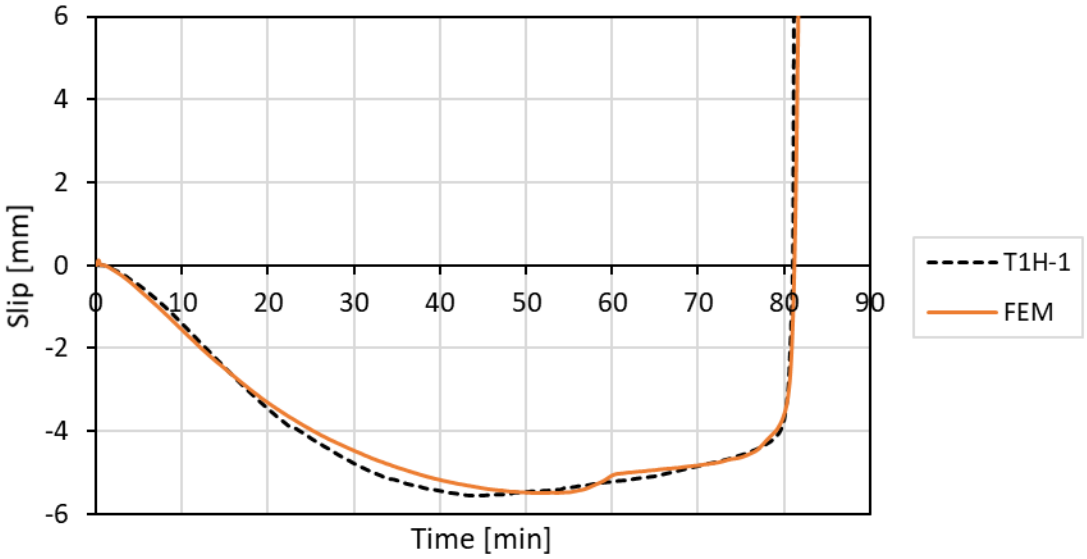

Figure 5-24. Verification of the 1.2-mm through-deck-welded model (T1H)

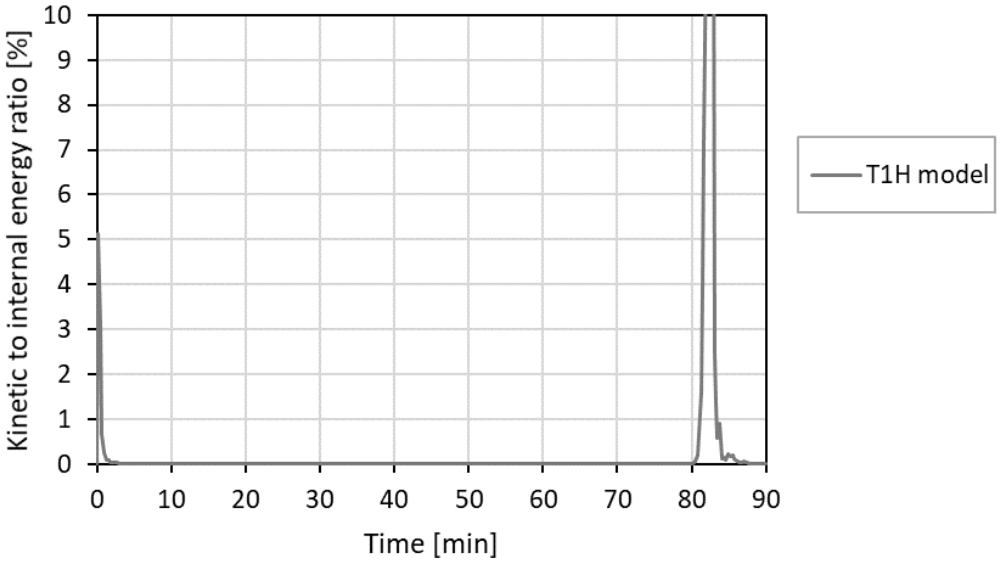

Figure 5-25. Kinetic to internal energy ratio of the 1.2-mm through-deck-welded model (T1H)

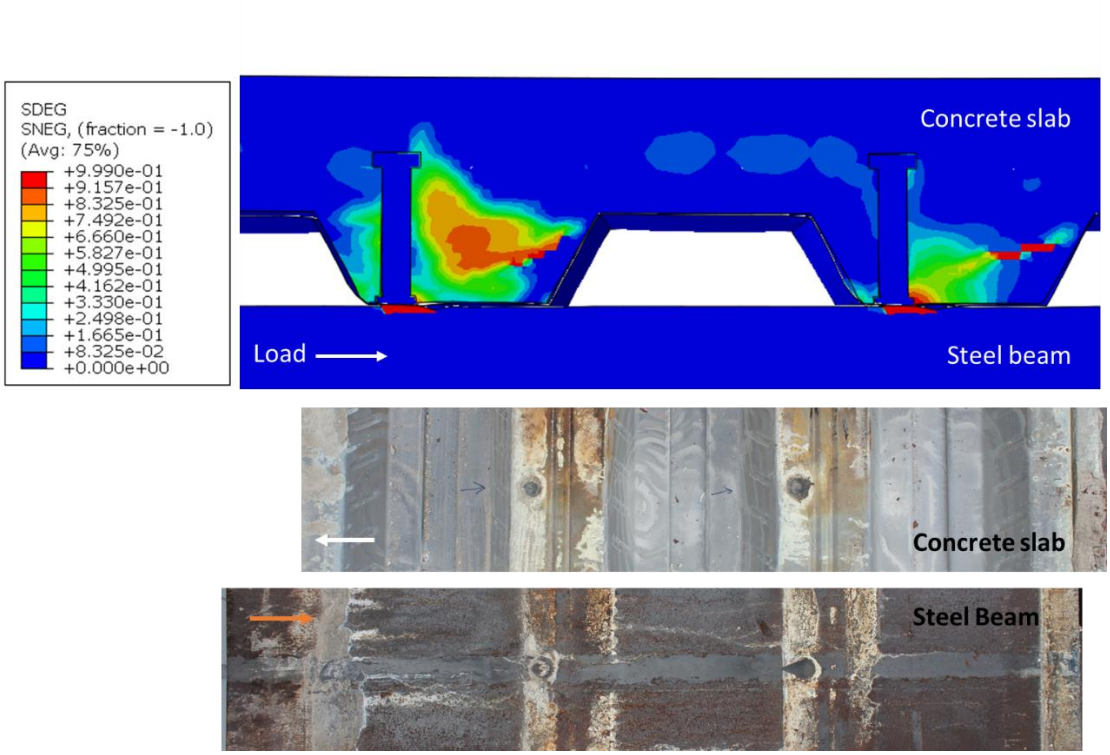

Figure 5-26. Damage contour of the 1.2-mm through-deck-welded model at failure (T1H)

Stud shearing failure was also observed in the 0.9-mm through-hole-welded model (T2H model) at high temperatures. The concrete crushed area near the shear stud reduces depending on the magnitude of the applied load. The shearing location and size of the concrete crushed area were also changed. A comparatively higher load causes a smaller fire resistance time accompanied by concrete crushing, whereas a relatively small load leads to a smaller concrete crushing area. This phenomenon can be found in the damage contour of the numerical models, as presented in Fig. 5-28.

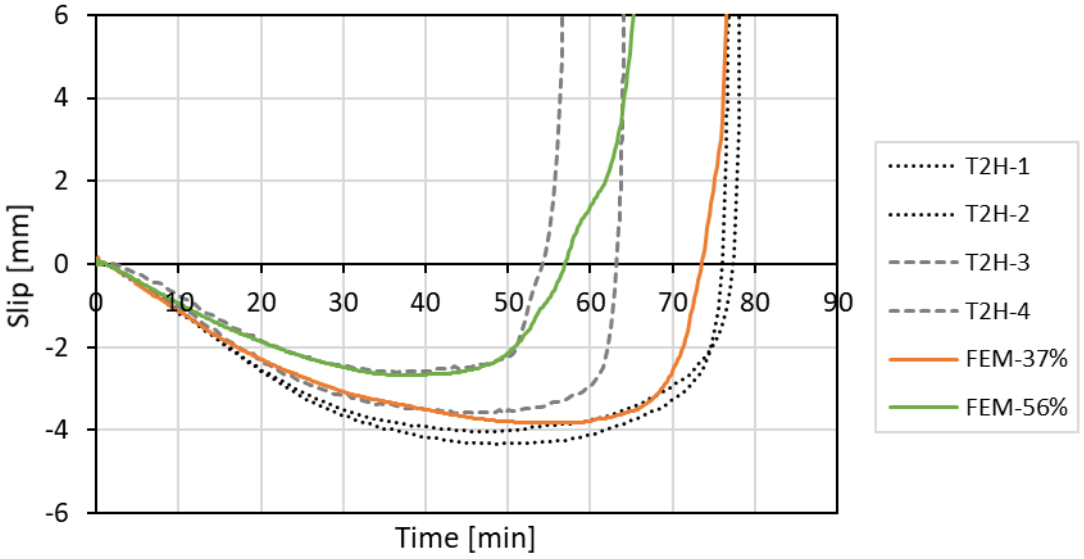

Figure 5-27. Verification of the 0.9-mm through-hole welded model (T2H)

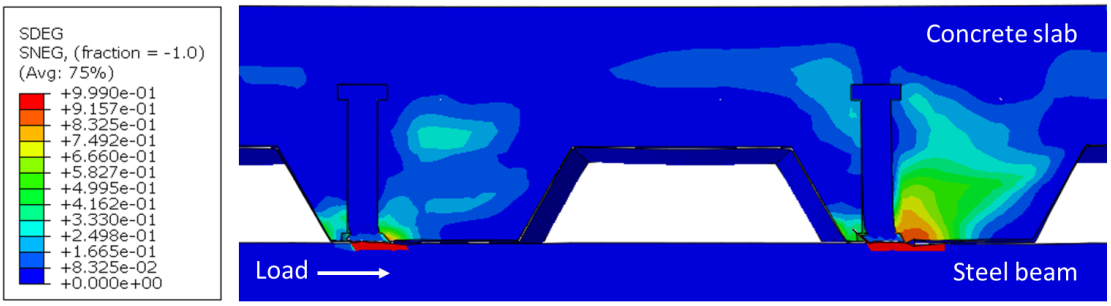

(a) Initial load of 30.4 kN (FEM-37%)

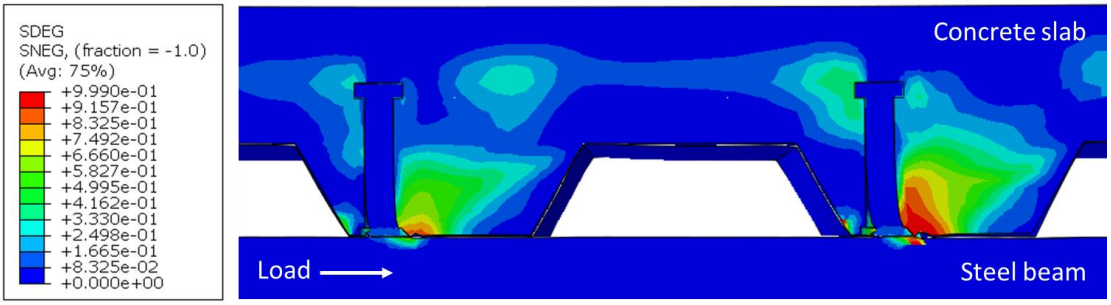

(b) Initial load of 45.6 kN (FEM-56%)

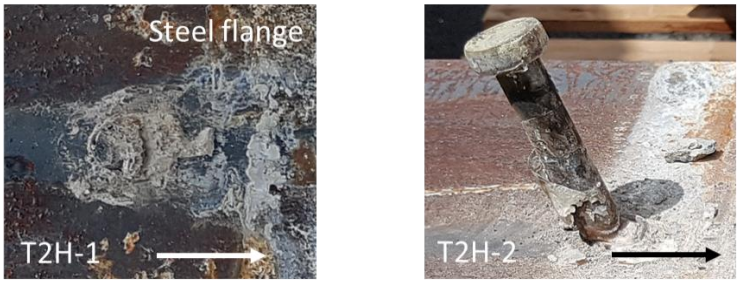

(c) Experimental investigation

Figure 5-28. Damage contour of the 0.9-mm through-hole-welded model at failure (T2H)

5.5. Conclusions

A three-dimensional thermomechanical finite element model has been developed and verified against the experimental results at both ULS and FLS. A configuration factor regarding the push-out test setup is adopted to radiation calculation. The convection coefficient for the ISO 834 standard fire condition and thermal conductivity for steel and concrete are taken from EC4-1-2 (2014) in the thermal analysis. The damage evolution of the stud material is defined based on the tensile test data, and a relatively small compressive damage is assumed to consider a triaxial compressive state at the surrounding concrete. The developed mechanical model illustrates stud shearing failure in the solid slab specimen and concrete pull-out failure in the transverse deck specimen. Thermal and mechanical models were combined to obtain a shear stud behaviour in a fire under the same mesh configuration which has 5 mm around the shear stud. Temperature-dependent plasticity parameters derived in Chapter 3 were used to the thermomechanical model with reference to its ULS value, which gives a strong correlation with respect to the load-slip relationship, failure mode, and slip-time curve against the experimental data. Parametric studies were conducted using the developed numerical models, which are described in Chapter 6.

Chapter 6
PARAMETRIC STUDY

6.1. Introduction

The developed finite element models were employed to investigate the shear stud behaviour embedded in solid and transverse deck slabs at high temperature. The current EC4-1-2 (2014) provides the shear resistance at FLS based on the experimental investigation using solid slab specimens. Although it corresponded to the stud behaviour in a solid slab, it showed a different response when employing a transverse deck slab. Parametric studies regarding the shear resistance with respect to several conditions such as the temperature, stud welding method, deck thickness, stud location, and number of studs in a trough were conducted. The shear stud behaviour at high temperature with a focus on transverse deck applications is described in this chapter.

6.2. Shear resistance at high temperatures

6.2.1. Structural capacity of the shear connection in a solid slab

The shear resistance was evaluated by inducing a structural load and exposing the ISO 834 standard fire condition using the developed numerical models. Different load ratios with respect to the shear resistance at ULS were used to investigate the structural performance at FLS. As presented in Table 6-1, a fire resistance time, flange temperature, and failure mode are observed under a given load level. The model name was made according to the slab type and applied load; the shear resistance at ULS is 135 kN for the solid slab model.

Table 6-1. Parametric study of the solid slab specimen

Model	Load [*kN*]	Load ratio[1]	Fire resistance time [*min*]	Flange temp. [°C]	Failure mode
SHR80	108	0.8	36.5	508	Shearing
SHR60	81	0.6	49.5	629	Shearing
SHR40	54	0.4	65.7	716	Shearing
SHR30	41	0.3	79.9	749	Shearing
SHR20	27	0.2	-	-	-

[1]load ratio is calculated as an applied load to the shear resistance at ULS (135 *kN*)

All the observed failure modes were stud shearing, regardless of the temperature. According to the temperature profiles shown in Fig. 5-18, the temperature of the shear stud was higher than the surrounding concrete. This means that the shear stud is prone to fracture owing to a comparatively significant thermal degradation. The same failure mode can also be found from other high-temperature experiments (Zhao and Kruppa, 1997; Imagawa *et al*., 2012; Chen *et al*., 2015).

A slip–time relationship at a given load level is plotted in Fig. 6-1: slip indicates a longitudinal slip between the concrete slab and steel section, and time means an exposed time to the ISO 834 fire condition. A higher negative slip and longer fire resistance time are observed depending on the applied load. A fracture does not occur within 90 min of the heating process when imposing less than 27 kN per stud which is 20 % of the ULS value.

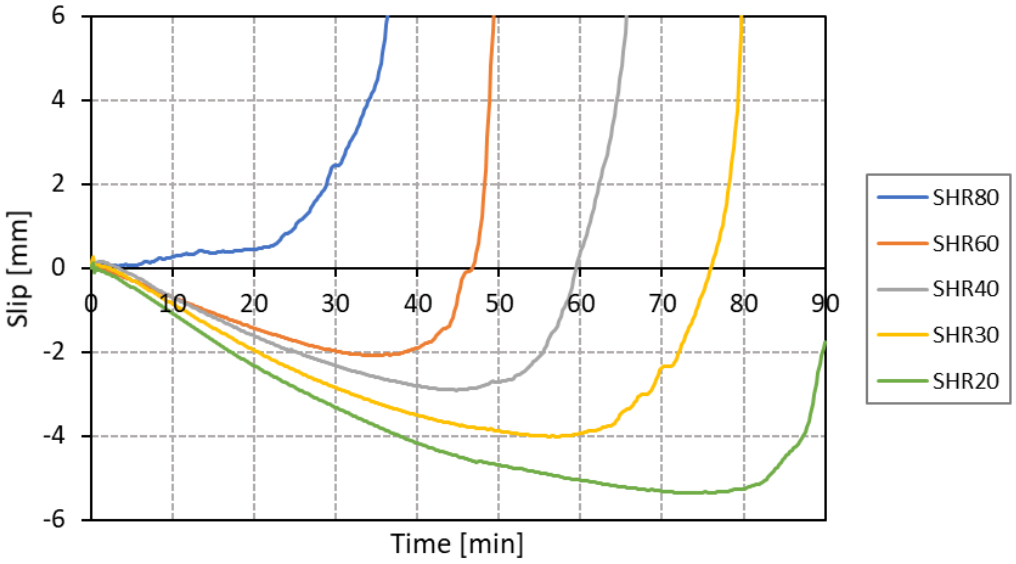

Figure 6-1. Slip-time curves with different load levels

Stress contours of the shear stud and surrounding concrete at the maximum negative slip are plotted in Fig. 6-2 and 6-3, respectively. The maximum stress was observed at around 10 mm from the bottom of the shear stud at ULS, which results in the shearing failure directly above the stud weld collar. For the FLS, the stud weld collar withstands the highest load at the beginning of the heating process, and the location of the maximum stress shifts in the upward direction along the stud shank owing to the thermal degradation of the stud root area. When the initial load was 41 kN (SHR30 model), the maximum stress formed around 40 mm from the stud root. As shown in Fig. 6-4(a), the stud shank above the weld collar exhibits the maximum stress contour at ULS, whereas the stress at the stud root is smaller than the stress at the middle of the stud shank in the SHR30 model. The shearing location gets progressively closer to the bottom of the stud root as the fire elapsed time increases. This is related to the strength degradation of the stud material, and the size of the concrete crushed area near the shear stud. The displacement contour shown in Fig. 6-5 proves the variation of the shearing location. In the case of the SHR30 model, the shearing eventually occurs at the boundary between the bottom of the shear stud and top side of the steel flange, as already shown in the experimental investigation. On the contrary, the crushed area at the surrounding concrete was reduced in accordance with the increasing of the fire resistance time. At ULS, a bottom concrete element initially withstands the highest

stress, after which the location of the maximum stress increases to 30 mm from the bottom of the concrete slab, as shown in Fig. 6-3. This means that the surrounding concrete less than 30 mm from the bottom concrete slab was crushed, which can be checked from the damage contour, as shown in Fig. 6-4(b) (S-ULS model). Xue *et al*. (2008) reported a concrete bearing zone in the push-out test as 18 to 30 mm from the bottom of the concrete slab when employing a 100 mm height shear stud. The location of the maximum stress on the surrounding concrete was 30 mm at ULS, which coincides with the experimental investigation. It moves in the downward direction along the stud shank as the fire resistance time increases. The maximum stress of the surrounding concrete was developed at approximately 10 mm from the bottom of the concrete slab in the SHR30 model. Accordingly, a comparatively small crushed area was found at the high-temperature model, as illustrated in Fig. 6-4(b).

Investigating the stress distributions of the shear stud and surrounding concrete of the 90 % load model (SHR90) provided in Fig. 6-2 and 6-3, the stud shank experienced a similar stress distribution in comparison to the ULS model (S-ULS). The maximum stress location at the surrounding concrete of the SHR90 model was closer to the bottom of the concrete slab. The stress of the surrounding concrete in the SHR90 model appears to be stronger than in the ULS model, owing to the relatively degraded strength of the stud material; the observed true-stress at the surrounding concrete in the SHR90 model is higher than its ULS model value. The surrounding concrete below the maximum stress location can be regarded as a crushed area. As a result, the shear resistance was reduced by 10 % at the flange temperature of 345 ℃ because the ultimate stress of the stud material starts to decrease from 300 ℃.

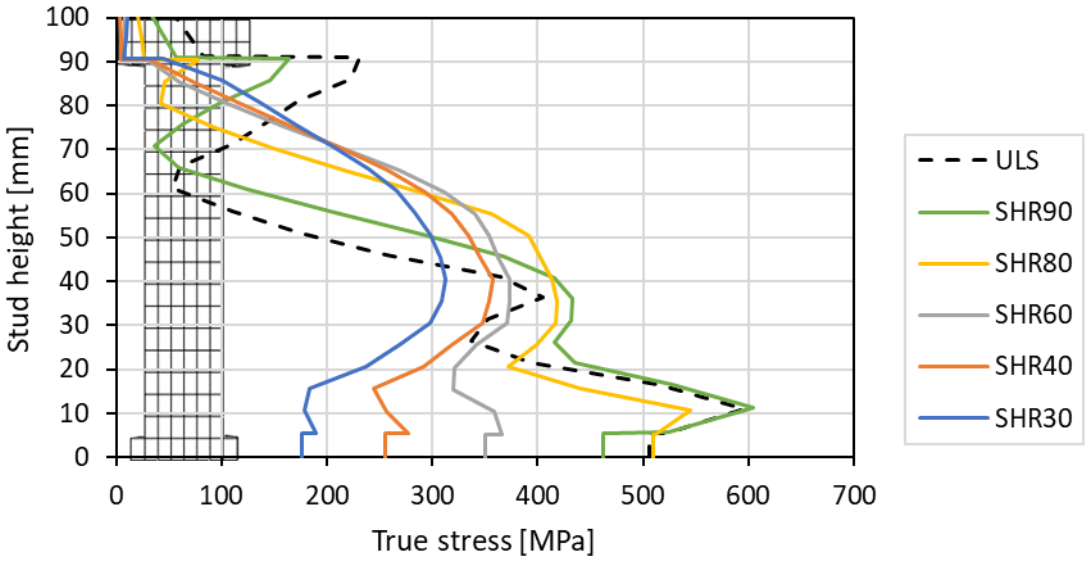

Figure 6-2. Stress distributions of the shear stud at the maximum negative slip (SH)

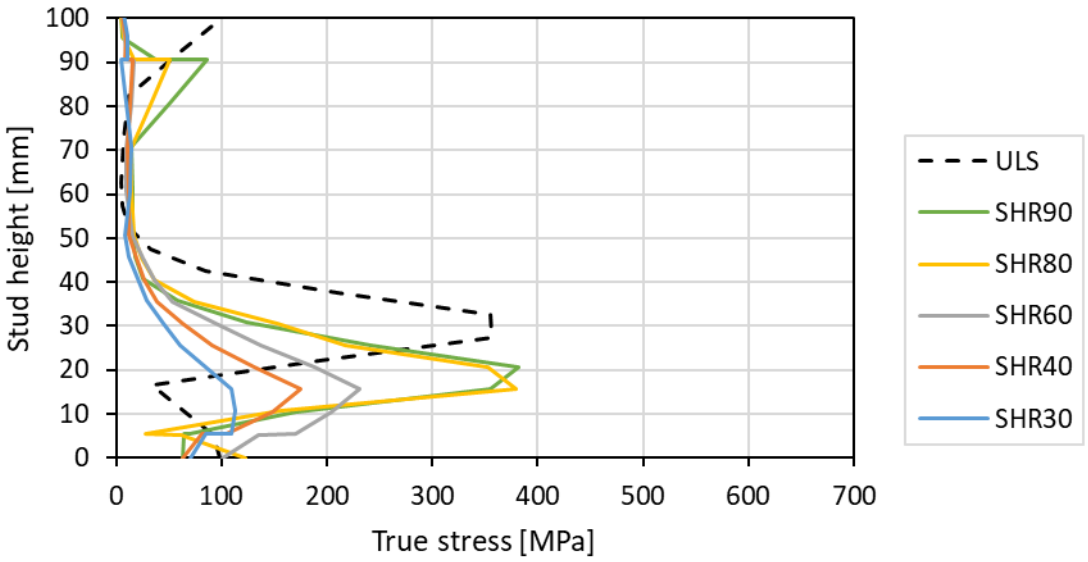

Figure 6-3. Stress distributions of the surrounding concrete at the maximum negative slip (SH)

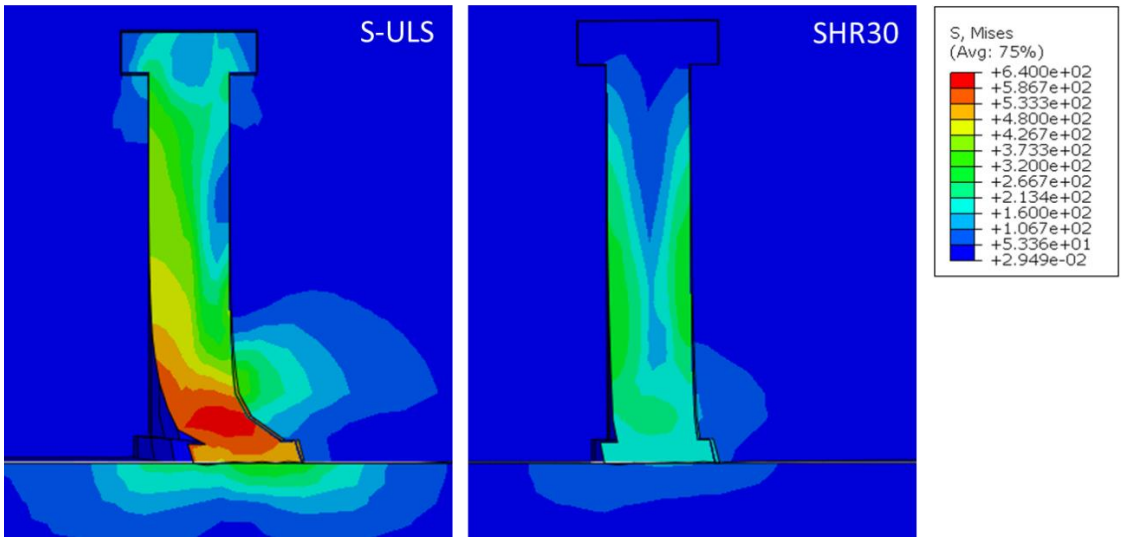

(a) Stress contour of the ULS and FLS models at the maximum load

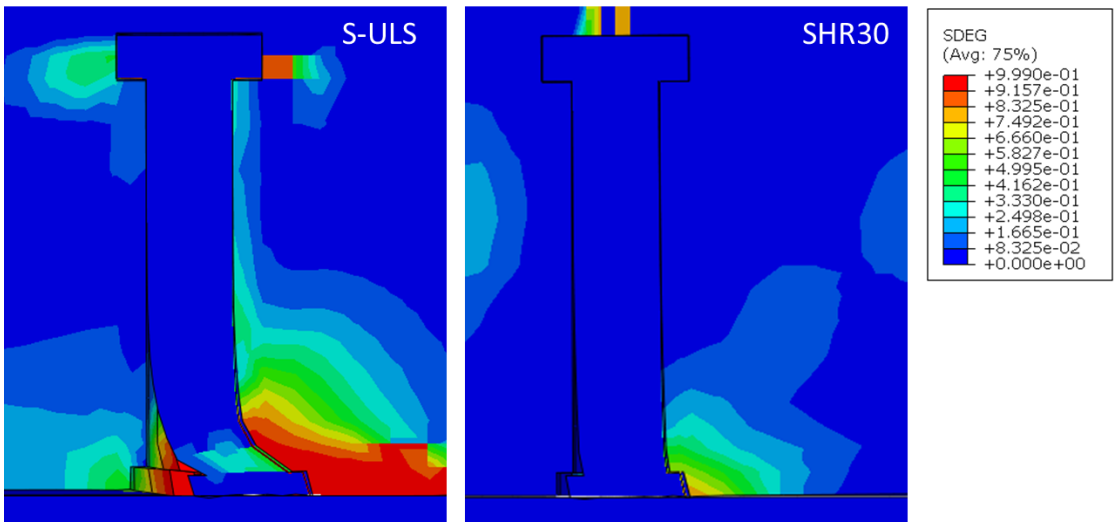

(b) Damage contour of the ULS and FLS models at fracture

Figure 6-4. Stress and damage contours of solid slab models

As presented in Fig. 6-5, the shearing occurs above the weld collar at ULS model, while it observed at the interlayer between the bottom of the weld collar and top side of the steel flange at the SHR30 model. The shearing location changes depending on temperature.

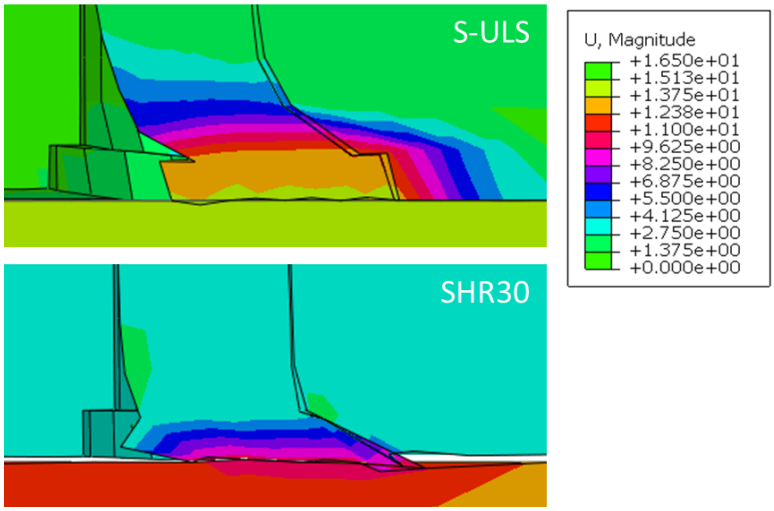

Figure 6-5. Displacement contour at the stud root before fracture

As discussed in Section 4.5.1, the stud temperature 5 mm above the stud root shows around 90 % of the flange temperature. Considering the change of the shearing location, the flange temperature is adopted as a reference value to illustrate the temperature at the failure location. This can be expressed using a different temperature ratio as follows:

$$\begin{aligned} \theta_{shear} &= 0.9\theta_{flange} && 20℃ < \theta_{flange} < 450℃ \\ \theta_{shear} &= 0.9 + \frac{0.09 \times (\theta_{flange} - 450)}{350} && 450℃ \le \theta_{flange} < 800℃ \\ \theta_{shear} &= 0.99\theta_{flange} && 800℃ \le \theta_{flange} \end{aligned} \quad (6\text{-}1)$$

where, θ_{shear} : temperature at the shearing position [℃]
θ_{flange} : temperature at the steel flange [℃]

The size of the stud weld collar is 1.2–1.3 times the stud diameter according to BS EN ISO 13918 (2018). Johnson and Oehler (1981) reported a typical diameter of the stud weld collar as 1.34 times the stud diameter. The area of the shearing position can be defined as an increasing value, because the shearing occurs at both the stud shank and weld collar

depending on the fire elapsed time. The cross-sectional area at the shearing position can be expressed as:

$$A_{sc,fi} = \frac{\pi}{4} d_{fi}^2 \tag{6-2}$$

$$\begin{aligned} d_{fi} &= d && 20℃ < \theta_{flange} < 450℃ \\ d_{fi} &= d + 0.34d \frac{(\theta_{flange} - 450)}{350} && 450℃ \leq \theta_{flange} < 800℃ \\ d_{fi} &= 1.34 \times d && 800℃ \leq \theta_{flange} \end{aligned}$$

where, $A_{sc,fi}$: area of the shearing position [mm^2]
d : diameter of the stud shank [mm]
d_{fi} : diameter of the shearing position at FLS [mm]

When the cause of failure is stud shearing, the shear resistance is determined by the shearing area and ultimate strength of the stud material. Considering the temperature and area of the shearing position, the shear resistance at high temperature can be calculated by the following equation which was used to plot the proposed SRF in Fig. 6-6.

$$P_{k,fi} = 0.8 f_u A_{sc,fi} \times \left(0.8 k_{u,\theta_{shear}}\right) \tag{6-3}$$

where, f_u : ultimate strength of the stud material [*MPa*]
$k_{u,\theta_{shear}}$: ultimate strength reduction factor of the stud material according to the temperature at the shearing position.

A load ratio with respect to its ULS value has been plotted in Fig. 6-6 according to the temperature of the steel flange, which is connected to the bottom of the shear stud. The modelling results and experimental data within the relevant literature were also compared with EC4-1-2 (2014) which gives an unconservative value along with all the temperature range. The proposed curve provides a more conservative response than EC4-1-2 (2014), and also it embraces all the modelling and experimental data when the load level is smaller than 80 %.

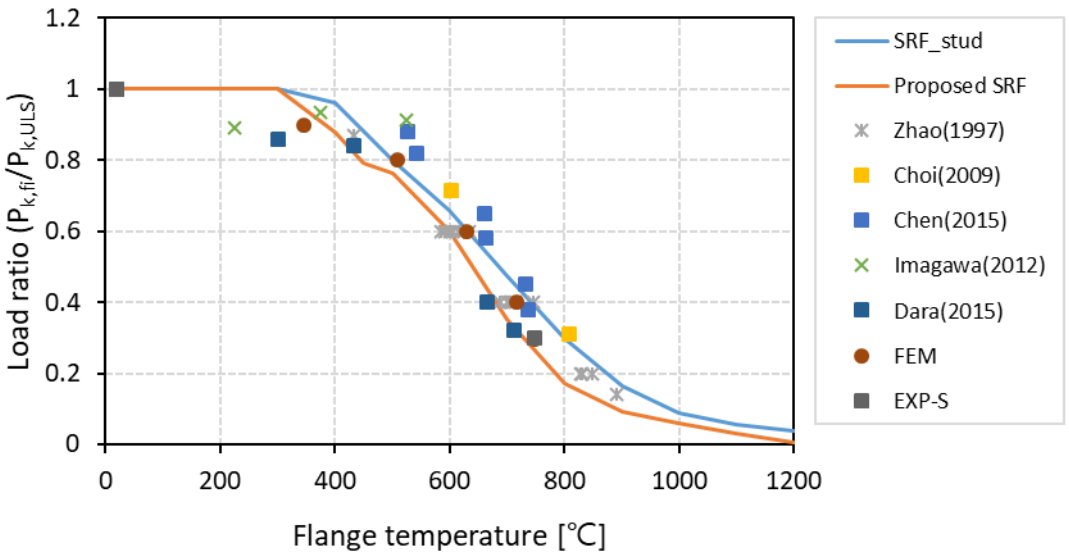

Figure 6-6. Shear resistance reduction of the solid slab specimen at FLS

6.2.2. Structural capacity of the shear connection in a transverse deck slab

Different loads were applied to the transverse deck model to investigate the shear resistance when exposed to the ISO 834 standard fire condition. The slip–time relationships, plotted in Fig. 6-7 and 6-9, show a similar curve form of the solid slab specimen, which has a negative slip and rapid displacement change before fracture. Two types of numerical models were used; one is the 1.2-mm through-deck-welded push-out test model (T1H), and the other is the 0.9-mm through-hole-welded model (T2H). Detailed modelling conditions and results are presented in Table 6-2.

Table 6-2. Parametric study of the transverse deck specimen

Model	Deck thickness	Load [*kN*]	Load ratio[1]	Fire resistance time [*min*]	Flange temp. [°C]	Failure mode
T1HR80	1.2 mm	103.2	0.8	17.6	404	Concrete
T1HR60		77.4	0.6	38.0	669	Shearing
T1HR40		51.6	0.4	51.1	731	Shearing
T1HR20		25.8	0.2	74.0	849	Shearing
T2HR80	0.9 mm	65.6	0.8	47.3	695	Concrete
T2HR60		49.2	0.6	62.1	737	Shearing
T2HR40		32.8	0.4	74.9	807	Shearing
T2HR20[2]		16.4	0.2	-	-	-

[1]load ratio is calculated as an applied load to the shear resistance at ULS: 129 kN and 82 kN for 1.2 mm and 0.9 mm deck specimens

[2]Failure does not occur within 90 min of the heating process

Severe concrete damage was observed in the 80 % load ratio model, and stud shearing occurred accompanied by relatively small concrete damage when applying less than 60 % of the shear resistance at ULS. A failure mode transition was found between the 80 % and 60 % load ratio models. The shear connection was governed by the stress of the stud root area below 60 % of the shear resistance at ULS, whereas it was determined by concrete cracks around the deck in the 80 % load ratio model. Observing Fig. 6-7, the T1HR80 model shows a gradual slope of the slip–time curve in the positive slip region, and the others show a steep inclination before exceeding 6 mm slip. Although the stud shearing generally occurred in a ductile manner at ULS, a rapid fracture was observed at elevated temperatures. A damage contour of the T1HR80 and T1H60 models showed these different failure modes as shown in Fig. 6-8.

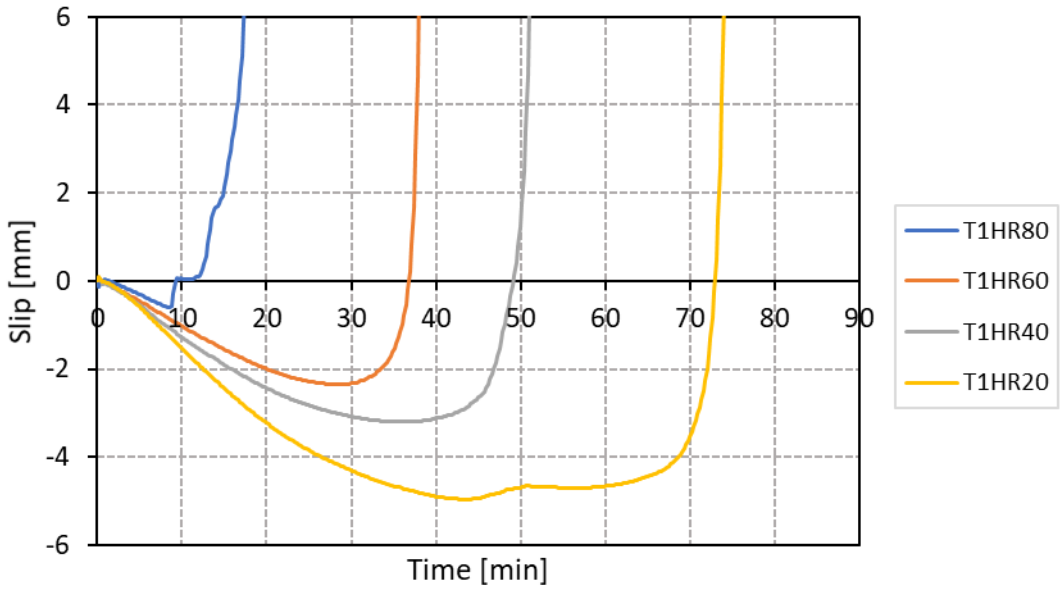

Figure 6-7. Slip-time curves with different load levels (T1H)

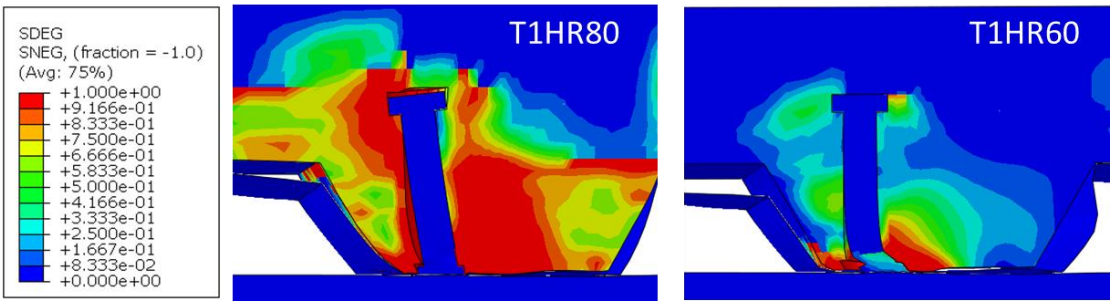

Figure 6-8. Damage contour of the 1.2-mm through-deck-welded model (T1H)

A fracture does not occur within 90 min of heating when inducing 16.4 kN to the 0.9-mm through-hole-welded model (T2HR20). Although the load ratio is the same, the amount of the applied load was different owing to the different shear resistance at ULS. This means the smallest load was applied to the T2HR20 model. The expected failure mode is the stud shearing at the top side of the steel flange considering the failure mode of the 0.9-mm through-hole-welded specimen presented in Fig. 4-26. A larger concrete damaged area was

shown in the through-hole-welded model than the through-deck-welded-model, and a more gradual slope of the slip–time curve was also observed, as plotted Fig. 6-9. A contrasting failure mode with respect to the fire resistance time was also obserbed as presented in Fig. 6-10.

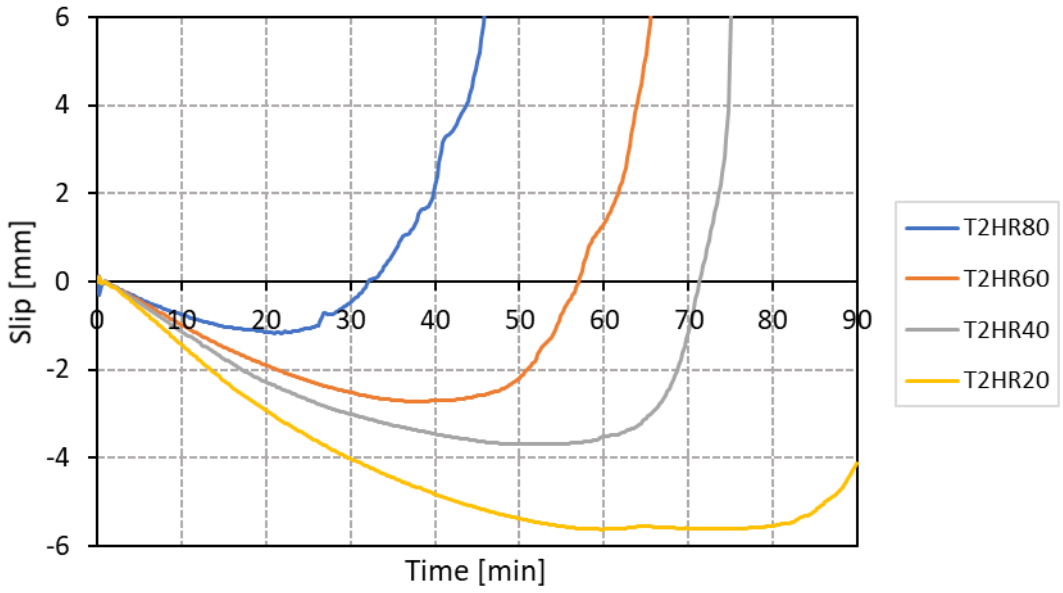

Figure 6-9. Slip-time curves with different load levels (T2H)

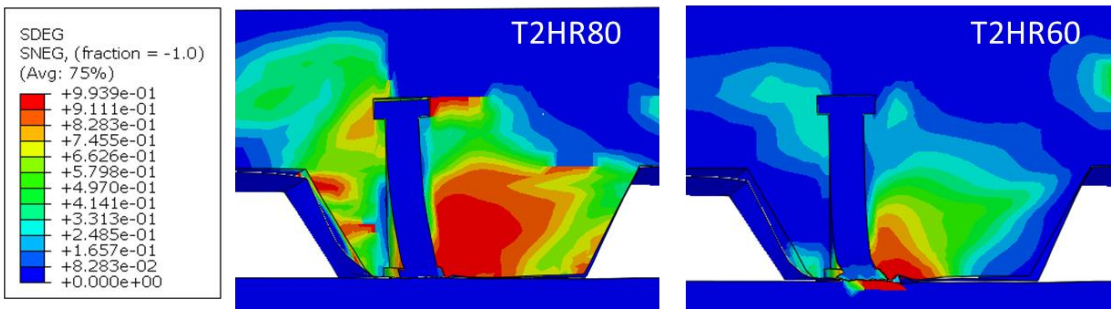

Figure 6-10. Damage contour of the 0.9-mm through-hole-welded model (T2H)

The stress contours of the 1.2-mm through-deck-welded model (T1H) around the shear stud at the maximum negative slip are plotted in Fig. 6-11: the maximum stress was formed around 40 mm of the stud height in the case of the T1HR20 model. It developed near the stud weld collar at the initial stage of the heating process and increased along the shear stud because of the thermal degradation at the stud root area. On the contrary, the highest stress was created above the weld collar at ULS and T1HR80 models, which show concrete-dominated failure. When applying 60 % of the shear resistance at ULS, the stress at the stud shank was higher than the stress at the weld collar. Consequently, stud shearing failure was observed. The stress distributions at the surrounding concrete are also illustrated in Fig. 6-12. Although the amount of the applied stress was smaller than the solid slab model, it gives the same trend of the stress variation as the temperature rises. The location of the maximum stress moves in the downward direction, and a concrete damaged area was reduced as with increasing temperature.

A parametric study with respect to the thermal conductance between the steel and concrete sections was conducted to evaluate the effect of the temperature distribution nearby the shear stud. The temperature of the shear stud rapidly increased, and the surrounding concrete temperature slowly increased when adopting a small thermal conductance value between the shear stud and the surrounding concrete (FEM-T1H-S). In the same manner, adopting a perfect thermal conductance decreases the temperature difference between the shear stud and the surrounding concrete (FEM-T1H-P). This makes the temperature of the surrounding concrete higher than in the model using a smaller thermal conductance. The load ratio with respect to the flange temperature of the experimental and numerical data are presented in comparison to the design guidance and proposed SRF in Fig. 6-13 and 6-14, depending on the stud shearing and concrete-dominated failure mode, respectively. An analogous load ratio was observed when the cause of failure was shearing at the stud root area beyond around 600 ℃. Meanwhile, a scattered data was shown for the flange temperature less than 600 ℃, accompanied by the concrete-dominated failure. The Eurocode estimation does not illustrate the strength reduction. The fire exposed time at fracture was different when the same load ratio of 80 % was applied. This graph explains a possible reason for the different experimental results of Mirza *et al*. (2011) and Chen *et al*. (2015). Therefore, a standardised test method including a specimen configuration and

heating condition is needed to obtain consistent experimental data in transverse deck applications.

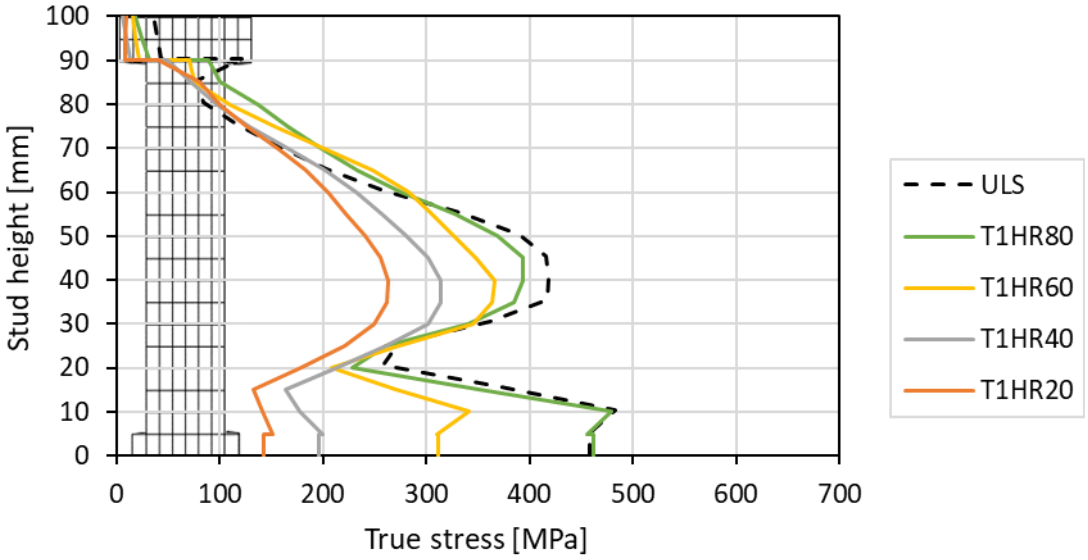

Figure 6-11. Stress distributions of the shear stud at the maximum negative slip (T1H)

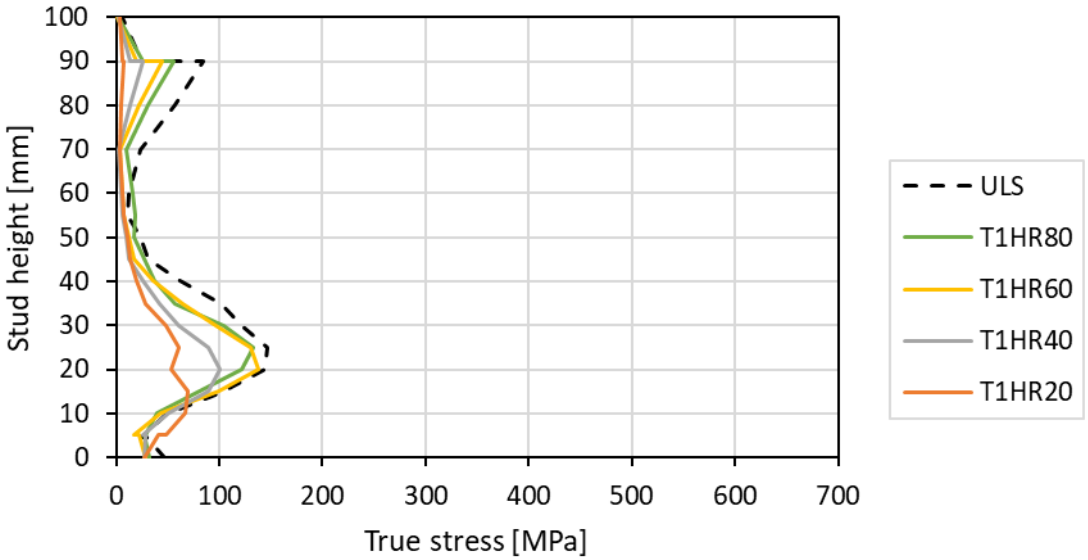

Figure 6-12. Stress distributions of the surrounding concrete at the maximum negative slip (T1H)

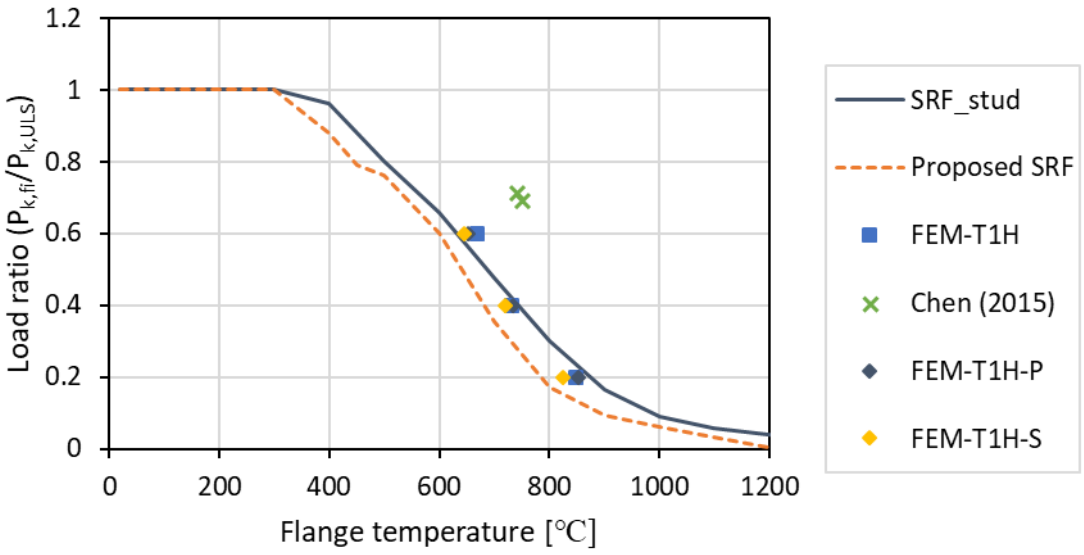

Figure 6-13. Stud shearing failure with different thermal conductance

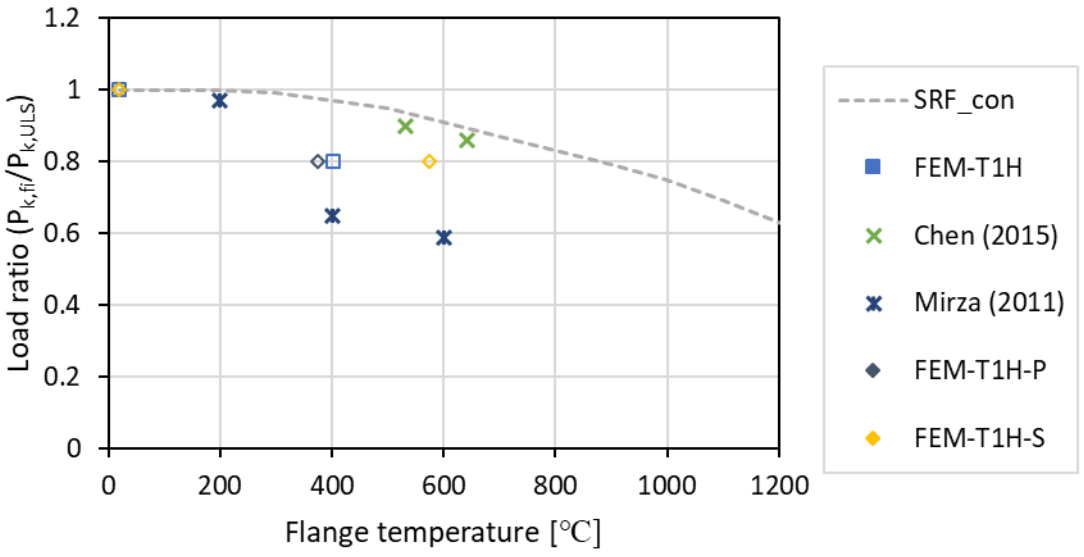

Figure 6-14. Concrete-dominated failure with different thermal conductance

The shear resistance of the 1.2-mm through-deck-welded model and 0.9-mm through-hole-welded model with respect to the flange temperature is shown in Fig. 6-15 and 6-16, respectively. It is clearly seen that the failure mode changes as the flange temperature increases. The hollow symbols indicate concrete-dominated failure, and the filled symbols represent stud shearing failure. Although a higher difference in shear resistance was observed at ULS owing to the concrete strength, deck thickness, and stud welding method, the shear resistance of the two models become equal under elevated temperature as the failure mode is stud shearing.

Modelling results and the corresponding design guidance of EC4-1-2 (2014) are plotted in the same graph in Fig. 6-15 and 6-16. In the case of the stud shearing failure, the design guidance of the T2H model (EC4 (stud-T2H)) excessively underestimates the shear resistance, because the deck reduction factor was included in calculating the shear resistance at both ULS and FLS. The shear connection is governed not by the deck geometry but by the thermally degraded strength around the shear stud area at high temperature. The stud shearing design guidance of the T1H model (EC4 (stud-T1H)) is the same as the solid slab specimen, because the calculated transverse deck reduction factor (k_t) of the T1H model was 1. It also gives a conservative estimation compared to all the modelling results of the transverse deck models, including the 0.9-mm through-hole-welded models.

Critical parameters such as the deck thickness, welding method, and concrete strength affect the determination of the shear resistance of the transverse deck specimen at ULS. However, their influence diminished at high temperature, considering the shear resistance shown in Fig. 6-15 and 6-16. The stud shearing criterion of the solid slab specimen is appropriate for the shear resistance prediction at high temperature. Thus, the failure mode should be considered to achieve an optimised estimation in a transverse deck application.

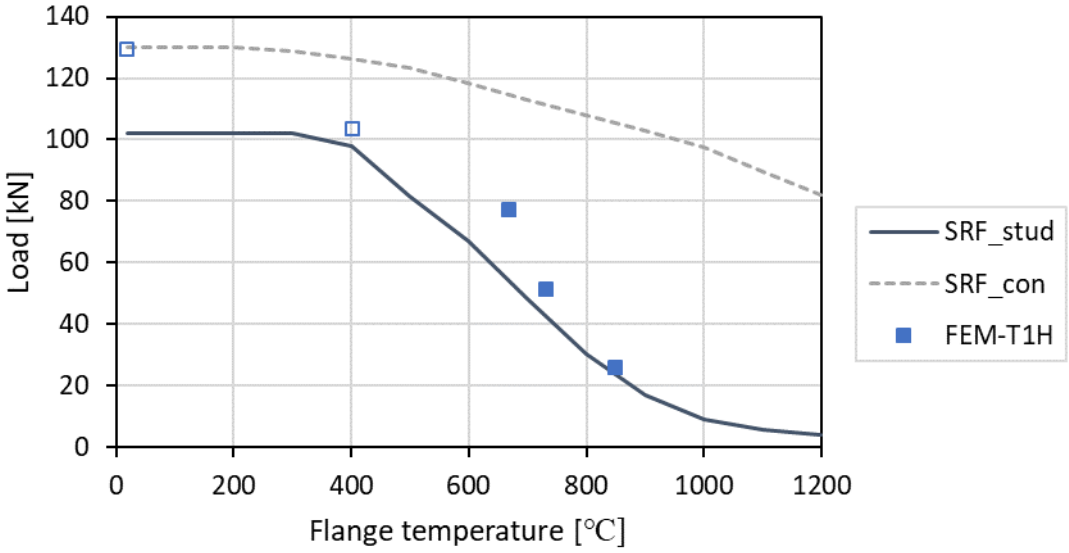

Figure 6-15. Shear resistance and flange temperature relationship of T1H model compared with EC4-1-2 (2014)

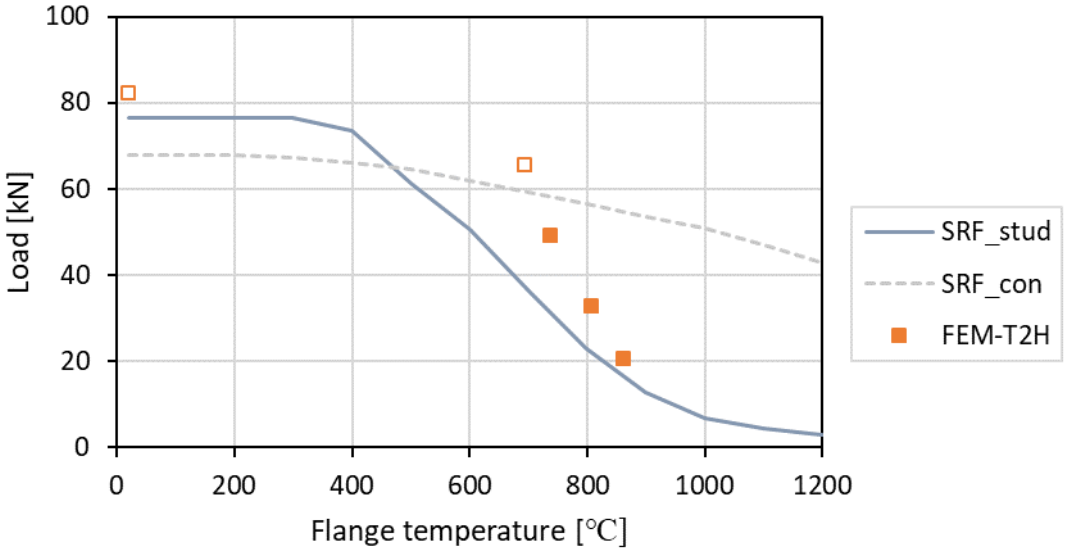

Figure 6-16. Shear resistance and flange temperature relationship of T2H model compared with EC4-1-2 (2014)

6.3. Parametric study on the deck thickness

Several experimental and numerical investigations revealed that the deck thickness should be considered in determining the structural capacity of the shear connection at ULS, because the shear resistance of the transverse deck specimen increased when adopting a thicker deck (Hanswille, 1993; Johnson and Yuan, 1998a; Qureshi *et al*., 2011b). The deck yield stress applied over an area (deck breadth × deck thickness) contributes to resisting an imposed load at the shear connection. EC4-1-1 (2009) presents the deck reduction factor depending on the deck thickness, and a further reduction is added when the deck thickness is less than 1 mm. The effectiveness of the deck thickness at high temperature was investigated using the developed finite element model in this section.

6.3.1. Finite element model

A finite element model with a different deck thickness was developed on the basis of the 1.2-mm through-deck-welded model (T1H-ULS), which was already verified with the experimental data as presented in Fig. 5-16. A 0.9-mm-thick deck was selected because it is the recommended minimum value in BS 5950-3.1 (2010), and a 1.5-mm-thick deck was also modelled for comparison. A difference of approximately 5 % in the shear resistance was obtained in comparison to the 1.2-mm deck model. Qureshi *et al*. (2011b) reported the same variation of the shear resistance in accordance with the deck thickness change by a numerical investigation at ULS. The obtained shear resistances with the variation in the deck thickness are summarised in Table 6-3.

Table 6-3. Shear resistance regarding the deck thickness at ULS

Model	Deck thickness [*mm*]	P [*kN*]	P_k [*kN*]	P_{EC4} [*kN*]	P_k / P_{EC4}
T109	0.9	122	110	87	1.26
T1	1.2	129	116	102	1.14
T115	1.5	136	122	102	1.20

The developed numerical models were combined with thermal analysis data to evaluate the deck thickness effect on the shear connection in a fire. The only difference among the thermal analysis models was the deck thickness, and identical heating conditions were applied. The same temperature distributions were obtained from the thermal analysis. Identical loading conditions were applied to compare the shear stud behaviour at high temperature. The failure mode transition from concrete-dominated failure to stud shearing was also found. The structural capacity of the shear connection obtained from the parametric study is presented in Table 6-4.

Table 6-4. Parametric studies on the deck thickness at FLS

Model	Deck thickness [*mm*]	Load [*kN*]	Load ratio	Fire resistance time [*min*]	Flange temp. [°C]	Failure mode
T1H09R80	0.9	103.2	0.85	11.7	282	Concrete
T1H09R60		77.4	0.63	35.8	651	Shearing
T1H09R40		51.6	0.42	48.4	726	Shearing
T1H09R20		25.8	0.21	70.9	835	Shearing
T1H15R80	1.5	103.2	0.76	21.2	473	Concrete
T1H15R60		77.4	0.57	40.1	681	Shearing
T1H15R40		51.6	0.38	53.8	734	Shearing
T1H15R20		25.8	0.19	74.3	846	shearing

6.3.2. Effect of the deck thickness

Although the deck thickness is an influencing parameter in determining the shear resistance at ULS, its effect decreases as the temperature rises. A noticeable gap in a fire resistance time was observed when inducing 103.2 kN as plotted in Fig. 6-17; this is approximately 80 % of the shear resistance at ULS. A thicker deck model was more robust to fire at a given load level, because the deck contributes to resisting the applied load at the initial stage of heating. However, a similar fire resistance was obtained when the applied load was less than 77. 4 kN as shown in Fig. 6-18. The shear resistance was determined by the thermal degradation of the stud root area, because all the observed failure modes were stud shearing. This indicates that the deck nearby the shear stud also influences the shear resistance. However,

its effect decreases as the temperature increases, because the deck strength was also degraded by the induced heat.

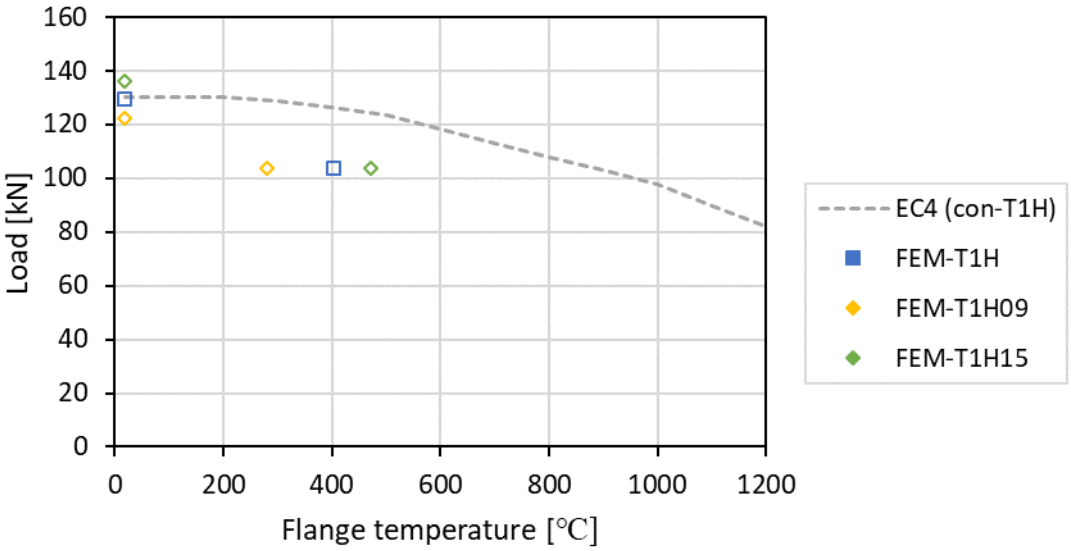

Figure 6-17. Shear resistance and flange temperature relationship with different deck thickness in the case of the concrete-dominated failure

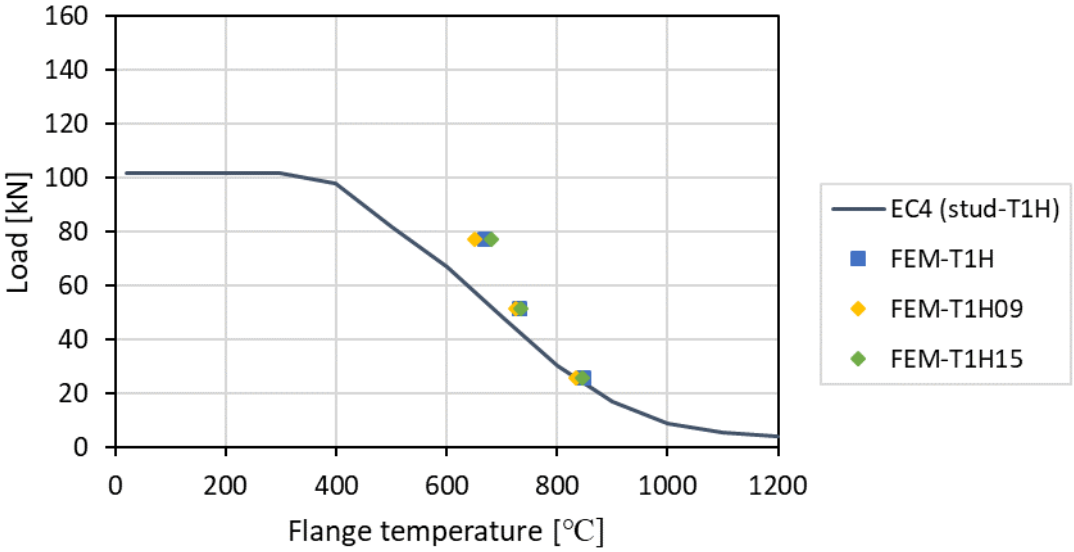

Figure 6-18. Shear resistance and flange temperature relationship with different deck thickness in the case of the stud shearing failure

The proposed SRF gives a more conservative estimation than the Eurocode design as depicted in Fig. 6-19 when the cause of failure is the stud shearing. The current EC4-1-2 (2014) defines the concrete temperature as 40 % of the flange temperature to calculate the shear resistance in a fire condition. The thermal reduction factor of the compressive strength of concrete ($k_{c,\theta}$) is multiplied by an obtained shear resistance at ULS according to the defined concrete temperature. Quevedo and Silva (2013) argued that following the definition of the concrete temperature of EC4-1-2 (2014) could overestimate the shear resistance, because it was obtained at the mid-height of the shear stud. They recommended the concrete temperature as 60 % of the flange temperature using a thermal analysis by measuring at a quarter height of the shear stud. However, modifying the concrete temperature cannot simulate the shear resistance reduction caused by the concrete-dominated failure in the transverse deck models. Investigating the shear resistance reduction with reference to the flange temperature, the design guidance of the concrete-dominated failure overrates the shear resistance as plotted in Fig. 6-20. A further reduction is required in a medium-to-low-temperature region to illustrate the strength reduction caused by the concrete-dominated failure.

A new design formula for the concrete-dominated failure was proposed based on the parametric studies. It is expressed with respect to the flange temperature because the location of the critical failure region changes as the temperature rises. It has a concave shape curve to take into account a failure at the initial stage of fire and the failure mode change. The concrete-dominated failure was observed when inducing less than 60 % of the shear resistance at ULS from the modelling result and relevant literature. Thus, the maximum resistance reduction was assumed to be 40 % at 700 °C. The anticipated failure mode beyond that temperature is stud shearing.

The proposed formula is as follows:

$$\begin{aligned} SRF_{concrete} &= 1 && \theta_{flange} \leq 20℃ \\ SRF_{concrete} &= a\theta_{flange}^2 + b\theta_{flange} + c && 20℃ < \theta_{flange} \leq 700℃ \\ SRF_{concrete} &= 0.6 && 700℃ < \theta_{flange} \leq 1000℃ \end{aligned} \quad (6\text{-}4)$$

where, $a = 8 \times 10^{-7}$; $b = -1.15 \times 10^{-3}$; $c = 1.02$
θ_{flange}: steel flange temperature

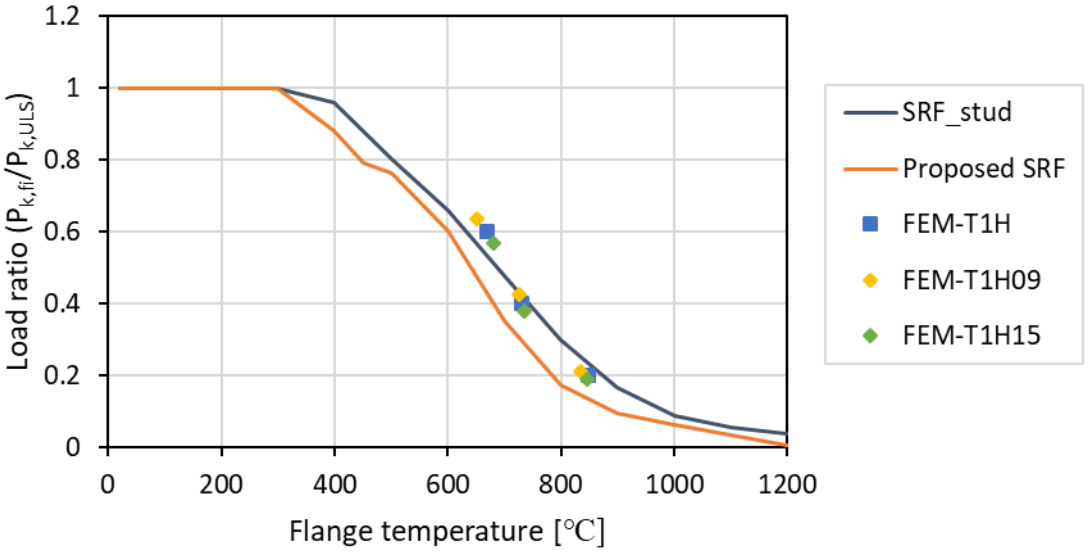

Figure 6-19. Shear resistance reduction with different deck thickness in the case of the stud shearing failure

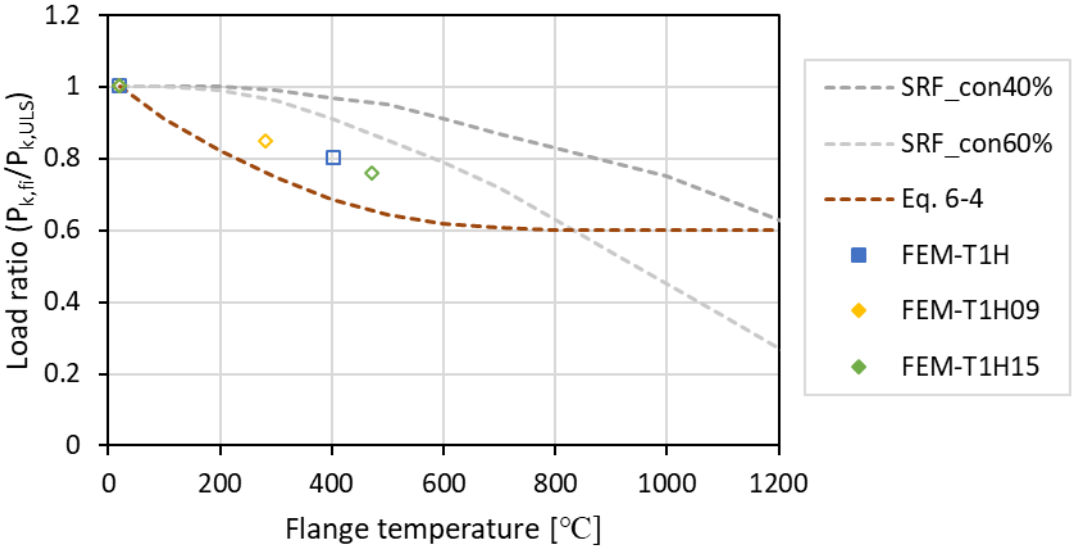

Figure 6-20. Shear resistance reduction with different deck thickness in the case of the concrete-dominated failure

The relationship between the shear resistance and fire resistance time is shown in Fig. 6-21 with variations of the deck thickness. When the shear resistance was 103 kN, the 1.5-mm deck model withstood 21.2 min of the ISO 834 standard fire, and the 0.9-mm deck model failed at 11.7 min. The difference in the fire resistance time decreased to 3.4 min when inducing 25.8 kN. As the failure mode turns from concrete-dominated failure into stud shearing, the difference in the fire resistance time was also reduced by half. This indicates that the effect of the deck thickness decreases as the temperature increases.

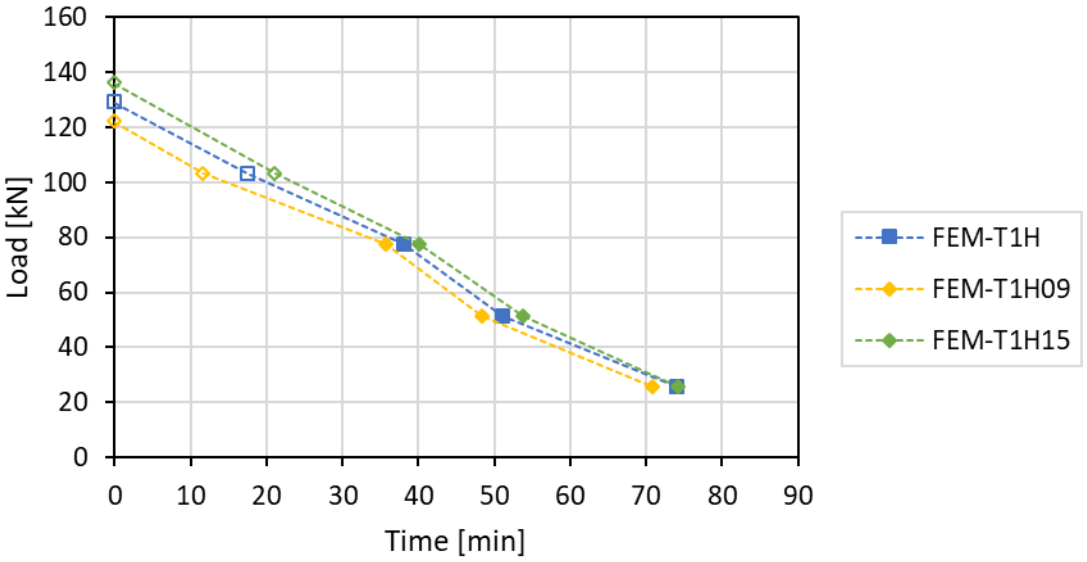

Figure 6-21. Shear resistance and fire exposure time relationship depending on the deck thickness

6.4. Parametric study on the stud welding method

It has been proven that the shear connection in a transverse deck slab is affected by the stud welding method at ULS. Stark and Hove (1991) and Hanswille (1993) reported the shear resistance change with respect to the stud welding method. A through-deck-welded shear stud shows a stronger shear connection than a directly welded shear stud via deck holes. The current EC4-1-1 (2009) defines the upper limit of the deck reduction factor with reference to the stud welding method, which gives a further reduction in the case of the directly welded shear connection. However, little evidence is available as to whether this

effect of the stud welding method is still valid at high temperature. In this section, the capacity of the shear connection with a focus on the stud welding method is investigated under the elevated temperature.

6.4.1. Finite element model

The numerical model based on the 0.9-mm through-hole-welded specimen was selected for the parametric study. The developed model (T2) was modified to have a through-deck-welded shear stud by connecting the stud weld collar to the steel deck. The material properties and configurations of the specimen are the same, except for the stud welding method. The modified model (T2w) gives the shear resistance of 103 kN at approximately 2 mm slip, which shows a higher value than the through-hole-welded model, as depicted in Fig. 6-22. Comparing the characteristic shear resistance based on EC4-1-1 (2009), a similar estimation was found depending on the stud welding method, as presented in Table 6-5.

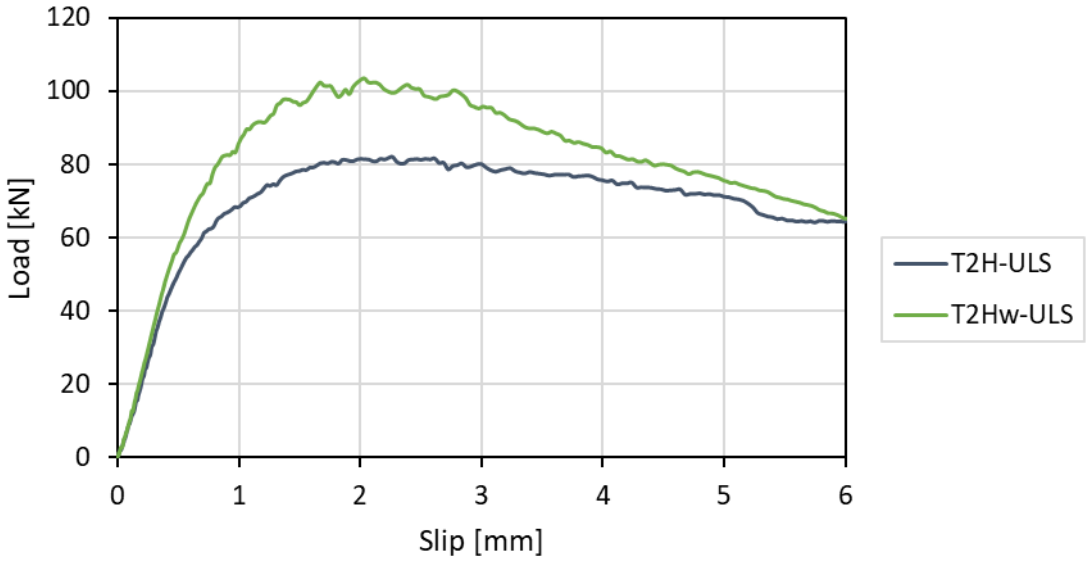

Figure 6-22. Load–slip curves depending on the stud welding method at ULS

Table 6-5. Shear resistance regarding the stud welding method at ULS

Model	Stud welding	P [*kN*]	P_k [*kN*]	P_{EC4} [*kN*]	P_k / P_{EC4}
T2	Direct welding through deck hole	82	73.8	68	1.1
T2w	Through-deck welding	103	92.7	77	1.2

The temperature distribution of the through-deck-welded model (T2Hw) was obtained by applying the same heating conditions of the through-hole-welded model (T2H), which was verified with the experimental data. Both the thermal models show an identical temperature profile at the web, flange, and stud with respect to the fire exposure time. The obtained temperature data were incorporated into the ULS model (T2w) to investigate the stud behaviour in a fire.

The shear resistance reduces as the temperature increases, and the failure mode transition was also found at around 80 % to 60 % of the load ratio, as presented in Table 6-6. Failure does not occur within 90 min of heating when applying 20 % of the shear resistance at ULS. A 25 % load model was used to compare the stud behaviour, which shows a shearing failure at the top surface of the flange at 83.9 min of the fire elapsed time.

Table 6-6. Parametric studies on the stud welding method at FLS

Model	Stud welding	Load [*kN*]	Load ratio	Fire resistance time [*min*]	Flange temp. [°C]	Failure mode
T2HwR80	Through-deck welding	82.4	0.8	33.1	595	Concrete
T2HwR60		61.8	0.6	49.7	708	Shearing
T2HwR40		41.2	0.4	68.9	775	Shearing
T2HwR25		25.8	0.25	83.9	849	Shearing

6.4.2. Effect of the stud welding method

The stud welding method does influence the determination of the shear resistance at ULS, although its effect decreases as the temperature rises. The difference in the shear resistance was 21 kN at ULS, whereas the difference in the fire resistance time was 0.4 minutes when inducing the same load of 32.8 kN at FLS. The modelling results with regard to the flange temperature are plotted in Fig. 6-23. The stud shearing and concrete-dominated failure are illustrated in accordance with the Eurocode and proposed design in the same graph. As the cause of failure is the thermal degradation of the stud root area, the proposed stud shearing design guidance shows a conservative estimation at high temperatures, regardless of the stud welding method.

The strength reduction with respect to the flange temperature is also considered with the Eurocode guidance in Fig. 6-24. Concrete-dominated failure was observed at both models when the SRF was less than 0.8. Comparing the concrete design guidance (SRF_con), the modelling data fell in an unconservative range. Although the calculated shear resistance may not exceed the concrete failure criterion by several safety parameters in the design guidance, the current SRF cannot illustrate the shear resistance reduction in the case of the concrete-dominated failure.

The shear resistance reduction ratio is affected by its ULS value. Eighty percent of the shear resistances at ULS was 82.4 kN and 65.6 kN for the through-deck and through-hole-welded models, respectively. The through-deck-welded model (T2Hw) fractured 16 min earlier than the through-hole-welded model in the given load level of 0.8. This time difference was decreased as the applied load level was reduced because the load difference also became small. Consequently, the proposed design for the stud shearing failure (EC4 (stud)) shows a conservative estimation, regardless of the stud welding method when stud shearing failure occurs at high temperature.

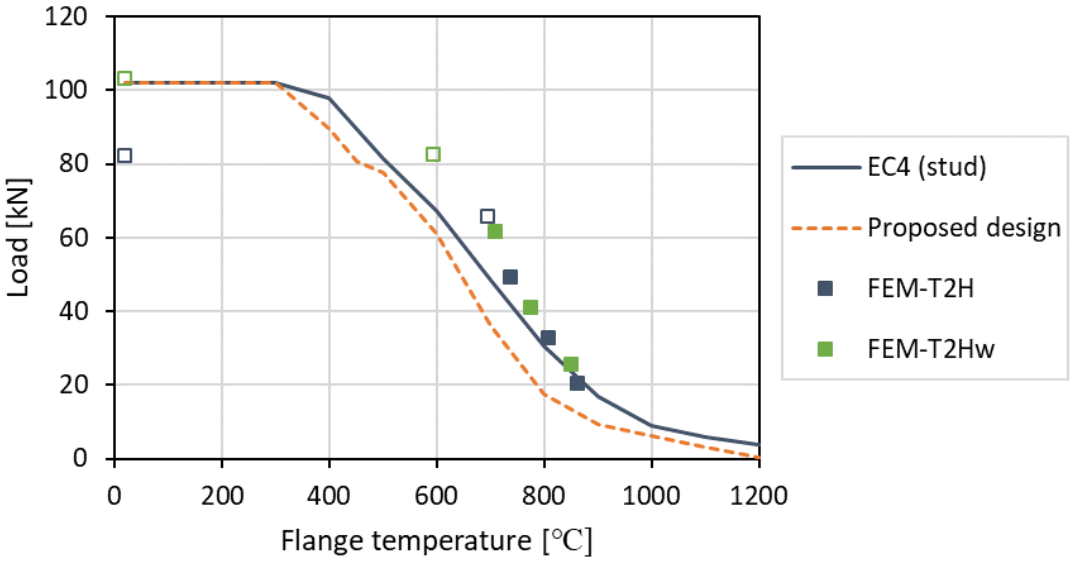

Figure 6-23. Comparisons of the shear resistance depending on the stud welding method

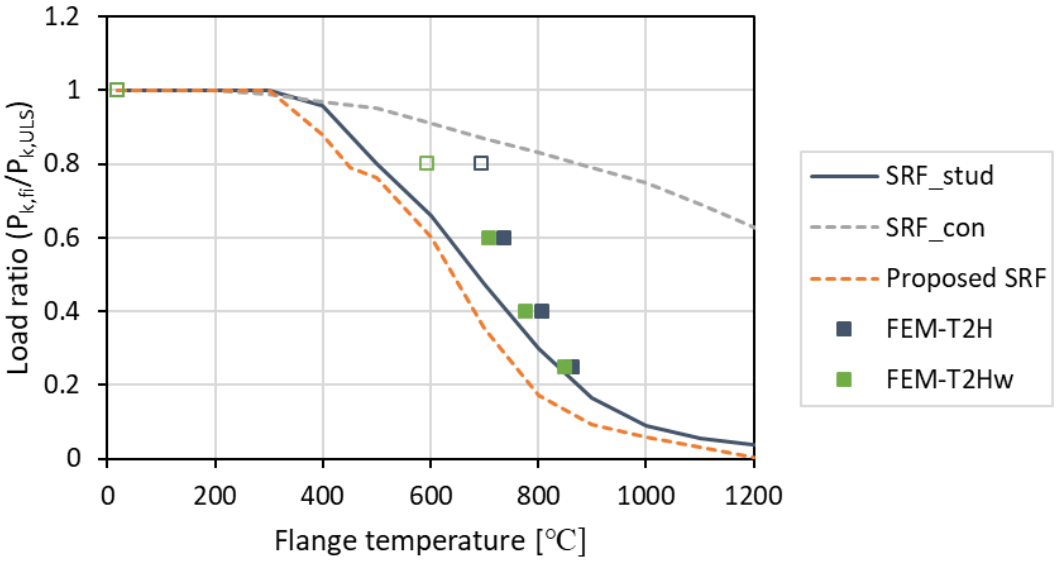

Figure 6-24. Comparisons of the strength reduction depending on the stud welding method

The shear resistance reduction in accordance with the fire exposure time was analysed. It gives the same reduction rate after approximately 50 min of heating, as shown in Fig. 6-25. All the failure modes were stud shearing beyond that time, which means that the thermal degradation at the stud root is a critical parameter of the shear connection. Thus, the effect of the stud welding method disappears when the failure mode changes to stud shearing in a fire.

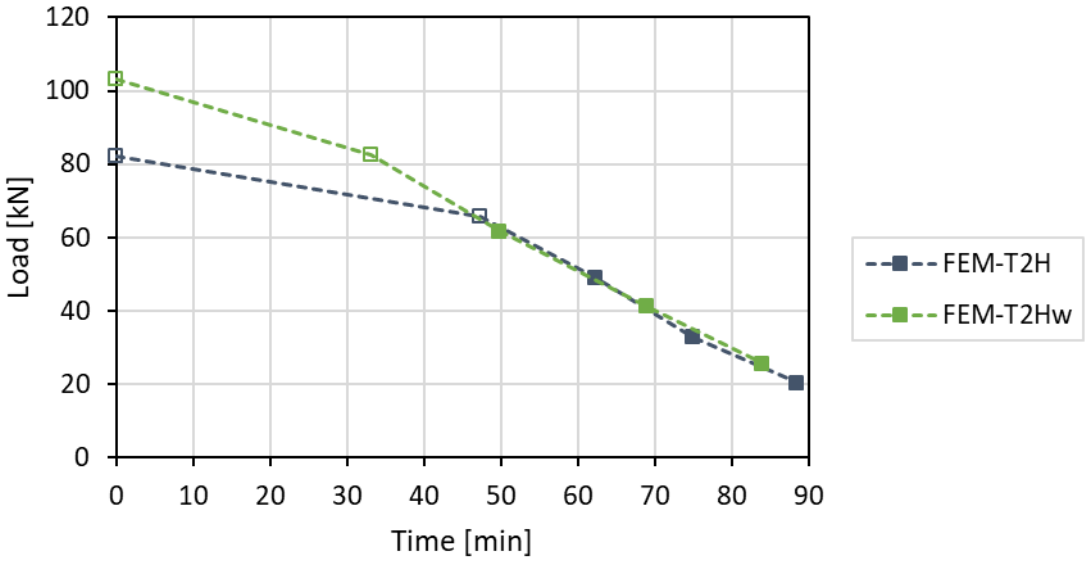

Figure 6-25. Shear resistance and fire exposure time relationship depending on the stud welding method

6.5. Parametric study on the stud location in a trough

It is generally accepted that the strength of the shear resistance changes with respect to the shear stud location in a trough in a transverse deck composite beam. AISC 360-10 (2010) provides a 25 % reduction in the shear resistance calculation for an unfavourably positioned shear stud compared to a shear stud in a favourable position. BS 5950-3.1 (2010) recommends the shear stud to be placed centrally or on the favourable side. EC4-1-1 (2009) also suggest that the shear stud be arranged centrally within a trough for a single stud, and at staggered positions for a pair of studs in a trough to consider a shear resistance reduction depending on the stud location in a trough. All the design codes and the experimental results supposed an ambient condition, and the effect of the stud location in a fire condition has not been investigated. The capacity of the shear connection with a focus on the stud location at high temperature is evaluated in this section.

6.5.1. Finite element model

A transverse deck model with an unfavourably positioned stud (T1UF) was developed on the basis of the 1.2-mm through-deck-welded model (T1). The only difference is the location of the shear stud. The stud welded position in a trough is illustrated in Fig. 6-26. The material properties and configuration of the specimen are the same. Mottram and Johnson (1990) reported that the shear resistance reduced by 35 % when the stud located on the unfavourable side compared to the shear stud in the favourable position. Rambo-Roddenberry (2002) also showed a degradation of approximately 30 % in the shear resistance according to the stud location in a rib. The shear resistance of the developed models was 129 kN and 87 kN when the stud was positioned on the favourable and unfavourable side, respectively. The shear connection with the unfavourably positioned stud was 32 % weaker than the favourably positioned stud, which corresponds to the experimental investigations mentioned above.

The obtained shear resistance at ULS is compared with EC4-1-2 (2014) and AISC 360-10 (2010) in Table 6-7. Both design codes provide a conservative estimation in the case of the favourably positioned shear connection. However, the Eurocode overrates the shear resistance when the shear stud is embedded in the unfavourable position. AISC 360-10

(2010) provides a similar prediction because it has a reduction parameter concerning the stud location in a trough. The shear resistance reduction with respect to the stud location should be considered in EC4-1-2 (2014) because a staggered arrangement is also recommended when incorporating a pair of studs in a trough.

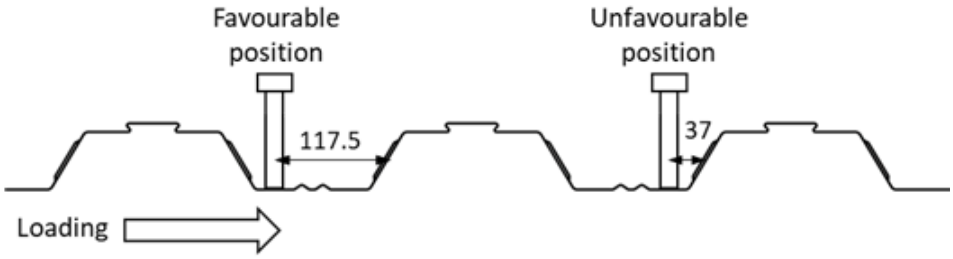

Figure 6-26. Shear stud location of the developed model

Table 6-7. Shear resistance regarding the stud location at ULS

Model	Stud location	P [*kN*]	P_k [*kN*]	P_{EC4} [*kN*]	P_{AISC} [*kN*]	P_k/P_{AISC}	P_k/P_{EC4}
T1	Favourable	129	116	102	100.8	1.15	1.13
T1UF	Unfavourable	86.8	78.1	102	80.6	0.97	0.77

Johnson and Yuan (1998b) reported that the rib punching failure occurred in a ductile manner when the shear stud was embedded in an unfavourable position. The developed model with the unfavourably positioned stud also shows a ductile load–slip curve, as plotted in Fig. 6-27. Investigating the damage contour of the unfavourable stud model (T1UF), a concrete crushing area near the shear stud in the loading direction with a deck bulge and severe damage of the deck at the opposite side of the crushed concrete were found, as depicted in Fig. 6-28. This is a common phenomenon of rib punching failure which was successfully illustrated in the developed model.

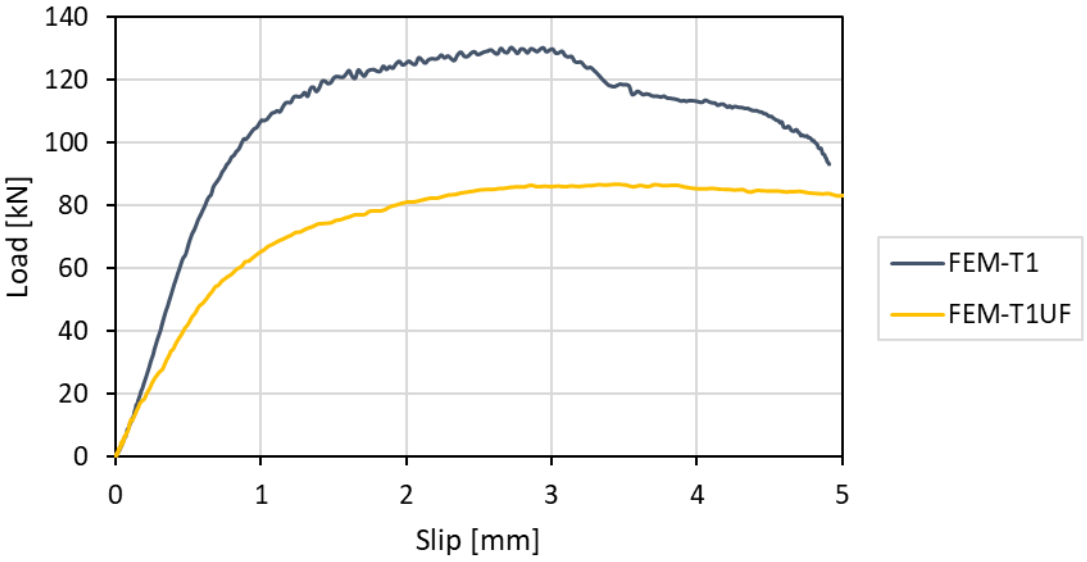

Figure 6-27. Load-slip curves according to the stud location

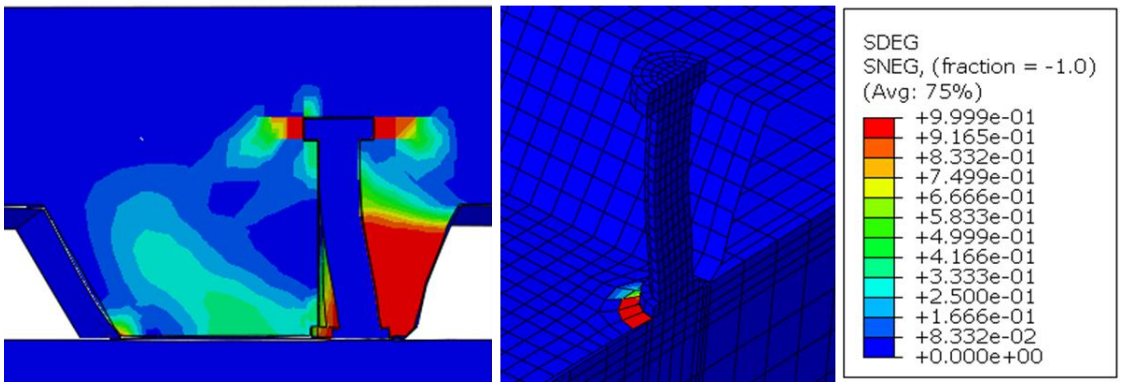

Figure 6-28. Damage contour of the unfavourably positioned stud model at ULS

In order to investigate the shear resistance of the unfavourably positioned stud in a fire, a thermal analysis model was developed first. The temperature profile of the developed model was the same as the reference model shown in Fig. 5-10, because the shear stud was embedded symmetrically in a trough. A parametric study with a different load level showed that the failure mode changes from rib punching to stud shearing beyond the flange temperature of approximately 800 °C, as presented in Table 6-8.

Table 6-8. Parametric studies on the unfavourably positioned stud at FLS

Model	Stud location	Load [*kN*]	Load ratio	Fire resistance time [*min*]	Flange temp. [°C]	Failure mode
T1HUFR80	Unfavourable	69.4	0.8	33.1	624	Rib punching
T1HUFR60		52.1	0.6	47.0	720	Rib punching
T1HUFR40		34.7	0.4	65.7	803	Shearing
T1HUFR20		17.4	0.2	86.6	893	Shearing

6.5.2. Effect of the stud location in a trough

The shear resistance with a variation in the stud location at high temperature is illustrated in Fig. 6-29. The favourably positioned stud model shows a stronger shear connection at ULS in comparison with the unfavourable stud model. Different failure modes of concrete pull-out and rib punching failure were observed, depending on the stud location. The shear resistance gap of the two models reduced as the temperature increased, and the same failure mode of stud shearing occurred when the flange temperature exceeded approximately 800 °C. The proposed design also gives a conservative estimation above that temperature. This means the stud temperature is also a primary parameter to determine the shear resistance in a fire.

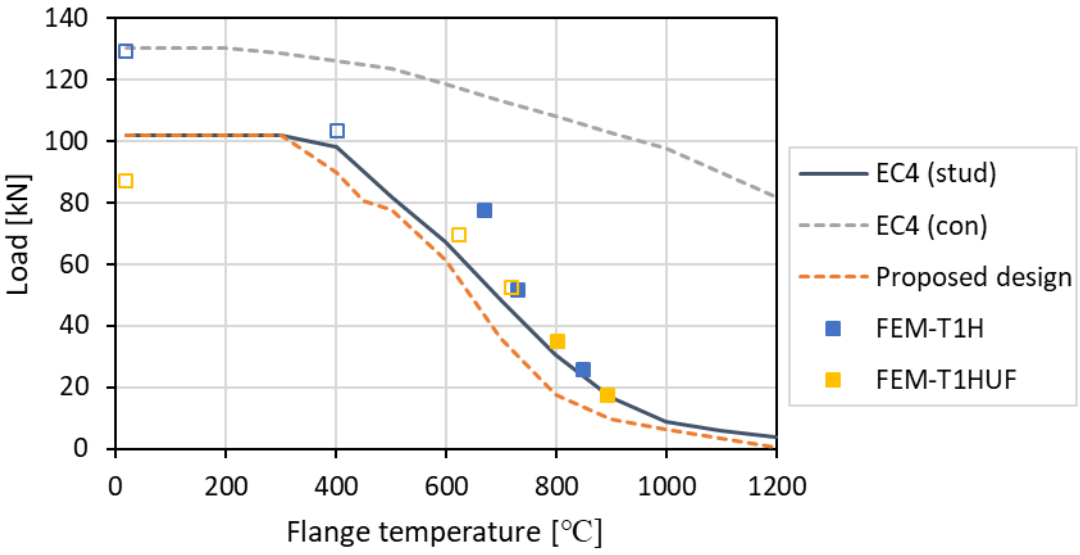

Figure 6-29. Comparisons of the shear resistance depending on the stud location

The unfavourably positioned stud model (T1HUF) seems to have a better fire resistance than the favourably positioned stud model (T1H) when comparing the load ratio according to the flange temperature, as plotted in Fig. 6-30. A comparatively longer fire elapsed time was found in the unfavourably positioned stud model because the ultimate state value of the shear resistance was different. The applied load was different at the given load ratio of 0.8; it was 103.2 kN in the favourable stud model, whereas it was 69.4 kN in the unfavourable stud model. Consequently, the unfavourable stud model appears to be more robust to fire because of the comparatively small shear resistance at ULS. The proposed design for strength reduction caused by the concrete-dominated failure in Eq. 6-4 also provides a conservative estimation regardless of the stud location at a medium-to-low temperature.

The shear resistance with regard to the fire exposure time is illustrated in Fig. 6-31. A different reduction rate was observed for less than 50 min of heating, and then the shear resistances with a different stud location coincide with each other when the failure mode changes to stud shearing in both models. This implies that the effect of the stud location decreases as the temperature rises.

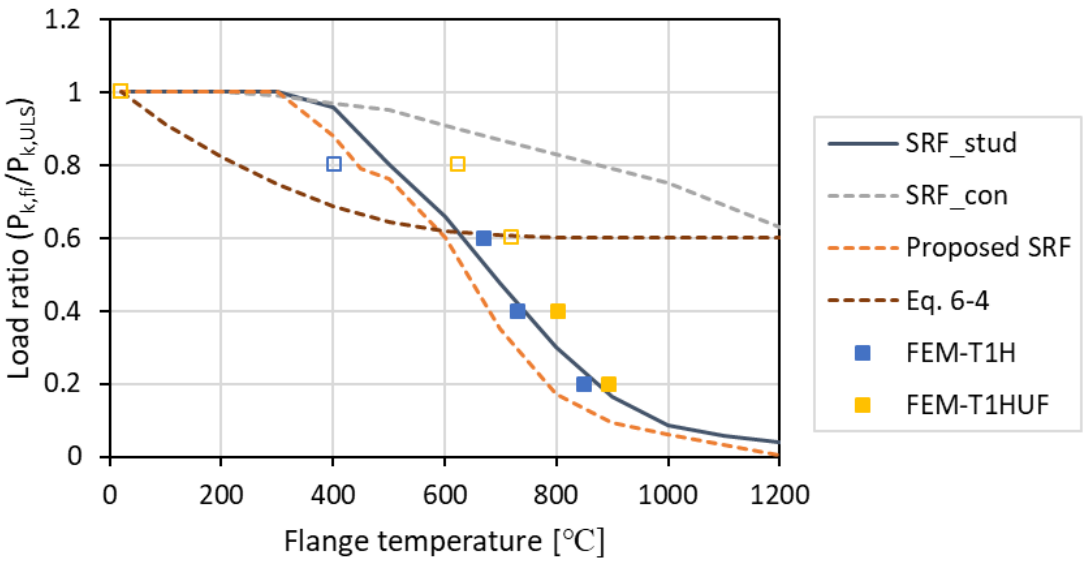

Figure 6-30. Comparisons of the strength reduction depending on the stud location

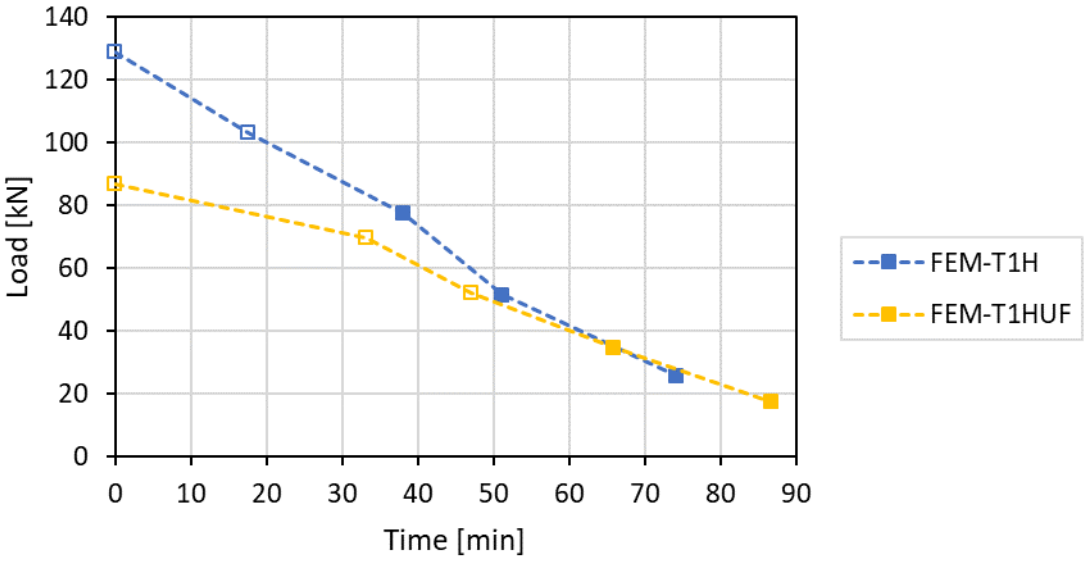

Figure 6-31. Shear resistance and fire exposure time relationship depending on the stud location

6.6. Parametric study on the stud numbers in a trough

The number of shear studs embedded in a trough affects the structural capacity of the shear connection in composite beams with a transverse deck slab. Comparing the shear resistance with a single stud and two studs in a rib, a stronger shear connection at each stud was observed in the single-stud specimen. For this reason, several design codes adopted a resistance reduction parameter with respect to the number of shear studs in a trough; when a pair of studs are used in a trough, EC4-1-1 (2009) recommends a 30 % reduction, BS 5950-3.1 (2010) provides a 46 % reduction, and AISC 360-10 (2010) suggests a 15 % reduction for each shear stud compared to the shear resistance incorporating single stud per rib. Although an extensive study regarding the stud numbers in a trough on the shear resistance was conducted at ULS, little work has been done regarding the shear resistance depending on the number of studs in a rib at FLS. The structural performance of the shear connection was examined using a parametric study by changing the number of studs in a trough under elevated temperatures.

6.6.1. Finite element model

A finite element model was developed and verified against existing literature which reported a push-out test incorporating one and two studs in a trough at ULS (Hicks, 2007). C12 concrete was used, and the characteristic cylinder compressive strength of concrete (f_{ck}) and elastic modulus of concrete (E_{cm}) were calculated according to EC2-1-1 (2014) for the numerical model. The CDP model with the dilation angle of 50° was incorporated into the developed model; the recommended values in Abaqus were adopted for the other plasticity parameters. The ultimate strength of 473 MPa was used for the stud material, because the cause of failure was concrete cracking and crushing in the experiment of Hicks (2007). Furthermore, this helps to obtain consistent modelling data at high temperature because the temperature distributions of the web, flange, and stud were referenced from the experimental results presented in this dissertation.

The structural performance with different stud strength shows the same load–slip relationship in both the single- and two-stud models shown in Fig. 6-32 and 6-33, because concrete cracking is the cause of the failure. The experimental data are identical to the modelling results, which show less than a 10 % deviation, as presented in Table 6-9.

Table 6-9. Shear resistance regarding the stud numbers per trough at ULS

Model	Stud numbers per rib	P_{FEM} [*kN*]	P_e[1] [*kN*]	P_e / P_{FEM}
1stud	1	83	84.7	1.02
2stud	2	56	51.2	0.91

[1]experimental data from Hicks (2007)

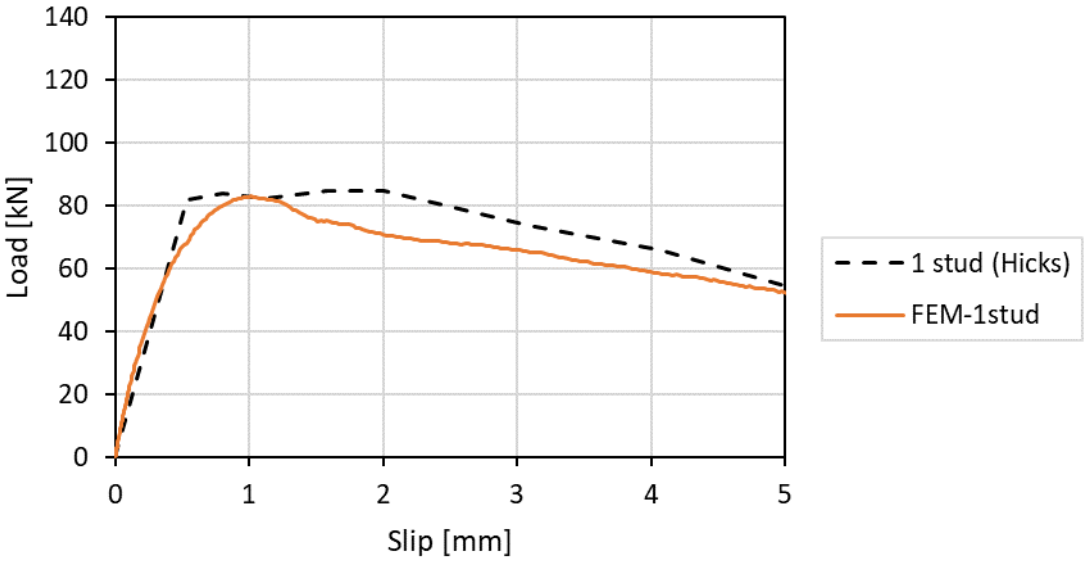

Figure 6-32. 1 Verification of the single-stud model at ULS

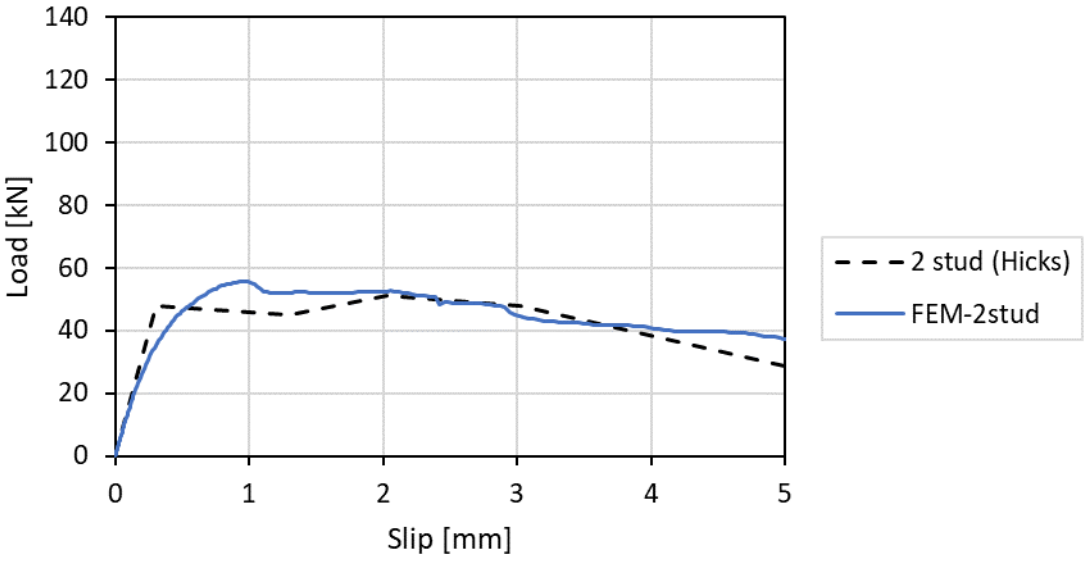

Figure 6-33. Verification of the two-stud model at ULS

A thermal model is needed to evaluate the structural capacity of the shear connection at high temperature. The calculated temperature at the web, flange, and stud were compared with the through-deck-welded model (T1H), which was already verified by the experimental data. As demonstrated in Fig. 6-34 and 6-35, the single-stud model shows good agreement for all the measuring points, whereas the stud temperature of the two-stud model presents a lower value by approximately 30 °C at 90 min of heating. The web and flange temperatures of the two-stud model successfully follow the reference value. This temperature difference at the shear stud, 5 mm from the bottom of the shear stud, was caused by the difference in the stud location. The shear stud was embedded in an off-centre position in the two-stud model, because the spacing between the studs should be conserved in a transverse deck application. On the contrary, the shear stud of the single-stud model was welded at the centre of the flange, which was directly connected to the web. Because the web part exhibits the highest temperature, the stud temperature of the single-stud model is higher when exposed to the same fire condition, as illustrated in Fig. 6-36.

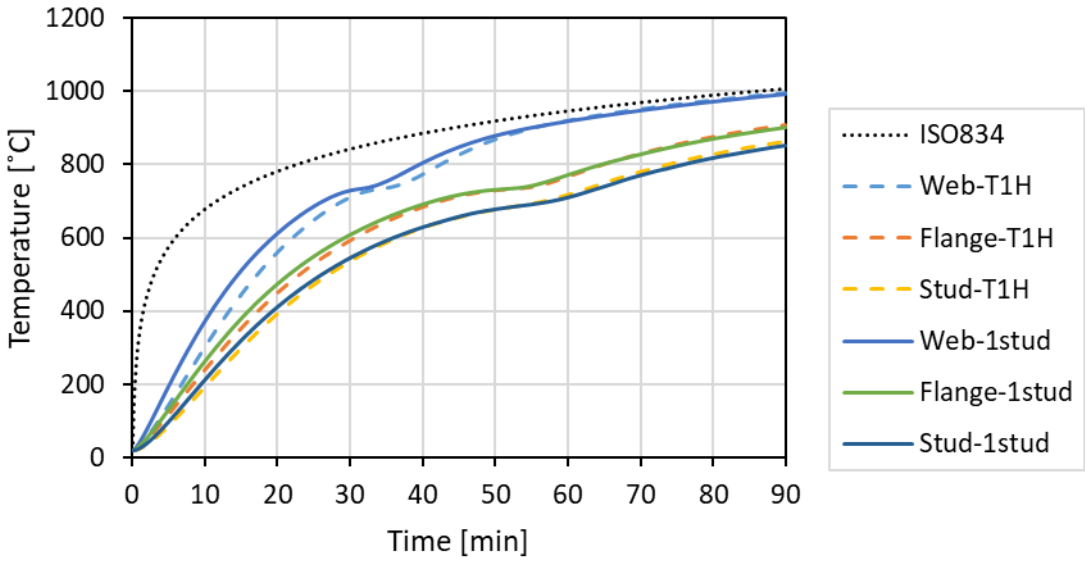

Figure 6-34. Comparisons of the temperature distributions of the single-stud model

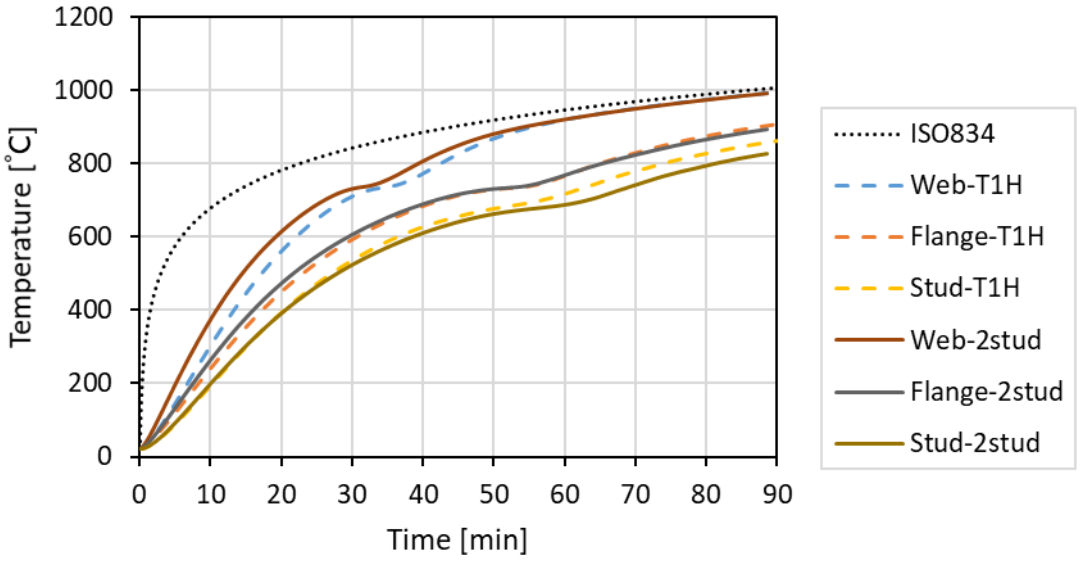

Figure 6-35. Comparisons of the temperature distributions of the two-stud model

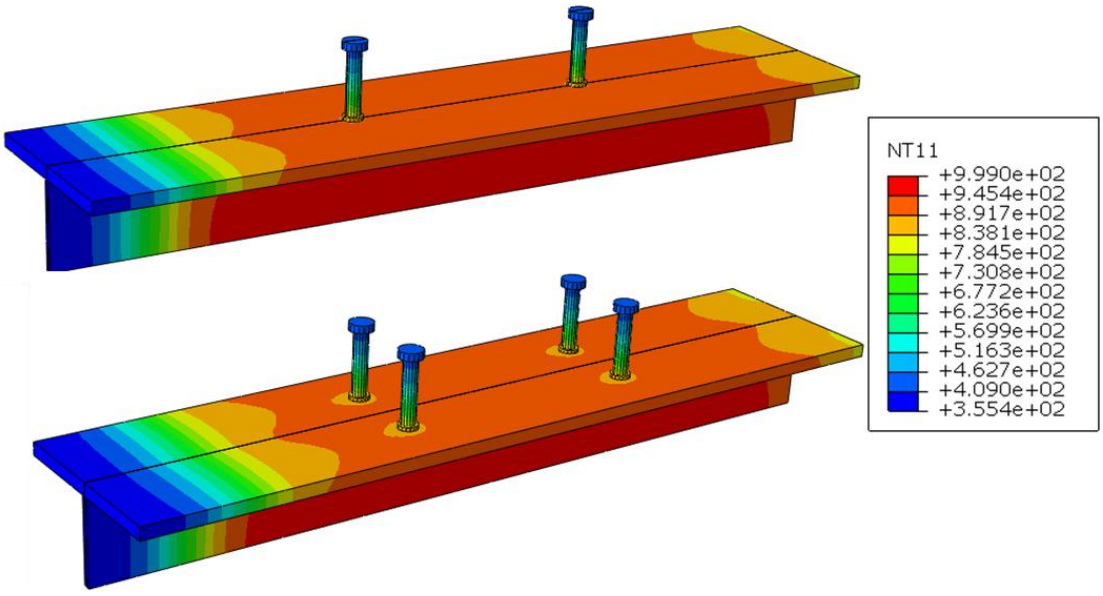

Figure 6-36. Temperature profiles of the single- and two-stud models at 90 min

The obtained temperature data were incorporated into the developed structural model with a different load. The capacity of the shear connection with respect to the stud number in a trough is summarised in Table 6-10. The shear resistance reduction was observed in both models as the fire exposure time increased. A failure mode transition was found, regardless of the stud number, and a similar fire resistance was observed when stud shearing occurred at high temperatures. The shear resistances of the 1studR30 and 2studR40 models were 24.6 and 22.4 kN, respectively, which shows 5 min difference in the fire resistance time. This indicates that the two-stud model is more robust to fire than the single stud-model in case of a fire.

Table 6-10. Parametric studies on the number of studs in a trough at FLS

Model	Embedded stud per rib	Load [*kN*]	Load ratio	Fire resistance time [*min*]	Flange temp. [°C]	Failure mode
1studR80	Single	65.6	0.8	14.4	372	Concrete
1studR60		49.2	0.6	44.3	713	Concrete
1studR40		32.8	0.4	68.6	820	Shearing
1studR30		24.6	0.3	77.9	861	Shearing
2studR80	Pair	44.8	0.8	25.7	555	Concrete
2studR60		33.6	0.6	60.9	775	Concrete
2studR40		22.4	0.4	82.8	874	Shearing
2studR30[1]		16.8	0.3	-	-	-

[1]Failure does not occur within 90 min of the heating process

6.6.2. Effect of the stud numbers in a trough

The shear resistance reduces as the flange temperature increases regardless of the number of studs in a trough. The strength reduction rate varied with respect to the number of embedded studs. The single-stud model shows a higher shear resistance at ULS, whereas the shear resistance decreases faster than the two-stud model as the temperature rises as shown in Fig. 6-37. When the concrete-dominated failure occurs, the Eurocode estimation provides an unconservative value. The proposed formula for the concrete-dominated failure successfully predicts the shear resistance reduction as depicted in Fig. 6-38. As the failure mode changes to the stud shearing due to the temperature, the proposed SRF also gives a conservative estimation without relation to the number of studs in a trough as presented in Fig. 6-39.

Because the ultimate state value of the two-stud model is comparatively small, a small resistance reduction with a longer fire resistance time was found at the given SRF of 0.8; the difference in the shear resistance was 21 kN, as shown in Table 6-10. As the fire exposure time increases, the shear resistance corresponds with each other as displayed in Fig. 6-40. This indicates that the capacity of the shear connection increases proportionally to the number of embedded shear studs at high temperature. Although employing two studs in a trough provides an adverse effect on the shear connection at ULS, increasing the number of studs in a trough gives a beneficial effect on the shear connection at FLS, because the cause of failure changes from the concrete cracking to stud shearing. Therefore, embracing two studs in a trough is efficient to achieve the integrity of the shear connection in a fire.

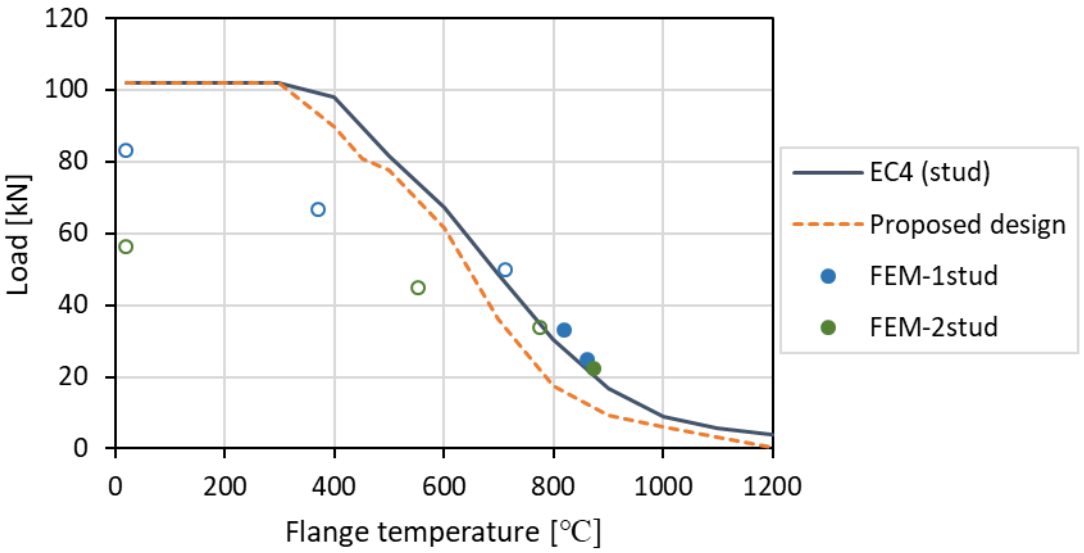

Figure 6-37. Comparisons of the shear resistance depending on the number of studs in a trough

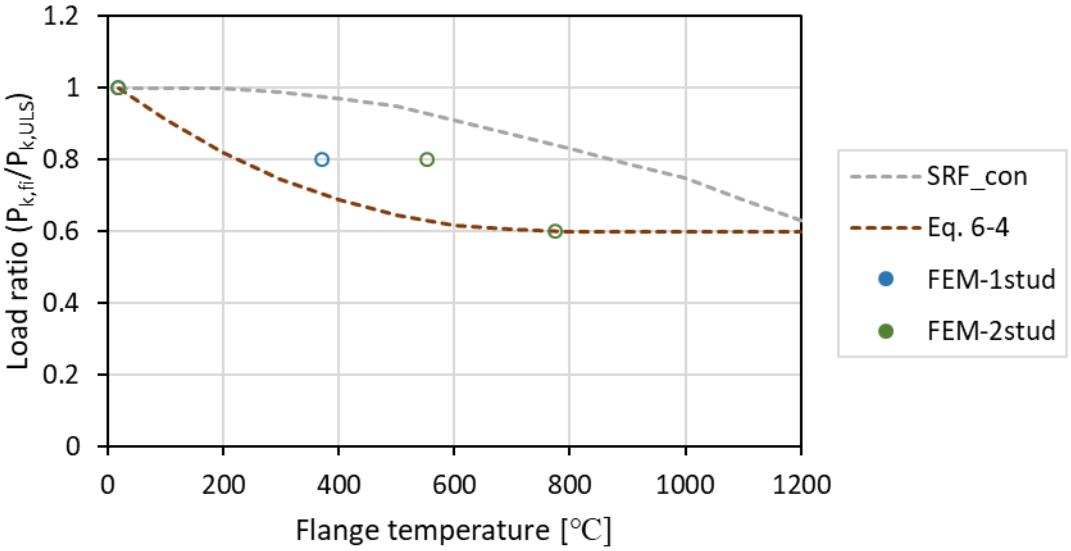

Figure 6-38. Comparisons of the strength reduction depending on the number of studs in a trough in the case of the concrete-dominated failure

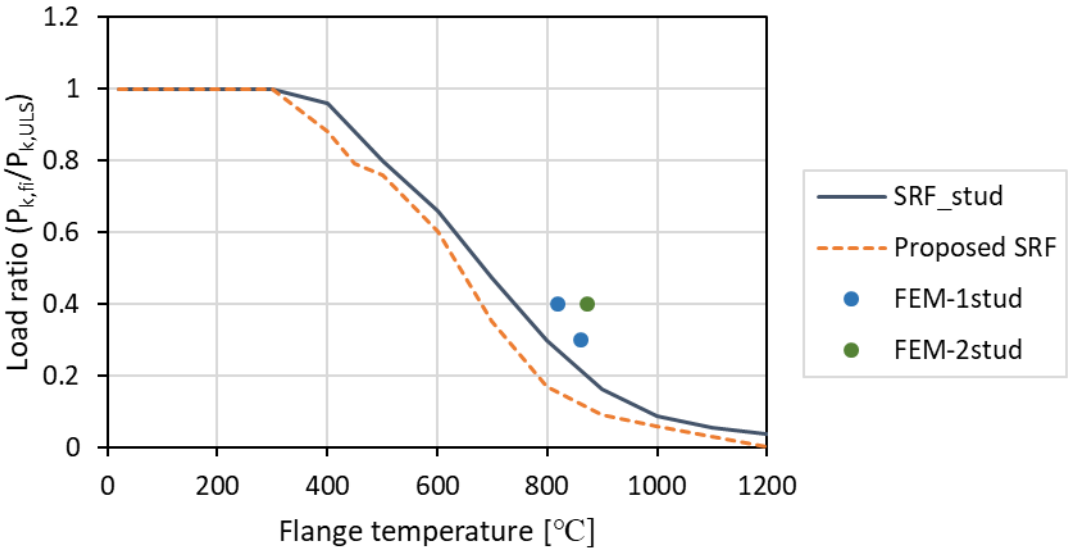

Figure 6-39. Comparisons of the strength reduction depending on the number of studs in a trough in the case of the stud shearing failure

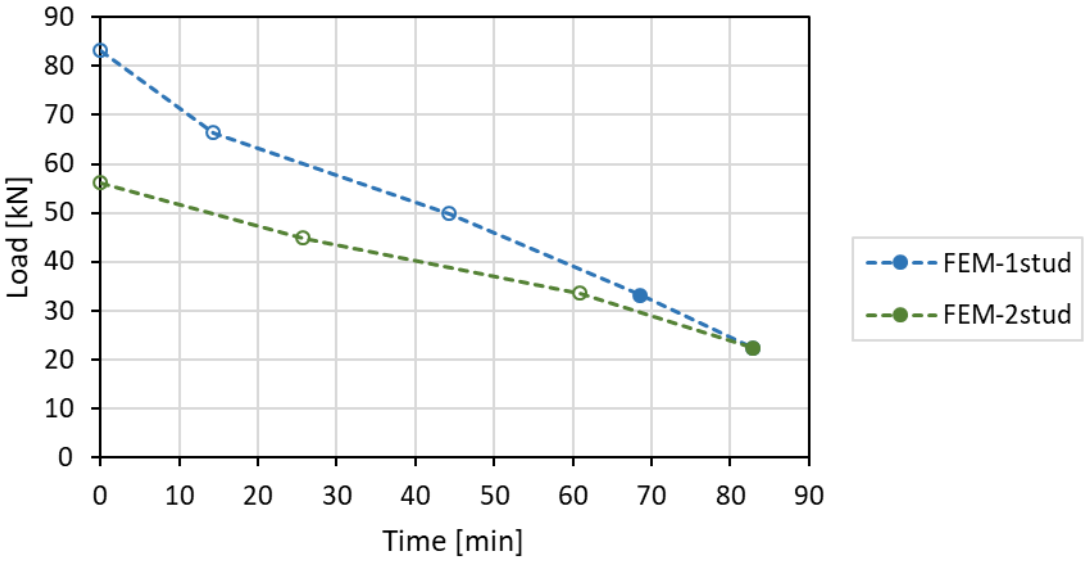

Figure 6-40. Shear resistance and fire exposure time relationship depending on the number of studs in a trough

6.7. Conclusions

The developed thermomechanical model was used to investigate the shear stud behaviour in a fire incorporating different construction conditions, such as the slab type, deck thickness, stud welding method, stud location, and number of studs in a trough. Although all the conditions mentioned above are influenced on the shear connection at ULS, those effects disappear as a temperature rises, because thermal degradation determines the shear connection failure at the stud root area. Moreover, employing two studs in a trough was found to be beneficial on the shear connection under elevated temperature. The location of the maximum stress at the shear stud moves to the upward direction along the stud shank, and the damaged concrete area beside the shear stud also reduced as the failure mode changed. A new design formula was proposed with reference to the flange temperature to consider this failure mode transition. A temperature and area at the shearing location were adopted instead of using fixed values in calculating the shear resistance caused by the stud shearing. The SRF of the concrete-dominated failure was also proposed to reflect a rapid strength degradation at the initial stage of heating. It gives a conservative estimation under various temperature conditions compared to the experimental and modelling results.

Chapter 7
CONCLUSIONS AND FUTURE WORK

7.1. Conclusions

The aim of this research was to investigate the behaviour of headed shear studs in composite beams with a transverse deck slab under elevated temperatures. This has been carried out through experimental and numerical studies, which provide insight into the structural behaviour and failure mechanism of the shear connection in a fire. A three-dimensional thermomechanical finite element model was developed, and it was verified against experimental results from relevant literature as well as the experiments conducted in this thesis. A parametric study and experimental investigation revealed that the structural performance of the shear connection is governed by thermal degradation around shear studs. It subsequently determines the failure mode and shear resistance. Overall this research has attained the objectives of this thesis, and the following conclusions are drawn:

1. High-temperature push-out tests have shown that the cause of failure turns to shear at the stud root area, regardless of the slab type, as the temperature rises. The failure mode changed from concrete-dominated failure to stud shearing in transverse deck specimens, and the same failure mode of stud shearing is observed in solid slab specimens.

2. Although the failure mode at ULS is different with respect to slab types, the observed failure mode at FLS is the same, stud shearing. Moreover, the location of the shearing moves to the top side of the steel beam flange as temperature rises. Investigating stress distributions at the shear stud, the stress applied to the stud

weld collar decreases when the fire elapsed time increases. Accordingly, a concrete crushed area is also reduced owing to the thermal degradation of the stud material. A stud shearing criterion with reference to the flange temperature is proposed adopting a temperature and area of the shearing location to estimate the shear resistance as the failure mode changes to the stud shearing. It gives a conservative estimation compared with the numerical and experimental data form the relevant literature.

3. A new strength reduction factor (SRF) for concrete-dominated failure was also proposed, as the current EC4-1-2 (2014) overrates the experimental and numerical results. It shows a conservative estimation in the medium-to-low-temperature region, and the maximum reduction rate is 40 % because the failure mode changes beyond that value.

4. Plasticity parameters of the CDP model such as α, β, γ, and dilation angle are proposed as linear and exponential functions of temperature. As temperature rises, the shape of the failure surface becomes triangular, and the concrete behaviour becomes more ductile. It successfully illustrates cracking and crushing of concrete slabs in the push-out test.

5. When the shear resistance is evaluated by incorporating a different deck thickness, 0.9 mm, 1.2 mm, and 1.5 mm, it shows differences of approximately 5 % in comparison to 1.2-mm deck model with the concrete pull-out failure at ULS. As the failure mode changes to the stud shearing under elevated temperature, the effect of the deck thickness in a transverse deck specimen decreases.

6. The observed shear resistance shows around 20 % difference depending on the welding method at ULS. This effect disappears as the failure mode changes to the stud shearing at high temperature. As a result, the shear resistance is decided by the thermal degradation of the stud material.

7. It has been a proven fact that a favourably positioned stud provides a stronger shear connection than the shear stud welded in an unfavourable position at ULS owing to a different cause of failure. When the failure mode becomes the same as the stud shearing at high temperature, the effect of the stud location diminishes.

8. A parametric study regarding the number of studs in a trough provides compelling evidence that embracing two studs in a trough is more robust to fire than adopting a single stud. This is an opposite phenomenon in comparison with the shear resistance at ULS. The structural capacity of the shear connection was proportional to the number of embedded shear studs at high temperature because the cause of failure changed from concrete cracking in a rib to shearing near the stud root area.
9. The current design code of EC4-1-2 (2014) cannot estimate the shear resistance reduction caused by the concrete-dominated failure because it highly affected by temperature distribution around the shear stud. Moreover, the effect of the transverse deck disappears when the failure mode changes to the stud shearing at high temperature. The new design guidance was proposed with a combination of the concrete-dominated failure and stud shearing cases. This could eventually lead to modification of the design code for composite beams in a fire.

7.2. Recommendations for future work

Based on the results presented in this study, the following issues are proposed for further investigations:

1. These findings are promising and should be explored with further experimental investigations. More high-temperature push-out tests should be conducted at medium-to-low temperatures to validate the finite element models and obtain experimental data.
2. As EC4-1-2 (2014) recommends the use of a staggered arrangement, the structural performance of the shear connection depending on the number of studs in a trough and their arrangement should be evaluated experimentally.
3. Further studies regarding a temperature gradient around the shear stud under various conditions such as applying an intumescent material on steel beams, bolted stud assemble with insulation materials, and different heating rate considering possible combustibles in a building are needed.

REFERENCES

American National Standard Institute (ANSI) (2010) AISC 360-10 Specification for Structural Steel Buildings.

Ansari, F. and Li, Q. (1998) High-Strength Concrete Subjected to Triaxial Compression. ACI Materials Journal, 95(6), 747-755.

ArchiEXPO (2018) Kingspan structure. Available from: http://www.archiexpo.com/prod/kingspan-structure/product-90888-884114.html [Accessed 01 August 2018].

Australian Standard (2003) AS 2327.1 Composite structures Part 1: Simply supported beams. Standard Australia

Bahr, O., Schnumann, P., Bollen, B. and Bracke, J. (2013) Young's modulus and Poisson's ratio of concrete at high temperatures: Experimental investigations, Materials and Design, 45, 421-429.

Baltay, P. and Gjelsvik, A. (1990) Coefficient of friction for steel on concrete at high normal stress, Journal of Material Civil Engineering, 2, 46-49.

Bangash, M. Y. H. (2001) Manual of numerical methods in concrete. Thomas Telford Publishing.

British Standard Institution (BSI) (1965), CP 117-1: 1965 Composite construction in structural steel and concrete. Simply-supported beams in building.

British Standard Institution (BSI) (1994) DD ENV 1994-1-1 Eurocode 4: Design of composite steel and concrete structures – Part 1.1: General rules and rules for buildings. British Standard Institute.

British Standard Institution (BSI) (2005), BS 5400-5: 2005 Steel, concrete and composite bridges. Code of practice for design of composite bridges, London.

British Standard Institution (BSI) (2008), *Eurocode 2* - design of concrete structures – Part 1-2: General rules – Structural fire design, BS EN 1992-1-2: 2004, London.

British Standard Institution (BSI) (2009), *Eurocode 3*: Design of steel structures – Part 1-2: General rules Structural fire design, EN 1993-1-2: 2005, London.

British Standard Institution (BSI) (2009), *Eurocode 4* - design of composite steel and concrete structures – Part 1-1: General rules and riles for buildings, EN 1994-1-1: 2004, London.

British Standard Institution (BSI) (2010), BS 5950-3.1: 1990+A1:2010 Structural use of steelwork in building. Design in composite construction. Code of practice for design of simple and continuous composite beams, London.

British Standard Institution (BSI) (2013) *Eurocode 1* – Actions on structures – Part 1-2: General actions – Actions on structures exposed to fire, BS EN 1991-1-2: 2002, London.

British Standard Institution (BSI) (2014), *Eurocode 2* - design of concrete structures – Part 1-1: General rules and rules for buildings, BS EN 1992-1-2: 2004, London.

British Standard Institution (BSI) (2014), *Eurocode 4* - design of composite steel and concrete structures – Part 1-2: General rules – Structural fire design, BS EN 1994-1-2: 2005, London.

British Standard Institution (BSI) (2018), BS EN ISO 13918: 2018 Welding – Studs and ceramic ferrules for arc stud welding, London.

Candappa, D. C., Sanjayan, J. G. and Setunge, S. (2001) Complete Triaxial Stress-Strain Curves of High-Strength Concrete. Journal of materials in civil engineering, 13, 209-215.

Carreira, D. J. and Chu, K. (1985) Stress-Strain Relationship for Plain Concrete in Compression, ACI Journal, 82, 797-804.

Chen, L.-Z., Ranzi, G., Jiang, S.-C., Tahmasebinia, F. and Li, G.-Q. (2015). Behaviour and design of shear connectors in composite slabs at elevated temperatures. Journal of Constructional Steel Research, 115, 387–397.

Chen, Ling-Zhu, Li, Guo-Qiang and Jiang, Shou-Chao (2012) Experimental studies on the behavior of headed stud shear connectors at elevated temperatures, Proceedings of the 7th International Conference on Structures in Fire, Zurich, Switzerland, June, 257-266.

Chen, W. F. (2007) Plasticity in reinforced Concrete, J. Ross Publishing edition.

Choi, S., Han, S., Kim, S., Nadjai, A., Ali, A. and Choi, J. (2009) Performance of Shear Studs in Fire, Application of Structural Fire Engineering, Czech Technical University in Prague, 490-495.

Cornelissen, H. A. W., Hordijk, D. A. and Reinhardt, G. W. (1986) Experimental determination of crack softening characteristics of normalweight and lightweight concrete, Heron, 31, 2, 45-56

Dara, S. (2015) Behavior of the Shear Studs in Composite Beams at Elevated Temepratures. PhD thesis, University of Texas at Austin.

Darwin, D. and Pecknold, D. A. (1977) Analysis of cyclic loading of plane R/C structures, Computer and Structures, 7, 137-147.

Department for Communities and Local Government (DCLG) (2013) The Building Regulations 2010. Approved Document B: Fire Safety. Volume 2: Building other than dwelling houses (2006 edition incorporating 2007, 2010 and 2013 amendments).

Ding, J. and Wang, Y. C. (2008) Realistic modelling of thermal and structural behaviour of unprotected concrete filled tubular columns in fire. Journal of Constructional Steel Research, 64, 1086-1102.

Döinghaus, P., Goralski, C. and Will, N. (2003). Design Rules for Composite Structures with High Performance Steel and High Performance Concrete. High Performance Materials in Bridges.

EUR 9886 EN (1985) Eurocode No. 4: Common unified rules for composite steel and concrete structures. Commission of the European Communities.

Fisher, J. W. (1970) Design of Composite Beams with Formed Metal Deck, AISC Engineering Journal, 7(3), 88-96.

Gernay, T., Millard, A. and Franssen, J.-M. (2013). A multiaxial constitutive model for concrete in the fire situation: Theoretical formulation. International Journal of Solids and Structures, 50(22-23), 3659–3673.

Ghojel, J. (2004) Experimental and analytical technique for estimating interface thermal conductance in composite structural elements under simulated fire conditions. Experimental Thermal and Fluid Science, 28, 347-354.

Gnanasambandam, C. (1995) HEADED STUD SHEAR CONNECTORS IN SOLID SLABS AND IN SLABS WITH WIDE RIBBED METAL DECK, MS thesis, University of Saskatchewan.

Goble, G.G. (1968) Shear Strength of Thin Flange Composite Specimens. In: Engineering Journal, AISC, 5(2), 62-65.

Grant, J. A., Fisher, J. W. and Slutter, R. G. (1977) Composite Beams with Formed Steel Deck, AISC Engineering Journal, 14, 24-43.

Green, S. J. and Swanson, S. R (1973) Static constitutive relations for concrete. Technical report AFWL-TR-72-244. Air force weapons laboratory.

Hammoud, R., Yahia, A., and Boukhili, R. (2014) Triaxial Compressive Strength of Concrete Subjected to High Temperatures. Journal of Materials in Civil Engineering, 26, 705-712

Han, D. J. and Chen, W. F. (1985) A nonuniform hardening plasticity model for concrete materials. Mechanics of Materials 4, 283-302.

Hanswille (1993) Shear Resistance of headed Studs with Profiled Steel Sheeting, Bergische Universität Wuppertal, 1993, Technical Paper H7 to Maintenance Group for END 1994-1-1 (Eurocode: Part 1.1).

Hawkins, N. M. and Mitchell, D. (1984). Seismic Response of Composite Shear Connections. Journal of Structural Engineering, 110(9), 2120–2136.

He, Z. and Song, Y. (2008). Failure mode and constitutive model of plain high-strength high-performance concrete under biaxial compression after exposure to high temperatures. Acta Mechanica Solida Sinica, 21(2), 149–159.

Hicks, S. (2007). Strength and Ductility of Headed Stud Connectors Welded in Modern Profiled Steel Sheeting. The Structural Engineer, 85(10), 32–38.

Hicks, S. (2009). Strength and Ductility of Headed Stud Connectors Welded in Modern Profiled Steel Sheeting. Structural Engineering International, 19(4), 415–419.

Hillerborg, M. M. and Petersson, P-E. (1976) Analysis of crack formation and crack growth in concrete by means of fracture mechanics and finite elements. Cement and Concrete Research 6, 773-782

Hordijk, D. A. (1991) Local approach to fatigue of concrete, PhD. Dissertation, Technische Universiteit Delft.

Houlsby, G. T. (1991) How the dilatancy of soils affects their behaviour, the 10th European Conference on Soil Mechanics and Foundation Engineering, Florence, Italy.

Imagawa, Y., Ohyama, O. and Kurita, A. (2012). Mechanical Properties of Shear Stud during and after Fire. Structural Engineering International, 22(4), 487–492.

International Code Council (ICC) (2017), 2018 International Building Code (IBC), International Code Council, Inc.

International Federation for Structural Concrete (FIB) (1993), CEB-FIB Model code 1990, Thomas Telford, London.

International Organization for Standardization (1999) ISO 834-1, Fire resistance tests-Elements of building Construction-Part 1: General requirements

International Organization for Standardization (2016) ISO 6892-1, Metallic materials-Tensile testing-Part 1: Method of test at room temperature

Jankowiak, T. and Lodygowski, T. (2005) Identification of parameters of concrete damage plasticity constitutive model. Foundations of Civil and Environmental Engineering 6, 53-69.

Jankowiak, T. and Lodygowski, T. (2010) Quasi-static failure criteria for concrete. Archives of Civil Engineering, LVI (2), 123-154

Jayas, B. S. and Hosain, M. U. (1988). Behaviour of headed studs in composite beams: push-out tests. Canadian Journal of Civil Engineering, 15(2), 240–253.

Jayas, B. S. and Hosain, M. U. (1989). Behaviour of headed studs in composite beams: full-size tests. Canadian Journal of Civil Engineering, 16(5), 712–724.

Johnson, R. and Oehlers, D. (1981). ANALYSIS AND DESIGN FOR LONGITUDINAL SHEAR IN COMPOSITE T-BEAMS. Proceedings of the Institution of Civil Engineers, 71(4), 989–1021.

Johnson, R. P. (2012) Designer's Guide to Eurocode 4: Design of Composite Steel and Concrete Structures:EN 1994-1-2, 2nd Edition, ICE Publishing

Johnson, R. P. and Yuan, H. (1998a). EXISTING RULES AND NEW TESTS FOR STUD SHEAR CONNECTORS IN TROUGHS OF PROFILED SHEETING. Proceedings of the Institution of Civil Engineers - Structures and Buildings, 128(3), 244–251.

Johnson, R. P. and Yuan, H. (1998b). MODELS AND DESIGN RULES FOR STUD SHEAR CONNECTORS IN TROUGHS OF PROFILED SHEETING. Proceedings of the Institution of Civil Engineers - Structures and Buildings, 128(3), 252–263.

King, S. and Richards, T. (2013) Solving Contact Problems with Abaqus, Dassault Systems

Kordina, K., Ehm, C. and Schneider, U. (1986). Effects Of Biaxial Loading On The High Temperature Behaviour Of Concrete. Fire Safety Science, 1, 281–290.

Kratzig, W. B. and Polling, R. (2004) An elasto-plastic damage model for reinforced concrete with minimum number of material parameters. Computers and Structures 82, 1201-1215

Kupfer, H. and Hilsdorf, H. K. (1969) Behaviour of concrete under biaxial stresses. ACI journal. 66(8), 656-666

Lam, D. and El-Lobody, E. (2005) Behaviour of Headed Stud Shear Connectors in Composite Beam. Journal of Structural Engineering, January 2005, 96-107.

Law, A. H. (2010) THE ASSESSMENT AND RESPONSE OF CONCRETE STRUCTURES SUBJECT TO FIRE, PhD thesis, The University of Edinburgh.

Lawson, R. M. (1997) SHEAR CONNECTION IN COMPOSITE BEAMS – INFLUENCE OF STEEL DECK SHAPE. Composite Construction in Steel and Concrete III Proceedings of an Engineering Foundation Conference, 312-324.

Lee, J. and Fenves, G. L. (1998). Plastic-Damage Model for Cyclic Loading of Concrete Structures. Journal of Engineering Mechanics, 124(8), 892–900.

Lee, J. and Fenves, G. L. (2001) A return-mapping algorithm for plastic-damage models: 3-D and plane stress formulation, International Journal for Numerical Methods in Engineering, 50, 487-506.

Lemaitre, J. (1985) A Continuous Damage Mechanics Model for Ductile Fracture. Journal of Engineering Materials and Technology, 107, 83-89.

Li, Q., and Ansari, F. (1999). Mechanics of Damage and Constitutive Relationships for High-Strength Concrete in Triaxial Compression. Journal of Engineering Mechanics, 125(1), 1–10.

Lloyd, R. M., and Wright, H. D. (1990). Shear connection between composite slabs and steel beams. Journal of Constructional Steel Research, 15(4), 255–285.

Logan, D. L. (2012) A First Course in the Finite Element Method, Fifth Edition, CL Engineering.

Lopez-almansa, F., Alfarah, B. and Oller, S. (2014) Numerical simulation of RC frame testing with damaged plasticity model comparison with simplified models. 2nd European Conference on Earthquake Engineering and Seismology, 25-29.

Lubliner, J., Oliver, J., Oller, S. and Oñate, E. (1989). A plastic-damage model for concrete. International Journal of Solids and Structures, 25(3), 299–326.

Malm, R. (2006) Shear cracks in concrete structures subjected to in-plane stresses, Royal Institute of Technology (KTH), Bulletin 88.

Maraveas, C., Swailes, T. and Wang, Y. (2012) A detailed methodology for the finite element analysis of asymmetric slim floor beams in fire, Steel Construction, 5, 191-198.

Ministry of Land, Infrastructure and Transport (MILT) (2018) Korean Building Code 2018 (KBC 2018).

Mirza, O. and Uy, B. (2009) Behaviour of headed stud shear connectors for composite steel-concrete beams at elevated temperatures. Journal of Constructional Steel Research 65(3), 662-674.

Mirza, O., Uy, B. and Krezo, S. (2011) Experimental studies on the behaviour of headed stud shear connectors for composite steel-concrete beams under elevated temperatures, Proceedings of the 7th International Conference on Steel & Aluminum Structures, Kuching, Malaysia, July.

Mottram, J. T. and Johnson, R. P. (1990) Push tests on studs welded through profiled steel sheeting, The Structural Engineer, 68(10), 187-193.

Neilsen, C. V. and Bicanic, N. (2003) Residual fracture energy of high-performance and normal concrete subject to high temperatures. Materials and Structures 36, 515-521

Newman, J. and Choo, B. S. (2003) Advanced concrete technology concrete properties. Butterworth-Heinemann.

Nguyen, H. T. and Kim, S. E. (2009) Finite element modelling of push-out tests for large stud shear connectors. Journal of Constructional Steel Research 65, 1909-1920

Oehlers, D. J. and Bradford, M. A. (1995) Composite steel and concrete structural members fundamental behaviour, Elsevier Science Ltd.

Oehlers, D. J. and Johnson, R. P. (1987) The strength of stud shear connections in composite beams, The Structural Engineer, 65(2), 44-48.

Ollgaard, J. G., Slutter, R. G., and Fisher, J. W. (1971) Shear Strength of Stud Connectors in Lightweight and Normal-Weight Concrete, AISC Engineering Journal, 8(2), 55-64.

Papanikolaou, V. K. and Kappos, A. J. (2007) Confinement-sensitive plasticity constitutive model for concrete in triaxial compression. Int. Journal of Solids and Structures 44, 7021-7048.

Pavlovic, M., Markovic, Z., Veljkovic, M. and Budevac, D. (2013) Bolted shear connectors vs. headed studs behaviour in push-out tests. Journal of Constructional Steel Research 88, 134-149

Pettersson, Ove, Magnusson, Sven Erik and Thor, Jörgen (1976) Fire Engineering Design of Steel Structures, In Bulletin of Division of Structural Mechanics and Concrete Construction, Bulletin 52 Lund Institute of Technology.

Poinard, C., Malecot, Y. and Daudeville, L. (2010) Damage of concrete in a very high stress state: experimental investigation. Materials and Structures, 43, 15-29

Popovics, S. (1973) A Numerical approach to the complete stress-strain curve of concrete, Cement and Concrete Research, 3, 583-599.

Purkiss, J. and Li, L.-Y. (2013). Fire Safety Engineering Design of Structures, Third Edition. CRC Press.

Quevedo, R. L. and Silva, V. P. (2013). Thermal analysis of push-out tests at elevated temperatures. Fire Safety Journal, 55, 1–14.

Qureshi J. (2010) Finite element modelling of steel-concrete composite structures. PhD dissertation. University of Leeds

Qureshi, J., Lam, D. and Ye, J. (2011a). Effect of shear connector spacing and layout on the shear connector capacity in composite beams. Journal of Constructional Steel Research, 67(4), 706–719.

Qureshi, J., Lam, D. and Ye, J. (2011b) The influence of profiled sheeting thickness and shear connector's position on strength and ductility of headed shear connector, Engineering Structures, 33, 1643-1656.

Rabbat, B. G., and Russell, H. G. (1985) Friction coefficient of steel on concrete or grout. Journal of Structural Engineer, 111, 505-515.

Rackham, J. W., Couchman, G. H. and Hicks, S. J. (2009) Composite Slabs and Beams using Steel Decking: Best Practice for Design and Construction, SCI Publication No. P300.

Rambo-Roddenberry, M. D. (2002) BEHAVIOR AND STRENGTH OF WELDED STUD SHEAR CONNECTORS. PhD dissertation. Virginia Polytechnic Institute and State University.

Richart, F.E., Brandtzaeg, A. and Brown, R.L. (1928) A study of the failure of concrete under combined compressive stresses. University of Illinois Bulletin no. 185.

Rodriguez, J., Martinez, F., and Marti, J. (2013) Concrete Constitutive Model, Calibration and Applications, 2013 SIMULIA Community Conference, 1-15.

Roik K, Hanswille G., and Cunze O. Lanna A. (1989) Harmonisation of the European construction codes – Eurocode 2, 4 and 8/Part 3 – Report on Eurocode 4 Clause 6.3.2 Stud connectors. Report EC4/8/88. Institut fur Konstruktiven Ingenicurbau. Ruhr-Universitat-Bochum.

Saenz, Luis P. (1964) Discussion of "Equation for the Stress-Strain Curve of Concrete" by Prakash Desayi and S. Krishnan, ACI journal, Proceedings, 61, 9, 1229-1235

Schneider, U. (1988) Concrete at High Temperatures – A General Review, Fire Safety Journal, 13, 55-68.

Shi, Z. (2009) Crack Analysis in Structural Concrete. Butterworth-Heinemann.

Siegel, R. and Howell, J. (2002) Thermal Radiation Heat Transfer 4th ed, Taylor and Francis.

Simms W. I, and Smith A. L. (2009) Performance of Headed Stud Shear Connectors in Profiled Steel Sheeting. Steel Concrete Composite and Hybrid Structures: Proceedings of the 9th International Conference on Steel Concrete Composite and Hybrid Structures (ASCCS 2009), Leeds, UK, 8-10 July 2009, 729-736

Simulia (2015) Abaqus 6.13 Analysis User's Guide. Available from: http://129.97.46.200:2080/v6.13/ [Accessed 02 April 2015]

Slutter, R. G. and Driscoll, G. C. Jr. (1962) Test results and design recommendations for composite beams, progress report no. 3, January 1962, Fritz Laboratory Reports. Paper 1803.

Smith, A. L. and Couchman, G. H. (2010) Strength and ductility of headed stud shear connectors in profiled steel sheeting. Journal of Constructional Steel Research, 66, 748-754.

Standards Council of Canada (2001) CSA-S16-01 Limit State Design of Steel Structures.

Stark, J. W. B. and Hove, B. W. E. M. (1991) Statistical analysis of push-out tests in stud connectors in composite steel and concrete structures, TNO Report BI-91-163, Delft.

Steel Construction Institute (SCI) (2010) PN001a-GB, NCCI: Resistance of headed stud shear connectors in transverse sheeting. Available from: www.steel-ncci.com,

SteelConstruction.info (2018) Cost of structural steelwork (online). Available from: https://www.steelconstruction.info/Cost_of_structural_steelwork [Accessed 01 August 2018]

Taqieddin, Ziad N. (2001) Elasto-plastic and damage modelling of reinforced concrete, PhD thesis, Louisiana state University.

The Institution of Structural Engineers. (1964) Report of a Committee on Composite Construction in Structural Steel and Concrete. Institution of Structural Engineers London.

van Mier (1986) Fracture of Concrete under Complex Stress, Heron, 31, 3, 1-90

Viest, I. M. (1956) Investigation of Stud Shear Connectors for Composite Concrete and Steel T-Beams, ACI Journal Proceedings, 52(4).

Vonk, R. A. (1992) Softening of Concrete Loaded in Compression. PhD Thesis, Eindhoven University of Technology, Netherlands.

Wang, A. J. (2011). Numerical studies on shear connectors in push-out tests under elevated temperatures. Structural Engineering and Mechanics, 39(3), 317–338.

Xu, C., and Sugiura, K. (2013) FEM analysis on failure development of group studs shear connector under effects of concrete strength and stud dimension. Engineering Failure Analysis 35, 343-354.

Xu, X. and Liu, Y. (2016). Analytical and numerical study of the shear stiffness of rubber-sleeved stud. Journal of Constructional Steel Research, 123, 68–78.

Xue, D., Liu, Y., Yu, Z. and He, J. (2012). Static behavior of multi-stud shear connectors for steel-concrete composite bridge. Journal of Constructional Steel Research, 74, 1–7.

Xue, W, Ding, M., Wang, H. and Luo, Z. (2008) Static Behavior and Theoretical Model of Stud Shear Connectors, Journal of Bridge Engineering, 13, 623-634

Yasuda, S, Michikoshi, S., Kobayashi, Y. and Narihara, H. (2008) Experimental study on shear strength of headed stud shear connectors at high temperature, Journal of Structural and Construction Engineering (Transactions of AIJ), 73 (630), 1417-1423.

Yu, T., Teng, J. G., Wong, Y. L. and Dong, S. L. (2010). Finite element modeling of confined concrete-I: Drucker–Prager type plasticity model. Engineering Structures, 32(3), 665–679.

Zhang, B. and Bicanic, N. (2002) Residual fracture toughness of normal- and high-strength gravel concrete after heating to 600℃. ACI Material Journal 99(3), 217-26.

Zhao, B. and Kruppa, J. (1993) Fire resistance of composite slabs with profiled steel sheet and of composite steel concrete beams Part 2: Composite beams, Final Report of Technical Steel Research.

APPENDIX A

Basic plasticity

A.1. Stress invariant

A stress state in a certain infinitesimal material can be expressed as nine components of stresses with three orthogonal planes: it is called Cauchy stress tensor. For the sake of simplicity, a principal stress is used because the shear stress components are regarded as zero on the principal axis. In this case, the coupled stress terms, σ_{ij} and σ_{ji}, are the same due to the complementary stress concept. The principal stress is defined as the stress that acts parallel to the principal axis.

$$\sigma = \begin{pmatrix} \sigma_{11} & \sigma_{12} & \sigma_{13} \\ \sigma_{21} & \sigma_{22} & \sigma_{23} \\ \sigma_{31} & \sigma_{32} & \sigma_{33} \end{pmatrix} = \begin{pmatrix} \sigma_1 & 0 & 0 \\ 0 & \sigma_2 & 0 \\ 0 & 0 & \sigma_3 \end{pmatrix} \quad \text{(A-1)}$$

[Cauchy stress] [Principal stress]

It is useful to express a material property as invariant values which are independent to coordinate systems. The principal stress invariants are composed of the first, second, and third values as follows:

$$\det \begin{vmatrix} \sigma_{11} - \sigma & \sigma_{12} & \sigma_{13} \\ \sigma_{21} & \sigma_{22} - \sigma & \sigma_{23} \\ \sigma_{31} & \sigma_{32} & \sigma_{33} - \sigma \end{vmatrix} = 0 \quad \text{(A-2)}$$

$$\sigma^3 - I_1\sigma^2 - I_2\sigma - I_3 = 0 \quad \text{(A-3)}$$

The coefficients of σ series are defined as the invariants, and the stress order is generally regarded as $\sigma_1 > \sigma_2 > \sigma_3$.

$$\begin{aligned} I_1 &= \sigma_1 + \sigma_2 + \sigma_3 \\ I_2 &= -(\sigma_1\sigma_2 + \sigma_2\sigma_3 + \sigma_3\sigma_1) \end{aligned} \quad \text{(A-4)}$$

$$I_3 = \sigma_1\sigma_2\sigma_3$$

where σ_i : the principal stress

An actual stress can be divided into a hydrostatic and deviatoric stress. The hydrostatic stress only affects the volume change of materials, and the deviatoric stress is related to the shape change, i.e., the deviatoric stress plays a prominent role in distortion of materials.

$$\sigma = \begin{pmatrix} \sigma_{11} & \sigma_{12} & \sigma_{13} \\ \sigma_{21} & \sigma_{22} & \sigma_{23} \\ \sigma_{31} & \sigma_{32} & \sigma_{33} \end{pmatrix} = \begin{pmatrix} \sigma_m & 0 & 0 \\ 0 & \sigma_m & 0 \\ 0 & 0 & \sigma_m \end{pmatrix} + \begin{pmatrix} \sigma_{11}-\sigma_m & \sigma_{12} & \sigma_{13} \\ \sigma_{21} & \sigma_{22}-\sigma_m & \sigma_{23} \\ \sigma_{31} & \sigma_{32} & \sigma_{33}-\sigma_m \end{pmatrix}$$

[stress tensor] [mean stress] [deviatoric stress]

Diviatoric stresses can be defined as:

$$s_{ij} = \sigma_{ij} - \delta_{ij}\sigma_m \quad \text{(A-5)}$$

where σ_m : the mean stress
δ_{ij}: the Kronecker delta

The eigenvalues of the deviatoric stress can be calculated in the same manner of the principal stress invariants: the third order characteristic equation.

$$s^3 - J_1 s^2 - J_2 s - J_3 = 0 \quad \text{(A-6)}$$

The diviatoric stress invariants are derived and expressed as the principal deviatoric stresses:

$$\begin{aligned} J_1 &= s_1 + s_2 + s_3 = 0 \\ J_2 &= -(s_1 s_2 + s_2 s_3 + s_3 s_1) \\ &= \frac{1}{6}[(\sigma_1 - \sigma_2)^2 + (\sigma_2 - \sigma_3)^2 + (\sigma_3 - \sigma_1)^2] \\ J_3 &= s_1 s_2 s_3 = I_3 + \frac{1}{3} I_1 I_2 + \frac{2}{27} I_1^3 \end{aligned} \quad \text{(A-7)}$$

where s_i : the deviatoric stress

A.2. Haigh-Westergaard stress space

It is useful to express a yield surface by a hydrostatic and deviatoric stress to understand the stress state of materials. The Haigh-Westergaard stress space is a kind of cylindrical coordinate system which expresses the stress state in the forms of the hydrostatic stress (ξ), deviatoric stress (ρ), and lode angle (θ_L). These three special axes are expressed by the principal stresses of material as follows:

$$\xi = \frac{1}{\sqrt{3}} I_1$$
$$\rho = \sqrt{2J_2}$$
$$cos\, 3\theta_L = \frac{3\sqrt{3}J_3}{2J_2^{\frac{3}{2}}} \qquad \text{(A-8)}$$

where I_1 : the first invariant of stress tensor

J_2 : the second invariant of the stress deviator

J_3 : the third invariant of the stress deviator

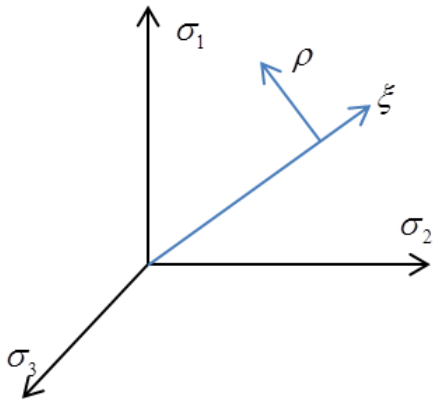

Figure A-1. Haigh-Westergaard stress space

A π-plane is the plane that is expressed by ρ and θ when the hydrostatic pressure is zero. It can visualize the yield surface more intuitively with respect to the hydrostatic stress. For example, the von Mises yield surface is shaped as a circle because it is independent on the hydrostatic axis. On the other hand, the Drucker-Prager yield surface has a cone shape

because its yield surface changes regard to the magnitude of the hydrostatic stress as shown in Fig. A-2.

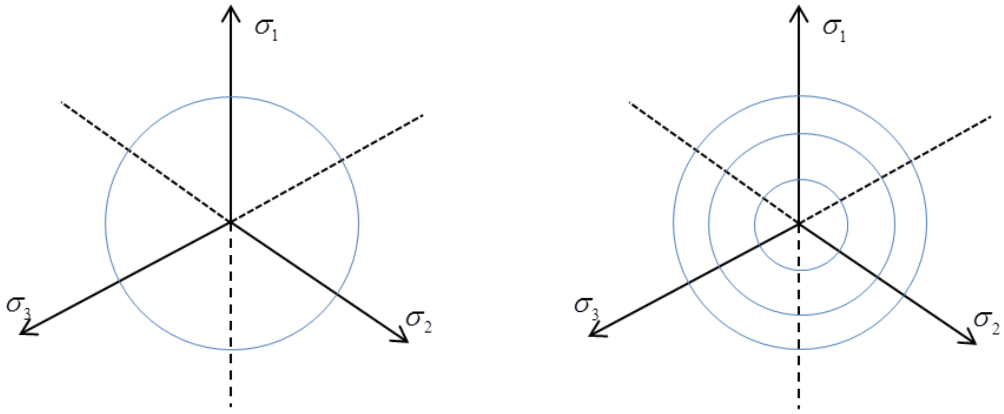

(a) von Mises criterion (b) Drucker-Prager criterion

Figure A-2. Yield surface in π-plane

A.3. Deviatoric stress with load angle

The relationship between the principal stresses and lode angle can be derived using a trigonometric identity and eigenvalues of the deviatoric stress tensor. A cosine function with a certain angle θ_L is

$$\begin{aligned}\cos(\theta_L + 2\theta_L) &= \cos\theta_L \cos 2\theta_L - \sin\theta_L \sin 2\theta_L \\ &= \cos\theta_L\,(cos^2\theta_L - sin^2\theta_L) - sin\theta_L(sin\theta_L cos\theta_L + cos\theta_L sin\theta_L) \\ &= cos^3\theta_L - 3sin^2\theta_L cos\theta_L \\ &= cos^3\theta_L - 3(1 - cos^2\theta_L)cos\theta_L \\ &= 4cos^3\theta_L - 3cos\theta_L\end{aligned}$$

$$\text{Therefore,}\quad cos^3\theta_L - \frac{3}{4}cos\theta_L - \frac{1}{4}cos3\theta_L = 0 \qquad \text{(A-9)}$$

where,

$$sin(\alpha \pm \beta) = sin\alpha\, cos\beta \pm cos\alpha\, sin\beta$$
$$cos(\alpha \pm \beta) = cos\alpha\, cos\beta \mp sin\alpha\, sin\beta$$
$$sin^2\alpha + cos^2\alpha = 1$$

The eigenvalue of the deviatoric stress is:

$$s^3 - J_2 s - J_3 = 0 \qquad \text{(A-10)}$$

Let the deviatoric stress $s = \rho cos\theta_L$, Eq. A-10 can be rewritten as

$$cos^3\theta_L - \frac{J_2}{\rho^2}cos\theta_L - \frac{J_3}{\rho^3} = 0 \qquad \text{(A-11)}$$

Comparing terms in Eq. A-9 and A-11,

$$\rho = \frac{2\sqrt{J_2}}{\sqrt{3}} \qquad \text{(A-12)}$$

$$cos3\theta_L = \frac{4J_3}{\rho^3} = \frac{3\sqrt{3}J_3}{2\sqrt{J_2^3}} \qquad \text{(A-13)}$$

The angle of $3\theta_L$ is in the range of 0 to π because the value of $\cos 3\theta_L$ is always within -1 to 1 due to its periodic property. Therefore, the angle θ_L should be within the range of 0 and $\pi/3$. All the possible value of $\cos 3\theta_L$ is $\cos(\theta_L \pm 2\pi n)$ due to the cyclic nature of cosine function. The deviatoric stress in a certain point can be expressed by the three principal stresses when assuming $\sigma_1 > \sigma_2 > \sigma_3$ and $s = \rho\cos\theta_L$ (Chen, 2007).

$$\begin{bmatrix} s_1 \\ s_2 \\ s_3 \end{bmatrix} = \begin{bmatrix} \sigma_1 \\ \sigma_2 \\ \sigma_3 \end{bmatrix} - \begin{bmatrix} \sigma_m \\ \sigma_m \\ \sigma_m \end{bmatrix} = \frac{2}{\sqrt{3}}\sqrt{J_2}\begin{bmatrix} cos\theta_L \\ cos\left(\theta_L - \frac{2}{3}\pi\right) \\ cos\left(\theta_L + \frac{2}{3}\pi\right) \end{bmatrix} \quad \text{(A-14)}$$

where σ_m : the mean stress $(= (\sigma_1 + \sigma_2 + \sigma_3)/3)$

APPENDIX B

Stress calculation procedure of the CDP model

When conducting the push-out test, concrete element near the shear stud exhibits a triaxial compression. A bearing stress of concrete changes with respect to the stress state of the applied force due to its pressure-dependent property of material. A compressive stress in a triaxial state changes with reference to a hydrostatic stress. In this appendix, a stress calculation procedure of the backward-Euler method with return mapping procedure using the Concrete Damaged Plasticity (CDP) model is described.

B.1. Stress-strain relationship

A uniaxial compressive and tensile stress-strain relationships are needed to an initial input data to calculate a multiaxial stress. The uniaxial compressive curve is used to calculated a cohesion value of the CDP model. The uniaxial stress-plastic strain relationships in tension and compression are also required to obtain a plasticity parameter (β).

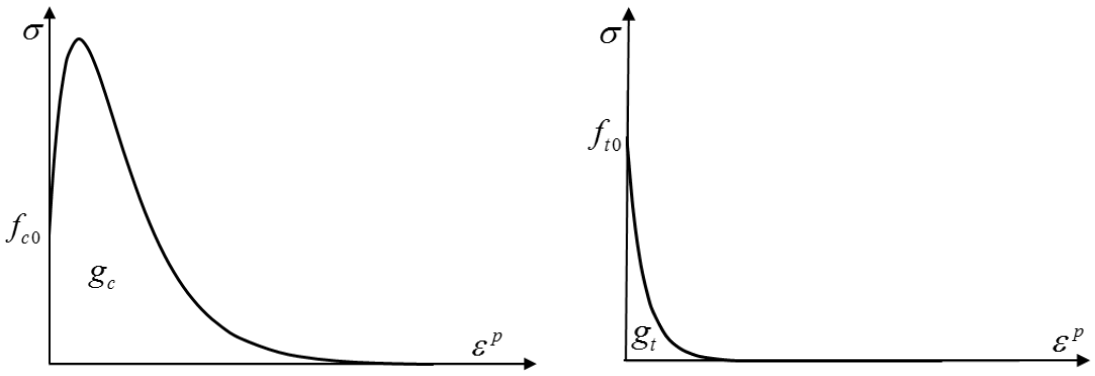

(a) Compressive curve (b) Tensile curve

Fig. B-1. Uniaxial stress-strain curve

Lubliner et al. (1989) reported a concrete compressive stress-strain curve using an exponential function. It was divided into two parts. One is a linear elastic part, and the other is a hardening and softening part. The uniaxial stress varies with reference to the parameter a and b provided in Eq. B.2. The higher the a value makes the higher the peak stress. The parameter b is related to the crushing energy value. The higher b value makes the stress-strain curve more brittle, and the smaller b value makes it more ductile. A tensile curve also used the same exponential function with different material parameters of a and b.

$$\sigma_c = E_{cm}\varepsilon \quad \text{for} \quad \sigma_c \le f_{c0} \tag{B-1}$$

$$\sigma_c = f_{c0}[(1+a)exp(-b\varepsilon^p) - aexp(-2b\varepsilon^p)] \quad \text{for} \quad \sigma_c \ge f_{c0} \tag{B-2}$$

where f_{cm}: the peak compressive strength of concrete

$f_{c0} = 0.4f_{cm}$: the maximum compressive stress in a linear region

ε^p: the plastic strain

a, b: the material parameters

An exponential function is used to express the damage parameter.

$$\mathrm{D} = 1 - \exp(-p\varepsilon^p) \tag{B-3}$$

where p: the material parameter for a damage function

D: the damage function

The effective stress-strain curve can be derived using the damage parameter. The stress and effective stress relationship can be expressed as:

$$\sigma_c = (1-D)\bar{\sigma}_c = exp(-p\varepsilon^p)\bar{\sigma}_c \tag{B-4}$$

$$\bar{\sigma}_c = \big(1 \div exp(-p\varepsilon^p)\big)\sigma_c \tag{B-5}$$

where $\bar{\sigma}_c$: the effective compressive stress

The effective stress is obtained by substitution Eq. B-2 into Eq. B-4.

$$\bar{\sigma}_c = f_{c0}\left[(1+a)\big(exp(-b\varepsilon^p)\big)^{(1-p/b)} - a\big(exp(-b\varepsilon^p)\big)^{(2-p/b)}\right] \tag{B-6}$$

B.2. Yield function

The CDP model proposed by Lubliner et al (1989) and modified by the Lee and Fenves (1998) is used to illustrate the failure surface of concrete. Its relationship is:

$$F(\bar{\sigma}, k) = \sqrt{3\bar{J}_2} + \alpha\bar{I}_1 + \beta\langle\hat{\bar{\sigma}}_{max}\rangle - \gamma\langle-\hat{\bar{\sigma}}_{max}\rangle - (1-\alpha)\bar{c}_c(k) \quad \text{(B-7)}$$

where α, β, γ: the concrete plasticity parameters

$\bar{c}_c(k)$: the cohesion stress with reference to the effective plastic strain

k: the equivalent plastic strain ($0 < k \leq 1$)

$\hat{\bar{\sigma}}_{max}$: the maximum effective principal stress

The nominal stress should be changed to the principal stress when using $\hat{\bar{\sigma}}_{max}$ term. A spectral decomposition method is used to convert the nominal stress to the diagonal matrix of eigenvalue (Lee and Fenves, 2001). Again, the eigenvalue stress will be converted to the nominal stress using eigenvectors after finishing the calculation.

The yield function in Eq. B-7 uses the maximum principal stress term. When adopting the Lode angle value, the yield function can also be expressed without the maximum principal stress term. It does not need to convert between the nominal and eigenvalue stress. In this study, the yield function with the Lode angle is adopted.

$$F(\bar{\sigma}, k) = \left(1 + \frac{2}{3}\rho cos\theta_L\right)\sqrt{3\bar{J}_2} + \left(\alpha + \frac{\rho}{3}\right)\bar{I}_1 - (1-\alpha)\bar{c}_c(k) \quad \text{(B-8)}$$

where $\rho = \beta$ when $\hat{\bar{\sigma}}_{max} > 0$

$\rho = \gamma$ when $\hat{\bar{\sigma}}_{max} \leq 0$

B.3. Flow rule

A flow rule defines the hardening and softening of the material. A non-associated flow rule is used to the concrete because the associated flow rule gives a larger dilation than expected. The Drucker-Prager hyperbolic function reads:

$$G(\sigma) = \sqrt{(\varepsilon_G \sigma_{t0} tan\psi)^2 + 3\bar{J}_2} + (tan\psi/3)\bar{I}_1 = \sqrt{B^2 + 3\bar{J}_2} + (tan\psi/3)\bar{I}_1 \quad \text{(B-9)}$$

where e_G : the eccentricity

σ_{t0} : the peak tensile stress

ψ : the dilation angle

$\mathrm{B} = e_G \sigma_{t0} tan\psi$

A plastic strain occurs in the normal direction to the plastic potential function. The dilation angle highly affects the flow direction because it decides the magnitude of the deviatoric and hydrostatic vectors. It can be expressed as:

$$\frac{\partial G}{\partial \bar{\sigma}} = \frac{1}{2}\frac{3\bar{s}}{\sqrt{B^2 + (3/2)\bar{s}:\bar{s}}} + \frac{tan\psi}{3}\boldsymbol{I} = \sqrt{\frac{3}{2}}\frac{\bar{s}}{\sqrt{(2/3)B^2 + \|\bar{s}\|}} + \frac{tan\psi}{3}\boldsymbol{I} \quad \text{(B-10)}$$

where $\bar{s}$: the effective deviatoric stress

$\boldsymbol{I}$: the unit matrix

B.4. Numerical integration

The backward-Euler method is widely used in a concrete plastic stress calculation because it is unconditionally stable. It uses a trial and correction stress to find a nonlinear stress value. The trial stress is calculated using the total strain increment of each step and the initial stiffness. The correction stress is a product of the initial stiffness and plastic strain. The stress can be obtained by extracting the trial stress to the correction stress.

$$\begin{aligned}\sigma_{n+1} &= E:\left(\varepsilon_{n+1}-\varepsilon_{n+1}^{p}\right)\\ &= E:\left(\varepsilon_{n}+\Delta\varepsilon-\varepsilon_{n}^{p}-\Delta\varepsilon^{p}\right)\\ &= E:\left(\varepsilon_{n}-\varepsilon_{n}^{p}\right)+E:\Delta\varepsilon-E:\Delta\varepsilon^{p}\\ &= \sigma_{n}+E:\Delta\varepsilon-E:\Delta\varepsilon^{p}\\ &= \sigma_{n+1}^{tr}-E:\Delta\varepsilon^{p}\end{aligned} \tag{B-11}$$

where $\Delta\varepsilon$: the strain increment

$\Delta\varepsilon^{p}$: the plastic strain increment

σ_{n+1}^{tr}: the trial stress

The CDP model is used to the concrete modelling which adopts a damage parameter and effective stress to calculate a yield stress. A nominal stress is converted to the effective stress using the damage parameter. A plastic stress is calculated in the effective stress space. After then, the effective stress is converted to the nominal stress using an updated damage value. It is assumed that the damage parameter is fixed until the plastic stress calculation. The damage parameter is updated using the effective plastic strain value that was obtained at the plastic stress calculation. The concrete stress in a nonlinear region can be obtained by the following steps:

1. Elastic predictor (trial stress) calculation: $\bar{\sigma}_{n}+E:\Delta\varepsilon=\bar{\sigma}_{n+1}^{tr}$
2. Plastic corrector calculation: $E:\Delta\varepsilon^{p}$
3. Damage corrector calculation: $D_{n+1}\bar{\sigma}_{n+1}$

The elastic predictor is easily obtained by using the current stress value, $\overline{\sigma}_n$, and the strain increment, $\Delta\varepsilon$. The initial stiffness is also given. When the trial stress is in the elastic domain, the stress of the next step is equal to the trial stress. The stress state whether it is in the elastic or plastic region is decided by the yield function. If the calculated yield value is below 0, its stress is in the elastic domain. On the other hand, the yield function is larger than 0, it needs to be corrected by the plastic corrector because its stress is in the plastic region.

$F(\bar{\sigma}, k) < 0$: Elastic domain

$F(\bar{\sigma}, k) \geq 0$: Plastic domain

The plastic strain can be obtained by iterative calculation until the residual is sufficiently small as provided in Fig. B-2. Parameters used in the following flow chart are:

σ: the stress

k: the equivalent plastic strain ($0 < k \leq 1$)

ε^p: the plastic strain

ε: the strain

D: the damage parameter

λ: the plastic multiplier

E: the elastic modulus

R: the residual

F^{tr}: the firstly calculated stress in a given strain value

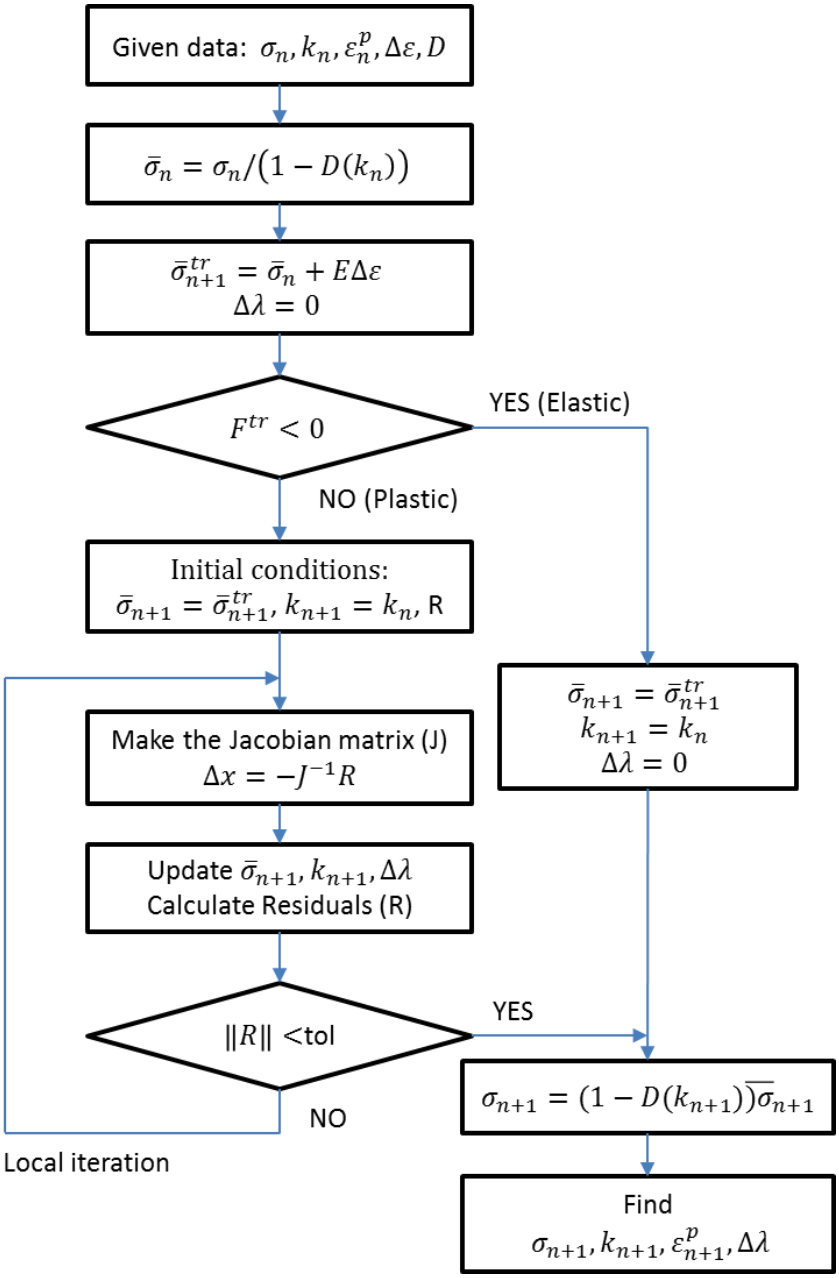

Fig. B-2. Flow chart of the stress calculation method

At the beginning, the initial plastic strain is assumed to be zero. Then, the plastic strain is modified by the local iteration process as shown in Fig. B-3; the Newton-Raphson method is used. The calculated values are accumulated with reference to the slope of the defined uniaxial curve. The difference between the trial stress and the targeted value is getting diminishing. When the difference is within the tolerance, the local iteration process is ended

and the stress is decided. This calculation concept can be used both in a hardening and softening region. Finding the plastic strain in a given strain increment is the key algorithm of this method.

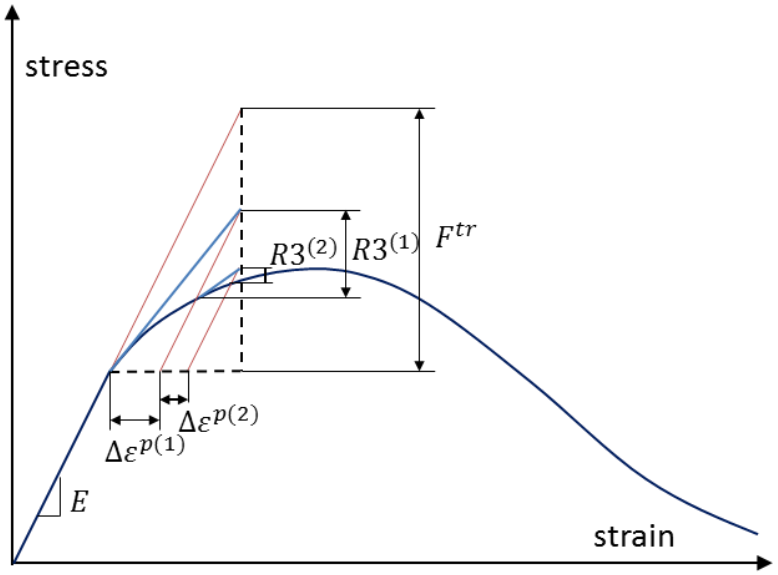

Fig. B-3. Plastic stress calculation method

The residuals of the stress, hardening parameter and plastic multiplier should be zero when all the variables are correctly decided; instead of zero, a predefined tolerance value is generally used. These are required to find the variables which satisfy all three residual equations. The residuals are defined as:

$$
\begin{aligned}
\mathrm{R1} &= \bar{\sigma}_{n+1} - \bar{\sigma}^{tr}_{n+1} + E\Delta\varepsilon^{p} \\
&= \bar{\sigma}_{n+1} - \bar{\sigma}^{tr}_{n+1} + \Delta\lambda E : m \\
\mathrm{R2} &= k_{n+1} - k_n - \Delta k_{n+1} \\
&= k_{n+1} - k_n - \Delta\lambda m \\
R3 &= \sqrt{3\bar{J}_{2,n+1}} + \alpha\bar{I}_{1,n+1} + \beta\langle\hat{\bar{\sigma}}_{max}\rangle - \gamma\langle-\hat{\bar{\sigma}}_{max}\rangle - (1-\alpha)\bar{c}(k_{n+1}) \\
&= \left(1 + \tfrac{2}{3}\rho cos\theta_L\right)\sqrt{3\bar{J}_{2,n+1}} + \left(\alpha + \tfrac{\rho}{3}\right)\bar{I}_{1,n+1} - (1-\alpha)\bar{c}(k_{n+1}) \\
&= AA\sqrt{3\bar{J}_{2,n+1}} + \mathrm{BB}\bar{I}_{1,n+1} - (1-\alpha)\bar{c}(k_{n+1})
\end{aligned}
\tag{B-12}
$$

where $\mathrm{m} = \dfrac{\partial G}{\partial \sigma}$

$\mathrm{AA} = \left(1 + \dfrac{2}{3}\rho cos\theta_L\right)$

$BB = \left(\alpha + \dfrac{\rho}{3}\right)$

$\rho = \beta$ when $\hat{\bar{\sigma}}_{max} > 0$

$\rho = \gamma$ when $\hat{\bar{\sigma}}_{max} \leq 0$

Jacobian matrix is required to find the incremental value when using the Newton-Raphson method. It is composed of partial differential forms of the stress, hardening variable and plastic multiplier. It indicates the slope of each calculation point as shown in Fig. B-3.

The Jacobian matrix is:

$$J = \begin{bmatrix} \dfrac{\partial R1}{\partial \sigma_{n+1}} & \dfrac{\partial R1}{\partial k_{n+1}} & \dfrac{\partial R1}{\partial \Delta\lambda} \\ \dfrac{\partial R2}{\partial \sigma_{n+1}} & \dfrac{\partial R2}{\partial k_{n+1}} & \dfrac{\partial R2}{\partial \Delta\lambda} \\ \dfrac{\partial R3}{\partial \sigma_{n+1}} & \dfrac{\partial R3}{\partial k_{n+1}} & \dfrac{\partial R3}{\partial \Delta\lambda} \end{bmatrix} = \begin{bmatrix} \boldsymbol{I}_6 & 0 & E:m \\ 0 & \boldsymbol{I}_2 & -m \\ \dfrac{\partial R3}{\partial \sigma_{n+1}} & \dfrac{\partial R3}{\partial k_{n+1}} & 0 \end{bmatrix}_{9\times 9} \quad \text{(B-13)}$$

The number in subscript shows the size of the identity matrix. The detailed expression of the Jacobian matrix is:

$$J = \begin{bmatrix} 1 & 0 & 0 & 0 & 0 & 0 & 0 & 0 & A1 \\ 0 & 1 & 0 & 0 & 0 & 0 & 0 & 0 & A2 \\ 0 & 0 & 1 & 0 & 0 & 0 & 0 & 0 & A3 \\ 0 & 0 & 0 & 1 & 0 & 0 & 0 & 0 & A4 \\ 0 & 0 & 0 & 0 & 1 & 0 & 0 & 0 & A5 \\ 0 & 0 & 0 & 0 & 0 & 1 & 0 & 0 & A6 \\ 0 & 0 & 0 & 0 & 0 & 0 & 1 & 0 & -B1 \\ 0 & 0 & 0 & 0 & 0 & 0 & 0 & 1 & -B2 \\ C1 & C2 & C3 & C4 & C5 & C6 & -D1 & -D2 & 0 \end{bmatrix} \quad \text{(B-14)}$$

where $P = 1/\sqrt{(2/3)B^2 + \|\bar{s}_{n+1}\|^2}$

$\mathrm{A1} = \mathrm{E}: m_1 = P\sqrt{6}G\bar{s}_1 + Ktan\psi$

$\mathrm{A2} = \mathrm{E}: m_2 = P\sqrt{6}G\bar{s}_2 + Ktan\psi$

$\mathrm{A3} = \mathrm{E}: m_3 = P\sqrt{6}G\bar{s}_3 + Ktan\psi$

$\mathrm{A4} = \mathrm{E}: m_4 = P\sqrt{6}G\bar{s}_4$

$\mathrm{A5} = \mathrm{E}: m_5 = P\sqrt{6}G\bar{s}_5$

$\mathrm{A6} = \mathrm{E}: m_6 = P\sqrt{6}G\bar{s}_6$

$\mathrm{B1} = r(\bar{\sigma})P\sqrt{3/2}\bar{s}_{max} + tan\psi/3$

$\mathrm{B2} = -\big(1 - r(\bar{\sigma})\big)P\sqrt{3/2}\bar{s}_{min} + tan\psi/3$

$$\mathrm{C1} = \frac{\partial \mathrm{R3}}{\partial \bar{\sigma}_1} = AA\sqrt{\frac{3}{2}}\frac{\bar{s}_1}{\|\bar{s}_{n+1}\|} + BB$$

$$\mathrm{C2} = \frac{\partial \mathrm{R3}}{\partial \bar{\sigma}_2} = AA\sqrt{\frac{3}{2}}\frac{\bar{s}_2}{\|\bar{s}_{n+1}\|} + BB$$

$$\mathrm{C3} = \frac{\partial \mathrm{R3}}{\partial \bar{\sigma}_3} = AA\sqrt{\frac{3}{2}}\frac{\bar{s}_3}{\|\bar{s}_{n+1}\|} + BB$$

$$\mathrm{C4} = \frac{\partial \mathrm{R3}}{\partial \bar{\sigma}_4} = 2AA\sqrt{\frac{3}{2}}\frac{\bar{s}_4}{\|\bar{s}_{n+1}\|}$$

$$\mathrm{C5} = \frac{\partial \mathrm{R3}}{\partial \bar{\sigma}_5} = 2AA\sqrt{\frac{3}{2}}\frac{\bar{s}_5}{\|\bar{s}_{n+1}\|}$$

$$\mathrm{C6} = \frac{\partial \mathrm{R3}}{\partial \bar{\sigma}_6} = 2AA\sqrt{\frac{3}{2}}\frac{\bar{s}_6}{\|\bar{s}_{n+1}\|}$$

$\mathrm{D1} = (1-\alpha)\frac{\partial \bar{c}_t(k_{max})}{\partial k_{max}}$: the slope of the uniaxial tensile curve at k_{max}

$\mathrm{D2} = (1-\alpha)\frac{\partial \bar{c}(k_{min})}{\partial k_{min}}$: the slope of the uniaxial compressive curve at k_{min}

$$\mathrm{K} = \frac{E}{3(1-2\nu)}$$

$$r(\bar{\sigma}) = \frac{\langle\bar{\sigma}_1\rangle + \langle\bar{\sigma}_2\rangle + \langle\bar{\sigma}_3\rangle}{|\bar{\sigma}_1| + |\bar{\sigma}_2| + |\bar{\sigma}_3|}$$

The incremental values are expressed as:

$$x_{i+1} = x_i - J^{-1}R(x_i)$$
$$\Delta x_{i+1} = x_{i+1} - x_i = -J^{-1}R(x_i) \quad \text{(B-15)}$$

where $R(x_i)$: the matrix form of the residuals

$x_i = \begin{Bmatrix} \bar{\sigma}_1 \\ \bar{\sigma}_2 \\ \bar{\sigma}_3 \\ \bar{\sigma}_{12} \\ \bar{\sigma}_{13} \\ \bar{\sigma}_{23} \\ k_{max} \\ k_{min} \\ \lambda \end{Bmatrix}$: the incremental values

The residual matrix is a column vector composed of R1, R2 and R3 presented in Eq. B-12.

From the initial conditions ($\bar{\sigma}_{n+1} = \bar{\sigma}_{n+1}^{tr}$, $k_{n+1} = k_n$), the initial residuals are zero except F^{tr} provided in Fig. B-3. The incremental values are:

$$\Delta x_{i+1} = -J^{-1}\begin{Bmatrix} 0 \\ 0 \\ 0 \\ 0 \\ 0 \\ 0 \\ 0 \\ 0 \\ F^{tr} \end{Bmatrix} = \frac{1}{A1C1 + A2C2 + A3C3 + A4C4 + A5C5 + A6C6 + B1D1 + B2D2}\begin{Bmatrix} -A1F^{tr} \\ -A2F^{tr} \\ -A3F^{tr} \\ -A4F^{tr} \\ -A5F^{tr} \\ -A6F^{tr} \\ B1F^{tr} \\ B2F^{tr} \\ F^{tr} \end{Bmatrix}$$

where $A1C1 + A2C2 + A3C3 + A4C4 + A5C5 + A6C6$

$$= \frac{AA3G\|\bar{s}_{n+1}\|}{\sqrt{(2/3)B^2 + \|\bar{s}_{n+1}\|}} + 3BBKtan\psi$$

$$B1D1 + B2D2 = r(\bar{\sigma})(1-\alpha)m_{max}\frac{\partial \bar{c}_t(k_{max})}{\partial k_{max}}$$

$$- (r(\bar{\sigma}) - 1)(1-\alpha)m_{min}\frac{\partial \bar{c}(k_{min})}{\partial k_{min}}$$

$$= (1-\alpha)\left\{r(\bar{\sigma})m_{max}\frac{\partial \bar{c}_t(k_{max})}{\partial k_{max}} - (r(\bar{\sigma}) - 1)m_{min}\frac{\partial \bar{c}(k_{min})}{\partial k_{min}}\right\}$$

The plastic multiplier is expressed as:

$$\Delta\lambda = \frac{F^{tr}}{\frac{AA3G\|\bar{s}_{n+1}\|}{\sqrt{(2/3)B^2 + \|\bar{s}_{n+1}\|}} + 3BBKtan\psi + (1-\alpha)slope} \quad \text{(B-16)}$$

where $slope = \left\{r(\bar{\sigma})m_{max}\frac{\partial \bar{c}_t(k_{max})}{\partial k_{max}} - (r(\bar{\sigma}) - 1)m_{min}\frac{\partial \bar{c}(k_{min})}{\partial k_{min}}\right\}$

B.5. Calculation examples

In the case of the uniaxial compressive state, the CDP model changes to the Drucker-Prager criterion because the additional parameters are only available in a bi and triaxial status. The yield function is:

$$f = (1 - \alpha)(\|\bar{\sigma}\| - \bar{c}(k)) \tag{B-16}$$

The calculation conditions are:

- C30/37 concrete
- E=33000 MPa, Poisson's ratio=0.2, α=0.1212
- Δε=0.0002
- Starts from $\sigma_n = k_n = \varepsilon_n^p = 0$

The stress is calculated at every strain increment. It shows the same response compared with the input data.

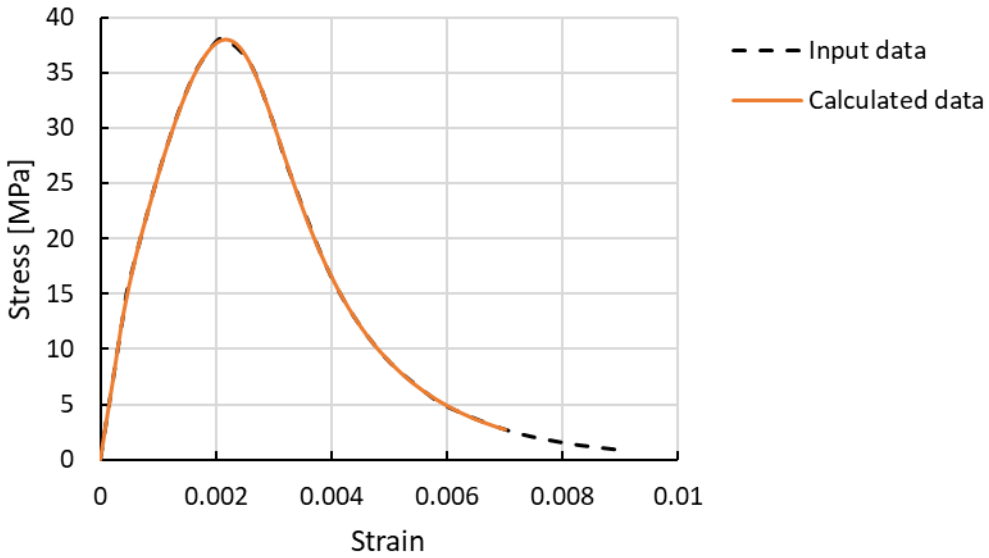

Fig. B-4. Uniaxial stress-strain curve

In the case of the triaxial compressive state, its stress changes with reference to the hydrostatic stress. The calculation conditions are:

- E=33000 MPa, Poisson's ratio=0.2, α =0.1212, γ =3, 1.5, 0
- Starts from $\sigma_n = k_n = \varepsilon_n^p = 0$
- Δε =[-0.0002 0.00004 0.00004 0 0 0]

Fig. B-5 shows the stress-plastic strain curve with respect to γ value. When the γ value increase, the failure surface becomes triangulated. The yield stress at the compressive meridian is getting larger according to the γ value increase.

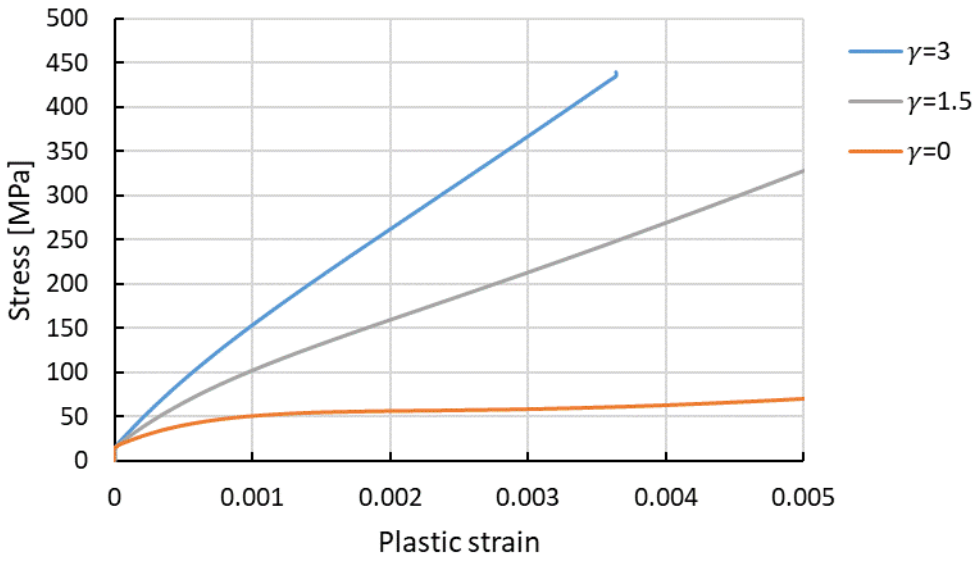

Fig. B-5. Triaxial stress-strain curve

B.6. MATLAB code for the triaxial stress calculation using the CDP model

```
function [stress, pstrain, k, D]=eCDP14(stressN, pstrainN,
dstrain, kn)
% concrete elastoplastic model ---- 3D with lode angle, 6
conponents
% EFFECTIVE stress
%
% stressN: current stress state [0 0 0 0 0 0]' using principal
stress
% pstrainN: current plastic strain [0 0 0 0 0 0]'
% dstrain: total strain increment
% kN: current equivalent plastic strain [0 0]'
%
% 0. initial functions included
% compression differential function for compressive hardening
ac=7.8729; bc=562.76; f0=15.2;
cc=@ (kc) f0*(-(1+ac)*bc*exp(-bc*kc)+2*ac*bc*exp(-2*bc*kc)); %
slope
% tension differential function for tensile hardening
at=-0.5; bt=163.13; ft0=2.9;
ct=@ (kt) ft0*(-(1+at)*bt*exp(-bt*kt)+2*at*bt*exp(-2*bt*kt)); %
slope
%
% compressive stress-plastic strain curve for cohesion stress
cohesion=@ (k) f0*((1+ac)*exp(-bc*k)-ac*exp(-2*bc*k));
% tensile stress-plastic strain curve for beta calculation
ctstress=@ (k) ft0*((1+at)*exp(-bt*k)-at*exp(-2*bt*k));
%
% EFFECTIVE Compressive/Tensile function for hardening and
softening
zc=501.2;
Dc=@ (kmin) 1-exp(-zc*kmin);
ecc=@ (kc) f0*(-(1+ac)*(zc-bc)*(exp(-bc*kc))^(1-zc/bc)-ac*(zc-
2*bc)*(exp(-2*bc*kc))^(2-zc/bc)); % EFF slope
zt=234.97;
Dt=@ (kmax) 1-exp(-zt*kmax);
ect=@ (kt) ft0*(-(1+at)*(zt-bt)*(exp(-bt*kt))^(1-zt/bt)-at*(zt-
2*bt)*(exp(-2*bt*kt))^(2-zt/bt)); % EFF slope
% Effective cohesion
ecohesion=@ (k) f0*((1+ac)*(exp(-bc*k))^(1-zc/bc)-ac*(exp(-
bc*k))^(2-zc/bc)); % check ok
%
%
% 0. Initial data defined
E=33000; nu=0.2; K=E/(3*(1-2*nu)); G=E/(2*(1+nu));
D0=(E/((1+nu)*(1-2*nu)))*[1-nu nu nu 0 0 0 ;
                          nu 1-nu nu 0 0 0 ;
                          nu nu 1-nu 0 0 0 ;
                          0 0 0 (1-2*nu)/2 0 0 ;
                          0 0 0 0 (1-2*nu)/2 0 ;
                          0 0 0 0 0 (1-2*nu)/2];
% 0. initial values for plastic flow
```

```
diang=36; phi=(pi/180)*diang; % dialtion angle
ft=2.9; e=0.1; B=ft*e*tan(phi); % B=0.2107
T=tan(phi); % T=0.7265
tol=1e-04; imax=20;
% failure function constants
a=0.1212; Iden=[1 1 1 0 0 0]'; kc=0.667; lamda=0;
beta=(1-a)*cohesion(kn(2))/ctstress(kn(1))-(1+a);
%
%
% 0. Converting EFFECTIVE stress
D=1-(1-Dc(kn(2)))*(1-Dt(kn(1))); % define damage
es=stressN/(1-D);
%
% 1. calculate trial stress from stressN and dstrain
str=es+D0*dstrain;  % EFFECTIVE
I1tr=sum(str(1:3));
devstr=str-(I1tr/3)*Iden;
normdevstr=sqrt(devstr(1)^2+devstr(2)^2+devstr(3)^2+2*(devstr(4)
^2+devstr(5)^2+devstr(6)^2));
%
% variable define for stress and hardening calculation
strp=str; knp=kn;
%
% 2. decides the Lode angle and rr using EIGEN VALUE
S=[str(1) str(4) str(5); str(4) str(2) str(6); str(5) str(6)
str(3)];
eigs=eig(S);
eigsI1=sum(eigs(1:3));
eigdevs=eigs-eigsI1/3;
angle=sqrt(3/2)*max(eigdevs)/normdevstr; % s(3) == s max
rr=(0.5*(abs(eigs(1))+eigs(1))+0.5*(abs(eigs(2))+eigs(2))+0.5*(a
bs(eigs(3))+eigs(3)))/(abs(eigs(1))+abs(eigs(2))+abs(eigs(3)));
%
% 3. define the roh value with respect to the max. principal
stress
if max(eigs)<= 1e-10  % this means zero for MATLAB error
    roh=(3*(1-kc))/(2*kc-1);
else roh=beta;
end
%
% parameter AA and BB
AA=(1+2*(roh/3)*angle);
BB=(a+(roh/3));
%
%
% 4. calculate incremental values %%% INITIAL  %%%
    ftr=sqrt(3/2)*AA*normdevstr+BB*I1tr-(1-
a)*ecohesion(kn(2)); % EFFECTIVE
    R=[0 0 0 0 0 0 0 0 ftr]'
%
% 5. verify the stress status
if ftr<0 % elastic
    stress=str*(1-D); % EFFECTIVE
```

```
    pstrain=pstrainN; k=kn;
else
%
% Iteration start
    for i=1:imax
%
% 6. calculate r(sigma) and flow rule parameter ------- LOOP
here
        P=1/(sqrt((2/3)*B^2+normdevstr^2)); % check ok
        m=zeros(6,1);
        m(1)=sqrt(3/2)*P*devstr(1)+(T/3);
        m(2)=sqrt(3/2)*P*devstr(2)+(T/3);
        m(3)=sqrt(3/2)*P*devstr(3)+(T/3);
        m(4)=sqrt(3/2)*P*devstr(4)*2;
        m(5)=sqrt(3/2)*P*devstr(5)*2;
        m(6)=sqrt(3/2)*P*devstr(6)*2;
        flow=D0*m;
%
% This is for the hardening parameter calculation
        m2=sqrt(3/2)*P*eigdevs+T/3;
%
% 7. make the jacobian
        A1=flow(1); % P*sqrt(6)*G*s(1)+K*T;
        A2=flow(2); % P*sqrt(6)*G*s(2)+K*T;
        A3=flow(3); % P*sqrt(6)*G*s(3)+K*T;
        A4=flow(4); % P*sqrt(6)*G*s(4)
        A5=flow(5);
        A6=flow(6);
        B1=rr*max(m2); %(P*sqrt(3/2)*s(3)+T/3); % === max
        B2=-(1-rr)*min(m2); %(P*sqrt(3/2)*s(1)+T/3); % === min
        C1=sqrt(3/2)*AA*devstr(1)/normdevstr+BB;
        C2=sqrt(3/2)*AA*devstr(2)/normdevstr+BB;
        C3=sqrt(3/2)*AA*devstr(3)/normdevstr+BB;
        C4=sqrt(3/2)*AA*devstr(4)*2/normdevstr;
        C5=sqrt(3/2)*AA*devstr(5)*2/normdevstr;
        C6=sqrt(3/2)*AA*devstr(6)*2/normdevstr;
        D1=(1-a)*ect(kn(1));  % slope (tension) EFFECTIVE
        D2=(1-a)*ecc(kn(2));   % slope (compression) EFFECTIVE
%
        J=[1  0   0  0  0  0  0  0  A1;
           0  1   0  0  0  0  0  0  A2;
           0  0   1  0  0  0  0  0  A3;
           0  0   0  1  0  0  0  0  A4;
           0  0   0  0  1  0  0  0  A5;
           0  0   0  0  0  1  0  0  A6;
           0  0   0  0  0  0  1  0  -B1;
           0  0   0  0  0  0  0  1  -B2;
           C1 C2 C3 C4 C5 C6 -D1 -D2 0];
%
% 8. Find the incremental values
        dx=-inv(J)*R;
% 9. update the values
        stress=str+dx(1:6);
```

```
        kn1=kn+dx(7:8);
        lamda=lamda+dx(9);
% 10. make a new deviatoric stress using updated stress
        I1up=sum(stress(1:3));
        sup=stress-(I1up/3)*Iden;

normsup=sqrt(sup(1)^2+sup(2)^2+sup(3)^2+2*(sup(4)^2+sup(5)^2+sup
(6)^2));
% 11. check the residuals
        R1=stress-strp+D0*lamda*m;
        R2=kn1-knp-lamda*[rr*max(m2) -(1-rr)*min(m2)]';
        R3=sqrt(3/2)*AA*normsup+BB*I1up -(1-
a)*ecohesion(kn1(2));
%
        if norm(R1)<tol && norm(R2)<tol && norm(R3)<tol
            i
            D=1-(1-Dc(kn1(2)))*(1-Dt(kn1(1)));
            stress=stress*(1-D);
            pstrain=pstrainN+lamda*m;
            k=kn1;
            break  % end calculation
% Otherwise update the Residual and stress. Do iteration
        else
            R=[R1(1) R1(2) R1(3) R1(4) R1(5) R1(6) R2(1) R2(2)
R3]';
            kn=kn1;
            str=stress;
            I1tr=sum(str(1:3));
            devstr=str-(I1tr/3)*Iden;

normdevstr=sqrt(devstr(1)^2+devstr(2)^2+devstr(3)^2+2*(devstr(4)
^2+devstr(5)^2+devstr(6)^2));
% Recalculate EIGEN VALUE terms
        S=[str(1) str(4) str(5); str(4) str(2) str(6); str(5)
str(6) str(3)];
        eigs=eig(S);
        eigsI1=sum(eigs(1:3));
        eigdevs=eigs-eigsI1/3;
        angle=sqrt(3/2)*max(eigdevs)/normdevstr; % s(3) == s max

rr=(0.5*(abs(eigs(1))+eigs(1))+0.5*(abs(eigs(2))+eigs(2))+0.5*(a
bs(eigs(3))+eigs(3)))/(abs(eigs(1))+abs(eigs(2))+abs(eigs(3)));
        AA=(1+2*(roh/3)*angle);
        BB=(a+(roh/3));
        end
        if i==imax
            break
        end
    end
end
```

APPENDIX C

Drawings of the push-out test specimens

The specimen with solid slabs

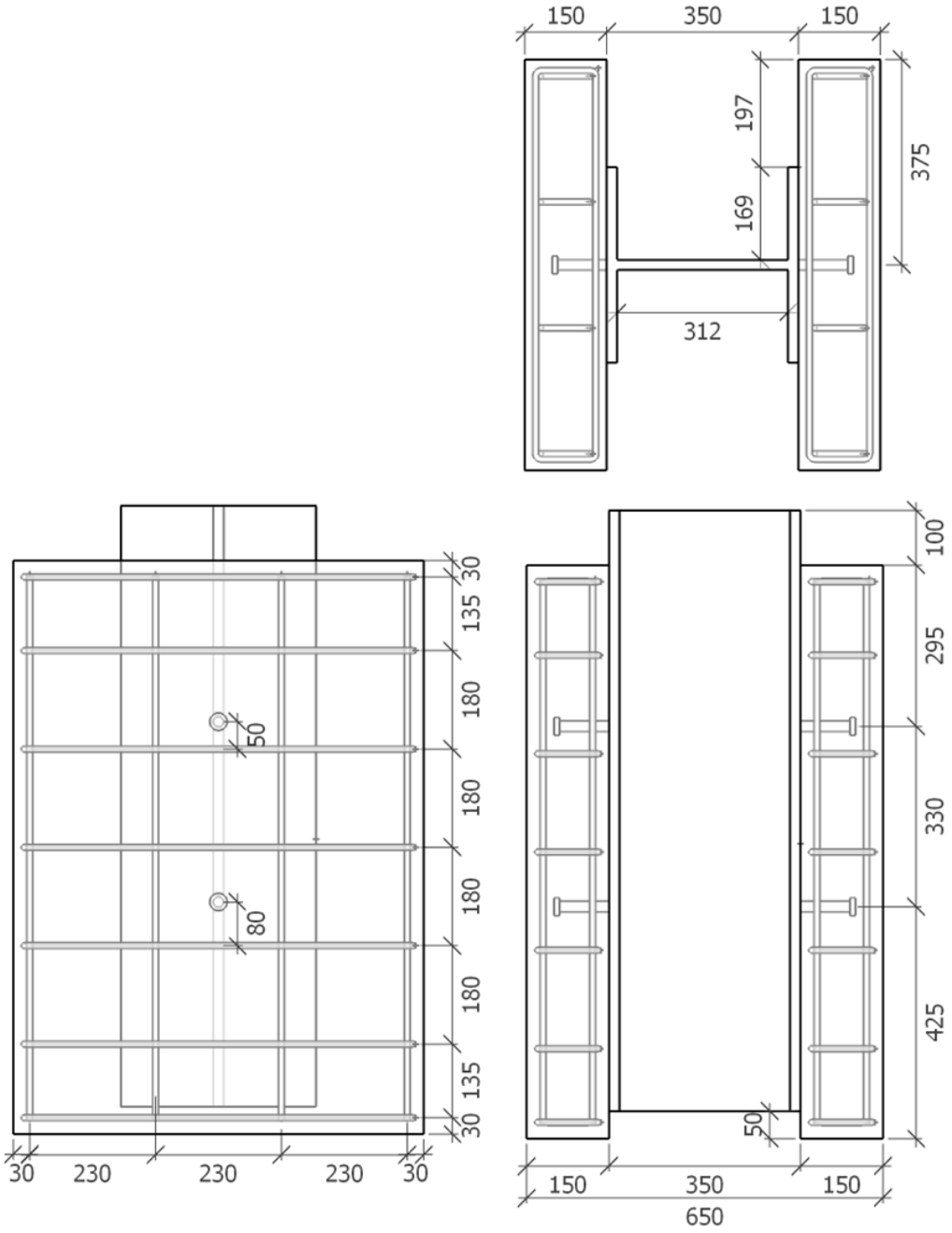

The specimen with transverse trapezoidal deck slabs